Swansea University
Prifysgol Abertawe

# Improved organic coating delamination resistance using physical vapour deposited Zn-Mg layers on strip steel

**Rebecca Shuriea Bolton**

Thesis submitted to Swansea University in fulfilment of the requirements for the degree of Engineering Doctorate (EngD) in Materials Engineering

**2020**

# Abstract

Physical vapour deposition (PVD) of zinc alloy coatings was investigated as a potential substitute process for commercially available hot dip galvanising (HDG) of strip steel. Therefore, zinc alloy coatings deposited by PVD were systematically compared with traditional sacrificial HDG zinc alloy coatings, in terms of bare metal corrosion resistance and resistance to corrosion-driven delamination of an organic overcoat, to establish the effects of magnesium content, microstructure and surface treatment. The effectiveness of modern corrosion inhibitor pigments, of known volume fraction, on HDG and PVD zinc coatings was also explored.

All PVD coatings and commercially available HDG coatings were characterised using microscopy techniques and x-ray diffraction to identify the microstructure and phases present as a function of magnesium content. It was confirmed that the PVD coatings were significantly thinner than the HDG coatings. The pure zinc PVD coating was comprised of hexagonal microplates, whereas the HDG counterpart contained grains 5-10 time larger. The PVD coating containing 4 wt% magnesium exhibited a discrete structure, a binary system of zinc-rich and $Mg_2Zn_{11}$-rich phases, much finer than the HDG Zn-Mg-Al (ZMA) coating. The PVD coatings containing 10 wt% and 20 wt% magnesium were studied using transmission electron microscopy as they possessed nanostructures containing $Mg_2Zn_{11}$ and $MgZn_2$ phases respectively.

Open circuit potential (OCP) measurements in chloride-containing solution established that an increase in magnesium content in PVD coating resulted in a decrease in the initial immersion open circuit potential. Additionally, increased magnesium content in the PVD layers also correlated with an increase in corrosion resistance, as made evident by reduced $E_{corr}$ and $I_{corr}$ values during potentiodynamic studies. Electrochemical impedance spectroscopy (EIS) comparative studies suggested an improvement in corrosion resistance exhibited by PVD0 compared to HDG, both zinc-only coatings, attributed to the finer and more compact surface morphology.

Bare metal corrosion response for all coatings was studied using a novel augmentation of the scanning vibrating electrode technique (SVET), known as SVET-TLI (time-lapse imaging). The combination of electrochemical mapping and photographic imagery revealed a potential optimum magnesium content within the PVD coatings. PVD4 exhibited the lowest anodic current density over a 24 hour study compared to the HDG, ZMA and other PVD coatings. Furthermore, the characteristic black staining attributed to magnesium corrosion was observed on the magnesium-containing PVD coatings. However, on the PVD Zn-Mg coatings the staining was observed in the regions established as net cathodes, which is contrary to association of staining with magnesium dissolution which takes place in local anodes.

Using the scanning vibrating kelvin probe (SKP) method, PVD4 was identified as the optimum magnesium composition as it was found to be resistant of both corrosion-driven cathodic delamination and anodic undermining. Cathodic delamination was observed on the zinc-only coatings, PVD0 and HDG, as well as PVD10 (although at a much slower rate). ZMA and PVD20, both $MgZn_2$-containing systems, showed resistance to cathodic delamination and evidence of anodic undermining.

Exploring several modern inhibitive pigments incorporated in the organic overcoat allowed the identification of a commercial pigment “PAM” to provide the greatest improvement in delamination resistance for the zinc-only metallic coatings.

# Declarations

This work has not previously been accepted in substance for any degree and is not being concurrently submitted in candidature for any degree.

Signed ......[redacted](candidate)

Date ..................15th April 2021.........................

This thesis is the result of my own investigations, except where otherwise stated. Other sources are acknowledged by footnotes giving explicit references. A bibliography is appended.

Signed .....[redacted] (candidate)

Date .................. 15th April 2021.........................

I hereby give consent for my thesis, if accepted, to be available for photocopying and for inter-library loan, and for the title and summary to be made available to outside organisations.

Signed ........[redacted].... (candidate)

Date .................. 15th April 2021.........................

# Acknowledgments

First and foremost I would like to thank Swansea University, Materials and Manufacturing Academy (M2A), TATA Steel, Engineering and Physical Sciences Research Council (EPSRC), European Social Fund (ESF) and Coated$^2$ for the opportunity and funding for this doctorate.

As my primary academic supervisor, I owe a lot of gratitude to Prof. Geraint Williams for his knowledge, guidance and absolutely contagious curiosity. You never just told me what to do and just get on with it, you provided the best environment for my own creativity and critical thinking to grow. For this I will always be grateful.

What is so great about Materials Engineering at Swansea University is the people (though the multi-million pound facilities were definitely appreciated). If I listed every single person whom I was able to approach comfortably and just gush over electrochemical maps, microstructure images and the like, I would need a separate volume to do them justice. Nevertheless, Prof. James Sullivan and Prof. Dave Penney, you are both key sources of my enthusiasm in corrosion and gave me confidence in my own work. Prof. Neil McMurray you are always a pleasure to talk to about anything. Dr Rees Charles your advice has been worth so much to me, and your passion for chemistry is infectious. Dr Natalie Wint you're the kind of researcher and academic I aspire to be and thank you for your help when I was writing my first paper.

I must also acknowledge all SVET and SKP users; Dr Rebecca Waldram, Dr Tom Lewis and Dr Phil Ansell in particular for their training. We all needed help at some point, and it was great to see everyone pass on the skills of tip making and troubleshooting.

Thank you also to the team over at TATA Steel IJmuiden, for accepting me as an intern for two weeks during my third year and providing support through my project.

Thank you to everyone else who has been a part of my life during my doctorate; whether we had a quick chat over a cuppa or a night out after a conference. I'm grateful for all the friendships I've made along the way. A special thank you to Dr Chris Griffiths for endless advice, support and proof reading over my entire thesis. Dr Sarah-Jane Potts and Dr Andrew Allman also provided invaluable support during my write-up year, for which I will always be grateful.

I wouldn't have even taken up the challenge of the doctorate without the support of my husband, Justin. Thank you for your partnership, patience and encouragement, my love. Thank you also to my mother and my sister for their love and inspiration to work hard. A special mention for my beloved cat, Binx, who was a great source of comfort and distraction during my doctorate.

This work is dedicated to my father, Martin Franklin. I think you'd have been proud.

# Contents

## Chapter 4. Electrochemical characterisation of PVD Zn-Mg coatings using DC electrochemistry and EIS .....91

# List of Figures

# List of Tables

# Chapter 1. Introduction and literature review

## 1.1 Introduction

In the last two decades there has been a focus on the potential for physical vapour deposition (PVD) technology to replace current galvanising techniques in the automotive industry [1–8]. The literature that currently exists explores the various PVD processes, their potential for in-line scale up and the quality of the coatings. PVD processes are inherently low temperature (<250 °C), and produce metallic coatings which are thinner and more homogeneous than those deposited using hot dip galvanising. Furthermore, PVD is considered a cleaner method for coating steel when compared with wet bath methods due to the lack of waste and limited pollution [2]. It is for these reasons that major steelmaking companies such as Tata Steel and POSCO have invested in research and development into PVD as a possible alternative coating method for strip steel.

The potential for scale-up of PVD processes to a continuous strip line has been established; multiple air-to-air strip pilot lines exist [5,6,9,10]. However, although the finishing costs of traditional methods, such as hot dip galvanising and electroplating, exceed those estimated for lines utilising PVD technology, the initial investment cost and complex management requirement discourages any change to pre-existing galvanising lines. It is clear that the end product benefits of PVD coatings must be revolutionary in the field of corrosion protection for the industry to consider the steep initial investment worthwhile for the long term.

However, there currently exists a gap in the catalogues of steelmakers; advanced high strength steels (AHSS) and ultra-high strength steels (UHSS) are currently not compatible with galvanising processes [10]. The parameters of the galvanising process and nature of the coating deposition have a significant effect on the local compositions and microstructure of advanced steels, which rely heavily on chemical distribution and grain morphology (designed through thermal cycling). For example, transformation induced plasticity (TRIP) steels have a relatively high Si content which negatively affects the wetting of the strip surface by the molten zinc [11]. Additionally, the relatively high temperature iso-thermal soaking of the substrate required for the hot dip galvanising process has been found to negatively influence mechanical properties [12]. Thus, numerous research and development projects have arisen in the attempt to overcome the incompatibility issue of AHSS grades and galvanising. One approach is to alter the composition of the steels to make them suitable for galvanising; however, this sacrifices the mechanical properties of the steel. A recent example of this was the addition of tin to the steel composition, which improved the wettability and adhesion of the galvanised layer [13], however tin is considered a tramp element which adversely effects the properties of steel [14]. Electroplating offers a lower temperature process, however it is well understood that high strength steels suffer from severe hydrogen embrittlement from the electroplating process [15–17].

The method adopted by Tata Steel involves the application of Zn-Mg PVD coatings to these tailored steels as a low temperature alternative. The collection of work set out in this thesis serves to provide evidence in support of the PVD coating process as a viable alternative to hot dip galvanising. Previous preliminary work has shown the potential for Zn-Mg PVD coatings in terms of their processability, corrosion resistance and resistance to organic coating failure [2, 5, 7,18–22]. Therefore the aim of this thesis is to expand on the pre-existing work with a systematic evaluation of PVD Zn and Zn-Mg coatings. This includes a full microstructural and electrochemical evaluation of pre-existing commercial Zn alloy coatings and a selection of novel PVD Zn-Mg coatings containing a range of magnesium concentrations. Investigating the microstructural properties of the metallic coatings provides potential explanations for the differences in corrosion response exhibited by the different coatings.

The localised bare metal corrosion behaviour of the commercial galvanised coatings and PVD coatings when immersed in corrosive electrolyte is characterised by using a novel combination method of a scanning vibrating electrode technique (SVET) and time-lapse imaging.

The compatibility of PVD Zn coatings with state of the inhibitive pigments is also investigated using the scanning kelvin probe (SKP) for a model coating system and compared with pigment-free control systems for PVD coatings and the well-established commercial galvanised coatings.

## 1.2 Corrosion theory

### *1.2.1 Aqueous corrosion*

Corrosion is a deteriorative mechanism which occurs between a metal and its environment resulting in impairment of the properties of the metal component [23]. The process is a result of metals possessing inherently higher free energy, G, than their corrosion products; in order to extract a metal from its ore, energy must be absorbed by the metal making it thermodynamically unstable. Therefore, the metal will tend to corrode to achieve stability (see **Figure 1.1**) and the free energy change from metal to corrosion products, $\Delta G$, will be negative. Hence corrosion can be considered as “the thermodynamic process by which metals revert to their natural form as ores” [24]. However, an activation energy barrier, $\Delta G^*$, prevents metals from spontaneously corroding in air and determines the rate of corrosion; the larger this barrier the slower the corrosion process.

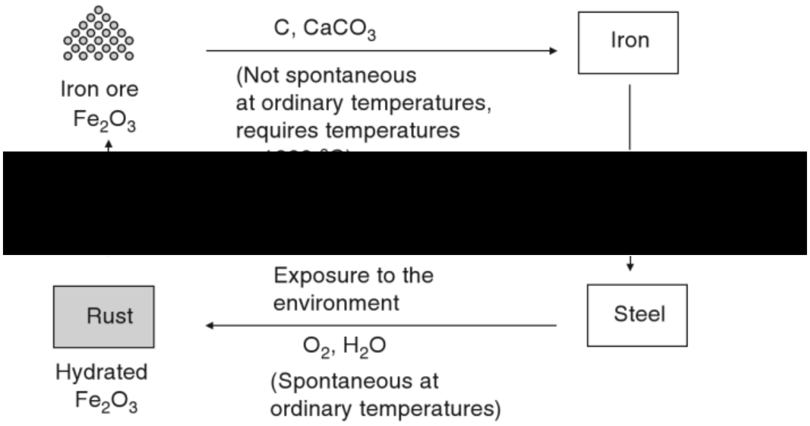

[redacted]

**Figure 1.1:** The thermodynamic cycle for steel [24].

**Figure 1.2** presents a graphical profile of free energy in a metal system; the input of thermodynamic energy during metal extraction is shown as a positive change in free energy, +ΔG, followed by the metastable state of an extracted metal. The tendency for a metal to corrode is shown by a decrease in free energy, -ΔG; the greater this value, the higher the driving force of corrosion.

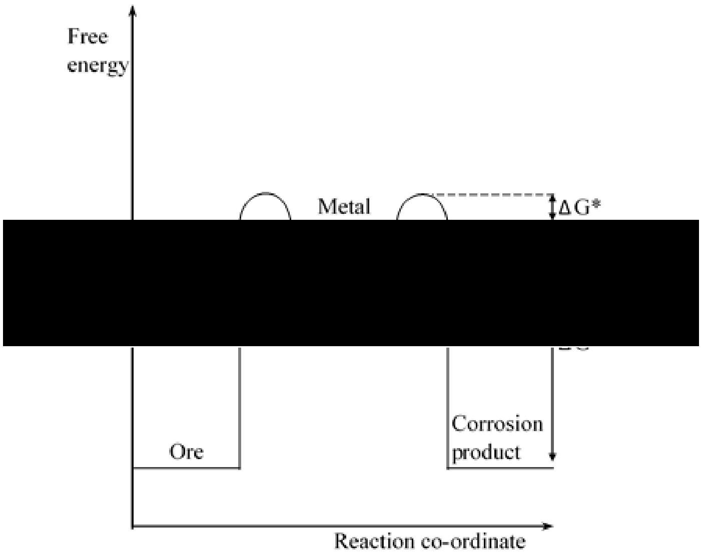

[redacted]

**Figure 1.2:** A thermodynamic energy profile for metals and their compounds [25].

In electrochemical terms, during the corrosion process, two or more reactions take place simultaneously, and each reaction will have a different potential. Current will flow from high to low potential within the presence of an electrolyte, creating an electrochemical cell. The anode of the cell (the metal) discharges electrons, which are used up in the reaction(s) at the cathode (the same metal, or another). A basic example of this process is shown in **Figure 1.3**; a "voltaic" or "galvanic" cell comprised of two different metal species, zinc and copper, submerged within solutions of equivalent ions (zinc sulphate solution and copper sulphate solution respectively). The metals are connected electrically via a wire and the solutions are separated by a semi-permeable membrane to prevent the copper ions from reaching the zinc electrode.

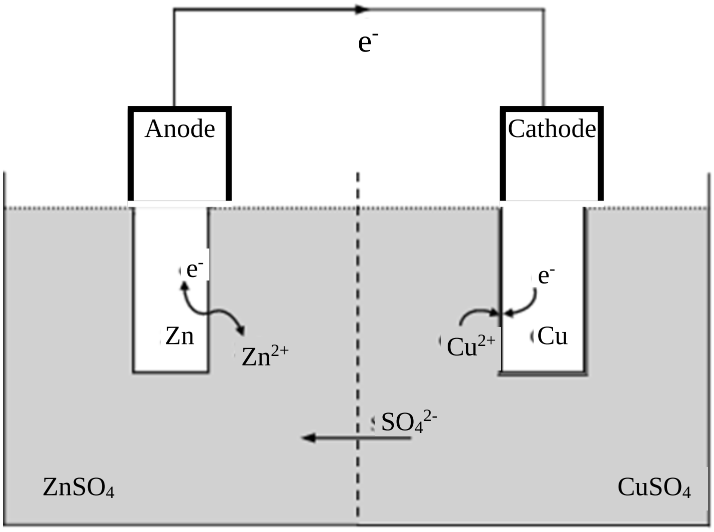

**Figure 1.3:** Diagram of the Daniell cell.

The zinc metal corrodes, producing zinc ions and electrons:

$$Zn \rightarrow Zn^{2+} + 2e^{-} \tag{1.1}$$

The free electrons pass along the connecting wire and into the copper electrode where they combine with copper ions at the surface to create copper metal:

$$Cu^{2+} + 2e^{-} \rightarrow Cu \quad (1.2)$$

The sulphate ions are permitted through the semi-permeable membrane in order to balance the charge. The complete cell reaction is both half cells combined:

$$Zn + Cu^{2+} \rightarrow Zn^{2+} + Cu \quad (1.3)$$

By convention, the half-cell containing the reduced species is considered the left-hand side equation, LHE, and therefore the half-cell containing the oxidised species is the right-hand side equation, RHE [26].

The driving force of the cell is created by the difference between the two standard electrode potentials of each half-cell. The change in Gibbs free energy can be expressed in volts as per the following relationship:

$$\Delta G = -nFE \quad (1.4)$$

Where n is the number of electrons transferred in the equation, F is the Faraday constant (96,485 $C.mol^{-1}$) and E is the EMF in volts [27]. Due to the negative operator in the equation, the more positive the value of E, the greater the tendency for the reaction to take place. The EMF value of a full cell, $E_{cell}$, is calculated by subtracting the EMF of the LHE from the EMF of the RHE:

$$E_{cell} = E^{0}_{RHE} - E^{0}_{LHE} \quad (1.5)$$

$E^0$ is the standard electrode potential of a half-cell and most values can be found in literature.

In order to take into consideration the concentration of reactants and products of a half-cell, the Nernst Equation, derived elsewhere [27], can be applied to calculate the exact EMF:

$$E = E^0 - \frac{RT}{nF} \ln \frac{[\text{reduced}]}{[\text{oxidised}]} \qquad (1.6)$$

The standard electrode potentials, $E^0$, of most half-cell reactions are ranked in the EMF series (**Figure 1.4**); the values are in reference to the standard hydrogen electrode (SHE) and are displayed as reduction reactions, with the reduction of hydrogen defined as zero potential.

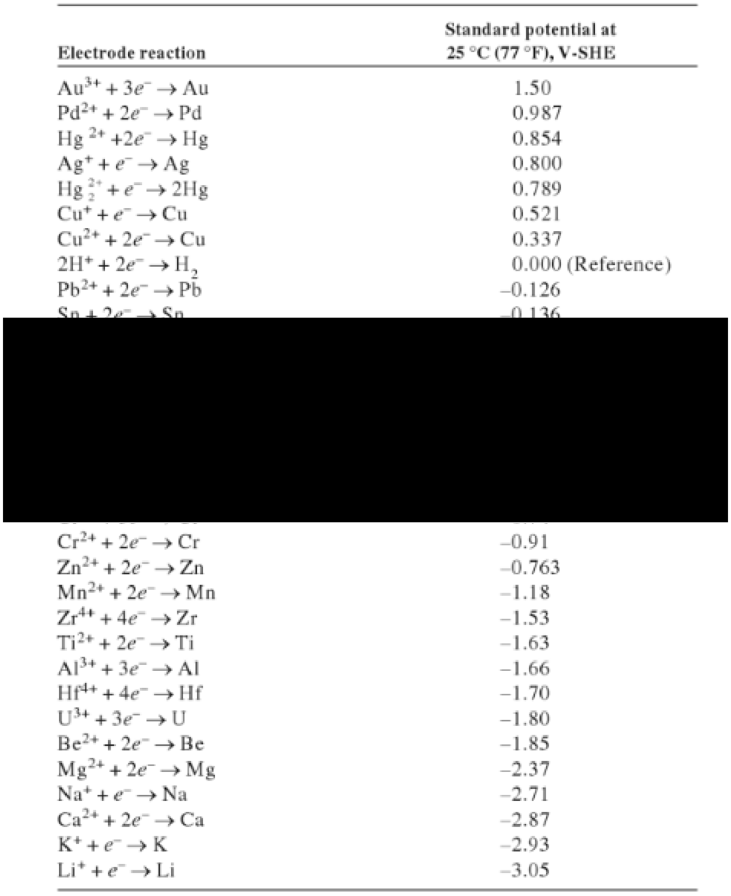

| Electrode reaction | Standard potential at 25 °C (77 °F), V-SHE |
|---|---|
| $Au^{3+} + 3e^- \rightarrow Au$ | 1.50 |
| $Pd^{2+} + 2e^- \rightarrow Pd$ | 0.987 |
| $Hg^{2+} + 2e^- \rightarrow Hg$ | 0.854 |
| $Ag^+ + e^- \rightarrow Ag$ | 0.800 |
| $Hg_2^{2+} + e^- \rightarrow 2Hg$ | 0.789 |
| $Cu^+ + e^- \rightarrow Cu$ | 0.521 |
| $Cu^{2+} + 2e^- \rightarrow Cu$ | 0.337 |
| $2H^+ + 2e^- \rightarrow H_2$ | 0.000 (Reference) |
| $Pb^{2+} + 2e^- \rightarrow Pb$ | –0.126 |
| [redacted] | [redacted] |
| $Cr^{2+} + 2e^- \rightarrow Cr$ | –0.91 |
| $Zn^{2+} + 2e^- \rightarrow Zn$ | –0.763 |
| $Mn^{2+} + 2e^- \rightarrow Mn$ | –1.18 |
| $Zr^{4+} + 4e^- \rightarrow Zr$ | –1.53 |
| $Ti^{2+} + 2e^- \rightarrow Ti$ | –1.63 |
| $Al^{3+} + 3e^- \rightarrow Al$ | –1.66 |
| $Hf^{4+} + 4e^- \rightarrow Hf$ | –1.70 |
| $U^{3+} + 3e^- \rightarrow U$ | –1.80 |
| $Be^{2+} + 2e^- \rightarrow Be$ | –1.85 |
| $Mg^{2+} + 2e^- \rightarrow Mg$ | –2.37 |
| $Na^+ + e^- \rightarrow Na$ | –2.71 |
| $Ca^{2+} + 2e^- \rightarrow Ca$ | –2.87 |
| $K^+ + e^- \rightarrow K$ | –2.93 |
| $Li^+ + e^- \rightarrow Li$ | –3.05 |

**Figure 1.4:** Electromotive force series [28].

For corrosion of a single metal in electrolyte the anodic reaction is always the oxidation of the metal into its respective ions. There are multiple cathodic reactions that can take place on the metal surface depending on the environment:

$$O_2 + 2H^+ + 4e^- \rightarrow 2H_2O \tag{1.7}$$

$$O_2 + 2H_2O + 4e^- \rightarrow 4OH^- \tag{1.8}$$

$$2H^+ + 2e^- \rightarrow H_2 \tag{1.9}$$

Equations 1.7 and 1.8 represent the reduction of oxygen; a common cathodic process in real life applications as dissolved $O_2$ is highly likely to be present. In acidic media, equation 1.7 dominates due to the abundance of $H^+$ ions. Neutral and basic media promotes equation 1.8. In acid or neutral environments where oxygen availability is limited, equation 1.9, the evolution of hydrogen, takes place.

### *1.2.2 Pourbaix Diagrams*

Pourbaix diagrams, or potential/pH diagrams, display the domains for stability of an electrochemical system, with respect to the voltage potential (vs. SHE) and pH, under equilibrium conditions. The diagrams were named after Marcel Pourbaix, a Belgian corrosion scientist who invented them and was first to publish a compendium of diagrams for numerous species [29].

The domain boundaries are calculated using the Nernst Equation (equation 1.6) if they represent redox equilibria; there are four reactants in equilibria with metallic Zn when immersed in water, which are represented by the following equations:

$$Zn^{2+} + 2e^{-} \leftrightarrow Zn \tag{1.10}$$

$$Zn(OH)_2 + 2H^{+} + 2e^{-} \leftrightarrow Zn + 2H_2O \tag{1.11}$$

$$HZnO_2^{-} + 3H^{+} + 2e^{-} \leftrightarrow Zn + 2H_2O \tag{1.12}$$

$$ZnO_2^{2-} + 4H^{+} + 2e^{-} \leftrightarrow Zn + 2H_2O \tag{1.13}$$

The dissolution of zinc to its respective ions (equation 1.10) is independent of pH and therefore corresponds to a horizontal line on the Pourbaix diagram (**Figure 1.5**). The reactions shown in equations 1.11-1.13 vary linearly with pH. It is important to note that the construction of a Pourbaix diagram relies on the selection of an arbitrary concentration of the $Zn^{2+}$ ions, which in this case is $10^{-6}$ M.

Purely chemical equilibria (non-redox) are electrode potential independent and take place at a specific pH, which is identified by first calculating the equilibrium constant [29]. In the case of zinc, the following equilibria exist:

$$Zn^{2+} + 2H_2O \leftrightarrow Zn(OH)_2 + 2H^{+} \tag{1.14}$$

$$Zn(OH)_2 \leftrightarrow HZnO_2^{-} + H^{+} \tag{1.15}$$

$$HZnO_2^{-} \leftrightarrow ZnO_2^{2-} + H^{+} \tag{1.16}$$

The calculated pH values for equations 1.14-1.16 are 8.48, 10.67 and 13.11 respectively and are plotted as vertical lines in **Figure 1.5**.

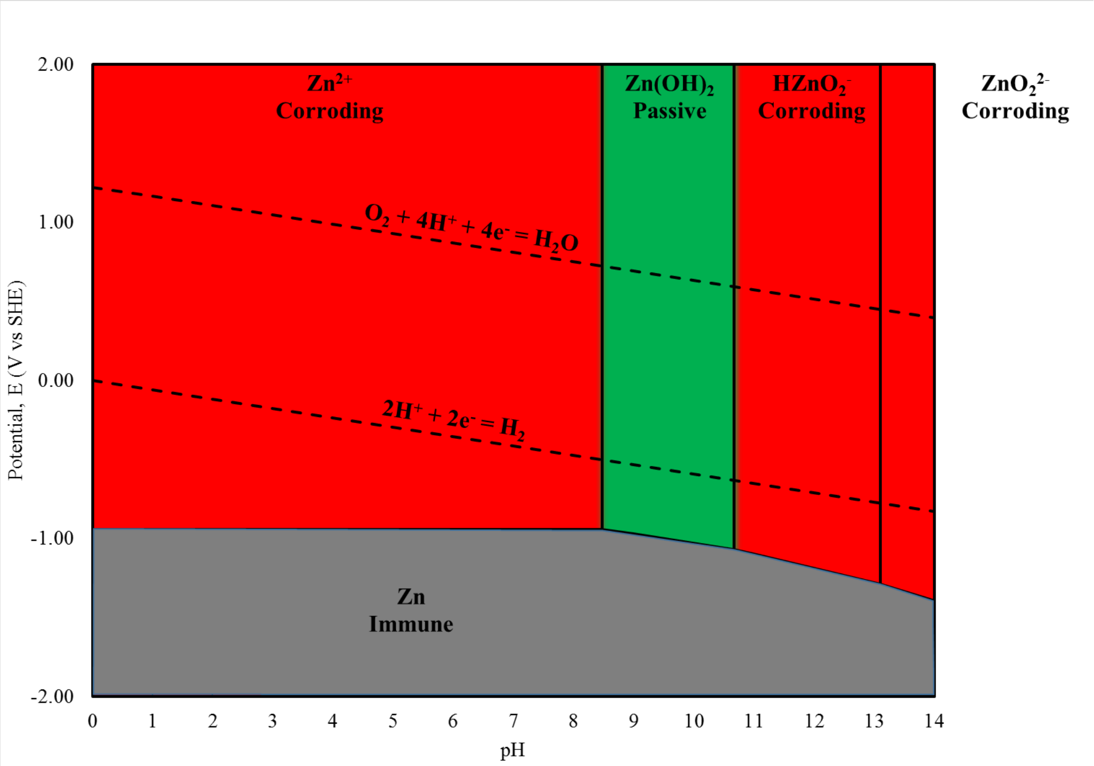

**Figure 1.5:** Potential/pH equilibrium diagram for zinc in water at room temperature; adapted from the original in Pourbaix's work [29].

Pourbaix diagrams serve the purpose to provide guidelines for the stability of a species. One key limitation of a potential-pH plot is the lack of rate information; Pourbaix diagrams are based solely on thermodynamic data and can therefore be inapplicable to real life systems. For example, the formation of a protective film, for a species, at a certain pH may only occur after a significantly long period of time which would allow further attack of the species in its absence. The Pourbaix diagrams are also restricted to wet corrosion and do not account for localised corrosive attack. Moreover, the existing atlas of Pourbaix diagrams [29] only contains plots for pure metals which is highly unrealistic to real world scenarios.

Nevertheless, a Pourbaix diagram can indicate conditions where a species is active, passive and immune which is highly useful in the field of corrosion control. They provide the fundamental stability behaviour of species under certain conditions, which can be considered invaluable when approaching a corrosion problem. Indeed, the diagrams are a useful starting tool even for the study of alloys as one can study both the constituent species separately to form a logical starting point. For example, the Pourbaix diagram shown in **Figure 1.6** suggests that magnesium is only stable in water, at room temperature, above pH 11.5 due to the formation of a protective passive film. This could imply that a Zn-Mg alloy would theoretically always be freely corroding, as one or both of the species would be active at any given pH. On the other hand, the combination of the diagrams could also suggest that within the zinc passive region the developed $Zn(OH)_2$ prevents both species from attack, and, likewise, in the magnesium passive region the amphoteric zinc is protected by $Mg(OH)_2$. The latter explanation is closer to what is seen in reality.

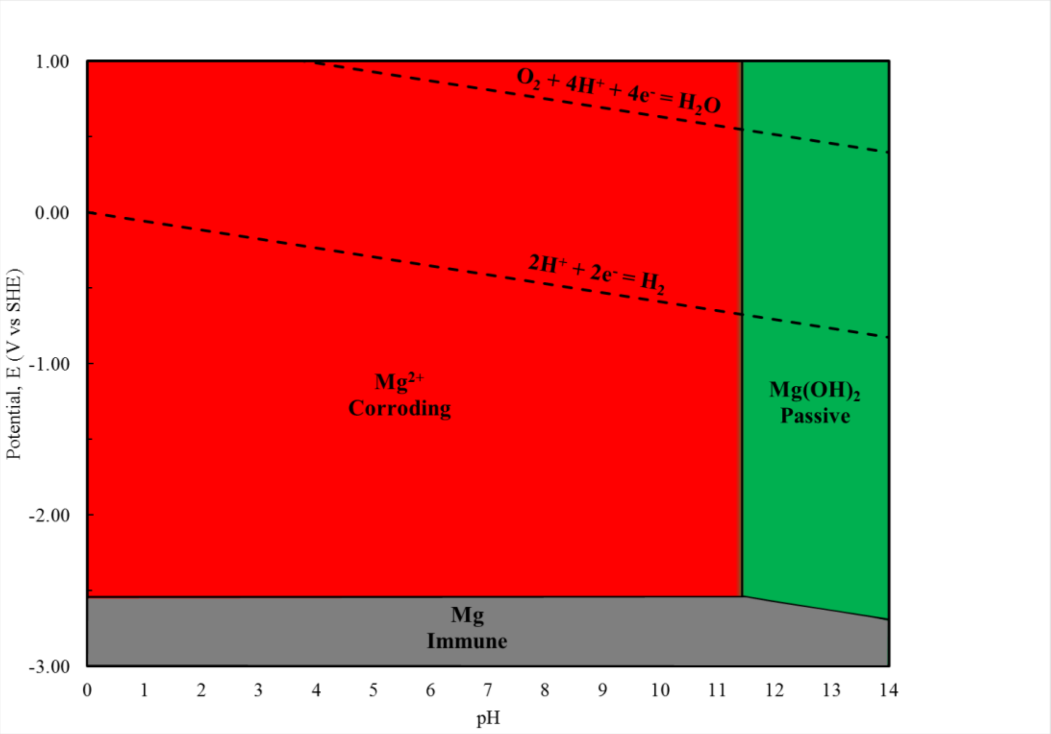

**Figure 1.6:** Potential/pH equilibrium diagram for magnesium in water at room temperature; adapted from the original in Pourbaix's work [29].

### 1.2.3 Corrosion Kinetics

A key property of sacrificial metals and alloys in industry is the rate at which they corrode. Corrosion is an inevitable process for metals as explained in 1.2.1. Whilst the thermodynamics of a system recognise the tendency for a material to corrode, the kinetics of the system detail the rate at which corrosion occurs. However, kinetic equations must reduce to thermodynamic equations under equilibrium conditions; in the case of corrosion rate theory, the equilibrium state is defined by the Nernst Equation previously mentioned (equation 1.6). Under non-equilibrium conditions, current flow is dependent on electrode potential. To maintain current flow, an overpotential ($\eta$) must be applied:

$$\eta = E - E_{eq} \tag{1.17}$$

where $E_{eq}$ is the equilibrium potential of an electrode and E is the actual potential of the electrode. In 1905, Julius Tafel published two papers containing a significant amount of data which he summarised to show the logarithmic relationship between overpotential and current, i:

$$\eta = a \pm b \ln i \tag{1.18}$$

where a and b were constants, and the signage of the equation depended on whether it was anodic or cathodic [30,31].

Butler and Velmer's approach to electrochemical rate also relied on the relationship between electrode current and overpotential; they assumed that the anodic and cathodic reactions were taking place on the same electrode:

$$j = j_0 \cdot \{ \exp [\frac{\alpha_a nF\eta}{RT}] - \exp [\frac{\alpha_c nF\eta}{RT}] \} \tag{1.19}$$

where j is the electrode current density, $j_0$ is the exchange current density, $\alpha_a$ is the anodic charge transfer coefficient, $\alpha_c$ is the cathodic charge transfer coefficient, n is the valency, F is Faraday's constant, η is the activation overpotential (as defined by equation 1.17), R is the gas constant and T is the absolute temperature. At sufficiently large anodic overpotentials, $\eta_a$, the Butler-Velmer equation can be simplified to:

$$j = j_0 \cdot \exp [\frac{\alpha nF\eta_a}{RT}] \tag{1.20}$$

Rearranging this results in a form of the Tafel equation for anodic polarisation:

$$\eta_a = b_a \log (j/j_0) \tag{1.21}$$

where $b_a$ is the anodic Tafel slope. The same equation can be used when substituting cathodic overpotential values, with $b_c$ as the corresponding cathodic Tafel slope:

$$\eta_a = -b_c \log (|j|/j_0) \tag{1.22}$$

The key milestone for theoretical corrosion kinetics was a German paper published by Wagner and Traud in 1938 [32]. An important concept first established in this paper was the "mixed potential theory". A mixed electrode is an electrode which is in contact with one or more redox reactions; the reactions take place at the phase boundary between the metal and electrolyte, as stated in the 1938 paper. The theory assumes that redox reactions can be divided into two or more partial reactions and that there is a conservation of charge as these reactions take place.

$$\sum i_{anodic} = -\sum i_{cathodic} = i_{corr} \tag{1.23}$$

Thus, the total current of all anodic partial reactions ($i_{anodic}$) must equal the total current density of all cathodic partial reactions ($i_{cathodic}$), and both combined give the rate of corrosion, $i_{corr}$. Under conditions where $i_{corr} = 0$, corroding species can be characterised by a free corrosion potential, $E_{corr}$.

Based on the previously established theory, Stern and Geary were able to derive the following equation in their 1957 paper [33]:

$$i_{corr} = \frac{b_a|b_c|}{(b_a+|b_c|2.3R_p)} \tag{1.24}$$

where $R_p$ is the polarisation resistance. Simplification of equation 1.24 results in the relationship $i_{corr} = B/R_p$, where B is a proportionality constant. If $b_a$ and $b_c$ are unequal, as is generally the case in practical electrochemistry, B becomes dominated by the smaller of the two values (e.g. under conditions of cathodic mass transport control, $B = b_a/2.3$) [34].

A Tafel plot can be drawn by plotting the individual electrode potential, E, against the log of the current, i. An Evans diagram is the depiction of two electrode reactions which intersect at the point of the free corrosion current density, $i_{corr} = 0$ (as defined by equation 1.23), where the free corrosion potential, $E_{corr}$, can be extrapolated as seen in **Figure 1.7**.

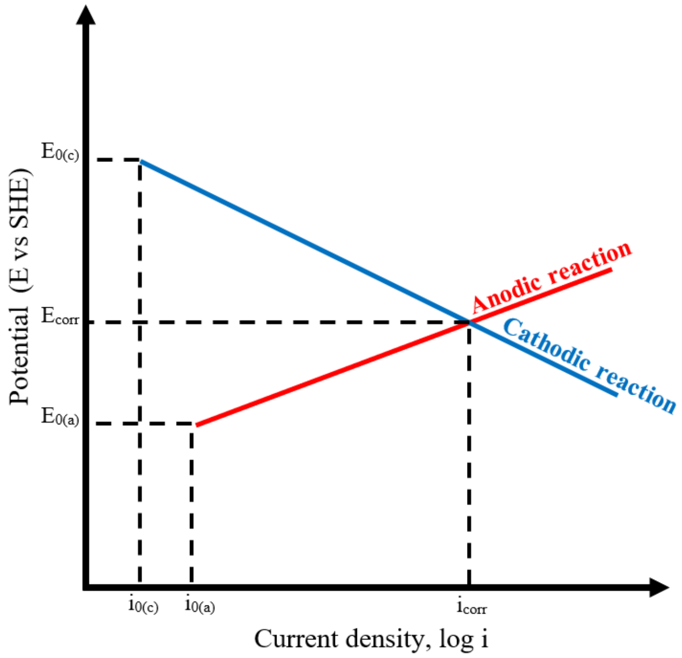

**Figure 1.7:** Basic elements of an Evans diagram.

### *1.2.4 The Electrochemical Double Layer*

An electrochemical double layer (EDL) is the formation of two layers of opposing charge built up on the surface of a metal in the presence of electrolyte. Helmholtz initially discovered that charged electrodes, submerged in electrolyte, would repel ions of like charge and attract ions of opposing charge. Furthermore, he elucidated the nature of this double layer as a molecular dielectric by showing that the surface of the electrode and plane of attracted ions act as parallel plates of opposite charge (much like a capacitor) [35]. **Figure 1.8** is a schematic of this early model, demonstrating the potential shift from the electrode into bulk solution.

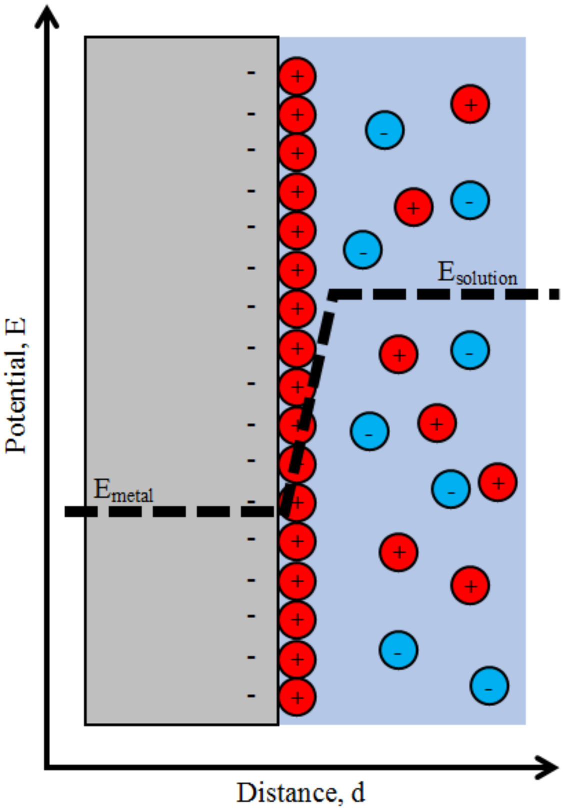

**Figure 1.8:** Helmholtz model of the double layer.

This early model neglects the influence of potential or ionic concentration on the capacitance, a flaw which Gouy and Chapman identified and remedied in their works [36,37]. However, they made assumptions in their work also which limited any quantitative applications; they assumed that ions act as point charges and there was no physical restriction for ions to reach the electrode surface. Thus, further improvements were made to the double layer theory by Stern to help form the more modern model [38]. However, in terms of corrosion kinetics, the Helmholtz model suffices to demonstrate the potential barrier required for the movement of ions near the interface.

Corrosion is an electrochemical process. In terms of the chemical reaction(s) taking place on the surface of a corroding metal, the kinetics are defined by the Arrhenius relationship:

$$k = k_0 \exp\left(\frac{-\Delta G}{RT}\right) \quad (1.25)$$

where k is the rate of the reaction and $k_0$ is the rate constant ($\Delta G$, R and T keep the definitions given previously). $\Delta G$ is the driving force for chemical reactions. However, as corrosion is considered partly electrical, the driving force becomes the overpotential (the difference between the applied potential and equilibrium potential, defined by equation 1.17). Therefore, it is concluded that the chemical driving force, $\Delta G$, and the electrical driving force, E, are equivalent (equation 1.4).

The EDL is an energy barrier that must be overcome by metallic ions in order for a metal to corrode and must be taken into consideration when performing electrical studies such as impedance spectroscopy.

## 1.3 Forms of aqueous corrosion

### *1.3.1 General corrosion*

Corrosion will occur in environments where it is thermodynamically favourable; the specific type of corrosion which takes place also relies on the environment, as well as the metal properties and physical design. General corrosion, also known as “uniform corrosion”, occurs evenly over the surface of a material with equal intensity at each anodic site. It is the most common, least aggressive forms of corrosion and the easiest to manage, however, it is also the most destructive forms of corrosion in terms of amount of metal attacked [39,40]. Consider the generic mechanism of an anode on the surface of a metal in **Figure 1.9**.

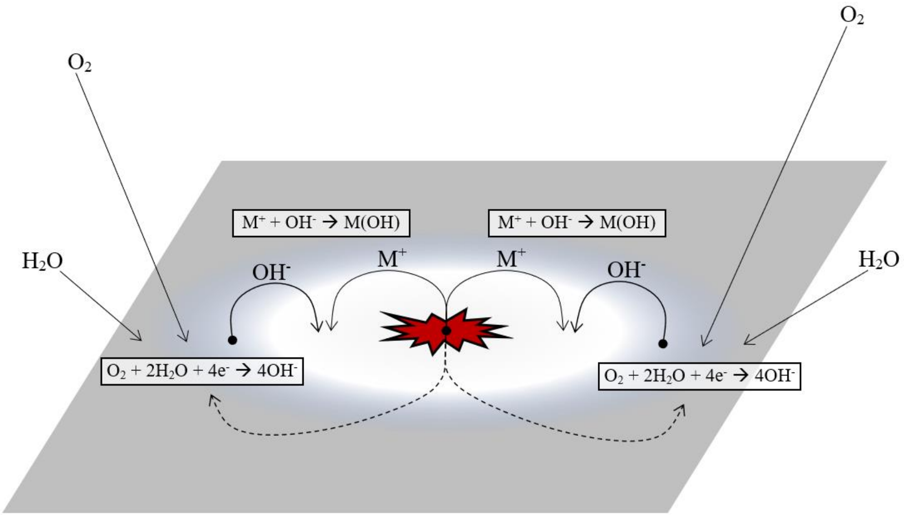

**Figure 1.9:** Schematic representation of a single, localised corrosion cell on a metal surface immersed in aggressive electrolyte.

The schematic assumes a metal surface, in contact with aerated water, releases metal ions into solution which combine with hydroxyl ions for form metal hydroxide corrosion products. General corrosion is the formation of many anodic sites, uniformly across a metal surface, which progress at the same, low rate as each other. The anodic sites are co-located with the cathodic sites and can therefore not be spatially resolved.

### *1.3.2 Galvanic Corrosion*

Galvanic corrosion, or “bimetallic corrosion”, is the preferential attack of one species over the other, when put in electrical contact, in the presence of electrolyte. Specifically, the species that is more electro active will become the anode and the more noble species will become the cathode, driving corrosive attack on the former [41]. Corrosion reactions take place as they would on a single metal; however, the rate is significantly increased. The EMF series in **Figure 1.4** can be used to predict which species will corrode in a bimetallic couple; the more negative the half-cell electrode potential for a species, the more active it is. Thus, for example, zinc ($E^0$ = -0.763) will preferentially corrode when coupled with iron ($E^0 = -0.440$). The EMF series contains absolute half-cell values for metals only, calculated from thermodynamics, under strict theoretical conditions; therefore, the use of these potentials is restricted to theoretical work only. On the other hand, the galvanic series, shown in **Figure 1.10,** provides measured free corrosion potentials of metals and alloys in a defined environment (flowing sea water at ambient temperature) compared to a reference electrode (saturated calomel electrode, SCE). The further left in the chart, the more positive the rest potential and therefore the nobler the metal. Conversely, metals found on the right of the chart have more negative rest potentials and would therefore be more active [42]. As the values are measured, the galvanic series has a more practical use when comparing bimetallic couples in real world applications. In the case of both the EMF series and the galvanic series, the greater the difference between the potentials of the two species, the greater the driving force and rate of corrosion.

In this mechanism of corrosion, anode to cathode size ratio is particularly important. Pairing a relatively small anodic metal with a significantly larger cathodic metal will result in a much larger current density on the anodic material and therefore a much higher corrosion rate. Conversely where the anodic metal is much larger than the cathodic metal, there will be much less, if any, corrosion that takes place. For example, if aluminium rivets were used to connect steel sheets together and fully exposed to electrolyte, the rivets would rapidly dissolve.

On the other hand, stainless steel fasteners are frequently used for connecting aluminium sheets (note: partial wetting of the joined metals will alter the size ratio). The galvanic corrosion mechanism is exploited in the corrosion prevention industry; a more anodic metal is coated onto a more noble substrate to provide galvanic protection.

Zinc is typically coated onto steel in the galvanising process as zinc will preferentially corrode if both the coating and the steel substrate are exposed.

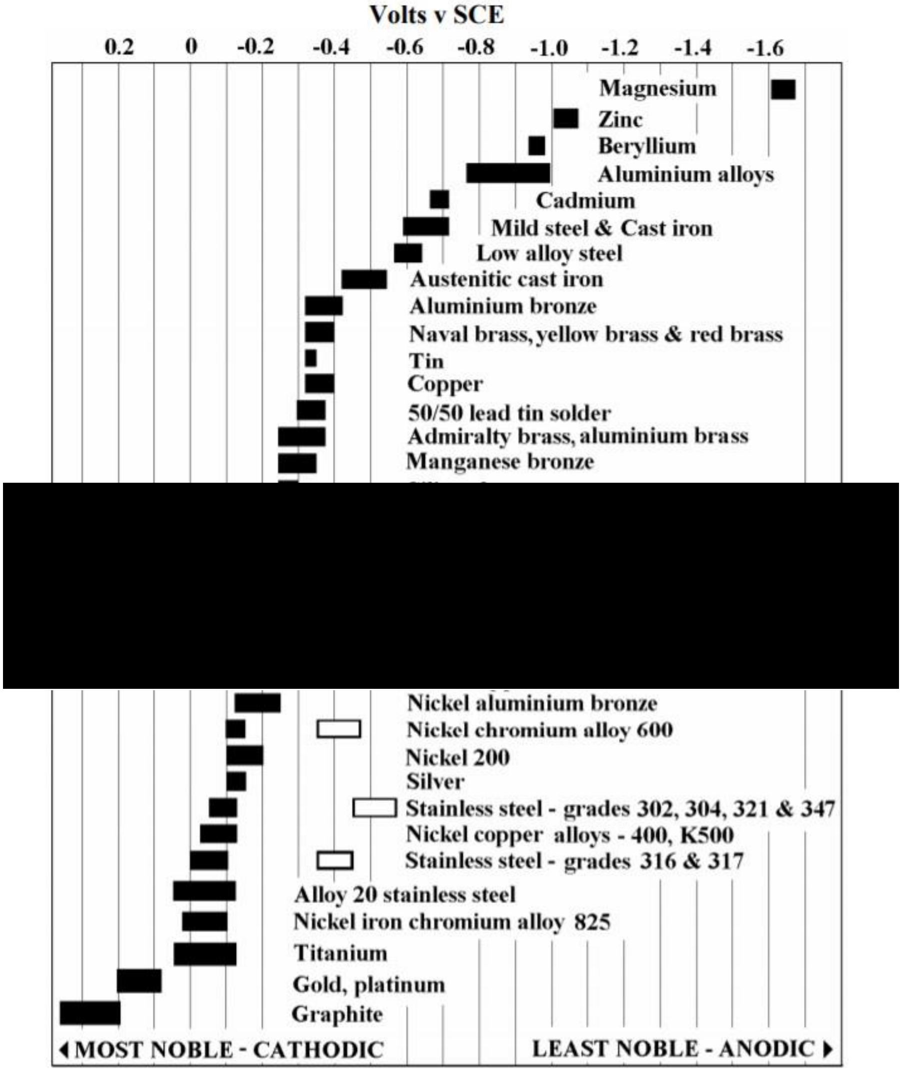

**Figure 1.10:** Galvanic series; corrosion potentials are exhibited in flowing sea water at ambient temperature. The further left the material in the chart, the more noble and would be protected by a material found placed to the right [42]**.**

### *1.3.3 Differential aeration*

Oxygen is a key factor in corrosion; literature typically shows a linear relationship between the oxygen presence in electrolyte and corrosion rates of submerged metals [43,44]. Differential aeration refers to an inconsistency of oxygen over the surface of a corroding material. The depletion of oxygen over a portion of a metal surface exposed to electrolyte leads to preferential anodic attack, whereas the remainder of the surface that has free access to oxygen becomes the cathodic site. Localised metal dissolution is considered more dangerous in industry as localised degradation of a component is more likely to lead to catastrophic failure. Furthermore, differential aeration can be difficult to design against as an oxygen gradient is likely to occur in many real-life instances. Consider the Evans droplet in **Figure 1.11**:

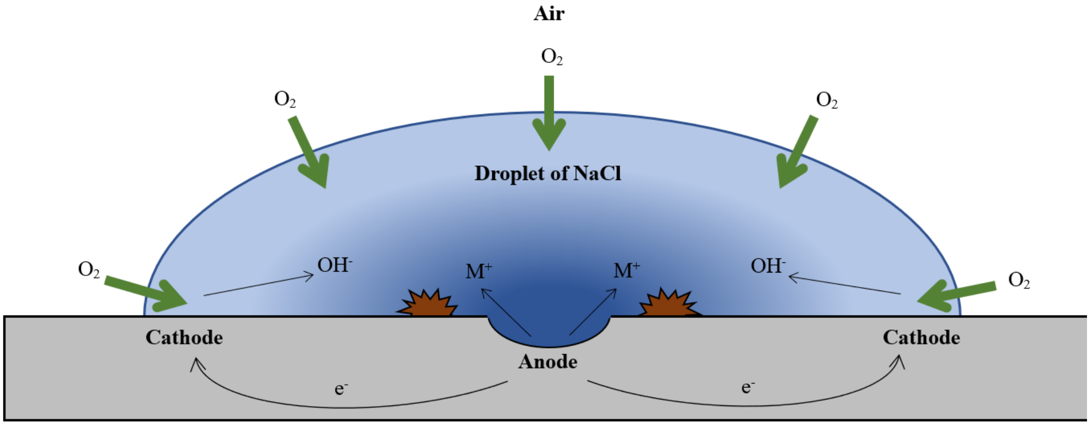

**Figure 1.11:** Adaption of the Evans droplet diagram [45].

The outer edges of the droplet are saturated in oxygen due to the proximity to the open air. This permits the cathodic processes to take place on the metal surface adjacent to these outer edges. As a result, the anodic attack takes place on the substrate toward the centre of the droplet.

This mechanism is an important consideration when studying underfilm corrosion and organic layer delamination as the diffusion or restriction of oxygen can exacerbate corrosion processes already taking place.

## 1.4 Corrosion protection – metallic coatings

### *1.4.1 Overview*

The application of a metal coating to a substrate is widely used as a form of corrosion prevention. There are two mechanisms by which metallic coatings can limit corrosion of a substrate: barrier and sacrificial. For corrosion to take place there must be electron transfer (the metal), ion transfer (liquid) and oxygen. To protect metals from corrosion, one of the three key components must be eliminated. In the case of barrier metallic coatings, current flow is prevented between the anodic and cathodic sites due to the insulating nature of oxides formed on the metallic coatings. Moreover, the barrier also limits access of electrolyte to the substrate, with limited access for oxygen also. However, coatings which provide only barrier properties cannot prevent corrosion if the coating is damaged and the undermining of the protective coating is in fact more damaging due to the differential aeration environment created.

Sacrificial coatings, such as zinc, provide continued cathodic protection if the coating itself is penetrated. The coating is comprised of a more electroactive material, therefore if both the substrate and coating are exposed at a given time, the coating will become active preferentially over the substrate. Consequently, sacrificial metal coatings require an additional overcoat to prevent continuous atmospheric attack to the coating alone. **Figure 1.12** shows the stages of protection when a defect exposes the substrate and coating. Initially a corrosion cell is setup whereby the steel, being the more noble material, becomes cathodic and subsequently the zinc becomes active. Attack on the zinc coating produces corrosion products which are precipitated within the defect, passivating the area and providing barrier protection to the steel.

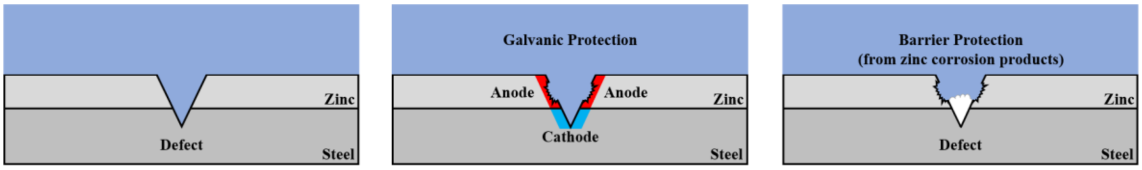

**Figure 1.12:** Schematic representation of the galvanic protection provided by a zinc layer on steel substrate. The defect extends through the sacrificial coating and into the substrate.

### *1.4.2 Zinc-aluminium coatings*

Zinc is the most common metal applied via the hot-dipping method. This is due to its relatively low melting point (420 °C) and its ability to alloy with steel. Hot-dip galvanising is the process by which a substrate is immersed in a bath of the molten zinc, during which a spontaneous reaction occurs between the substrate and molten metal to form alloy layers.

When the steel substrate is submerged in molten zinc, the surface reacts with zinc to produce several iron-zinc alloy phases, shown in **Figure 1.13**.

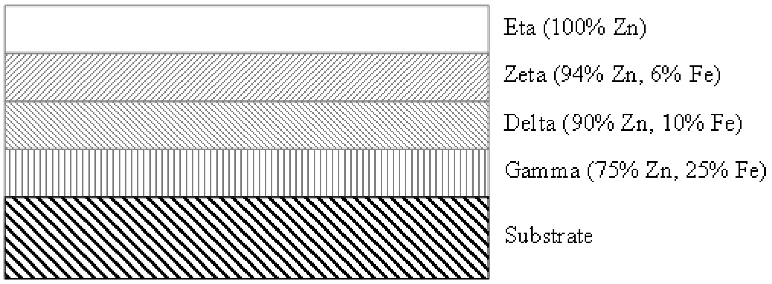

**Figure 1.13:** Intermetallic phases formed from the diffusion of zinc and iron during traditional hot-dip galvanising.

The uncontrolled formation of these phases improves the adhesion of the zinc coating at a cost of reduced formability and increased coating weight. In modern galvanising lines, a small amount of aluminium (<0.2 %) is added to the zinc bath to control the intermetallic phases formed. Iron will preferentially react with aluminium to form a thin, compact intermetallic layer between the steel substrate and zinc coating (**Figure**

**1.14**), which prevents further iron-zinc reaction diffusion, and therefore the brittle phases are not formed [46]. Good adhesion is maintained whilst formability and weight control are improved.

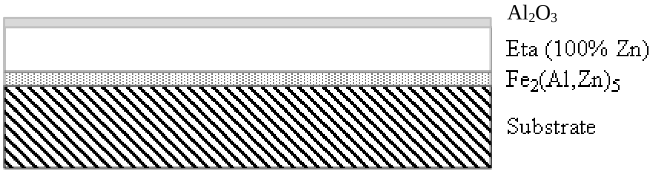

**Figure 1.14:** Aluminium intermetallic formed to prevent further reaction diffusion of zinc and iron.

The thickness of a HDG coating depends on the gauge of the steel substrate. In BS EN ISO 1461:2009 [47], the galvanising standards for the European industry, HDG coatings can range from 45-85 μm for steel gauges of <1.5 mm to >6 mm respectively for infrastructural galvanised steel. In the automotive industry, hot dip galvanised layers typically range from 7-12 μm, such as the GI coating in this work.

Tata Steel produce zinc coatings with aluminium additions beyond the minimum amount to retard the growth of Zn-Fe intermetallics: 5 wt% Al (Galfan) and 55 wt% Al (Galvalume).

### *1.4.3 Zn-Mg-Al coatings*

Magizinc is an iteration of hot-dip zinc coatings developed by Tata Steel, a Zn-Mg-Al alloy coating. The drive for improvement of the traditional pure zinc coating comes from the limitations of conventional zinc coatings within the automotive industry. Pure zinc coatings generally have restricted formability [48] and frequently cause process stability issues during forming; zinc flakes, from the coating, abrade forming tools which results in higher maintenance and cleaning costs [49]. Moreover, the desire for weight reduction and resource conservation in the automotive industry inspired research into new alloy additions for zinc coatings. The addition of a small amount of magnesium to the coating resulted in a significant increase in corrosion protection of the steel substrate, allowing the reduction of coating thickness whilst maintaining adequate environmental protection [4,50–58]. Furthermore, Magizinc shows negligible zinc flaking in the forming processes, which reduces galling considerably.

However, the addition of magnesium to the galvanising bath results in an oxide crust forming on the liquid metal that reduces adhesion and corrosion protection due to the presence of oxides; this problem is overcome by adding aluminium to the melt in an equal or higher amount to magnesium.

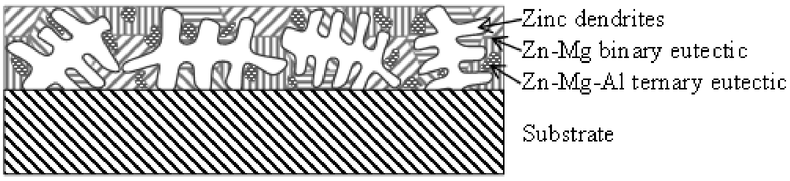

**Figure 1.15:** Cross-sectional microstructure of Zn-Mg-Al Magizinc coating.

The coating contains three phases: Zn rich dendrites, a binary eutectic structure (lamellar of $MgZn_2$ and Zn) and a ternary eutectic structure (lamellar of $MgZn_2$, Zn and Al-rich nodules), shown in **Figure 1.15**. The Al-rich phases are generally understood to be the more stable component of zinc-alloy coatings, including Zn-Mg-Al [53,59,60]. On the other hand, the magnesium-containing phases, such as $MgZn_2$ and $Mg_2Zn_{11}$, have been well documented to act as preferential sites for anodic attack [53,58–63]. The improved corrosion resistance exhibited by alloying magnesium and aluminium in zinc coatings has been shown in a significant number of accelerated testing works [4, 51–54, 58,59,64,65], and more recently long term exposure studies in the field have confirmed the benefits for real world applications [62,66,67]. Thierry et al. most recently showing a two to three times reduction in corrosion-driven mass loss from Zn-Mg-Al coated steel over four years exposure at various worldwide locations [62].

There is much debate as to the exact mechanisms that take place on Zn-Mg-Al coated steel to provide the improved corrosion resistance. Volovitch et al. proposed that the improved anti-corrosion properties of Zn-Mg alloys, compared to Zn, are a result of an increased stability of the highly compact simonkolleite ($Zn_5(OH)_8Cl_2{\cdot}H_2O$) [68]. The preferential anodic dissolution of magnesium phases results in the formation of $Mg^{2+}$ ions, these ions were then suggested to buffer the pH of the system by forming $Mg(OH)_2$. Moreover, the affinity for carbonate to react with $Mg^{2+}$ ions over $Zn^{2+}$ also enhances the stabilisation of Zn-based corrosion products, such as simonkolleite. In a similar vein, the preferential formation of $Mg(OH)_2$, over $Zn(OH)_2$, is also thought to hinder the oxygen reduction reaction (ORR) [60,69]. Prosek et al. have also observed the influence of $Mg^{2+}$ on the corrosion products formed at the cathodic sites, most notably the suppression of zinc oxide formation [60]. However, Krieg et al. believe that a greater influence on corrosion resistance comes from the microstructure, rather than the composition of the coating (for lower alloying contents) [55].

However, it is argued that discrepancies seen between literature is due to the difference between methods for corrosion testing [70].

## 1.5 Physical vapour deposition

### *1.5.1 Overview*

PVD is the collective name for multiple methods of thin film deposition with the key elements being: evaporation, transportation and condensation. It is the process of depositing thin films onto a substrate under vacuum conditions. The coating material is vaporised from solid or liquid form and transported via vacuum or plasma to the surface of a substrate material where it condenses to create the coating [71]. PVD layer thickness generally ranges from a few nanometres to a few microns, with deposition rates of up to 10 µm/s using the jet-evaporation technique [9].

PVD coatings have been applied for a range of purposes since the 1980s: to improve the hardness and lifetime of tooling steels [72,73], protection from corrosion product contamination in the food packaging industry [74] and fabrication of microelectronics [75]. The use of the PVD process to provide an alternative to traditional HDG coatings in the automotive industry has only recently been studied due to the demand for "cleaner" technologies and increased fuel efficiency via weight reduction. Research into this area has been positive, showing potential for PVD thin films to sufficiently replace traditional galvanic or barrier-type coatings on an industrial scale [2,3,9].

PVD possess several significant advantages over HDG and/or EZ:

- Many more elements can be deposited
- Low melting point substrates
- Alloy coatings
- Multi-layer coatings
- AHSS and UHSS grades can be coated

The properties of a thin film produced by any PVD process are governed by four key parameters: substrate surface condition (e.g. morphology, composition), deposition process and geometry (e.g. deposition rate, temperature), film growth mechanics (e.g. nucleation, surface mobility) and post-deposition processes (e.g. thermal treatment) [76].

### *1.5.2 Process Parameters*

The method currently employed at Tata Ijmuiden using a Von Ardenne roll-to-roll vacuum pilot line. The schematic of the EMELY line is shown in **Figure 1.16**. While the chamber is open a steel coil can be loaded onto W1 and the end of the strip is fed through the line and attached to W2. Tension is put on the line to prevent the strip from coming into direct contact with the vapour distribution box (VDB) and to ensure a consistent coat along the width of the strip. The chamber is then closed and pumped down to $10^{-4}$mbar. EMELY is designed for multiple passes to take place without the need to re-open the chamber: there are two material sources (VDB1 and VDB2) and two reverse magnetron sputters that prepare the strip immediately before deposition (E1 and E2). During the first pass, the strip is decoiled from W1 and recoiled on W2 after passing E1 and VDB1. The line is then reversed, after a period of cooling, and the strip passes E2 and VDB2.

The system for the introduction of source material has changed since first installation. Initially the coating metal or alloy was wire-fed into an induction coil setup which would heat the material to the necessary temperature for evaporation. The speed at each wire source was fed into the coil would control the weight percentage of each material within the coating and was inspired by the potential for continuous production. More recently, the source material is placed into the vacuum chamber within a ceramic crucible prior to the run. This allows accurate weight measurements and greater control over the final coating composition. Once evaporated, the coating material rises through a VDB which is pre-heated to a temperature sufficiency higher than that of the vapour to prevent premature condensation within the equipment itself. The VDB is positioned close to the steel strip to prevent wastage of the evaporated material. The design of the VDB is such that the evaporated material is evenly distributed over the surface of the steel.

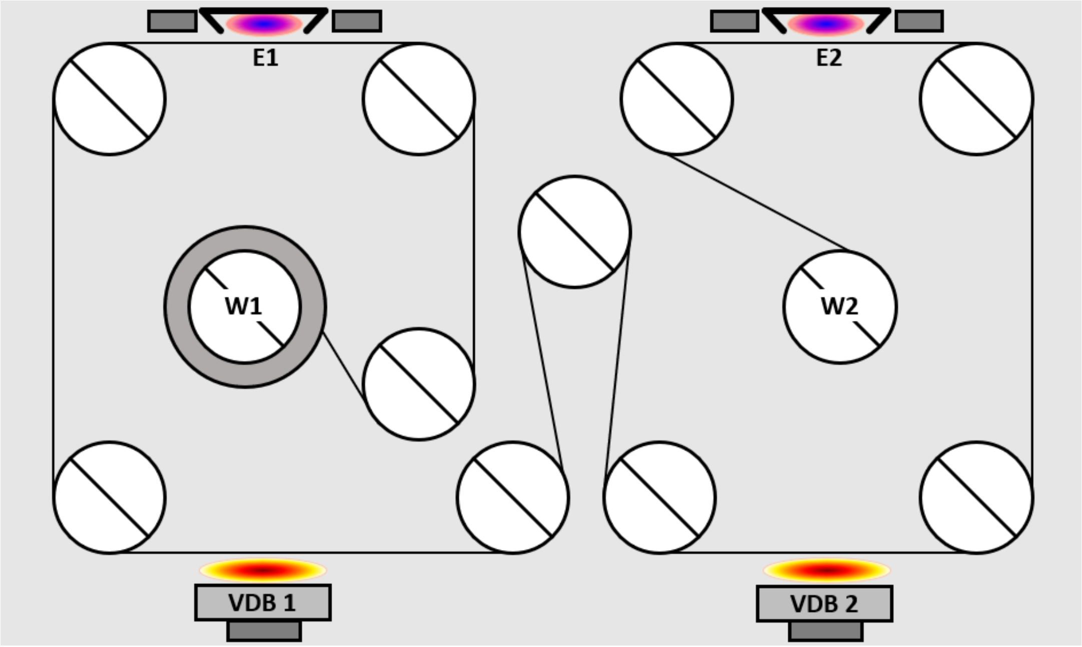

**Figure 1.16:** Schematic of the EMELY pilot line.

### *1.5.3 Film growth*

At the substrate surface, during PVD, the impinging atoms either reflect, re-evaporate or condense. A successful PVD process will be adjusted to ensure that the ratio of condensing atoms to impinging atoms (known as the sticking coefficient) is high. In order to condense on the substrate surface the sputtered atoms must lose energy by bonding to the surface atoms. If the sputtered atoms do not immediately react with the surface atoms due to weak interactivity, they are called adatoms. They are mobile on the surface and will instead nucleate at preferential sites which are typically inclusions, steps or defects in the substrate surface. On the other hand, if the interaction between a sputtered atom and surface atom is strong, the surface mobility is low and thus every surface atom can act as a nucleation point [76]. In this case, surface contamination can be a highly influencing factor on the heterogeneity of the film which is why reverse magnetron sputtering has been used in the EMELY system. To prevent pinholing and porosity the nucleation density should be high, which is dependent on the composition of the substrate and deposited material. The PVD Zn-Mg coatings in this thesis are notably deposited as a dual coating system. It was previously found that the adhesion of the Zn-Mg film was dependant on the presence of the zinc base layer [20].

Growth of the nuclei occurs as subsequent atoms impinge on the already deposited atoms. There are three previously established mechanisms for growth, as shown in **Figure 1.17**.

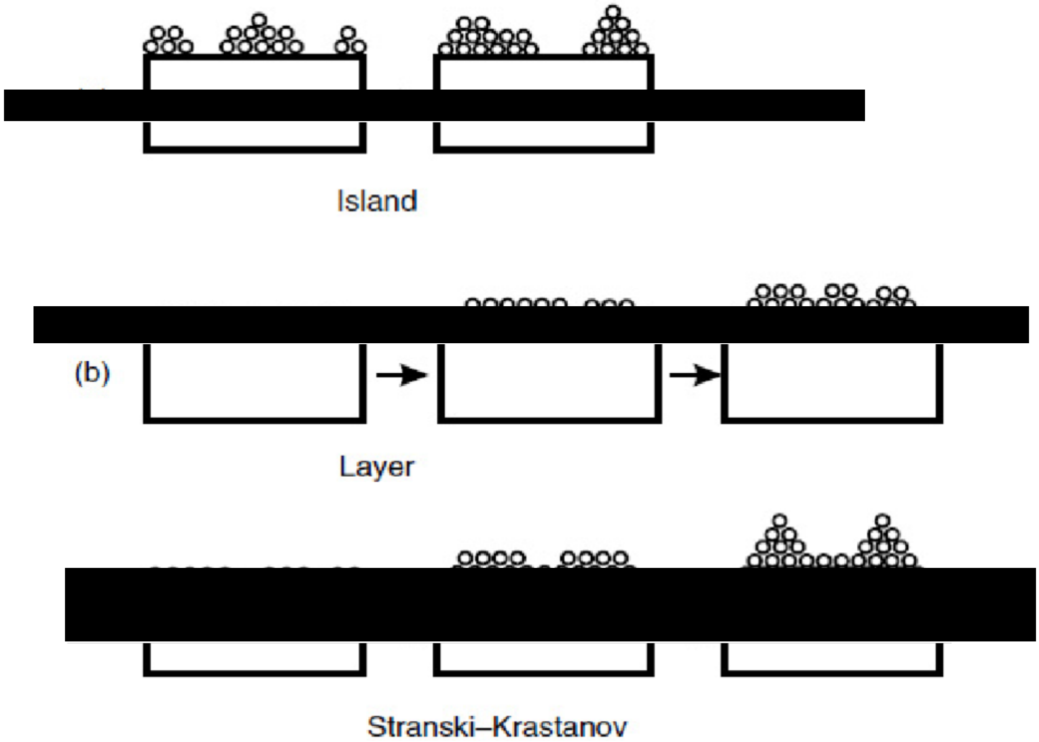

**Figure 1.17:** Thin film growth mechanisms: a) Volmer-Weber island growth, b) Frank-vander Merwe layer growth and c) Stranski-Krastanov layer plus island growth [77].

For zinc and magnesium in a low temperature deposited process, such as that in this work, the surface atom mobilities are expected to be low and therefore the Stranski-Krastanov mechanism for nucleation is likely [76]. Initially, complete films of atoms are growth layer by layer on the substrate, permitting limited growth and resulting in relatively small grains. Beyond the critical layer thickness the island growth mechanism takes over [78,79].

Film growth is a result of the continuous deposition of sputtered material onto the existing nuclei on the substrate surface. By the nature of this process, PVD film growth is typically columnar. Unlike the commonly described columnar grains of cold hardened metals, the columnar features of a PVD film are polycrystalline.

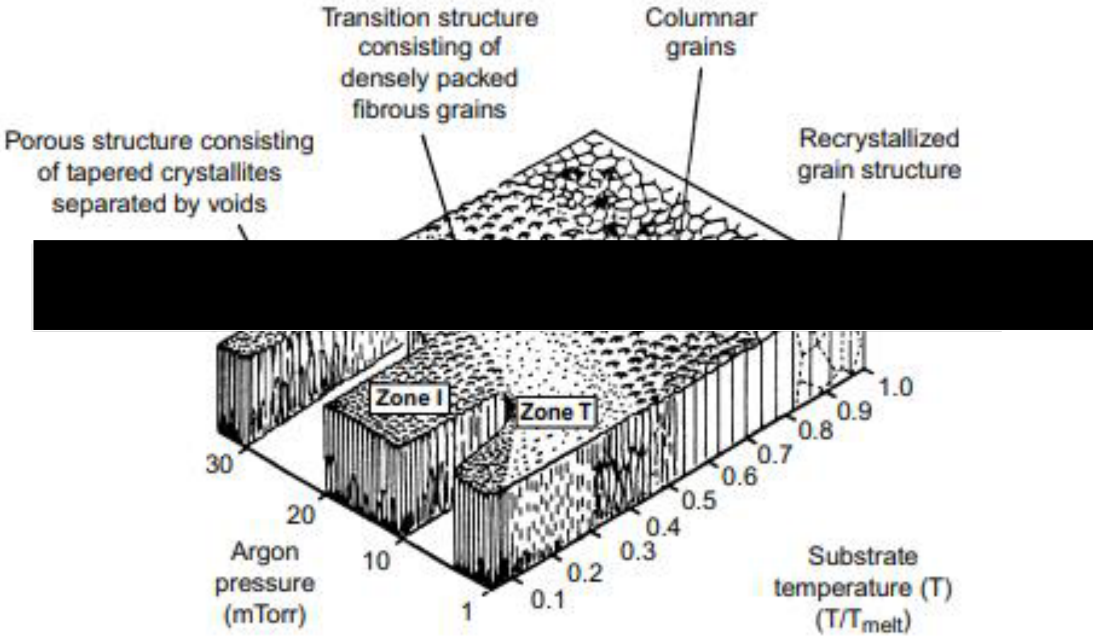

[redacted]

**Figure 1.18:** Structure Zone Model (SZM) of PVD films, adapted by Mattox [71] from Thornton [80].

The growth mode of a PVD film is not established until a reasonable distance away from the substrate interface. **Figure 1.18** shows the basic Structure Zone Model that dictates the film morphology in relation to the chamber pressure and substrate temperature. It is understood that additional process parameters also have an influence on morphology, such as deposition rate and the angle-of-incidence, however the model does present a basic variety of morphology expected to form via the PVD process. In addition to this, low mobility adatoms, such as zinc, are susceptible to geometric shadowing during deposition; this results in a globular surface morphology which becomes more exaggerated as deposition continues [71].

### 1.5.4 Coating characteristics

The superior corrosion resistance of magnesium containing HDG coatings, such as Magizinc, prompted research into Zn-Mg alloy PVD coatings. Pure Zn PVD coatings have not been considered for commercial use as it is well understood the corrosion performance of Zn coatings is directly related to the thickness of said coating [81,82]. **Figure 1.19** shows a cross-section of a dual layer Zn Zn-Mg coating produced using EMELY. The pure Zn layer applied first serves the purpose of improving wetting and adhesion between the topcoat and the substrate [22]. The Zn-Mg coating applied during the second pass has a globular micro surface topography characteristic of this PVD process.

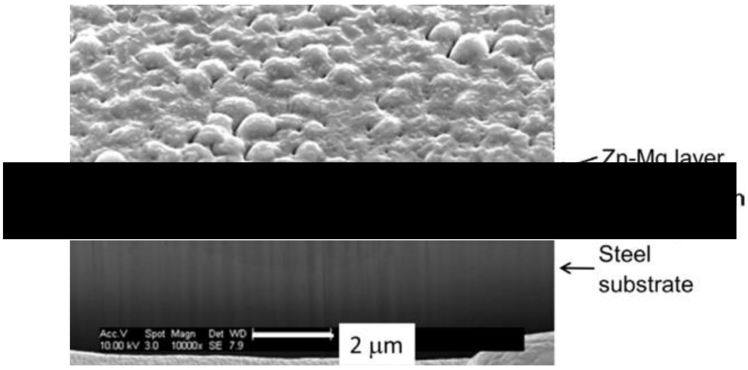
[redacted]
[redacted]

**Figure 1.19:** Typical Zn-Mg PVD coated steel showing the pure Zn adhesion layer and Zn-Mg topcoat [19].

As early as 1991, zinc PVD binary systems such as Zn-Mg, Zn-Al, Zn-Cr, Zn-Ni and Zn-Ti were compared for their capability of limiting rest rust formation [83]. It was found that the Zn-Mg system exhibited up to 24 times better corrosion resistance in salt spray testing compared to electrogalvanised steel. In a similar vein, the incorporation of magnesium into an electroplated zinc coating has also been previously observed to improve corrosion resistance in salt spray tests by 5 times at room temperature, and 10 times for 10 °C increased temperature [84–86]. More recently, Prosek et al. explored a systematic approach in varying the magnesium content within a zinc alloy, finding that between 4-8 % there was a 10-fold decrease in mass loss compared to zinc alone, under atmospheric conditions and in the presence of chloride [64]. Although this work was conducted on cast metals, a key advantage of the PVD method for coating deposition is the potential for increased alloy content in the zinc coating. It was proposed by Thébault et al. that superior cut edge corrosion resistance exhibited by Zn-5.8Mg and Zn-15.5Mg was due to two protective mechanisms acting in the humid environments: the zinc cations acted to inhibit cathodic reactions on the steel surface close to the coating itself, but the magnesium cations provide protection over the entire steel surface as the magnesium hydroxides maintain stability at higher pH. Thus during the drying phase, when zinc can no longer provide galvanic protection, the magnesium hydroxides previously formed continue to provide protect to the steel and limit formation of red rust [8].

Although research into the potential substitution of hot dip galvanising with PVD is still ongoing, it would not be the first time an existing industry has been successfully replaced by a sputtering equivalent. Navinšek et al. previously highlight the potential for further fine tuning of the process, however, initial tests showed that sputtered nickel could replace electroplated nickel on an aluminium heat sink, without the need for an intermediate adhesion layer, with a much thinner coating that provided equal corrosion resistance [2].

Another key factor when considering PVD zinc alloy coatings as substitutes for hot dip galvanising is the compatibility within a full coating system. This has recently been explored by Davies et al., with the optimum magnesium content having been identified as 10 wt% to resist both cathodic delamination and anodic undermining [19]. It was shown that magnesium contents higher than 10 wt% caused significant depression in the intact potential for delamination tests initiated with chloride which, as previously deduced by Hausbrand et al. [69], limits the driving force for delamination.

## 1.6 Corrosion protection – organic coatings

### *1.6.1 Overview*

Organic coatings include: paints, lacquers and temporary coatings such as wax or oil. For the long-term corrosion protection of metal components, the most widely used organic coating is paint. Paint can be easily applied to metal substrates; however, the adhesion and continuity of the coating is crucial in maintaining the barrier protection. Metal substrates with inherent corrosion resistance, such as aluminium, are typically painted for aesthetic purposes only. In contrast to this, steel and zinc-based metallic coatings benefit from the additional barrier to the environment as water, oxygen and aggressive ion specie mobility is significantly hindered through the organic layer. This is necessary for components exposed to relatively aggressive environments where their natural oxide layer is continuously broken down, allowing the exposure of the metal to corrosive attack [87].

Zinc-coated steels further over-coated with an organic layer are termed “duplex” coatings, creating a synergistic effect whereby the lifetime of a duplex system is greater compared to the sum of the expected lifetimes of a zinc coating or organic coating applied alone to a steel substrate [88].

### *1.6.2 Automotive coating systems*

In order to ensure a complete barrier between a metallic substrate and its environment, a multilayer paint system is applied to galvanised steel with each layer formulated to serve an individual purpose in a specific anticipated service environment (**Figure 1.20**).

Firstly, surface pre-treatment is essential to maximise adhesion and limit defects. For automotive coating systems, a galvanised steel substrate is typically cleaned, to remove oils and oxides (which have been shown to be the cause of many coating failures [89]), and then "phosphated" to form a corrosion resistant, insoluble phosphate layer. Phosphating is the process by which zinc coated steel strip is treated with diluted phosphoric acid in order to improve the adhesion of a subsequent primer organic coating to the zinc [90]. The primer layer is applied to the phosphate steel substrate and contains pigments that serve the purpose of UV and corrosion protection. The top coat is applied directly to the primer layer and it is typically designed for the aesthetics of a product (colour, finish) as well as an initial barrier to the environment.

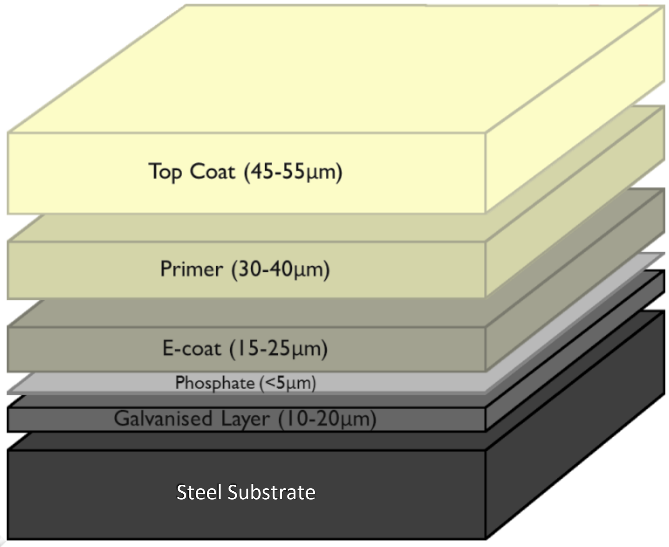

**Figure 1.20:** Schematic showing the component layers of an automotive paint system.

### *1.6.3 Failure*

There are several different mechanisms by which organic coating disbondment can occur [90,91], those relevant to this thesis are cathodic disbondment and anodic undermining. Cathodic disbondment is the delamination of the paint from the substrate due to the reduction of oxygen (equations 1.7 and 1.8) at the interface between the organic coating and metal substrate, as shown in **Figure 1.21**, and is the most common mechanism for coating failure on galvanised steel [87]. The cathodic reaction at the coating interface causes a rise in pH (alkalisation) which rapidly degrades the organic layer and also dissolves any zinc hydroxide present [92,93]. Without a defect, oxygen and water can diffuse slowly through the organic coating (which can cause cathodic blistering); however, a defect allows the reactants to rapidly reach the disbondment interface. For an unpigmented coating undergoing cathodic disbondment, the rate-limiting step has previously be identified as ion migration through the underfilm electrolyte from the defect [94]. In contrast to this, a pigmenting coating may instead be limited by the rate of oxygen diffusion as the pigment itself may hinder the path through the coating [95].

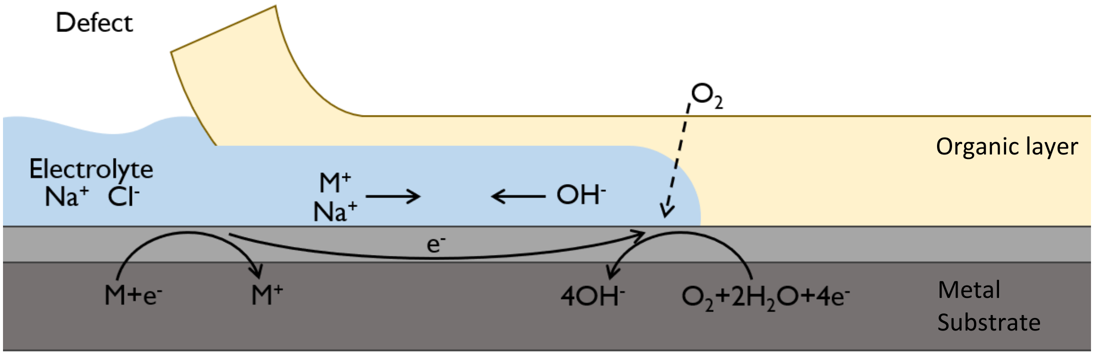

**Figure 1.21:** Basic mechanism of cathodic delamination.

In order to quantitatively study this method of coating disbondment, Stratmann et al. were the first to utilise the Scanning Kelvin Probe (SKP) to map the free corrosion potential of a metal surface, $E_{corr}$, over the distance from the defect, x [92, 94,96]. In order to study cathodic delamination, Stratmann et al. developed a novel sample preparation technique now known as a “Stratmann cell” whereby an artificial defect is created, by peeling back the organic coating to expose the metallic layer beneath, and put in contact with the selected electrolyte [97]. The SKP then measures an $E_{corr}$ profile perpendicular to the artificial defect repeatedly over time, such that time-dependent profiles can be overlaid to show the kinetics of delamination.

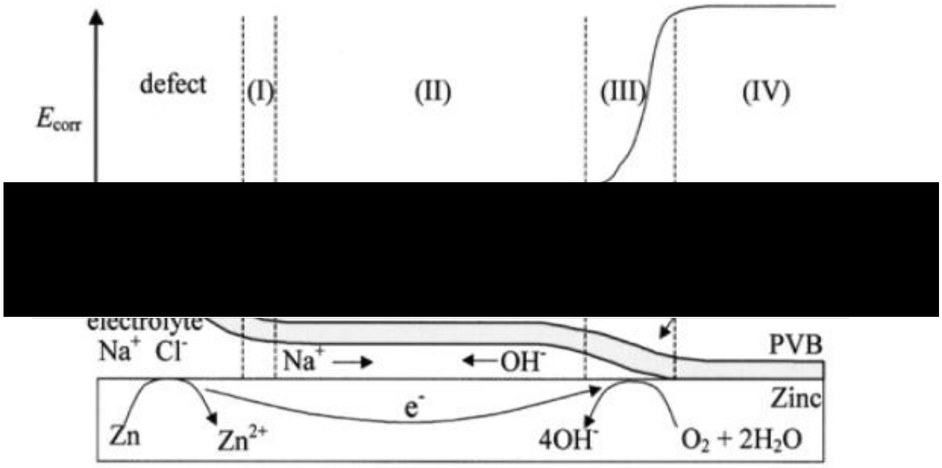

[redacted]

**Figure 1.22:** A schematic diagram to illustrate the five distinct regions of a delamination cell as they correlate to a typical $E_{corr}$ profile from a SKP study [93].

As shown in **Figure 1.22**, there are five distinct segments of an SKP profile:

- Defect: artificial defect area of exposed metallic substrate where anodic dissolution takes place, as such the $E_{corr}$ value corresponds to the free corrosion potential of the metal substrate.
- (I) Defect edge: noted as the end point of the defect preceding the delaminated area.
- (II) Delaminated area: a gradual increase in $E_{corr}$ from (I) to (III) represents the ohmic resistance generated by ionic transfer through the underfilm electrolyte in this section.
- (III) Delamination front: a sharp and usually distinct increase from $E_{corr}$ to the intact potential value, $E_{intact}$, indicating the progressive front of disbondment.
- (IV) Intact coating: a second plateau of more positive corrosion potential representing the un-delaminated coating.

It was observed by Hausbrand et al. that $MgZn_2$, a predominant phase found in commercial Zn-Mg-Al coatings [58,59], resists cathodic delamination due to a depression in the intact potential and subsequent reduction in the driving force for underfilm disbondment [69,98,99]. However, it was discovered that $MgZn_2$ instead had a vulnerability to anodic undermining.

Anodic undermining is the dissolution of the metal below the paint film initiated by an aggressive corrosive media reaching the metal via diffusion through the paint or an invasive defect. Filiform corrosion, FFC, is a type of anodic undermining and is considered the primary mechanism for coating failure on multiple organically coated metal systems [100]. Most relevant to this work is the occurrence of FFC on magnesium [101] and magnesium-containing zinc coatings [19,102] following the exposure of penetrative defects in the organic coating to particularly aggressive electrolytes, such as HCl. It is generally presumed that a droplet of aggressive electrolyte propagates beneath an organic coating via anodic attack of the metal substrate at the head of the droplet, coupled with cathodic oxygen reduction at the tail of the droplet (**Figure 1.23**). FFC has not previously been seen on zinc coatings. The recent work by Davies et al. indicated a correlation between magnesium content and susceptibility to anodic undermining for zinc PVD coatings. Indeed, a magnesium content greater than 10 wt% resulted in a vulnerability to FFC which was not seen on coating systems containing less than 10 wt% magnesium.

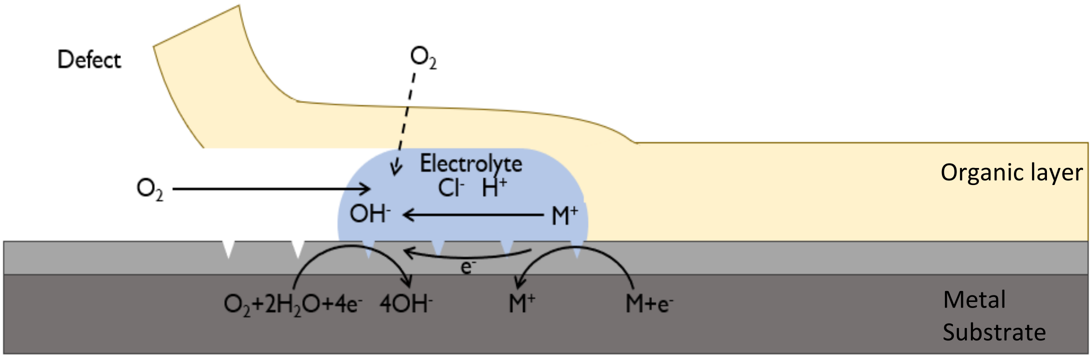

**Figure 1.23:** Basic mechanism of filiform corrosion.

Wint et al. proposed a schematic diagram (**Figure 1.24**) correlating the FFC mechanism to a typical SKP profile, identifying the head of the propagating filament and the dry, porous tail following. The head is characterised in the SKP profile as a region of lower potential, corresponding to the free corrosion potential of the metallic surface, and the tail is identified by a gradual increase in potential.

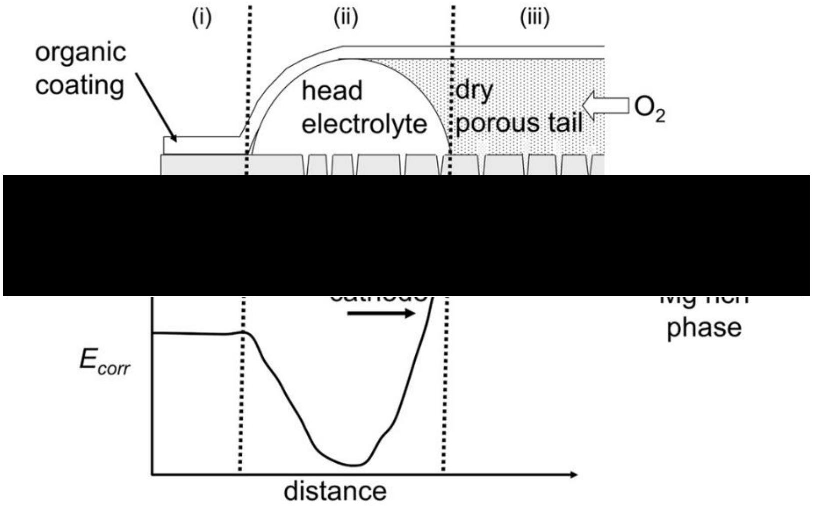

[redacted]

**Figure 1.24:** A schematic diagram to illustrate the three regions of a FFC cell as they correlate to a typical Ecorr profile from a SKP study, measured along the filiform axis [102].

### 1.6.4 Corrosion inhibitor pigments

Corrosion inhibitor pigments are often included in the primer layer of an organic coating system. They are separated into three main categories based on the method by which they inhibit corrosion of the coating: anodic, cathodic or mixed inhibitors.

Anodic inhibitors are further classed as either precipitating or oxidising. Precipitating anodic inhibitors, such as phosphates ($PO_4^{3-}$), chromates ($CrO_4^{2-}$) or molybdates ($MoO_4^{2}$) [103], form an insoluble salt in the defect region which physically stops ionic flow between the anodic and cathodic reactions (as shown in **Figure 1.25**).

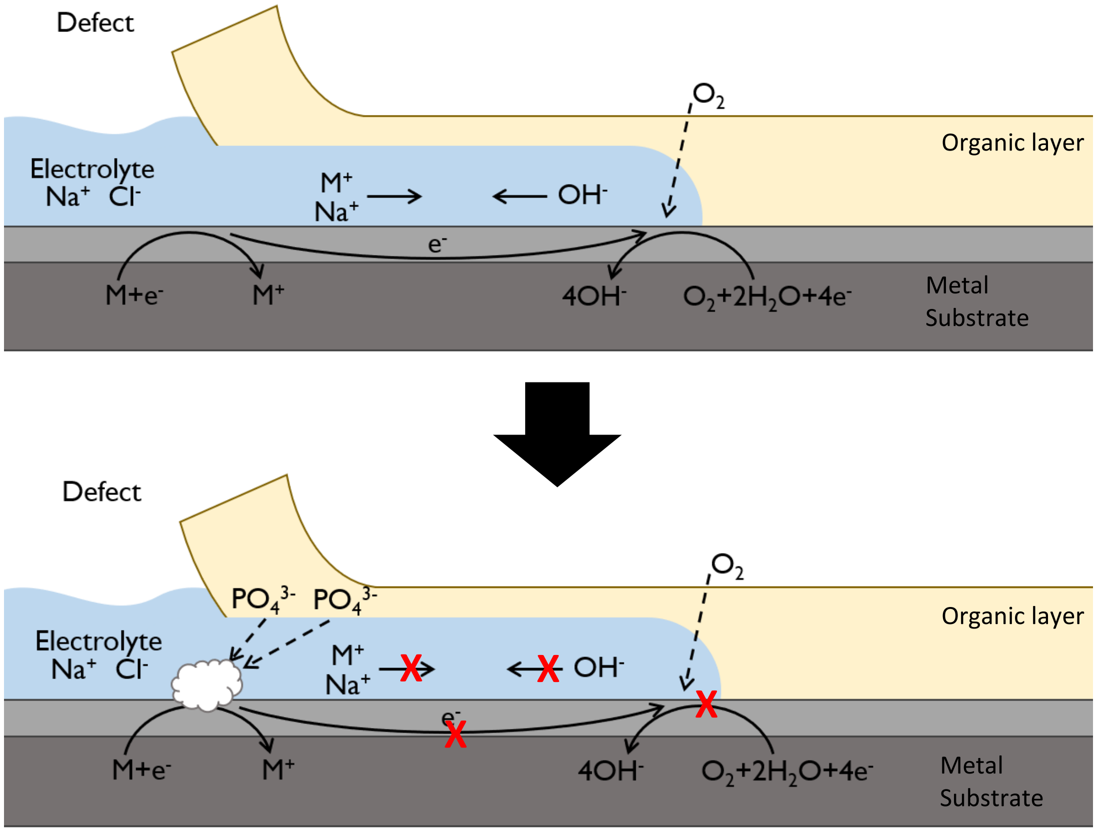

**Figure 1.25:** Schematic representation of phosphate ions forming with metal ions from the defect to form an insoluble salt and prevent ionic transport between the defect and delamination front during cathodic delamination.

Oxidising anodic inhibitors shift the free corrosion potential of the system by increasing the rate of oxygen reduction which lowers the corrosion current but increases the free corrosion potential, as shown via the Evans diagram in **Figure 1.26**. For certain metals, such as steel, increasing the free corrosion potential will shift the corrosion reaction into the passive region of the Pourbaix diagram and reinforce the formation of the passive film [104]. However, without careful control of the amount of inhibitor in the system, the increase in potential can instead accelerate corrosion.

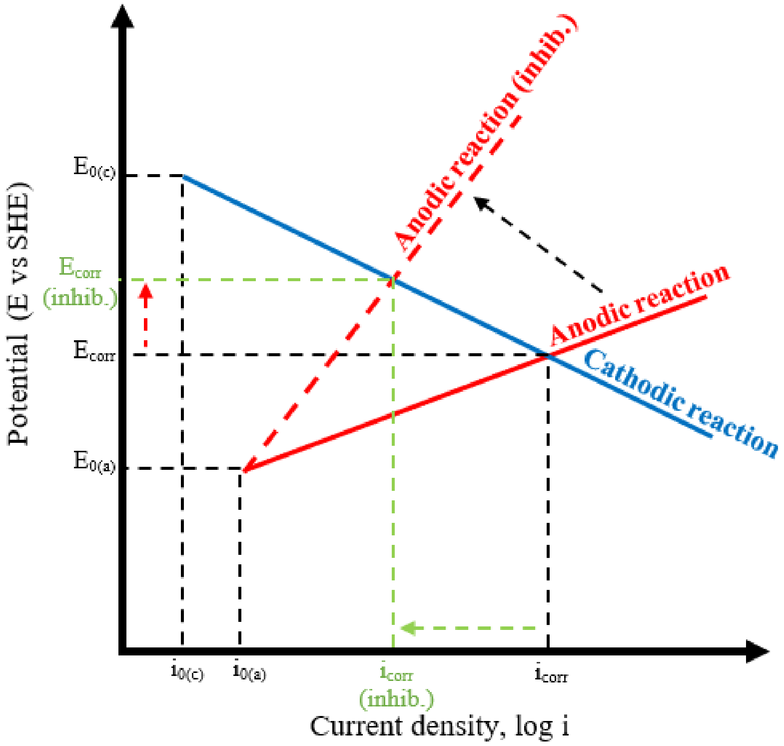

**Figure 1.26:** Evans diagram showing the influence on the anodic reaction Tafel plot by an anodic inhibitor.

Cathodic precipitation inhibitors work in a similar way to their anodic counterparts; though the insoluble salts are instead deposited in the cathodic region of the system. Work by Powell et al. demonstrated the highly efficient cathodic inhibition of HDG in the presence of rare earth metals [105]. Other common cathodic precipitates include $CaCO_3$, $MgCO_3$ or zinc sulphates [105]. Cathodic poisoning inhibitors, such as sulphides, selenides, arsenates, bismuth and antimony [105], decrease the rate of hydrogen evolution via deposition on the metal surface. However, consequently a cathodic poison can increase the susceptibility of the metal to hydrogen embrittlement from the non-recombined hydrogen. Oxygen scavengers, such as sulphite and hydrazine [105], are another form of cathodic inhibitor which react with the dissolved oxygen in the electrolyte, thus restricting the amount reduced at the surface of the metal. The Evans diagram in **Figure 1.27** demonstrates the effect of reducing the rate of the cathodic reaction via cathodic inhibition. Both the corrosion potential and current are reduced, making cathodic inhibitors safer to use than anodic.

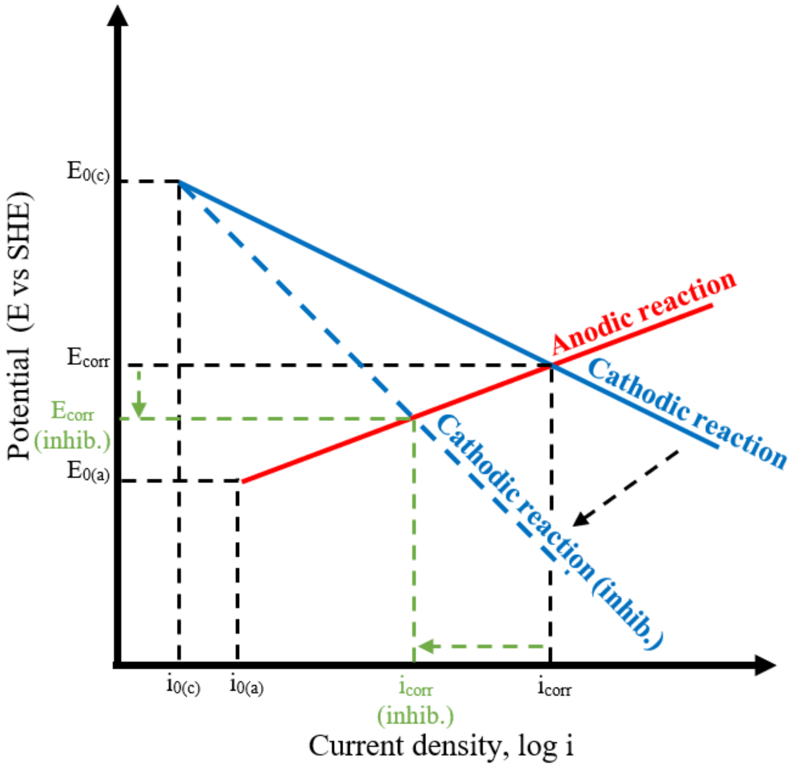

**Figure 1.27:** Evans diagram showing the influence on the cathodic reaction Tafel plot by a cathodic inhibitor.

## 1.7 Accelerated electrochemical scanning techniques

### *1.7.1 Scanning Vibrating Electrode Technique (SVET) theory*

The SVET is an advanced electrochemical scanning method derived from the pre-existing scanning reference electrode technique (SRET) [105]. The SVET spatially and temporally monitors electrochemical behaviour in electrolyte directly above a corroding surface and has been used extensively to study the localised corrosion of bare metal surfaces under full immersion [106–114]. Specifically, the vibrating probe tip detects potential gradients in solution generated by the ionic flow between the anodic and cathodic sites of an actively corroding surface (**Figure 1.28**). The peak-to-peak voltage, $V_{pp}$, detected can be converted to current density in the axis of vibration, $j_z$, with the following relationship:

$$V_{pp} = j_z(a_{pp}/\kappa) \qquad (1.26)$$

Where $a_{pp}$ is the peak-to-peak amplitude of vibration and $\kappa$ is the conductivity of the solution. Full calibration of the SVET is described in section 2.4.2. The spatial resolution of the SVET is limited by the experimental probe height and the diameter of the probe electrode (for a scan height of 100 µm, the theoretical width at half maximum, whm, has been previously identified as 0.26 mm [109]). This limits the applications for the SVET as electrochemical features smaller than the whm cannot be resolved, such would be the case for general corrosion or preferential attack of micro phases. An example of this would be the de-alloying of the lamellar phases within a ZMA coating microstructure; the anodic attack of the more susceptible phase, $MgZn_2$, which has an inter-lamellar spacing of <10 µm, is not resolved with the SVET. Previous work by Sullivan et al. utilised optical microscopy to confirm the preferential attack on the $MgZn_2$ phase present in Zn-Mg-Al coatings [58] whereas SVET was used to compare mass loss between different magnesium-containing alloy coatings [59,115].

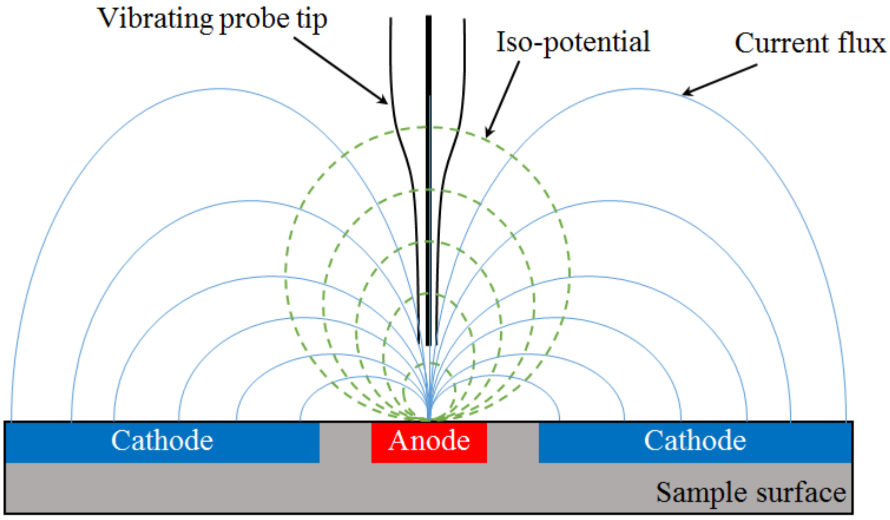

**Figure 1.28:** Schematic of the potential and current distribution in the electrolyte directly above a corroding surface.

Nevertheless, the SVET has been a vital tool in numerous works, such as the identification of Zn(PP) salt formations on anodic sites recorded by Glover et al. [116], the characteristic narrow anodic ring expansion and correlation of an intense internal cathode with visual black staining on freely corroding magnesium observed by Williams and McMurray [112] and the increased lateral anodic spreading of anodes on Zn-Mg-Al coatings compared to the through-coating depth penetration as a function of coating cooling rate identified by Wint et al. [117].

The SVET used in this thesis was designed and assembled at Swansea University; its components are fully described in previous work [108, 110,118].

### *1.7.2 Scanning Kelvin Probe (SKP) theory*

The SKP is a non-perturbing technique than can measure the electrochemical potential of surfaces beneath a thin layer of electrolyte or electrically resistive coatings. Unlike the SVET, the SKP does not require immersion in electrolyte and instead measures corrosion phenomena in response to atmospheric conditions. As previously mentioned, it was first applied by Stratmann et al. [92, 94,96] to study corrosion-driven delamination under organic coatings applied to metallic substrate, the technique has been extensively used to compare the organic coating disbondment, as well as determine the underlying mechanisms, as a function of substrate [19, 64,119], organic coating composition [93,120,121] and surface preparation [122].

**Figure 1.29** illustrates the principle theory behind the SKP method. The gold wire Kelvin probe is positioned at distance d above the metallic sample, such that the cross-section of the tip is parallel to the sample surface (**Figure 1.29a**). Due to the difference in work functions ($\Phi_t$ and $\Phi_s$ for the tip and sample respectively), once electrical contact is made between the tip and the sample, they form a parallel plate capacitor, where the air gap between them is the capacitor dielectric (in delamination studies, the organic coating also contributes toward this insulating layer). Additionally, the Fermi levels of tip, $E_{ft}$, and sample, $E_{fs}$, equilibrate with a corresponding drop the in vacuum energy level of the sample, $E_{vac}$, and a Volta potential, $\Delta\Psi$, is established. The Kelvin probe vibrates in the plane perpendicular to the sample surface, thus creating a variance in the plate separation, and therefore the Volta potential, over time. The variance of the Volta potential results in an alternating current in the circuit, $i_{ac}$ (**Figure 1.29b**). The SKP cannot directly measure this alternating current; instead a bias potential, $V_{DC}$, is applied to nullify $i_{ac}$ (**Figure 1.29c**). Under null-current conditions, the measured Kelvin potential, $E_{KP}$, is equal to $-V_{DC}$ and is therefore equal to $\Delta\Psi$ when $V_{DC} = 0$.

The Kelvin probe scans over the surface of a sample, indirectly measuring and mapping the Volta potential across the surface. Section 2.5 describes the method for monitoring the rate of delamination of an organic coating on a metal substrate using the SKP apparatus.

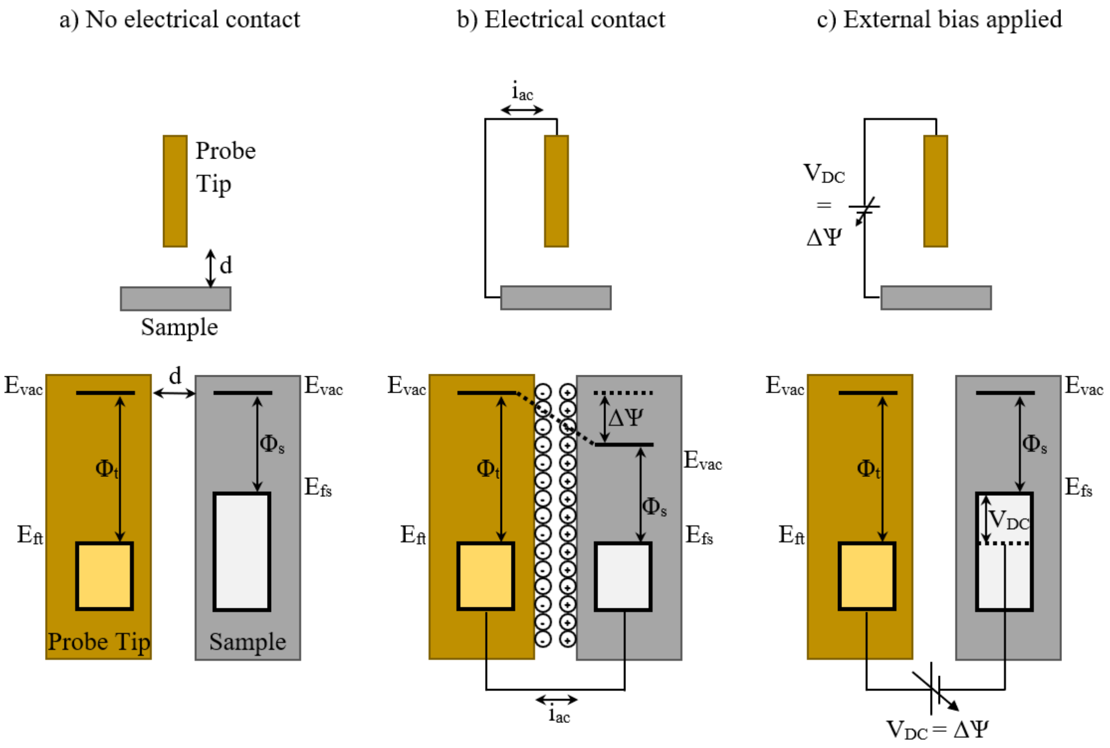

**Figure 1.29:** Electronic energy levels and the principle of SKP operation: (a) the SKP probe tip (work function = $\Phi_t$) vibrates at frequency ω above the metallic sample (work function = $\Phi_s$) separated by distance d with no electrical contact, (b) electrical contact is established between the tip and sample (a Volta potential, ΔΨ, forms as the vacuum energy level of the sample, $E_{vac}$, drops and the Fermi level of the sample, $E_{fs}$, equilibrates with the Fermi level of the probe, $E_{ft}$), and (c) an external bias, $V_{DC}$, is applied to nullify ΔΨ.

## 1.8 References

1. C. Metzner, K. Goedicke, G. Hoetzsch, B. Scheffel, J.-P. Heinss, Surf. Coatings Technol. 94–95 (1997) 663–668.
2. B. Navinšek, P. Panjan, I. Milošev, Surf. Coatings Technol. 116–119 (1999) 476–487.
3. L. Guzman, G.K. Wolf, G.M. Davies, Surf. Coatings Technol. 174–175 (2003) 665–670.
4. N.C. Hosking, M.A. Ström, P.H. Shipway, C.D. Rudd, Corros. Sci. 49 (2007) 3669–3695.
5. L. Baptiste, N. van Landschoot, G. Gleijm, J. Priede, J. Schade van Westrum, H. Velthuis, T.-Y. Kim, Surf. Coatings Technol. 202 (2007) 1189–1193.
6. T.-Y. Kim, M. Goodenough, Corros. Sci. Technol. 10 (2011) 194–198.
7. E. Zoestbergen, J. van de Langkruis, T. Maalman, E. Batyrev, S. Melzer, M. Zuijderwijk, "Diffusion of Zinc and Magnesium in Physical Vapour Deposited Thin Films at 175°C", in: Galvatech, AIST, Toronto, (2015) pp. 36–43.
8. F. Thébault, B. Vuillemin, R. Oltra, C. Allely, K. Ogle, O. Heintz, Corros. Sci. 97 (2015) 100–106.
9. B. Schuhmacher, C. Schwerdt, U. Seyfert, O. Zimmer, Surf. Coatings Technol. 163–164 (2003) 703–709.
10. E. Reinhold, J. Richter, U. Seyfert, C. Steuer, Surf. Coatings Technol. 188–189 (2004) 708–713.
11. J. Mahieu, B.C. De Cooman, S. Claessens, Metall. Mater. Trans. A Phys. Metall. Mater. Sci. 32 (2001) 2905–2908.
12. H. Liu, F. Li, W. Shi, S. Swaminathan, Y. He, M. Rohwerder, L. Li, Surf. Coatings Technol. 206 (2012) 3428–3436.

13. M. Pourmajidian, J.R. McDermid, Surf. Coatings Technol. 357 (2019) 418–426.
14. S. Bell, B. Davis, A. Javaid, E. Essadiqi, Final Report on Effect of Impurities in Steel, (2006).
15. M.A. V. Devanathan, Z. Stachurski, W. Beck, J. Electrochem. Soc. 110 (1963) 886.
16. M.J. Carr, M.J. Robinson, Trans. IMF. 73 (1995) 58–64.
17. E.M.K. Hillier, M.J. Robinson, Corros. Sci. 46 (2004) 715–727.
18. B. Schuhmacher, K.D. Ehlers, F.-J. Floßdorf, J. Hagler, C. Metzner, B. Scheffel, R. Steffen, Vak. Forsch. Und Prax. 13 (2002) 233–235.
19. J.L.L. Davies, C.F.F. Glover, J. van de Langkruis, E. Zoestbergen, G. Williams, Corros. Sci. 100 (2015) 607–618.
20. E. Zoestbergen, J. van de Langkruis, T.F.J. Maalman, E. Batyrev, Surf. Coatings Technol. 309 (2016) 904–910.
21. C. Ye, L. Jia, G. Xu, F. Wang, X. Wang, H. Zhang, Surf. Coatings Technol. 366 (2019) 214–226.
22. S. Sabooni, E. Galinmoghaddam, M. Ahmadi, R.J. Westerwaal, J. van de Langkruis, E. Zoestbergen, J.T.M. De Hosson, Y.T. Pei, Surf. Coatings Technol. 359 (2019) 227–238.
23. W.D. Callister, D.G. Rethwisch, "Corrosion and Degradation of Materials", in: Mater. Sci. Eng., 8th ed., John Wiley & Sons, Inc., (2011) pp. 673–718.
24. E. McCafferty, "A Brief Review of Thermodynamics", in: Introd. to Corros. Sci., Springer Science & Business Media, Alexandria, (2010) pp. 57–72.
25. K.R. Trethewey, J. Chamberlain, "The Theory of Aqueous Corrosion", in: Corros. Students Sci. Eng., 3rd ed., Longman Scientific & Technical, (1992) pp. 61–106.

26. E.E. Stansbury, R.A. Buchanan, "Electrochemical Thermodynamics: The Gibbs Function, Electrochemical Reactions, and Equilibrium Potentials", in: Fundam. Electrochem. Corros., ASM International, (2000) pp. 23–86.

27. R.W. Revie, H.H. Uhlig, "Thermodynamics: Corrosion Tendency and Electrode Potentials", in: Corros. Corros. Control An Introd. to Corros. Sci. Eng., 4th ed., John Wiley & Sons, Inc., (2008) pp. 21–42.

28. J.R. Davis, "Basic Concepts Important to Corrosion", in: Corros. Underst. Basics, J.R. Davis (Ed.), ASM International, (2000) pp. 21–48.

29. M. Pourbaix, Atlas of electrochemical equilibria in aqueous solutions (English edition), Pergamon Press, Oxford, (1966).

30. J. Tafel, Zeitschrift Für Phys. Chemie. 50 (1905) 641–712.

31. J. Tafel, K. Naumann, Zeitschrift Für Phys. Chemie. 50 (1905) 713–752.

32. C. Wagner, W. Traud, Zeitschrift Für Elektrochemie. 44 (1938) 391–454.

33. M. Stern, A.L. Geary, J. Electrochem. Soc. 104 (1957) 56–63.

34. R.G. Kelly, J.R. Scully, D. Shoesmith, R.G. Buchheit, Electrochemical techniques in corrosion science and engineering, 1st ed., Marcel Dekker, (2003).

35. H. Helmholtz, Ann. Der Phys. Und Chemie. 165 (1853) 211–233.

36. M. Gouy, J. Phys. Theor. Appl. 9 (1910).

37. D.L. Chapman, London, Edinburgh, Dublin Philos. Mag. J. Sci. 25 (1913) 475–481.

38. O. Stern, Zeitschrift Für Elektrochemie. 30 (1924) 508–516.

39. H.H. Uhlig, C. V. King, J. Electrochem. Soc. 119 (1972) 327C.

40. J.C. Scully, "Aqueous Corrosion", in: Corrosion, 3rd ed., Pergamon Press, Oxford, (1990) pp. 54–129.

41. J.C. Scully, "Corrosion Failures and Attack", in: Fundam. Corros., 3rd ed.,

Pergamon Press, Oxford, (1990) pp. 165–215.

42. ATLAS STEELS GALVANIC CORROSION, (2010). www.atlassteels.com.au (accessed December 10, 2018).

43. G.L. Cox, B.E. Roetheli, Effect of Oxygen Concentration on Corrosion Rates of Steel and Composition of Corrosion Products Formed in Oxygenated Water, Whitman, (1931).

44. R.W. Revie, H.H. Uhlig, "Iron and Steel", in: Corros. Corros. Control An Introd. to Corros. Sci. Eng., 4th ed., (2008) pp. 115–148.

45. U.R. Evans, Met. Ind. 29 (1926) 481–482.

46. N.P. Ahmadi, E. Rafiezadeh, Int. J. ISSI. 6 (2009) 25–29.

47. British Standards Institution, (2009) 16.

48. L.G. Wang, T. Zhou, Y. Huang, Key Eng. Mater. 575–576 (2014) 510–514.

49. N. van Landschoot, C. Dane, R. Bleeker, M. Vlot, ATZ Worldw. 115 (2013) 4–8.

50. K. Nishimura, H. Shindo, H. Nomura, K. Katoh, Tetsu-to-Hagane. 89 (2003) 174–179.

51. S. Schuerz, M. Fleischanderl, G.H. Luckeneder, K. Preis, T. Haunschmied, G. Mori, A.C. Kneissl, Corros. Sci. 51 (2009) 2355–2363.

52. T. Prosek, N. Larché, M. Vlot, F. Goodwin, D. Thierry, Mater. Corros. 61 (2010) 412–420.

53. P. Volovitch, T.N.N. Vu, C. Allély, A. Abdel Aal, K. Ogle, Corros. Sci. 53 (2011) 2437–2445.

54. D. Persson, D. Thierry, N. LeBozec, T. Prosek, Corros. Sci. 72 (2013) 54–63.

55. R. Krieg, A. Vimalanandan, M. Rohwerder, J. Electrochem. Soc. 161 (2014) C156–C161.

56. T. Lostak, A. Maljusch, B. Klink, S. Krebs, M. Kimpel, J. Flock, S. Schulz, W. Schuhmann, Electrochim. Acta. 137 (2014) 65–74.

57. M. Salgueiro Azevedo, C. Allély, K. Ogle, P. Volovitch, Corros. Sci. 90 (2015) 482–490.

58. J. Sullivan, N. Cooze, C. Gallagher, T. Lewis, T. Prosek, D. Thierry, Faraday Discuss. 180 (2015) 361–379.

59. J. Sullivan, S. Mehraban, J. Elvins, Corros. Sci. 53 (2011) 2208–2215.

60. T. Prosek, D. Persson, J. Stoulil, D. Thierry, Corros. Sci. 86 (2014) 231–238.

61. J. Han, K. Ogle, J. Electrochem. Soc. 164 (2017) C952–C961.

62. D. Thierry, D. Persson, G. Luckeneder, K.H. Stellnberger, Corros. Sci. 148 (2019) 338–354.

63. T. Prosek, J. Hagström, D. Persson, N. Fuertes, F. Lindberg, O. Chocholatý, C. Taxén, J. Šerák, D. Thierry, Corros. Sci. 110 (2015) 71–81.

64. T. Prosek, A. Nazarov, U. Bexell, D. Thierry, J. Serak, Corros. Sci. 50 (2008) 2216–2231.

65. S. Schürz, G.H. Luckeneder, M. Fleischanderl, P. Mack, H. Gsaller, A.C. Kneissl, G. Mori, Corros. Sci. 52 (2010) 3271–3279.

66. E. Diler, B. Rouvellou, S. Rioual, B. Lescop, G. Nguyen Vien, D. Thierry, Corros. Sci. 87 (2014) 111–117.

67. M. Salgueiro Azevedo, C. Allély, K. Ogle, P. Volovitch, Corros. Sci. 90 (2015) 472–481.

68. P. Volovitch, C. Allely, K. Ogle, Corros. Sci. 51 (2009) 1251–1262.

69. R. Hausbrand, M. Stratmann, M. Rohwerder, Corros. Sci. 51 (2009) 2107–2114.

70. E. Diler, B. Lescop, S. Rioual, G. Nguyen Vien, D. Thierry, B. Rouvellou, Corros. Sci. 79 (2014) 83–88.

71. D.M. Mattox, Met. Finish. 99 (2001) 409–423.

72. W. König, R. Fritsch, D. Kammermeier, Surf. Coatings Technol. 49 (1991) 316–324.

73. P.C. Jindal, A.T. Santhanam, U. Schleinkofer, A.F. Shuster, Int. J. Refract. Met. Hard Mater. 17 (1999) 163–170.

74. V. Teixeira, J. Carneiro, P. Carvalho, E. Silva, S. Azevedo, C. Batista, Multifunct. Nanoreinforced Polym. Food Packag. (2011) 285–315.

75. A. Ulman, Thin Film. 26 (1998) 1–81.

76. D.M. Mattox, Handbook of Physical Vapor Deposition (PVD) Processing, Noyes Publications, (1998).

77. K.S. Harsha, Principles of physical vapor deposition of thin films, Elsevier, (2005).

78. A. Pimpinelli, J. Villain, Physics of crystal growth, Cambridge University Press, (1998).

79. J.A. Venables, (2000).

80. J.A. Thornton, Annu. Rev. Mater. Sci. 7 (1977) 239–260.

81. M.S.N. Idora, M.M. Rahman, M. Ismail, W.S.W. Nik, Appl. Mech. Mater. 554 (2014) 213–217.

82. A. Sen, M.S.H. Tareq, Sci. Eng. Investig. 5 (2016) 134–137.

83. J. Kawafuku, J. Katoh, M. Toyama, K. Ikeda, H. Nishimoto, H. Satoh, "Properties of zinc alloy coated steel sheets obtained by continuous vapor deposition pilot-line", in: SAE Tech. Pap., SAE International, (1991).

84. M. Morishita, K. Koyama, M. Murase, Y. Mori, ISIJ Int. 36 (1996) 714–719.

85. M. Morishita, K. Koyama, Y. Mori, ISIJ Int. 37 (1997) 55–58.

86. M. Morishita, K. Koyama, Y. Mori, Mater. Trans. JIM. 38 (1997) 719–723.

87. O.O.Ø. Knudsen, A. Forsgren, Corrosion control through organic coatings, second edition, Second, CRC Press, Taylor & Francis Group, 6000 Broken Sound Parkway NW, Suite 300, Boca Raton, FL 33487-2742, (2017).
88. T. Wall, Surf. Eng. 11 (1995) 29–29.
89. S. Spring, Metal cleaning, Reinhold, New York, (1963). https://www.worldcat.org/title/metal-cleaning/oclc/636335686 (accessed August 1, 2019).
90. A. Amirudin, D. Thierry, Prog. Org. Coatings. 28 (1996) 59–75.
91. R.D. Granata, "Mechanism of Coatings Disbondment", in: Automot. Corros. Prot., R. Baboian (Ed.), NACE International, (1992).
92. W. Fürbeth, M. Stratmann, Prog. Org. Coatings. 39 (2000) 23–29.
93. G. Williams, H.N. McMurray, J. Electrochem. Soc. 148 (2001) B377–B385.
94. M. Stratmann, R. Feser, A. Leng, Electrochim. Acta. 39 (1994) 1207–1214.
95. J.D.. Sharman, J.M. Sykes, T. Handysidem, Corros. Sci. 35 (1993) 1375–1383.
96. M. Stratmann, A. Leng, W. Fürbeth, H. Streckel, H. Gehmecker, K.H. Große-Brinkhaus, Prog. Org. Coatings. 27 (1996) 261–267.
97. W. Fürbeth, M. Stratmann, Corros. Sci. 43 (2001) 207–227.
98. R. Hausbrand, M. Stratmann, M. Rohwerder, Steel Res. Int. 74 (2003) 453–458.
99. R. Hausbrand, M. Stratmann, M. Rohwerder, J. Electrochem. Soc. 155 (2008) C369.
100. A. Bautista, Prog. Org. Coatings. 28 (1996) 49–58.
101. G. Williams, R. Grace, "Chloride-induced filiform corrosion of organic-coated magnesium", in: Electrochim. Acta, Pergamon, (2011) pp. 1894–1903.
102. N. Wint, D. Eaves, E. Michailidou, A. Bennett, J.R. Searle, G. Williams, H.N. McMurray, Corros. Sci. 158 (2019).

103. H. Silman, Br. Corros. J. 7 (1972) 98–98.

104. A.M. Rosenberg, J.M. Gaidis, Mater. Perform. 18 (1979) 45–48.

105. S.M. Powell, H.N. McMurray, D.A. Worsley, Corrosion. 55 (1999) 1040–1051.

106. B.N. Popov, B.N. Popov, "Chapter 14 – Corrosion Inhibitors", in: Corros. Eng., (2015) pp. 581–597.

107. H.S. Isaacs, Corros. Sci. 28 (1988) 547–558.

108. H.S. Isaacs, A.J. Aldykiewicz, D. Thierry, T.C. Simpson, Corros. 52 (1996) 163–168.

109. D.A. Worsley, H.N. McMurray, A. Belghazi, Chem. Commun. 36 (1997) 2369–2370.

110. S. Böhm, H.N. McMurray, S.M. Powell, D.A. Worsley, Electrochim. Acta. 45 (2000) 2165–2174.

111. H.N. McMurray, S.M. Powell, D.A. Worsley, Br. Corros. J. 36 (2001) 42–48.

112. R.M. Souto, Y. González-García, A.C. Bastos, A.M. Simões, Corros. Sci. 49 (2007) 4568–4580.

113. G. Williams, H.N. McMurray, Electrochem. Soc. 155 (2008) C340–C349.

114. G. Williams, H.A.L. Dafydd, R. Grace, Electrochim. Acta. 109 (2013) 489–501.

115. B. Łosiewicz, M. Popczyk, M. Szklarska, A. Smołka, P. Osak, Solid State Phenom. 228 (2015) 353–368.

116. J. Sullivan, C. Weirman, J. Kennedy, D. Penney, Corros. Sci. 52 (2010) 1853–1862.

117. C.F. Glover, G. Williams, J. Electrochem. Soc. 164 (2017) C407–C417.

118. N. Wint, K. Khan, J.H. Sullivan, H.N. McMurray, J. Electrochem. Soc. 166 (2019) C3028–C3038.

119. D.A. Worsley, A. Belghazi, S.M. Powell, Ironmak. Steelmak. 26 (1999) 387–

392.

120. T. Prosek, A. Nazarov, A. Le Gac, D. Thierry, Prog. Org. Coatings. 83 (2015) 26–35.

121. G. Williams, R.J. Holness, H.N. McMurray, D.A. Worsley, Electrochem. Commun. 6 (2004) 549–555.

122. A.P. Nazarov, D. Thierry, Electrochim. Acta. 49 (2004) 2955–2964.

123. K. Wapner, M. Stratmann, G. Grundmeier, Electrochim. Acta. 51 (2006) 3303–3315.

# Chapter 2. Experimental Methods

## 2.1 Materials

### *2.1.1 Metallic Coatings*

All metallic coated steel samples in this thesis were produced by Tata Steel Netherlands. Two zinc alloy coatings were applied using the traditional hot dip method and are commercially available: hot dip galvanised “GI” coating (HDG) and Magizinc® (ZMA).

Four PVD zinc alloy coatings were produced using a Von Ardenne roll-to-roll “Electro Magnetic Evaporation Line IJmuiden”, EMELY. It is now a batch process, under $10^{-4}$ bar pressure, which utilizes thermal evaporation to deposit pure or alloy coatings onto steel strip. The EMELY line produces the Zn-Mg coatings via bi-layer co-deposition: an initial pure zinc layer (referred to as the basecoat) is deposited in one “pass” and, when the line direction is reversed, zinc and magnesium are deposited simultaneously in the second pass to form the topcoat. These are single-sided coatings all deposited on 0.2 mm gauge blackplate steel. Due to the nature of the process, the PVD coatings vary in thickness as strict control of the line speed and melt temperature must be maintained. The properties of all samples are summarized in **Table 2.1**.

**Table 2.1:** Properties for all metallic coated strip steel samples analysed in this thesis.

| **Sample I.D.** | **Details** | **Supplier** |
|---|---|---|
| HDG | Commercial coating "GI"<br>Process: hot-dip galvanising<br>Coating composition: Zn-0.2 wt% Al<br>Coating thickness: 20 µm<br>Mean surface roughness: 1.30 µm | Tata Steel IJmuiden |
| ZMA | Commercial coating "Magizinc®"<br>Process: hot-dip galvanising<br>Coating composition: Zn-1.6 wt% Al-1.6 wt% Mg<br>Coating thickness: 10 µm<br>Mean surface roughness: 1.00 µm | Tata Steel IJmuiden |
| PVD0 | Pilot line sample<br>Process: physical vapour deposition<br>Coating composition: Zn<br>Coating thickness: 3.30 µm<br>Mean surface roughness: 300 nm | Tata Steel IJmuiden |
| PVD4 | Pilot line sample<br>Process: physical vapour deposition (dual layer)<br>Base coat composition: Zn<br>Base coat thickness: 2.10 µm<br>Top coat composition: Zn-4 wt% Mg<br>Top coat thickness: 4.10 µm<br>Mean surface roughness: 390 nm | Tata Steel IJmuiden |
| PVD10 | Pilot line sample<br>Process: physical vapour deposition (dual layer)<br>Base coat composition: Zn<br>Base coat thickness: 0.95 µm<br>Top coat composition: Zn-10 wt% Mg<br>Top coat thickness: 3.80 µm<br>Mean surface roughness: 270 nm | Tata Steel IJmuiden |
| PVD20 | Pilot line sample<br>Process: physical vapour deposition (dual layer)<br>Base coat composition: Zn<br>Base coat thickness: 1.10 µm<br>Top coat composition: Zn- 20 wt% Mg<br>Top coat thickness: 4.10 µm<br>Mean surface roughness: 290 nm | Tata Steel IJmuiden |

### *2.1.2 Organic Coatings*

Poly(vinyl butyral-co-vinyl alcohol-co-vinyl acetate) (PVB) powder ($M_w$ 70,000-100,000) supplied by Merck (Sigma-Aldrich) was dissolved in Ethanol (≥99 % purity) supplied by Merck (Sigma-Aldrich) for use as a model organic coating in all delamination tests. The standard coating solution used in this work was 15.5 % w/w of PVB power in ethanol made up using an IKA high shear mixer, with the PVB powder added slowly and incrementally to avoid agglomeration. The PVB solution was degassed in an ultrasonic bath for at least an hour (the bath and PVB solutions were maintained below room temperature during degassing by the replacement of the sonic bath DI water). Once bar coated to a metal substrate, the model PVB coating air dries completely within 20 minutes and provides good adhesion to the substrate. Furthermore, exposure to salt solution causes the model PVB coating to delaminate within a reasonable timeframe during accelerated testing.

For the identification of compatible corrosion inhibitor pigments, a selection of phosphate-based pigments were supplied by Société Nouvelle des Couleurs Zincique (SNCZ), and designated as shown in

**Table 2.2**.

**Table 2.2:** List of pigments selected for delamination resistance compatibility testing, compositions are taken from the company MSDS files.

| **Pigment I.D.** | **Composition** | **Density, $\rho_{pig}$ (g.cm$^{-3}$)** |
|---|---|---|
| PZ20 | 94 % $Zn_3(PO_4)_2.xH_2O$<br>6 % ZnO | 3.30 |
| NOVINOX PAT15 | ~100 % $MgHPO_4.xH_2O$<br><2.5 % $Zn_3(PO_4)_2.xH_2O$ | 2.20 |
| NOVINOX ePAZ | 63 % $AlH_2P_3O_{10}.2H_2O$<br>37 % ZnO<br><2.5 % $Zn_3(PO_4)_2.xH_2O$ | 2.90 |
| NOVINOX PAM | 70 % $AlH_2P_3O_{10}.2H_2O$<br>30 % “Non-hazardous substance”<br><2.5 % ZnO | 2.60 |

In order to appropriately compare the compatibility and effectiveness of the corrosion inhibitor pigments, PVB pigment formulations were calculated using equation 2.1:

$$M_{pig} = \frac{\emptyset.\, M_{pol} \cdot \rho_{pig}}{(1-\emptyset).\, \rho_{pol}} \qquad 2.1$$

where $M_{pig}$ is the calculated mass of pigment required to formulate the desired volume fraction, $\emptyset$. $M_{pol}$ is the mass of the polymer (PVB), $\rho_{pig}$ is the density of the pigment (given in **Table 2.2**) and $\rho_{pol}$ is the density of the polymer (~0.8 g.cm$^{-3}$ [1]). It is important to note that $M_{pol}$ refers to the mass of the PVB powder; the 15.5 wt% PVB solution of mass $M_{polsol}$ would be (equation 2.2):

$$M_{polsol} = \frac{M_{pol} \cdot 100}{15.5} \qquad 2.2$$

which is more practically relevant as the pigment-free PVB is formulated prior to the addition of the pigment powder. Likewise, $\rho_{pol}$ is the density of the PVB powder before it is added to ethanol.

### *2.1.3 Electrolytes*

All electrolyte solutions were prepared from de-ionised (DI) water of 99.998 % purity. **Table 2.3** lists the salts used in this work to create solutions for electrochemical study. The specific concentration of the solutions are listed in the associated chapters.

**Table 2.3:** List of salts dissolved in deionised water to form electrolytes in the electrochemical studies.

| **Material** | **Details** | **Supplier** |
|---|---|---|
| NaCl | ≥99.0 % purity | Merck (Sigma-Aldrich) |
| NaOH | ≥98.0 % purity | Merck (Sigma-Aldrich) |
| ZnCl | ≥98.0 % purity | Merck (Sigma-Aldrich) |
| MgCl | ≥98.0 % purity | Merck (Sigma-Aldrich) |
| CsCl | ≥99.0 % purity | Merck (Sigma-Aldrich) |

### *2.1.4 Consumables*

The general consumables used in this work are listed in **Table 2.4** (glassware excluded).

**Table 2.4:** List of laboratory consumables used.

| **Material** | **Details** | **Supplier** |
|---|---|---|
| PTFE tape | 25 mm wide | RS |
| Scotch tape | 19 mm wide | RS |
| Electrical tape | 19 mm wide, 30 µm thick, blue | RS |
| Carbon tape | 10 mm wide | RS |
| Silicon Rubber | Non-corrosive, white | RS |
| Acetone | ≥99 % purity | Merck (Sigma-Aldrich) |
| Ethanol | ≥99 % purity | Merck (Sigma-Aldrich) |

## 2.2 Surface and Compositional Characterisation

### *2.2.1 Scanning Electron Microscopy (SEM) and Energy Dispersive X-Ray Spectroscopy (EDX)*

The majority of SEM images were captured using a Hitachi TM 3000 electron microscopy using 5 kV or 15 kV accelerating voltage and a working distance of 10 mm. All EDX maps were generated using Quantax 70 software, in combination with the Hitachi TM 3000 electron microscope, with scan times of 5 min minimum.

### *2.2.2 Transmission Electron Microscopy (TEM)*

Gallium focused ion beam (FIB) milling was achieved using a FEI Helios UC G4 system combined with a JEOL 7800F field emission gun scanning electron microscope (FEGSEM). A gas injector system (GIS) attachment for the FEI Helios was used for sample control and transport. Transmission electron microscopy was conducted using a FEI Titan TEM on samples sectioned to 10 µm x 10 µm x 50 nm. These TEM and associated imaging studies were conducted at the University of Virginia by expert operator Helge Heinrich.

### *2.2.3 X-Ray Powder Diffraction (XRD)*

XRD analysis was undertaken using a Bruker D8 Discover, with Davinci design, and Cu Kα radiation with a wavelength of 1.5418 Å. All scans used an applied voltage of 40 kV and a current of 40 mA. The scanning range varied between 5 and 70 ° in Bragg-Brentano geometry and a 0.3 mm slit size. Data was assessed using the diffract.eva program with reference data from Crystallographic Open Database. The XRD was operated by Dr Thomas Dunlop of Swansea University.

## 2.3 Electrochemical Characterisation

### *2.3.1 Potentiodynamic Testing and Electrochemical Impedance Spectrosxopy (EIS)*

Potentiodynamic polarisation, open circuit potential (OCP) and electrochemical impedance spectroscopy (EIS) analyses were all carried out in a three-electrode cell setup using a Bio-Logic SP2001 potentiostat at the University of Virginia with assistance from Gregory Kubacki. The coated steel samples acted as working electrodes

(WE) with a 1 $cm^2$ area exposed, a platinum-niobium mesh was the counter electrode (CE) and a saturated calomel electrode (SCE) was used as the reference (0.241 V vs. SHE).

### *2.3.2 Rotating Disk Electrode (RDE)*

The RDE method was used in this work to characterise facilitation of the oxygen reduction reaction (ORR) on the bare metal surface of the coatings via a series of quasi potentiostatic polarisation experiments. The equipment used was an RDE-2 rotating disk electrode system supplied by Sycopel Scientific (shown in **Figure 2.1**). A Solartron 1280 potentiostat and standard desktop PC were used for data capture and processing. In the RDE experiments, a Gamry mercury/mercurous sulphate reference electrode and a platinum gauze counter electrode were used.

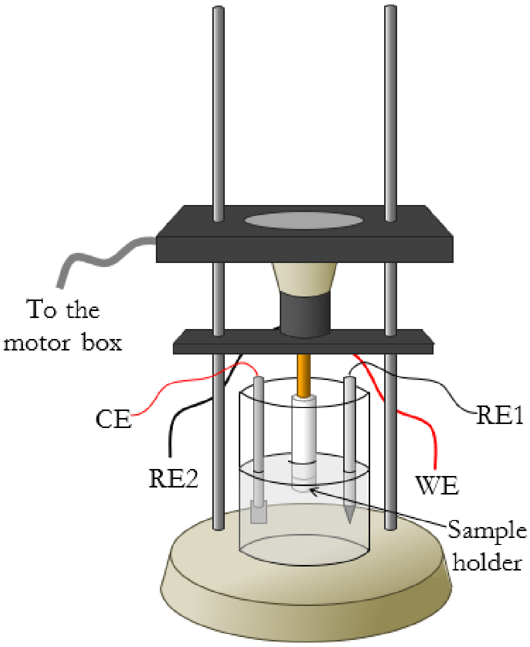

**Figure 2.1:** RDE apparatus.

## 2.4 Scanning Vibrating Electrode Technique

### *2.4.1 Apparatus*

The SVET in this thesis was assembled in Swansea University laboratories and has been extensively used previously to study electrochemistry of bare metal coatings under immersion conditions [2–10]. The probe assembly unique to Swansea University is shown schematically in **Figure 2.2**. It consists of a 125 µm platinum wire sealed within a capillary glass sheath resulting in a total cross-sectional diameter of 250 µm. The tip of the glass-encased platinum wire was polished flat using 1200 grit SiC paper, exposing the full diameter of the platinum wire. The probe tip glass casing was connected to another glass capillary tube, termed the “push rod”, via a PTFE connector and sealed with super glue. The push rod was encased within an aluminium cylindrical screen, fed out the top into a µ-metal enclosure that housed the electromechanical driver to which the push rod is connected. The reference electrode (a 2.5 cm x 2.5 cm low-impedance silver chloride sheet) was secured directly to the aluminium cylindrical screen.

The platinum wire tip was connected to a coaxial cable into a Perkin Elmer model 7260 lock-in amplifier which detects and digitises the signal potential. The vibration of the electrochemical driver is determined by a lock-in oscillator. The probe assembly positioning was controlled by stepper motors which drive three orthogonal linear bearings arrangement (Time and Precision Ltd.).

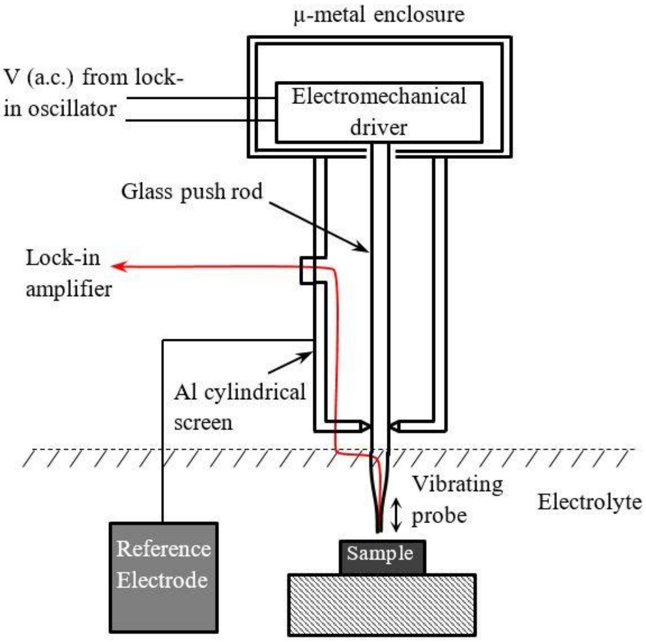

**Figure 2.2:** Schematic of the Swansea University SVET probe assembly (adapted from Williams and McMurray, 2008 [8]).

SVET experiments were conducted on samples affixed to the interior base of 3.5 L crystallisation dish filled with the selected electrolyte. The samples would typically be cut to 10 mm by 10 mm, rinsed with ethanol and an area of 6 mm by 6 mm would be isolated using PTFE tape which would also fix the coupons to the bottom of the crystallisation dish.

### *2.4.2 Calibration and setup*

For every SVET experiment, the SVET probe tip was first cleaned via immersion in a tailored PTFE well containing 2 M HCl solution for 15 minutes and subsequently rinsed with DI water. Following the cleaning procedure, the SVET was also calibrated using a previously devised two-part calibration cell, shown in **Figure 2.3.**

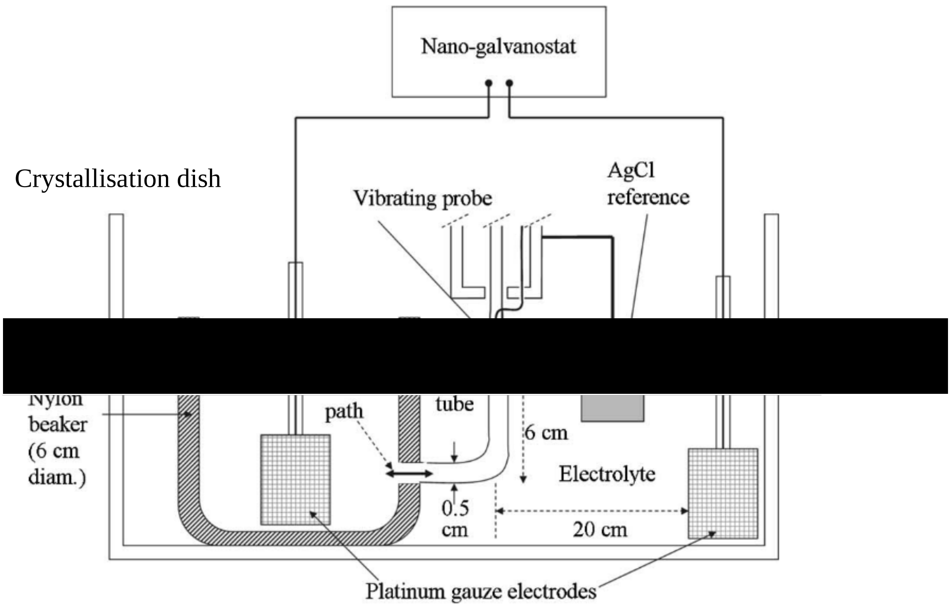

[redacted]

**Figure 2.3:** Schematic of the standard calibration cell used in this work [8].

The calibration cell was comprised of a nylon beaker both immersed in the electrolyte (within a 3.5 L crystallisation dish) and containing the electrolyte; the bodies of solution were separated by a vertically oriented glass tube (with an internal diameter of 0.5 cm). Platinum gauze electrodes were fitted on the inside and the outside of the beaker and were each connected to the positive and negative terminals of a nano-galvanostat to allow the passing of a set current into the solution and purposefully through the vertical glass tube.

During calibration, the SVET probe tip was inserted approximately 5mm into the vertical glass tube and the SVET reference electrode was immersed in the exterior electrolyte. When current was passed between the two platinum gauze electrodes, the current flux in the glass tube was aligned vertically and thus parallel with the probe axis of vibration. Moreover, the current flux density across the tube was constant and equal to the cell current divided by the internal cross-sectional area of the glass tube.

A systematic variance in current was passed through the calibration cell in order to record the measured potential in a calibration plot; the calibration factor was the gradient of the plot of E (nV) vs. $J_z$ ($A.m^{-2}$).

The measured potential in solution during the SVET experiment over a corroding bare metal surface can be converted to current density via equation 1.20. The calibration step allows the determination of the calibration factor, G, which is the combination of both $a_{pp}$ and $\kappa$:

$$G = \kappa / a_{pp} \tag{2.3}$$

Thus, the current density for all SVET experiments was calculated by dividing the measured peak-to-peak voltage by the predetermined calibration factor.

**Table 2.5** provides the standard parameters used for the initial automatic height scan (which maps out the 3 dimensional location of the sample for the software) and the data scanning. The importance of maintaining a consistent probe-to-specimen distance due to the inverse square relationship of field strength vs. probe height was previously explored by Searle et al. [11]. The samples analysed in this thesis were all relatively flat and required no additional height scan mapping. The scan dimensions correlate to the exposed sample area, which was selected as the maximum size visible for a submerged camera in the SVET time-lapse work described in chapter 5. The scan resolution was a compromise between the resolution of the data and the time taken to fully scan a rapidly corroding sample area.

**Table 2.5:** SVET software parameters.

| Parameter | Value for Height Scan | Value for Data Scan |
|---|---|---|
| Amplitude (V) | 0.020 | 0.015 |
| Frequency (Hz) | 900 | 140 |
| Sensitivity (mV) | 10 | 0.50 |
| AC gain (dB) | 40 | 40 |
| Time constant (ms) | 50 | 50 |
| Scan dimensions (mm) | - | 6.0 x 6.0 |
| Scan resolution (mm) | - | 0.20 |
| Scan time interval (min) | - | 10 |
| Scan rest distance (mm) | - | 40 |
| Total number of scans | - | 144 (24 hours) |

## 2.5 Scanning Kelvin Probe

### *2.5.1 Apparatus*

The SKP apparatus is shown schematically in **Figure 2.4**. All SKP experiments were conducted under 95 % relative humidity (R.H.) conditions; this was achieved with a sealed steel chamber humidified using two petri dishes of 0.86 M NaCl. The steel chamber also acted as a faraday cage to limit any outside electrical noise interference.

The SKP probe tip was a 125 µm diameter gold wire vibrated normal to the sample surface to create the parallel plate setup described in section 1.7.2. The gold wire was attached to a glass push rod connecting it to an electromechanical driver (like the SVET the electromechanical driver was housed in a µ-metal box).

Sample preparation methods are explained fully in section 2.5.3, however all samples intended for SKP analysis were adhered to an M8 nut which allowed the sample to be screw-mounted onto the SKP stage. Electrical contact was made between the back of the sample and the transconductance amplifier via a stainless steel spring through the nut.

As with the SVET, SKP tip vibration was controlled by a lock-in oscillator and positioning was controlled by stepper motors which drive three orthogonal linear bearings arrangement (Time and Precision Ltd.), however, unlike the SVET the SKP probe remained stationary and the sample stage moves.

As stated in section 1.7.2, the vibration of the SKP results in a variance in the parallel plate capacitance and thus generates an alternating current. The dc-biased transconductance amplifier converted the current to an a.c. voltage which was detected by a Perkin Elmer 7620 lock-in amplifier. An integrator-based feedback system within the lock-in amplifier measured the corresponding d.c. output voltage and adjusted the bias voltage, $E_{kp}$, applied to the sample to automatically nullify the detected current. $E_{kp}$ was recorded by the SKP software and was converted to $E_{corr}$ using the standard calibration procedure in section 2.5.2.

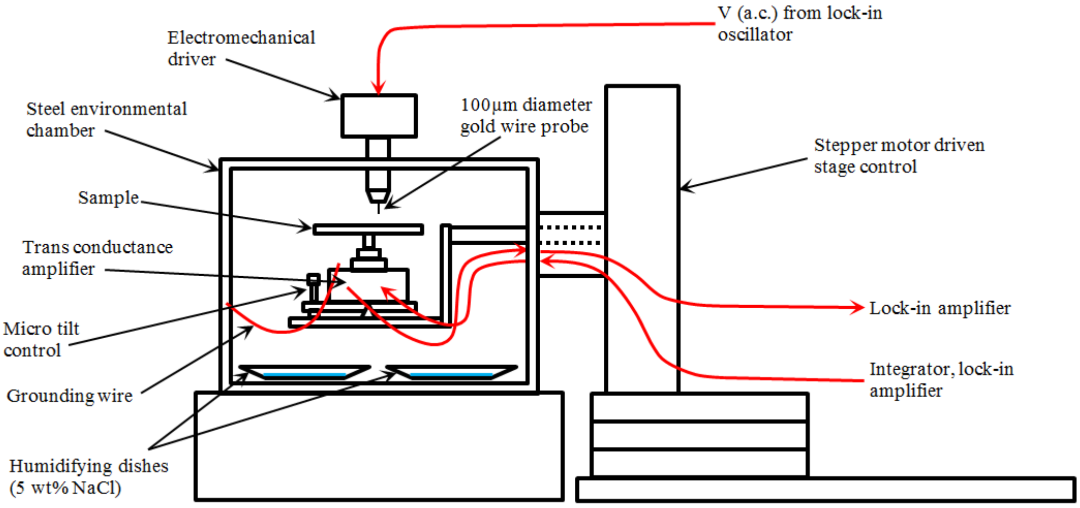

**Figure 2.4:** Full schematic of the Swansea University SKP.

### 2.5.2 Calibration and setup

For every SKP experiment, the SKP gold wire probe tip was first cleaned via immersion in a tailored PTFE well containing 2 M HCl solution for 15 minutes, followed by immersion in a well containing DI water.

$E_{corr}$ can be calculated from the measured $E_{kp}$ via the application of a constant which, when acquired via a calibration procedure, considers the specific environment in which the experiment is taking place (relative humidity, temperature etc.):

$$E_{corr} = E_{kp} + \text{constant} \qquad (2.4)$$

Calibration of the SKP in this work was carried out using a copper well (15 mm internal diameter, 5 mm depth) containing 0.5 M $CuSO_4$ solution. The SKP tip was vibrated approximately 100 µm above the surface of the copper sulphate and the $E_{kp}$ value was recorded. The $Cu/Cu^{2+}$ redox couple has a known $E_{corr}$ value of 298 mV vs. SHE (previously established by inserting a saturated calomel reference electrode into the electrolyte filled well and measuring OCP using a potentiostat [12]), therefore if the $E_{kp}$ of the copper well is measured to be 300 mV, equation 2.4, gives a constant of 598 mV. However, during delamination experiments, a previously calculated offset [12] of -220 mV must also be applied to the constant to reflect the presence of PVB, thus the final calibration constant in this instance would be 378 mV. Prior to every SKP experiment the $E_{kp}$ of the $Cu/Cu^{2+}$ calibration well was measured to eliminate any differences in environment or surface oxides. The SKP constant was then applied to the corresponding recorded $E_{kp}$ values from the experiment.

Standard SKP delamination studies monitor the propagation of a steep difference in $E_{corr}$, which represents the movement of the delamination front. **Table 2.6** lists the standard parameters used (adaptations to procedure are noted in the relevant chapter). The probe tip was scanned along four 12 mm parallel lines at 100 µm above the surface of the sample.

**Table 2.6:** SKP software parameters.

| **Parameter** | **Value for Data Scan** |
|---|---|
| Amplitude (V) | 0.04 |
| Frequency (Hz) | 280 |
| Sensitivity (mV) | 10 |
| AC gain (dB) | 0 |
| Time constant (ms) | 50 |
| Scan dimensions (mm) | 12.0 x 1.0 |
| Scan resolution (mm) | 0.05 |
| Scan time interval (min) | 60 |
| Total number of scans | 24 (24 hours) |

Data from SKP experiments was plotted using Microsoft Excel as $E_{corr}$ vs. distance for all four scan lines.

### *2.5.3 Sample preparation*

There were two general methods of sample preparation used in this work depending on the delamination mechanism being measured. **Figure 2.5** depicts the process of making a "Stratmann cell" (as explored in section 1.6.2); the sample configuration designed to monitor cathodic delamination.

As-received samples were cut to 50 mm x 50 mm square coupons, cleaned with ethanol and dried using nitrogen gas. Two strips of electrical tapes were applied parallel to the PVD/HDG coating direction and masked 10 mm x 50 mm of the coupon on either side. Scotch tape was applied normal to the electrical tape, masking 12 mm x 50 mm of one end of the coupon and overlapping the electrical tape. PVB coating solution was dropped onto the masking tape and bar coated over the bare surface of the sample using a glass stirring rod and the electrical tape as height guides. The wet coating was then left to dry in air at room temperature (18 °C) for 20 minutes, creating a dry coating thickness of ~20 µm. A scalpel was used to cut the masking tape along the interface between the masking tape and electrical tape only.

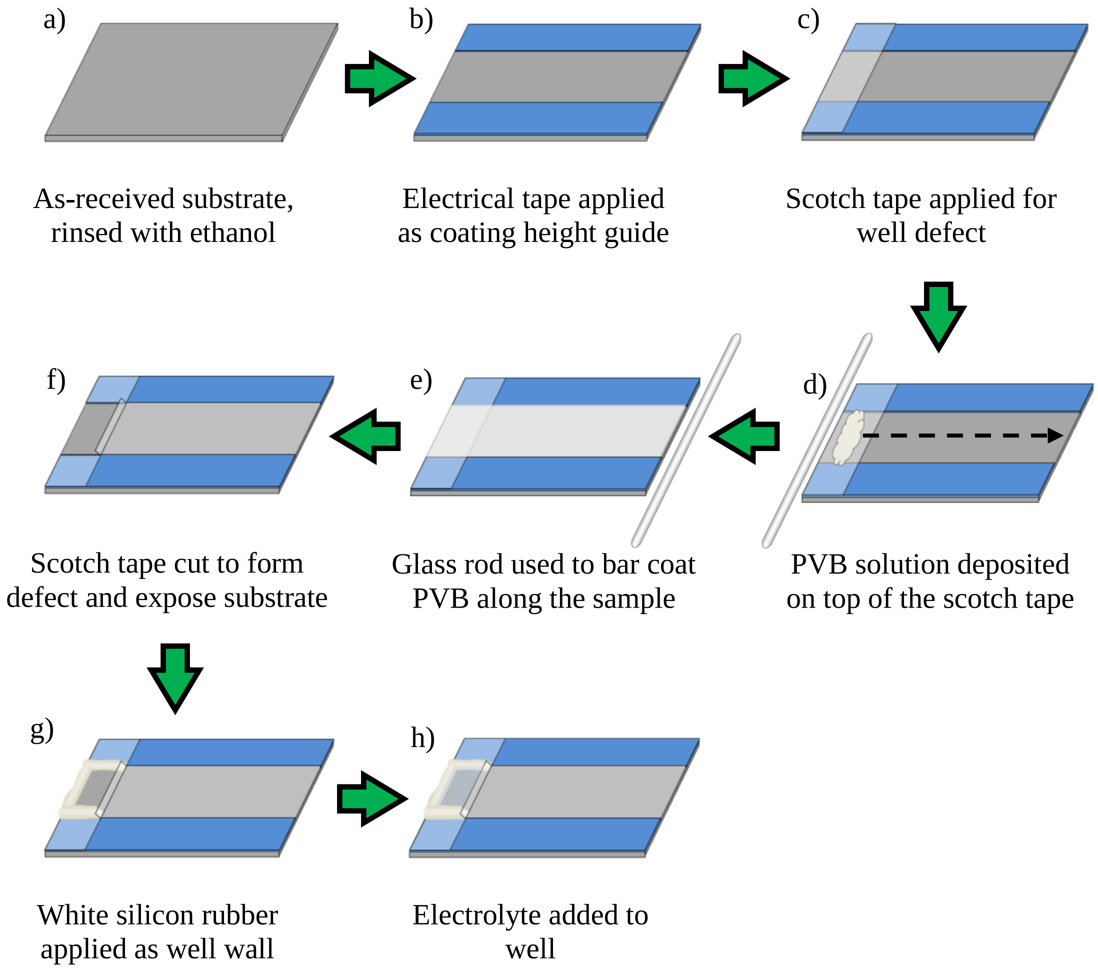

a) As-received substrate, rinsed with ethanol

b) Electrical tape applied as coating height guide

c) Scotch tape applied for well defect

d) PVB solution deposited on top of the scotch tape

e) Glass rod used to bar coat PVB along the sample

f) Scotch tape cut to form defect and expose substrate

g) White silicon rubber applied as well wall

h) Electrolyte added to well

**Figure 2.5:** Method for preparing a "Stratmann cell" sample for cathodic delamination study.

This allowed the sectioned masking tape to be peeled away from the bare metal surface and trimmed down to form a 3-4 mm lip height and the manmade organic coating defect. The back of a scalpel blade was used to fully separate the masking tape from the metal surface at the defect to ensure exposure of the PVB-metal interface. Silicon rubber was deposited along the electrical tape adjacent to the exposed sample surface and along the coupon edge to form the electrolyte well and support the lip. The Stratmann cell would then be left to dry in air at room temperature overnight.

For anodic undermining studies, sample preparation was similar to that of a Stratmann cell with the exclusion of the well formation. Therefore no masking tape was applied. After the PVB was bar coated and dried, a scalpel was used to make a 10 mm scribe in the centre of the coupon, parallel to the electrical tape, exposing both the zinc alloy coating and the steel substrate.

For both sample cell configurations, an M8 nut would be adhered to the back of the sample using a 2-part epoxy system (Loctite Double Bubble). The samples would then be mounted and sealed inside the SKP to equalise within the chamber and reduce the charging of the surface built up during manufacture of the cell. After the calibration procedure outlined in section 2.5.2, the sample cells would be returned to the chamber and balanced using the micro tilt control and systematic measurements of the SKP height signal along the scan area. Immediately before the start of the experiment, the required electrolyte would be added via a Pasteur pipette to the well of the Stratmann cell, or via micro syringe to the centre of the scribe on an anodic cell.

### *2.5.4 Time-lapse delamination*

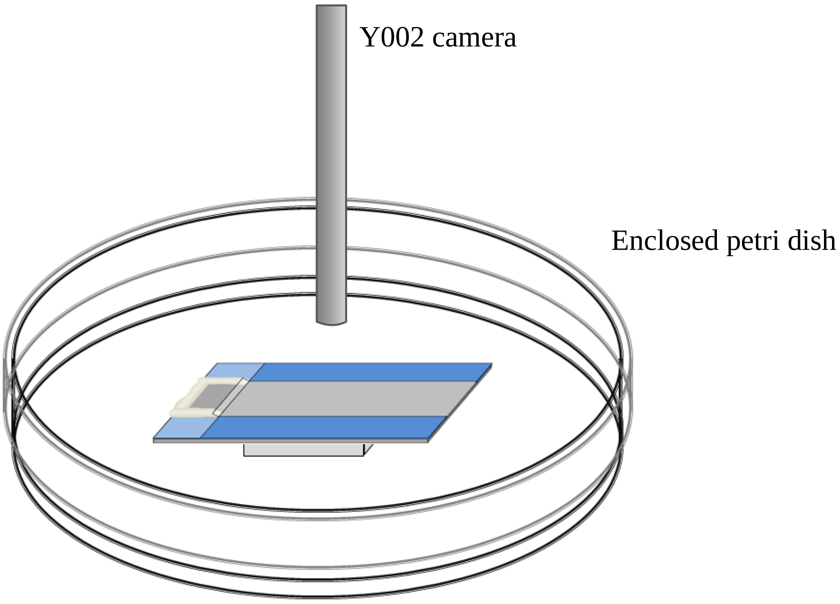

**Figure 2.6:** Setup for time-lapse photography of cathodic delamination.

To capture time-lapse photographs of cathodic disbondment or anodic undermining, the prepared sample was placed inside a sealed petri dish containing 0.86 M NaCl solution to create the 95% R.H. atmosphere. There was no contact between the sample coupon and the NaCl bath. A Y002 microscope endoscope camera was positioned directly above the petri dish for image capture (**Figure 2.6**). Automatic photograph capture was managed by Sky Studio at intervals of 1 min.

## 2.6 References

1. H. Domininghaus, Plastics for Engineers: Materials, Properties, Applications, Munich, (1993).
2. H.S. Isaacs, Corros. Sci. 28 (1988) 547–558.
3. H.S. Isaacs, A.J. Aldykiewicz, D. Thierry, T.C. Simpson, Corros. 52 (1996) 163–168.
4. D.A. Worsley, H.N. McMurray, A. Belghazi, Chem. Commun. 36 (1997) 2369–2370.
5. S. Böhm, H.N. McMurray, S.M. Powell, D.A. Worsley, Electrochim. Acta. 45 (2000) 2165–2174.
6. H.N. McMurray, S.M. Powell, D.A. Worsley, Br. Corros. J. 36 (2001) 42–48.
7. R.M. Souto, Y. González-García, A.C. Bastos, A.M. Simões, Corros. Sci. 49 (2007) 4568–4580.
8. G. Williams, H.N. McMurray, Electrochem. Soc. 155 (2008) C340–C349.
9. G. Williams, H.A.L. Dafydd, R. Grace, Electrochim. Acta. 109 (2013) 489–501.
10. B. Łosiewicz, M. Popczyk, M. Szklarska, A. Smołka, P. Osak, Solid State Phenom. 228 (2015) 353–368.
11. J.R. Searle, B.P. Wilson, K. Yliniemi, D.A. Worsley, H.N. McMurray, ECS Trans. 64 (2015) 69–80.
12. G. Williams, H.N. McMurray, J. Electrochem. Soc. 148 (2001) B377–B385.

# Chapter 3. Compositional analysis and characterisation of PVD Zn-Mg coatings on strip steel

## 3.1 Introduction

The coating of strip steel with zinc for sacrificial protection is well established in industry. Zinc is a less noble metal and will therefore act sacrificially if both zinc and steel are exposed to an environment where corrosion will take place [1], the formation of compact zinc corrosion products further improves the protection of steel. Research into zinc alloy coatings was prompted by the susceptibility of zinc to corrode more rapidly in aggressive environments. One of the more recent iterations of hot dip zinc alloy coatings is Zn-Mg-Al (ZMA), with commercial coatings such as Magizinc® (Zn-1.6 wt% Mg-1.6 wt% Al) from Tata Steel, Magnelis® (Zn-3 wt% Mg-3.5 wt% Al) from ArcelorMittal and SuperDyma® (Zn-3 wt% Mg-11 wt% Al) from Nippon Steel & Sumitomo Metal. These, and other compositions of ZMA coatings, have been extensively studied and established to provide superior corrosion protection compared to traditional pure zinc coatings [2–11]; improved corrosion resistance allows for much thinner coatings which are highly desirable in the automotive industry.

The limited solubility of magnesium in the zinc bath and rapid dross formation restricts the maximum magnesium content for galvanized ZMA coatings. Therefore, other technologies such as PVD have been suggested as alternative coating methods for the automotive industry [12]. The thermal evaporation PVD method first established in 2003 by Corus Technology B.V. (now Tata Steel Europe) utilised a unique vapour generation and transport system: the source metal was heated and levitated within an induction coil then guided through a vapour distribution box to the steel substrate while under continuous vacuum [13]. This process permitted the co-deposition of Zn-Mg onto strip steel, with composition being controlled accurately by source metal feed rate and temperature. The technology has evolved significantly over the last decade; multiple papers have been published on the adhesion properties of these PVD coatings [14–18], and a full air-to-air scale-up of the method was accomplished by POSCO in collaboration with Tata Steel Europe in 2011 [19]. Previous publications highlight the potential for improved corrosion resistance, however there is limited characterisation of the precise structure and composition of the studied coatings.

For zinc alloy coatings, it has been previously established that the microstructure plays a significant role in corrosion rate and mechanism [8,20–22], the same is true for aluminium and magnesium alloys [23–25]. Wint et al. recently reported the effect of microstructural refinement on localised corrosion and overall kinetics; much coarser structures limited the lateral anodic spreading, whereas grain refinement resulted in the opposite. It was proposed that increasing the size of cathodes, local to anodic sites, creates a much larger diffusion distance for the aggressive species within the electrolyte, thus reducing lateral spreading and consequently increasing the rate of coating depth penetration. Grain refinement reduces the diffusion distance and therefore shifts the affinity for coating penetration to lateral spread across the surface, reducing the time for substrate exposure [26].

This chapter aims to fully characterise the PVD Zn-Mg coatings and subsequently compare their microstructures to the commercially available HDG and ZMA hot dip galvanising coatings. Knowledge of the composition and heterogeneity of phase distribution will be necessary to assist in the explanation of corrosion behaviour in the following chapters. Due to the nature of the PVD method, the structure of the coatings required the use of the TEM in order to resolve the nanoscale features. In addition, the use of XRD was necessary to accurately confirm the phases present.

## 3.2 Experimental details

### *3.2.1 Materials*

In this chapter the PVD coated steel samples listed in **Table 2.1** are studied and compared to the commercially available HDG and ZMA coating strip steel.

### *3.2.2 Methods*

The surface of all coatings was viewed, as received, by a JEOL 7800F field emission gun scanning electron microscope (FEGSEM). Cross-sectional samples for transmission electron microscopy of the PVD4, PVD10 and PVD20 coated steel strip samples were prepared in a FEI Helios UC G4 system with a gallium focused ion beam (FIB) to obtain slices of 50-100 nm thickness. The ZMA and PVD4 microstructures were imaged by the FEGSEM. The phases present in PVD4 were identified using a FEI Titan transmission electron microscope (TEM) at the University of Virginia; the FIB cross sections were studied in the TEM using imaging, energy-dispersive X-ray spectroscopy, and selected area electron diffraction (SAED). The PVD10 and PVD20 nanostructures were also imaged using the FEI Titan TEM after FIB milling.

Phase compositional data was also acquired using XRD using the method and parameters outlined in section 2.2.3. All magnesium-containing PVD coatings were further studied using EDX; cross-sections were mounted in epoxy resin and element wt.% was acquired in five separate locations along the Zn-Mg top coat cross-section. Surface roughness was measured using White Light Interferometry.

## 3.3 Results and discussion

### *3.3.1 HDG and ZMA*

Commercial HDG and ZMA coating samples were characterised to establish the baseline industry standard for zinc-alloy coated strip steel as a reference for subsequent electrochemical analysis. In **Figure 3.1a**, the imaged surface shows a heterogeneous surface morphology. The cross-sectional microstructure shown in **Figure 3.1b** exhibits the eta phase zinc grains, ranging from 5-8 µm in diameter, separated from the steel substrate by a 0.1 µm thick aluminium intermetallic layer. The images adhere to previous evidence of HDG structure [27], and also support the commercially quoted thickness of 20 µm.

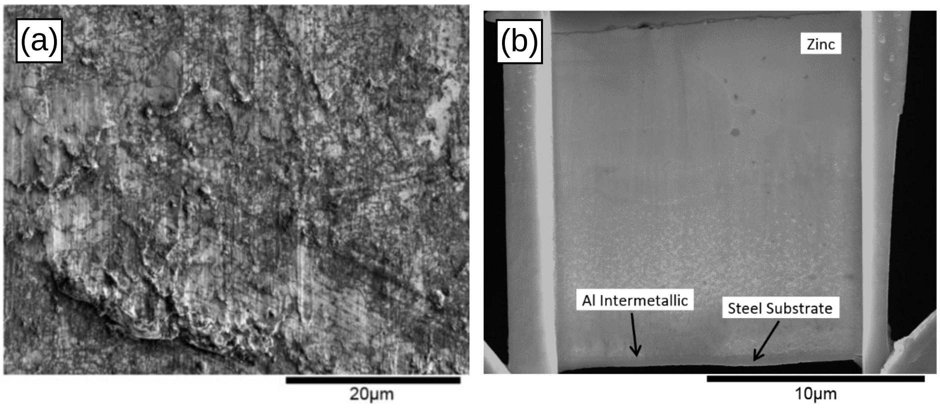

**Figure 3.1:** (a) The surface of the HDG coating observed using the FEGSEM, (b) the microstructure of HDG sectioned using a focused gallium ion beam and imaged by the FEGSEM.

In **Figure 3.2a**, the surface of the ZMA coating appears more homogeneous compared to HDG, with evidence of the rolling direction and possible scratches caused by roll slippage during galvanising. The microstructure presented by ZMA in **Figure 3.2b** is typical of Zn-Mg-Al coatings [11, 20,28,29], with primary zinc dendrites situated in a matrix of both the binary eutectic (zinc and $MgZn_2$ lamellae) and tertiary eutectic (zinc and $MgZn_2$ lamellar with aluminium-rich globules interspersed).

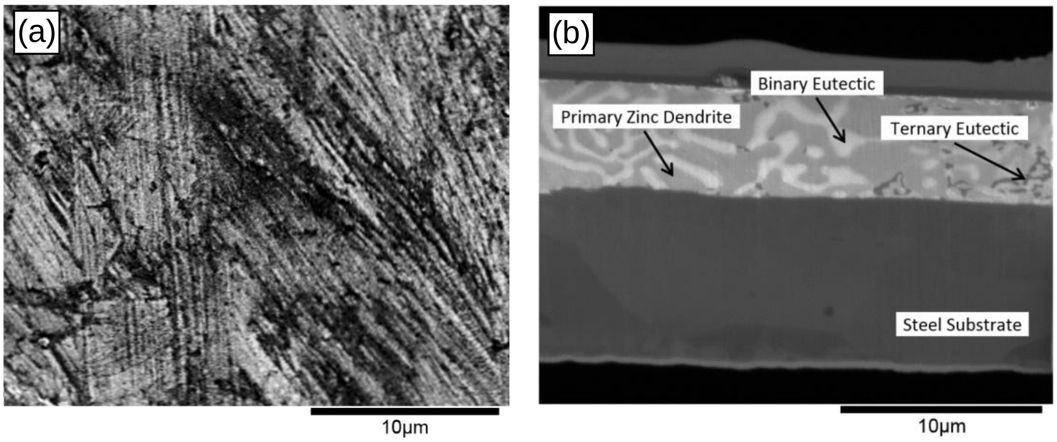

**Figure 3.2:** (a) The surface of the ZMA coating observed using the FEGSEM, (b) the microstructure of ZMA sectioned using a focused gallium ion beam and imaged by the FEGSEM.

Additionally, the ZMA coating is significantly thinner compared to HDG as it is fully accepted in industry that the addition of magnesium to a zinc coating permits a reduction in coating thickness owning to the superior corrosion resistance [27].

### 3.3.2 PVD coatings

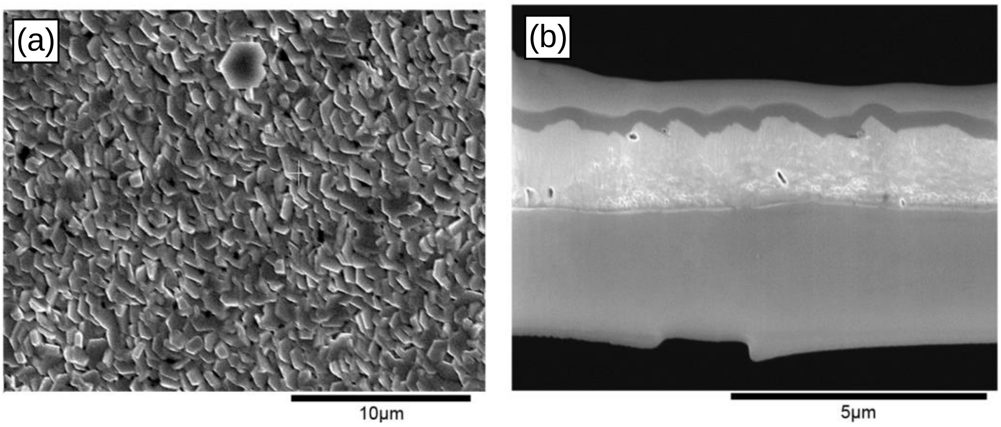

**Figure 3.3:** (a) The surface of the PVD0 coating observed using the FEGSEM, (b) the microstructure of PVD0 sectioned using a focused gallium ion beam and imaged by the FEGSEM.

The surface of PVD0 observed in **Figure 3.3a** appears to be comprised of hexagonal microplates, ranging from 1.0-3.0 μm in diameter. The loose packing of the plates to each other has resulted in an overall porosity of the coating, which is further supported by the holes observed in the cross-sectional image in **Figure 3.3b**. The size of the plates being approximately equal to the thickness of the zinc layer causes significantly sized gaps between the plates, however it does not appear that the steel substrate is exposed.

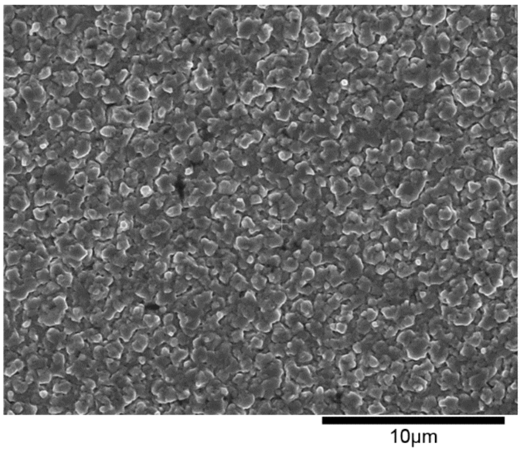

**Figure 3.4:** The surface of the PVD4 coating observed using the FEGSEM.

The surface of PVD4 in **Figure 3.4** demonstrates the influence of magnesium on the overall morphology of the coating. The coating has a more globular texture and the globules are significantly smaller (0.5-1.0 μm) than the zinc crystals observed in the PVD0 coating. It is proposed that, at the processing temperature, the vapour pressure of magnesium is greater than zinc [30], therefore the driving force for condensation is greater than for pure zinc. This creates more nucleation points on the steel substrate and consequently limits the growth of the Zn-Mg globules. Additionally, as described in section 1.5.3, the low mobility of zinc and magnesium exacerbate the geometric shadowing, causing pinholing at the interconnections between islands of deposited material.

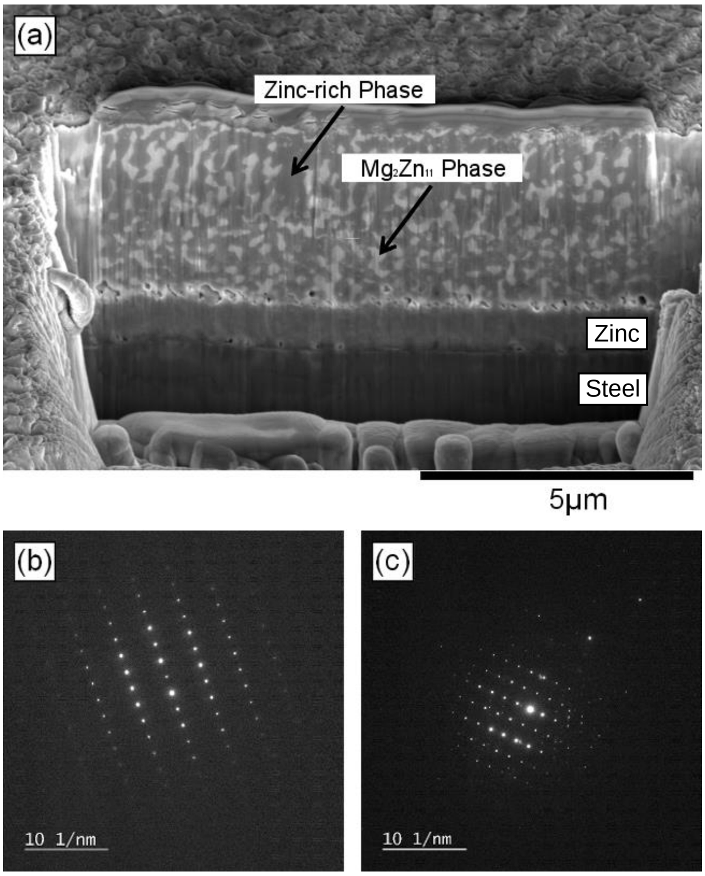

**Figure 3.5:** (a) Microstructure of PVD4 sectioned using a focused gallium ion beam and imaged by the FEGSEM. The two phases present have been labelled after identification via SAED in the TEM; the TEM pattern shown in (b) corresponds to a [100] beam direction for zinc with measured lattice parameters of a = 2.659 Å and c = 4.86 Å, while (c) yields a measured lattice parameter of 8.487 Å, in [110] beam direction, which corresponds to $Mg_2Zn_{11}$.

The microstructure of the PVD4 topcoat seen in **Figure 3.5a** is discrete and significantly finer than that of ZMA. The microconstituents of ZMA are in the order of several microns in diameter, whereas the features of PVD4 are 1 µm maximum. As indicated in the figure, there are two distinct phases present: zinc-rich and $Mg_2Zn_{11}$. These were identified using electron diffraction performed in the TEM; the patterns observed are shown in **Figure 3.5b** and **Figure 3.5c**.

The PVD4 Zn-Mg coating exhibits two different microstructures; a fine and equal distribution of equiaxed grains adjacent to the previously-deposited zinc layer, and a columnar growth structure on top. It is expected that during the PVD process, zinc and magnesium vapours rapidly condensed on top of the zinc adhesion layer, creating more sites for the nucleation with little growth. This results in a small amount of porosity at the zinc adhesion layer interface, followed by a region of densely packed, fine grains and finally columnar growth toward the top of the coating. As predicted by the SZM in **Figure 1.19** in section 1.5.3, the increase in temperature that accompanies the deposition process alters the growth mode of the coating.

In **Figure 3.6a** the surface of PVD10 is also globular, but appears smoother than PVD4 which suggests an increase in mobility of the surface atoms during the final surface deposition, compared to the situation when less magnesium is present in the vapour phase. The cross-sectional structure of PVD10 was not resolvable using SEM, therefore the TEM method was applied to identify the nanostructure exhibited by PVD10 (**Figure 3.6**). The sub-micron grains of PVD10 have similar characteristics to that of PVD4. The grains closest to the zinc adhesion layer appear equiaxed, and the grains further away from the zinc layer appear to have undergone columnar growth during solidification.

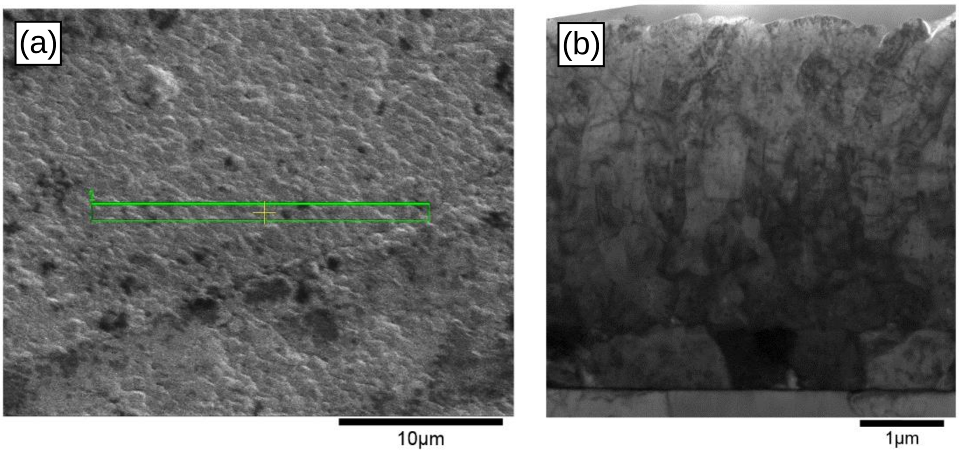

**Figure 3.6:** (a) The surface of the PVD10 coating observed using the FEGSEM, (b) the microstructure of PVD10 sectioned using a focused gallium ion beam and imaged by the TEM.

**Figure 3.7a** shows a more planar surface morphology for PVD20 compared to the previous PVD coatings. It is therefore suggested that the magnesium content is an influencing factor in determining surface morphology. The cross-section of PVD20 in **Figure 3.7b** reveals a nanostructure which is significantly finer than both PVD10 and PVD4. Indeed, the grains are, on average, 100 nm in diameter.

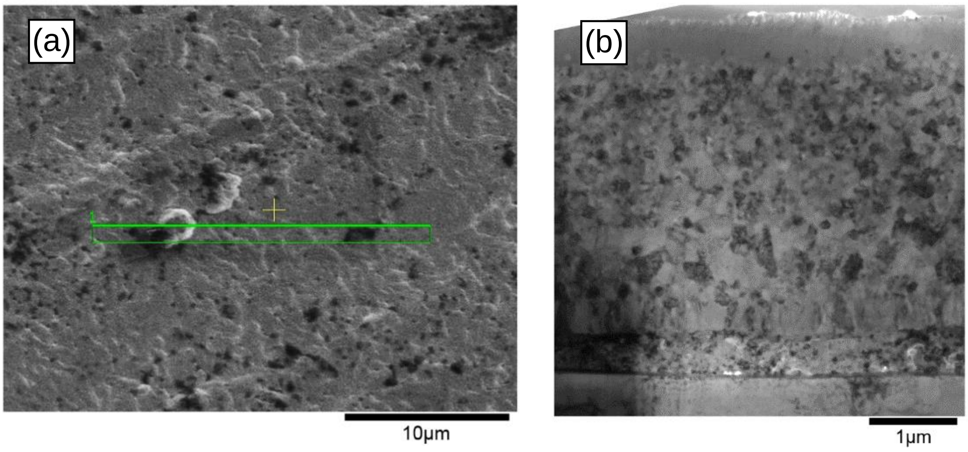

**Figure 3.7**: (a) The surface of the PVD20 coating observed using the FEGSEM, (b) the microstructure of PVD20 sectioned using a focused gallium ion beam and imaged by the TEM.

Moreover, the nanostructure of PVD20 toward the top of the Zn-Mg layer contains regions of concentrated zinc only 5 nm in diameter, as shown in **Figure 3.8**. To confirm the quantity of magnesium in the PVD4, PVD10 and PVD20 topcoats, cross-sections were mounted in epoxy resin and quantitatively studied using EDX. Area scans were conducted over five separate locations along the cross-sections of the Zn-Mg PVD topcoats, the results are shown in **Table 3.1**. The average magnesium content values found using EDX are satisfactorily similar to the supplied compositions by Tata.

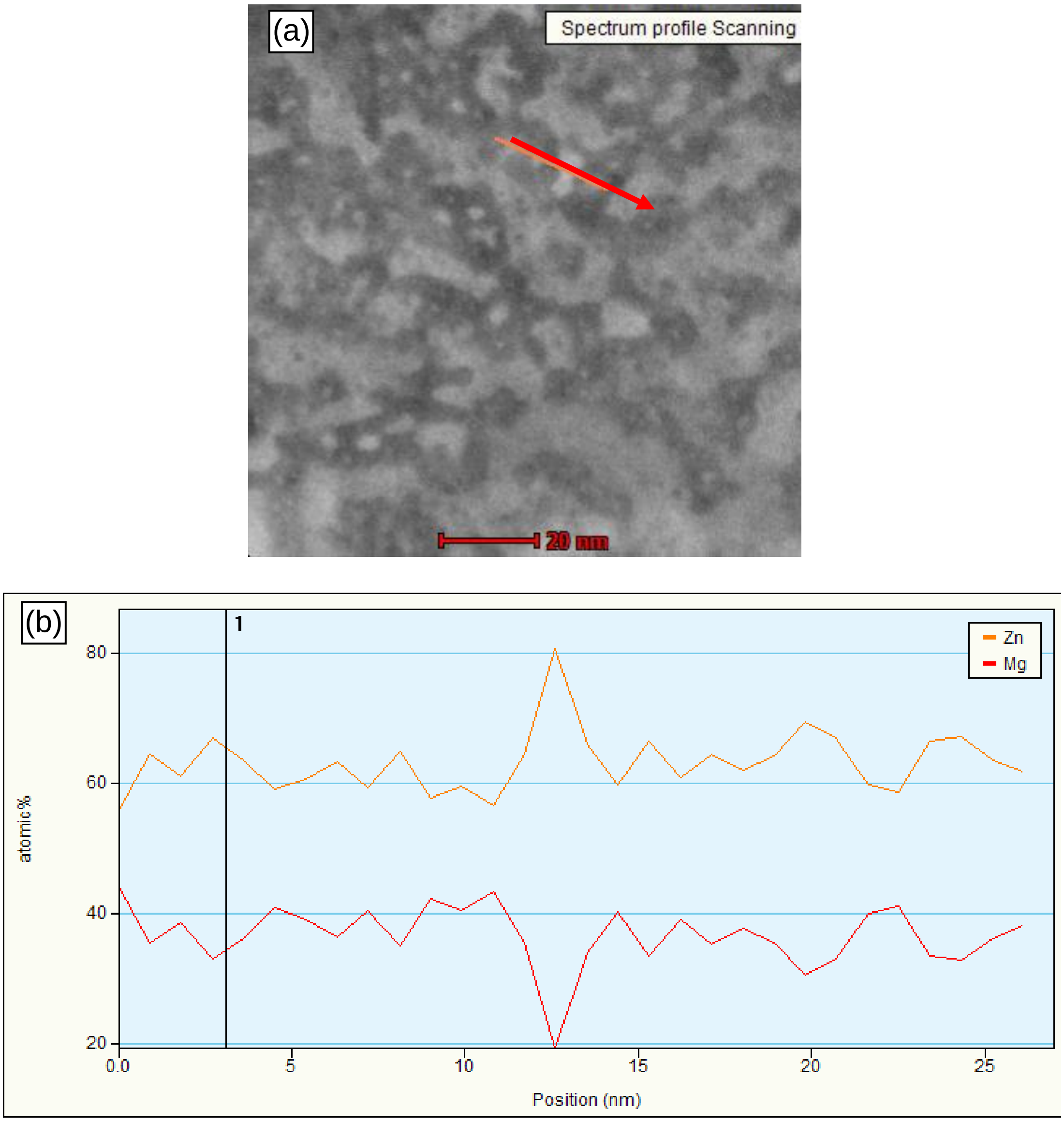

**Figure 3.8:** (a) TEM image of the finer PVD20 structure with reference arrow for the (b) STEM scan profile showing a spike in zinc concentration.

**Table 3.1:** Magnesium content of PVD4, PVD10 and PVD20 identified using EDX cross-sectional study.

| **Sample I.D.** | **Average magnesium content (wt.%)** | **Standard Deviation (wt.%)** |
|---|---|---|
| PVD4 | 4.4 | ± 0.2 |
| PVD10 | 10.1 | ± 0.4 |
| PVD20 | 19.7 | ± 0.9 |

XRD was used to accurately identify the phases present in the PVD coatings. The spectra for all PVD coatings studied are shown in **Figure 3.9**. PVD0 was confirmed to contain solely zinc, with a large characteristic peak at 36 °. The aforementioned zinc and $Mg_2Zn_{11}$ phases identified in PVD4 via TEM diffraction, in **Figure 3.5b**, were confirmed with this data as peak matching software locates the characteristic peaks for the phase. Furthermore, the spectrum for PVD10 also established the presence of the $Mg_2Zn_{11}$ phase, as the peaks are in identical positions to those of PVD4. PVD20 did not appear to be comprised of $Mg_2Zn_{11}$ phase, instead the characteristic triple peak features for $MgZn_2$ were detected between 19 ° and 22 ° and between 40 ° and 43 °. This confirms that the greater magnesium content alters the affinity for phase growth from the $Mg_2Zn_{11}$ phase to $MgZn_2$, the phase that is notably present in ZMA [11,28].

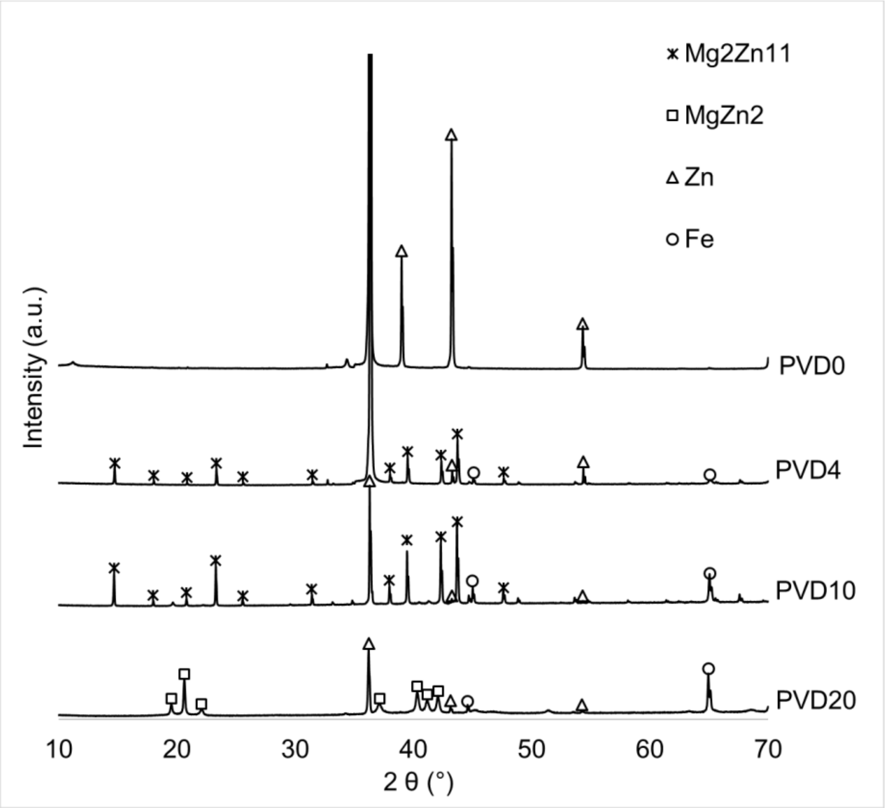

**Figure 3.9:** XRD spectra of all PVD coatings.

### *3.3.3 Surface roughness*

A white light interferometer was used to obtain the vales for surface area roughness, shown in **Table 3.2**. It is clear that the PVD coatings are considerably smoother than commercial hot dip galvanised coatings. Moreover, the pinholing observed on PVD4 in **Figure 3.4** appears to increase the roughness of the surface notably compared to the other three PVD coatings. This difference in coating morphology and roughness is likely more related to the processing parameters than the magnesium content as there is no statistically significant trend between the magnesium content and the surface properties.

**Table 3.2:** Mean surface roughness, Sa, of all PVD coatings and reference galvanised coatings with standard deviation.

| **Sample I.D.** | **Mean Surface Roughness, $S_a$ (nm)** | **Standard Deviation (nm)** |
|---|---|---|
| HDG | 1336 | ± 102.0 |
| ZMA | 984.6 | ± 98.80 |
| PVD0 | 296.7 | ± 20.66 |
| PVD4 | 385.3 | ± 10.93 |
| PVD10 | 269.6 | ± 12.50 |
| PVD20 | 285.9 | ± 30.29 |

## 3.4 Conclusions

This initial work served the purpose of characterising the morphology, microstructures and phases present in the novel PVD coatings, to compare to traditional hot dip galvanised zinc and Zn-Mg-Al coatings. It was evident that the deposition process had a significant effect on the coating growth and structure. The PVD0 zero coating was notably thinner than the HDG coating, with a compact structure comprised of hexagonal zinc microplates. The HDG grains, on the other hand, were in the order of 5-8 µm. The ZMA coating exhibited the well-established structure containing primary zinc dendrites, a binary eutectic lamellar structure of zinc and $MgZn_2$ and the ternary eutectic structure with the zinc and $MgZn_2$ lamellar with aluminium-rich nodules. Similarly to this, the PVD4 coating had a discrete structure, although much finer than ZMA. Additionally, the magnesium phase present in PVD4 was $Mg_2Zn_{11}$, as confirmed by both XRD and SAED-TEM. PVD10 and PVD20 both had nanostructures of zinc crystallites and magnesium-containing crystallites. However, for PVD10 the magnesium phase was $Mg_2Zn_{11}$ and for PVD20 the magnesium phase was $MgZn_2$ (as determined by XRD), owing to the sufficient amount of magnesium in the melt. EDX analysis confirmed the magnesium contents of the Zn-Mg PVD topcoats, all within a 5 % tolerance of the expected wt%. Finally, it was evident that the PVD process produces much smoother coatings compared to the commercial hot dip galvanised.

## 3.5 References

1. X.G. Zhang, "Galvanic Protection of Steel by Zinc", in: Corros. Electrochem. Zinc, Plenum Press, New York, (1996) pp. 213–217.
2. N.C. Hosking, M.A. Ström, P.H. Shipway, C.D. Rudd, Corros. Sci. 49 (2007) 3669–3695.
3. K. Nishimura, H. Shindo, H. Nomura, K. Katoh, Tetsu-to-Hagane. 89 (2003) 174–179.
4. S. Schuerz, M. Fleischanderl, G.H. Luckeneder, K. Preis, T. Haunschmied, G. Mori, A.C. Kneissl, Corros. Sci. 51 (2009) 2355–2363.
5. T. Prosek, N. Larché, M. Vlot, F. Goodwin, D. Thierry, Mater. Corros. 61 (2010) 412–420.
6. P. Volovitch, T.N.N. Vu, C. Allély, A. Abdel Aal, K. Ogle, Corros. Sci. 53 (2011) 2437–2445.
7. D. Persson, D. Thierry, N. LeBozec, T. Prosek, Corros. Sci. 72 (2013) 54–63.
8. R. Krieg, A. Vimalanandan, M. Rohwerder, J. Electrochem. Soc. 161 (2014) C156–C161.
9. T. Lostak, A. Maljusch, B. Klink, S. Krebs, M. Kimpel, J. Flock, S. Schulz, W. Schuhmann, Electrochim. Acta. 137 (2014) 65–74.
10. M. Salgueiro Azevedo, C. Allély, K. Ogle, P. Volovitch, Corros. Sci. 90 (2015) 482–490.
11. J. Sullivan, N. Cooze, C. Gallagher, T. Lewis, T. Prosek, D. Thierry, Faraday Discuss. 180 (2015) 361–379.
12. B. Navinšek, P. Panjan, I. Milošev, Surf. Coatings Technol. 116–119 (1999) 476–487.

13. J. Schade van Westrum, G. Gleijm, Method and device for coating a substrate, WO 03/071000 A1, (2003).

14. E. Zoestbergen, T.F.J. Maalman, J. van de Langkruis, M.R. Goodenough, Substrate with a double layered coating, WO2013091889 A1, (2013).

15. E. Zoestbergen, J. van de Langkruis, T. Maalman, E. Batyrev, S. Melzer, M. Zuijderwijk, "Diffusion of Zinc and Magnesium in Physical Vapour Deposited Thin Films at 175°C", in: Galvatech, AIST, Toronto, (2015) pp. 36–43.

16. E. Zoestbergen, J. van de Langkruis, T.F.J. Maalman, E. Batyrev, Surf. Coatings Technol. 309 (2016) 904–910.

17. J.L.L. Davies, C.F.F. Glover, J. van de Langkruis, E. Zoestbergen, G. Williams, Corros. Sci. 100 (2015) 607–618.

18. S. Sabooni, E. Galinmoghaddam, M. Ahmadi, R.J. Westerwaal, J. van de Langkruis, E. Zoestbergen, J.T.M. De Hosson, Y.T. Pei, Surf. Coatings Technol. 359 (2019) 227–238.

19. T.-Y. Kim, M. Goodenough, Corros. Sci. Technol. 10 (2011) 194–198.

20. A. Vimalanandan, A. Bashir, M. Rohwerder, Mater. Corros. 65 (2014) 392–400.

21. J. Elvins, J.A. Spittle, J.H. Sullivan, D.A. Worsley, Corros. Sci. 50 (2008) 1650–1658.

22. J. Han, K. Ogle, J. Electrochem. Soc. 164 (2017) C952–C961.

23. D. Zander, C. Schnatterer, Corros. Sci. 98 (2015) 291–303.

24. S.K. Kairy, P.A. Rometsch, K. Diao, J.F. Nie, C.H.J. Davies, N. Birbilis, Electrochim. Acta. 190 (2016) 92–103.

25. G.S. Frankel, J. Electrochem. Soc. 145 (1998) 2186–2198.

26. N. Wint, N. Cooze, J.R. Searle, J.H. Sullivan, G. Williams, H.N. McMurray, G.

Luckeneder, C. Riener, J. Electrochem. Soc. 166 (2019) C3147–C3158.

27. N. van Landschoot, C. Dane, R. Bleeker, M. Vlot, ATZ Worldw. 115 (2013) 4–8.

28. J. Sullivan, S. Mehraban, J. Elvins, Corros. Sci. 53 (2011) 2208–2215.

29. T. Prosek, J. Hagström, D. Persson, N. Fuertes, F. Lindberg, O. Chocholatý, C. Taxén, J. Šerák, D. Thierry, Corros. Sci. 110 (2015) 71–81.

30. D.T. Hellman, Met. Finish. (2003).

# Chapter 4. Electrochemical characterisation of PVD Zn-Mg coatings using DC electrochemistry and EIS

## 4.1 Introduction

Zinc and zinc alloy coatings applied to strip steel exist to prevent or hinder corrosive attack of the steel substrate, extending the service life of the component significantly. These coatings act as a barrier to corrosive media (barring contact with aggressive specie and eliminating the capacity for ionic transport) and offer sacrificial protection if the underlying steel is exposed (see section 1.3.2 on galvanic corrosion). The preferential attack of zinc in the presence of steel leads to the formation of protective corrosion products, ZnO and $Zn(OH)_2$ [1–6], which provide more substantial barrier protection. In pursuit of the advancement in zinc alloy coatings, it is crucial to be able to establish key quantitative base-lines for corrosion resistance for comparison for future novel systems. One of the most basic methods for comparing the corrosion resistance of a material is gravimetric analysis (the measure of mass loss before and after exposure), however the data attained via this method is highly open to interpretation and requires many assumptions to be made to begin to describe corrosion behaviour (e.g. constant corrosion rate during exposure and equal distribution of anodic attack). Electrochemical techniques can provide more data to elucidate mechanistic information [7]. They can be split into the following categories: direct current (DC) methods, alternating current (AC) methods and localised corrosion mapping techniques, such as SVET and SKP.

Open circuit potential (OCP) measurements are a standard starting point for electrochemical analysis. In the case of galvanised steel, monitoring OCP with time in a corrosive test solution can show you when sacrificial protection has been lost; i.e. the

$E_{corr}$ value for an intact galvanised layer will reflect the OCP of zinc, exposure of the underlying steel would tend toward the $E_{corr}$ of iron. The OCP is the equilibrium potential of an electrode (i.e. the equilibrium between the oxidation and reduction reaction), similar to the standard electrode potential ($E^0$) and the free corrosion potential ($E_{corr}$), under zero current conditions. OCP is typically measured in a two electrode setup; the working electrode (sample) and a reference electrode. The OCP is a reasonable estimate for the $E_{corr}$ of a material which relates back to the galvanic series in **Figure 1.11** (or the electromotive series, **Figure 1.4**, depending on the reference electrode). Measuring the OCP of a material is essential prior to polarisation studies, to know the point of zero current to vary the applied voltage around, and it is also essential for electrochemical impedance spectroscopy (EIS) to monitor stability.

Polarisation resistance studies are widely used [8–12] three electrode DC electrochemical methods that allow the identification of corrosion properties of materials, such as $E_{corr}$ and the kinetics of the anode and cathode of a corroding system. A potentiostat controls the applied potential and therefore the driving force of electrochemical activity, which in turn dictates the rate of the anodic and cathodic reactions. As explained in chapter 1, dissolution of metal and (typically) reduction of oxygen are the reactions that take place at the anode and cathode respectively, however it is essential to have a full understanding of the corrosion processes taking place to correctly interpret data. During a polarisation study, the potential (i.e. the driving force) is varied between two values either side of the OCP at a set rate, and the net change in reaction rate (i.e. the current) is measured. The reaction rate is controlled by two forms of kinetic phenomena: charge transfer or mass transfer. During the charge transfer mechanism, reaction rate increases as the inputted driving force (potential) is increased. When the mass transfer mechanism takes over, the reaction rate is instead controlled by the diffusion of specie through the electrolyte to the surface of the electrode, such as oxygen. The current reaches a plateau, limited by the concentration and diffusivity of the reactant, thus further increases in potential do not increase the current [13].

Impedance is the AC theory equivalent of resistance in DC theory, thus Ohm's law:

$$E = IR \tag{4.1}$$

where E is the potential, I is the current and R is resistance, becomes:

$$\hat{E} = \hat{I}Z \tag{4.2}$$

where $\hat{E}$ is the amplitude of the potential waveform, $\hat{I}$ is the amplitude of the current waveform and Z is the impedance (**Figure 4.1**). Full explanations and derivations of EIS can be found in literature [14,15]. In brief, EIS involves the application of an AC potential and the measurement of the electrochemical system response (AC current signal), over a broad range of frequencies, ω, in order to determine to impedance of the system as a function of frequency. The capacitance, C, and resistance, R, of a system can then be established by observation of the in-phase and out-of-phase current responses.

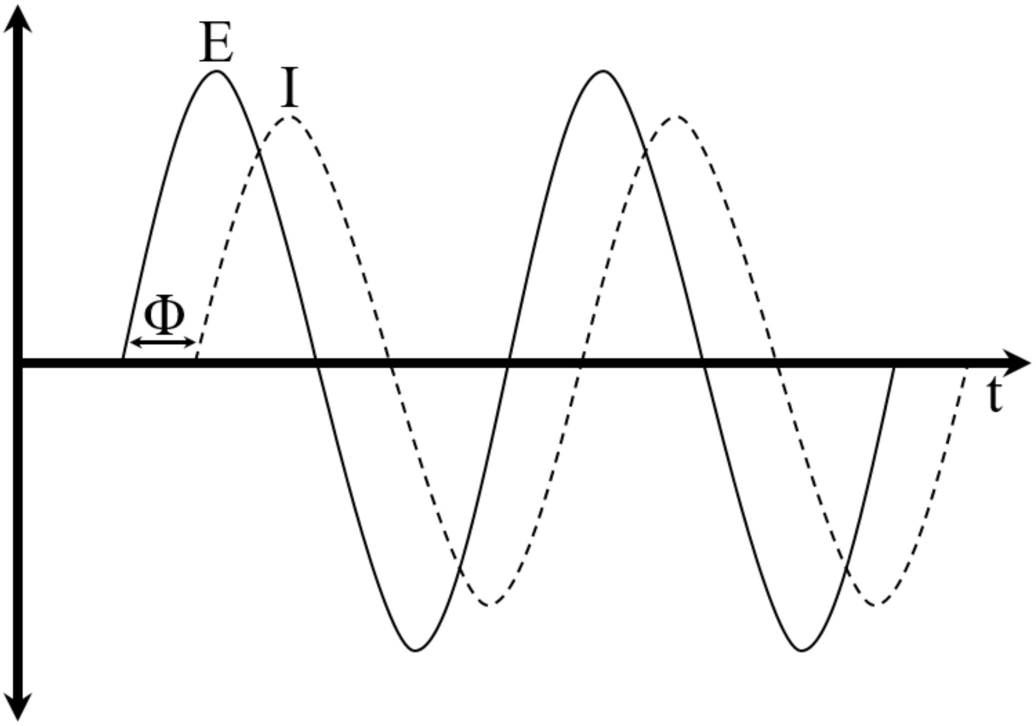

**Figure 4.1:** Applied potential waveform, E, and the response current waveform of equal frequency, i, with a phase shift Φ.

Characteristic impedance plots generated by EIS measurements can be fitted against equivalent circuit models to identify the components of an electrochemical system. In this work, the type of plot used is the Nyquist plot where the imaginary impedance (Z’’) is plotted against the real impedance (Z’) at each frequency (it is worth noting that Z’’ is conventionally plotted as –Z’’, such that capacitive impedances appear above the origin and negative impedances below). Examples of the relevant simple circuit components are shown in **Figure 4.2**.

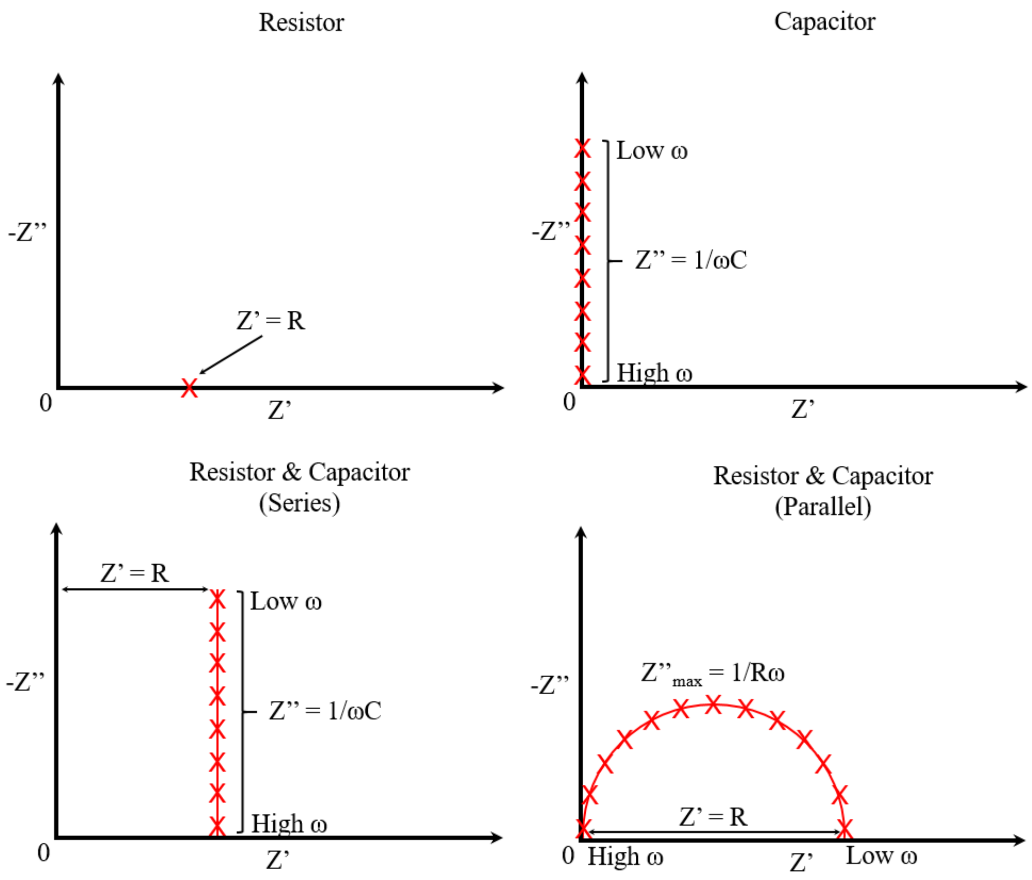

**Figure 4.2:** Nyquist plot profiles for simple circuit components.

The simple circuit component models can be recognised at an electrode-solution interface, thus impedance plots measured during EIS are subsequently fitted to similar simple circuit profiles. As shown in **Figure 4.3**, the basic equivalent circuit for a metal electrode in solution is comprised of the solution resistance, $R_S$, in series with the parallel combination of a polarisation resistance, $R_P$, and the double-layer capacitance, $C_{DL}$, at the interface. In real world experiments, a perfect $C_{DL}$ does not exist, instead it is referred to as a constant phase element (CPE) which is an imperfect capacitor, such as ionic double-layers on the surface of a corroding metal. Non-uniform current distribution and surface morphology contribute toward the flaws of a surface capacitor, as such the Nyquist semi-circle is generally depressed below the Z’ axis.

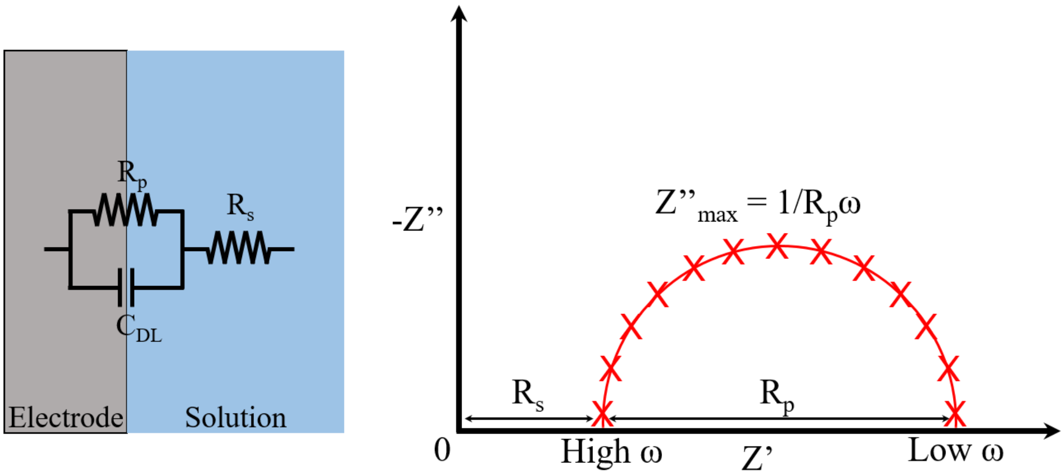

**Figure 4.3:** Schematic and equivalent circuit of a metal electrode in solution (left) with the corresponding Nyquist model plot (right).

The $R_p$ value identified in the Nyquist plot can be used to calculate $i_{corr}$, and subsequently mass loss, using the Stern Geary equation discussed previously in chapter 1 (equation 1.18).

Rotating disk electrode (RDE) is an additional electrochemical technique that induces laminar flow towards and cross the working electrode. It has been used previously to study the oxygen reduction reaction (ORR) on zinc alloy coatings [16–18]. Zinc coatings offer sacrificial protection of the steel substrate which leads to the formation of zinc hydr(oxide) formation on the surface. This hydr(oxide) corrosion product subsequently inhibits the reduction of oxygen and therefore the overall electrochemical activity on the surface. Moreover, hindering the ORR has a greater benefit for metallic-organic coating systems, as cathodic delamination is driven by the oxygen reduction and subsequent alkalinisation of the delamination front [19].

This chapter will utilise all aforementioned electrochemical analysis techniques to characterise the behaviour of PVD coatings in corrosive electrolyte.

## 4.2 Experimental details

### *4.2.1 Materials*

In this chapter the PVD coated steel samples listed in **Table 2.1** are studied and compared to the commercially available HDG and ZMA coating strip steel, as received, supplied by Tata Steel.

### *4.2.2 Methods*

OCP monitoring, polarisation and EIS studies in this chapter were conducted at the University of Virginia at 20 °C. All samples were first cut to 1.2 cm by 1.2 cm and rinsed with ethanol before being mounted into a specialised Perspex electrochemical assessment chamber (EAC) shown in **Figure 4.4**. The EAC consisted of a cylindrical electrolyte chamber with an end plate and sealing plate at each end. The end plates were securely adhered to the cylinder, making it watertight aside from two 1cm$^2$ holes on each end plate, concentric to the cross-section of the cylinder. Sealing plates were connected to the end plates with four bolt and wing nut fixtures. The platinum mesh counter electrode and the working electrode (specimen to be studied) were positioned between the end plates and sealing plates, at opposite ends of the cylinder. O-rings were used with each 1 cm$^2$ hole to form a watertight seal between the electrodes and the electrolyte chamber. The EAC chamber was subsequently filled with 0.17 M NaCl solution. A luggin capillary saturated calomel reference electrode was inserted into the top spout of the EAC, such that the tip of the reference electrode was within a 10mm distance to the working electrode. The three electrodes were connected to a Bio-Logic VMP3 mutli-channel potentiostat for polarisation and an SP-150 for OCP and EIS.

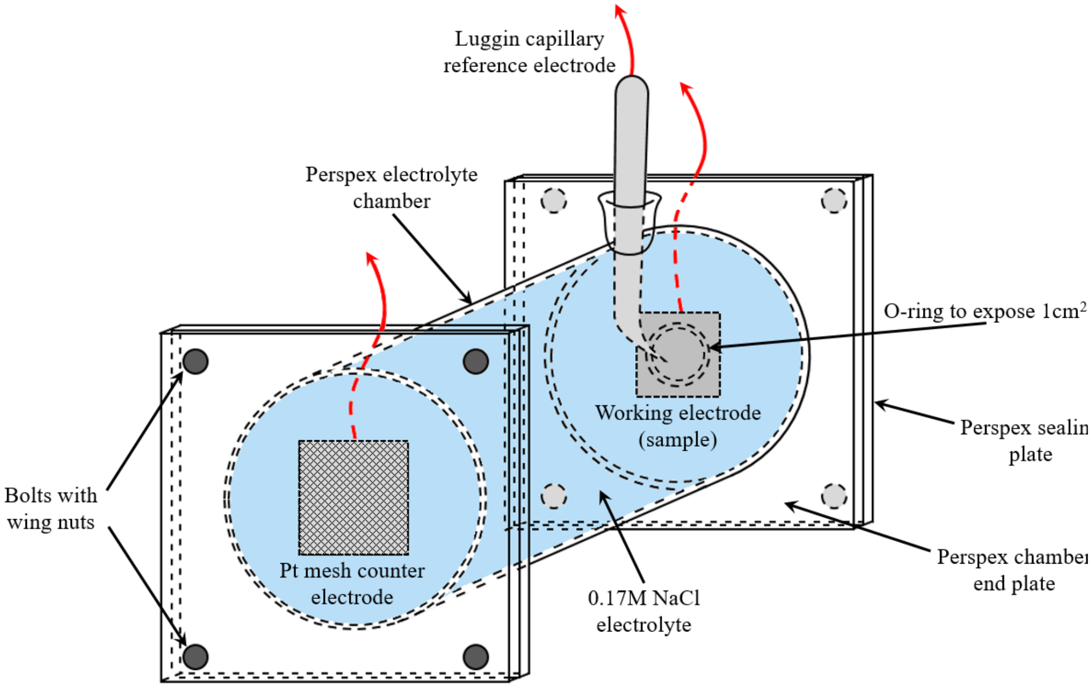

**Figure 4.4:** Schematic of the Perspex electrochemical analysis chamber used by the University of Virginia.

Separate potentiodynamic measurements were performed at 0.2 mV/s scan rate in the cathodic going (0.1 V to -1.4 V) and anodic going (-0.1 V to 0.5 V) directions about the OCP (obtained via a 30 minute OCP stabilisation step). EIS measurements were carried out every hour over 24 hours with an AC signal amplitude of 10 mV over the frequency range 100 kHz to 10 mHz with zero DC bias. OCP stabilisation was conducted over approximately 50 minutes prior to each scheduled EIS measurement step. Potentiodynamic and OCP data plotting was conducted using EC-Lab software by Bio-Logic, then transferred to Microsoft Excel. EIS Nyquist plots were created with Z Plot software from Scribner Associates.

For RDE, 18 mm diameter circular samples of each coating were punched out and rinsed with ethanol. All electrochemical studies using the RDE method were conducted at 20 °C in aerated 0.5 M $NaSO_4$ buffered to pH 9.2 using 0.05 M $Na_2B_4O_7 \cdot 10H_2O$ and

0.07 M NaOH. Specimen disks were mounted into the PTFE sample holder of an Oxford Instruments RDE-2 (**Figure 4.5**), exposing only a 16 mm area of the sample coating to electrolyte. A mercury/mercurous sulphate reference electrode was used in combination with a platinum gauze counter electrode. Quasi-steady state polarisation analysis was conducted using a linear potential sweep rate of 3.3 x $10^{-4}$ V.$s^{-1}$ systematically over a range of angular velocities: 55, 108, 163, 217 and 314 rad.$s^{-1}$ as per previous work [17].

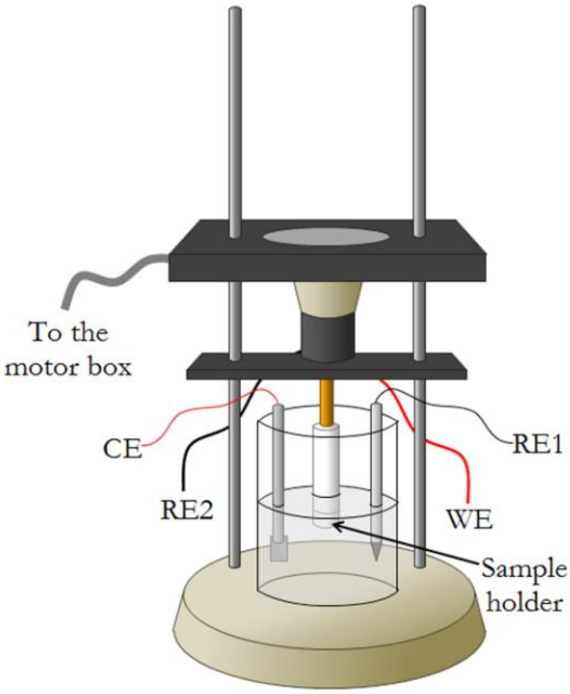

**Figure 4.5:** Schematic of the RDE setup: WE is the working electrode, CE is the counter electrode, RE1 is the first reference electrode and RE2 is the second reference electrode.

## 4.3 Results and discussion

### *4.3.1 OCP*

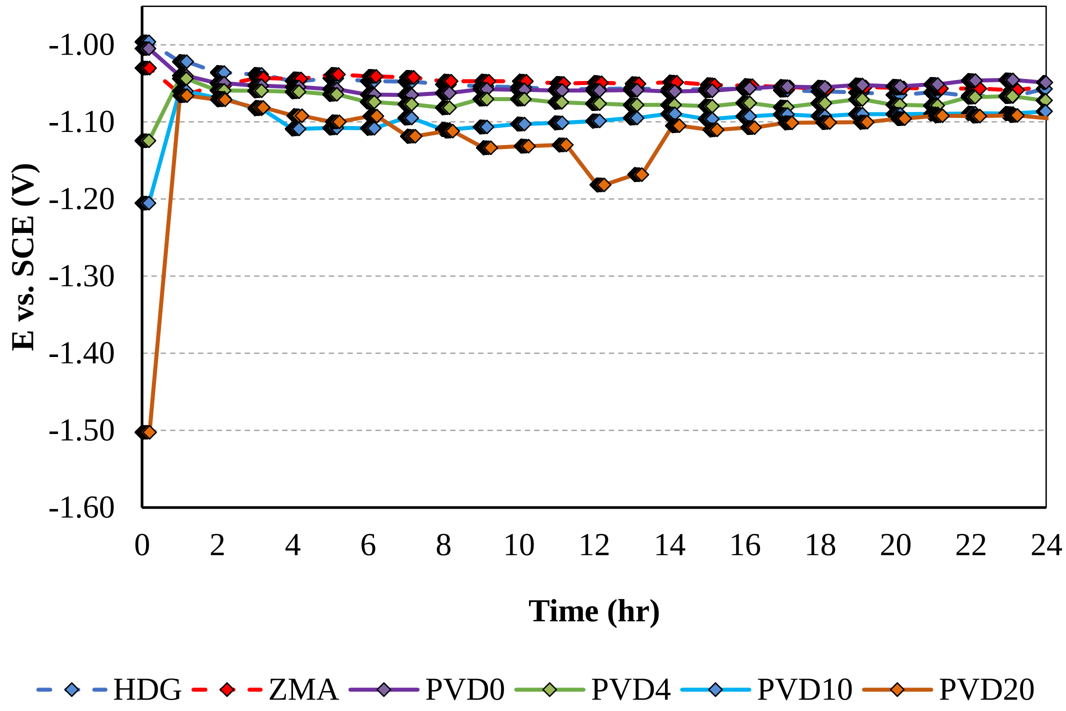

**Figure 4.6:** Time-dependent variation of the open circuit potential of all coatings immersed in 0.17 M NaCl solution. OCP values were monitored in the periods between EIS measurements over 24 hours.

The OCP stabilisation was recorded prior to each EIS sweep and plotted to monitor variance in OCP over 24 hours. **Figure 4.6** shows a clear difference between the starting OCP for the coatings in relation to the magnesium content. The HDG and PVD0 samples (both absent of magnesium) initially had an OCP value of -1.00 V which decreased and stabilised to -1.06 V over the 24 hour period. Both values are within the expected range of OCP for pure zinc vs SCE (**Figure 1.11**). ZMA was similar to the pure zinc coatings, however the small depression (30 mV) in the initial OCP value could be attributed to the 1.6 wt% magnesium content of the ZMA coating.

The magnesium containing PVD coatings exhibit a negative trend of the initial OCP and 24 hour stabilised OCP in relation to the increasing magnesium content, as shown in **Table 4.1**. Initial OCP values become progressively more negative with increasing magnesium content.

**Table 4.1:** Initial OCP and 24 hour averaged stabilised OCP values for magnesium containing PVD coatings in 0.17M NaCl solution.

| Coating I.D. | Initial OCP (V) | Stabilised OCP (V) |
|---|---|---|
| PVD4 | -1.12 | -1.08 |
| PVD10 | -1.21 | -1.09 |
| PVD20 | -1.50 | -1.11* |

*stabilised OCP for PVD20 temporarily dropped to -1.18 between 12 and 14 hours

The galvanic series in **Figure 1.11** identifies magnesium to have a corrosion potential of -1.6 V vs SCE, thus it can be presumed that the significant depression in initial OCP value for the PVD coatings is a result of the preferential attack of magnesium-containing phases. This can further be supported by previous work by Kwak et al. [20] which demonstrated a free-potential shift, for an alloy comprised of both $MgZn_2$ (OCP -1.5 V vs SCE) and $Mg_2Zn_{11}$ (OCP -1.1 V vs SCE) phase when immersed in aqueous NaCl. In the case of PVD20, it was shown in chapter 3 that corrosion initiated at the $MgZn_2$ phase. Following two hours of immersion, the OCP was shifted positively which indicates a change in preferential attack from $MgZn_2$ de-alloying to (possible) $Mg_2Zn_{11}$ de-alloying and finally zinc dissolution (a period of depressed OCP between 12 and 14 hours may indicate further exposure of $Mg_2Zn_{11}$ and subsequent depletion). This suggests that the preferential de-alloying on $MgZn_2$ is only predominant in the first hour immersion, following this the dissolution of zinc becomes the major anodic reaction. The effect was less pronounced in PVD4 and PVD10, however the initial OCP value indicates preferential dissolution of $Mg_2Zn_{11}$ phase before stabilisation.

### *4.3.2 Potentiodynamic*

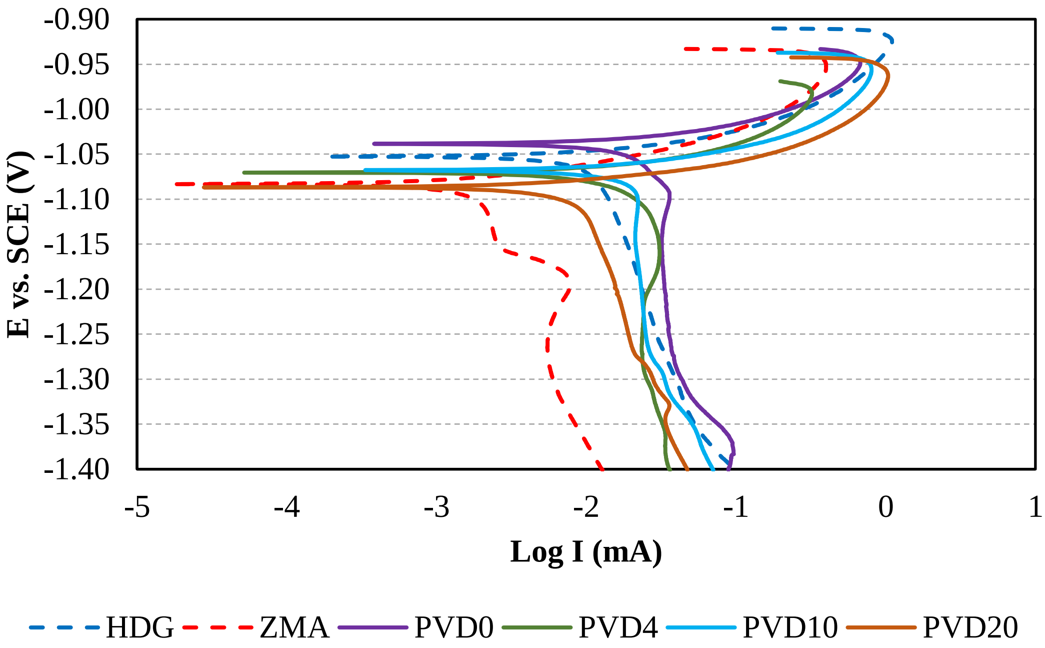

**Figure 4.7:** Cathodic going polarisation of all coatings in 0.17 M NaCl solution from 0.10 V to -1.40 V about the stabilised OCP value. *Note: Current drops observed > -1.00 V are assumed to be artefacts as zinc are Zn-Mg alloys should not show passivation at these potentials.*

**Figure 4.7** and **Figure 4.8** show the typical responses of all coatings to cathodic and anodic polarisation experiments. There is a noticeable depression in $E_{corr}$ in relation to the increase in magnesium content. Furthermore, the magnesium-containing coatings exhibit much lower $I_{corr}$ values, suggesting improved corrosion resistance. Indeed, the ZMA coating shows a factor of 10 reduction in current density compared to the HDG coating. However, the decreasing trend in current density exhibited by the PVD coatings is more modest, indicating a greater influence of the Al in ZMA, on the deactivation of the surface to cathodic oxygen reduction, as opposed to Mg. This is supported by previous work which reports Al as a poorer electrode for oxygen reduction [17]. The cathodic branches in **Figure 4.7** for ZMA and PVD4 demonstrate notable current peaks which may be attributed to the reduction of surface oxides grown electrochemically from zinc dissolution [17]. The absence of the peak from the HDG plot can be explained by the Al-containing surface oxide, characteristic of the GI coating (**Figure 1.14**). Dafydd et al. have previously expressed the featureless voltammograms obtained from pure aluminium [17], thus it may logically follow that, within the timeframe of the potentiodynamic experiment in this work, the dissolution of aluminium suppressed the deviation from the cathodic slope. It is not presently clear why the PVD0, PVD10 and PVD20 coatings lack the aforementioned deviation, although this may be tentatively attributed to the rapid formation of insoluble simonkolleite.

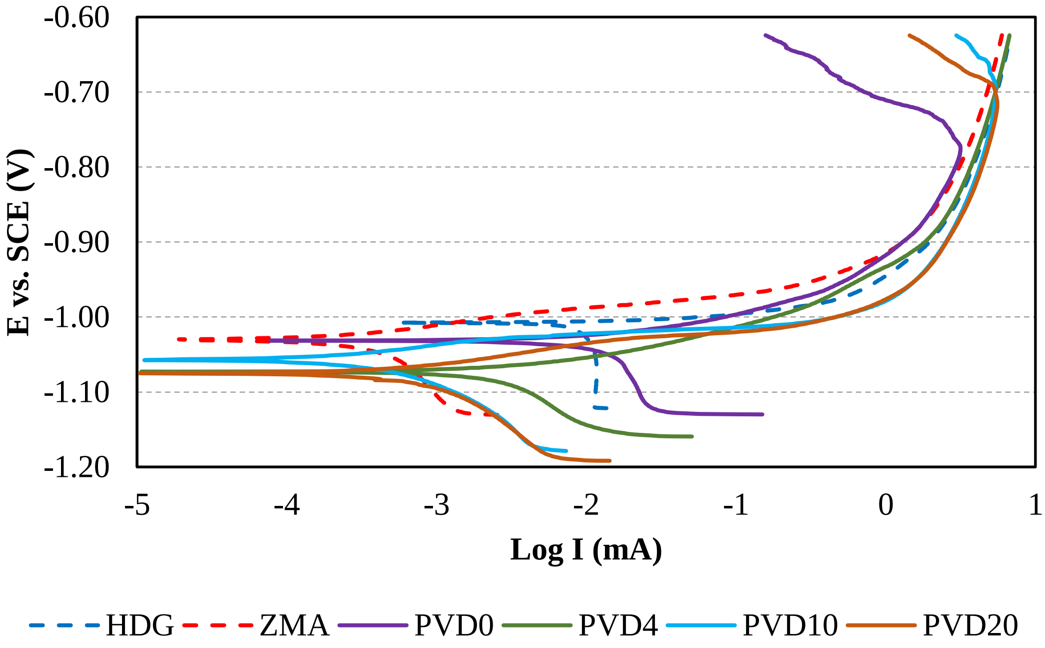

**Figure 4.8:** Anodic going polarisation of all coatings in 0.17 M NaCl solution from -0.10 V to 0.50 V about the stabilised OCP value. *Note: Current drops observed > -1.00 V are assumed to be artefacts as zinc are Zn-Mg alloys should not show passivation at these potentials*

The cathodic branches displayed in both figures also suggest that the magnesium-containing coatings are less efficient oxygen cathodes, notably the ZMA coating is a significantly less effective cathode than HDG, identified by the much shallower slope of the cathodic branch. Moreover, PVD0 shows a steep slope similar to HDG, whereas the Mg-containing PVD coatings demonstrate poorer facilitation of the oxygen reduction reaction than ZMA. Additionally, the highest magnesium-containing coating, PVD20, shows evidence of anodic activation, unlike the pure zinc PVD coating, PVD0. However, the interpretation of polarisation data is difficult for non-steady-state systems, and it was made clear by the results from the OCP measurements in **Figure 4.6** that the OCP fluctuates over time, considerably within the first hour.

### *4.3.3 EIS*

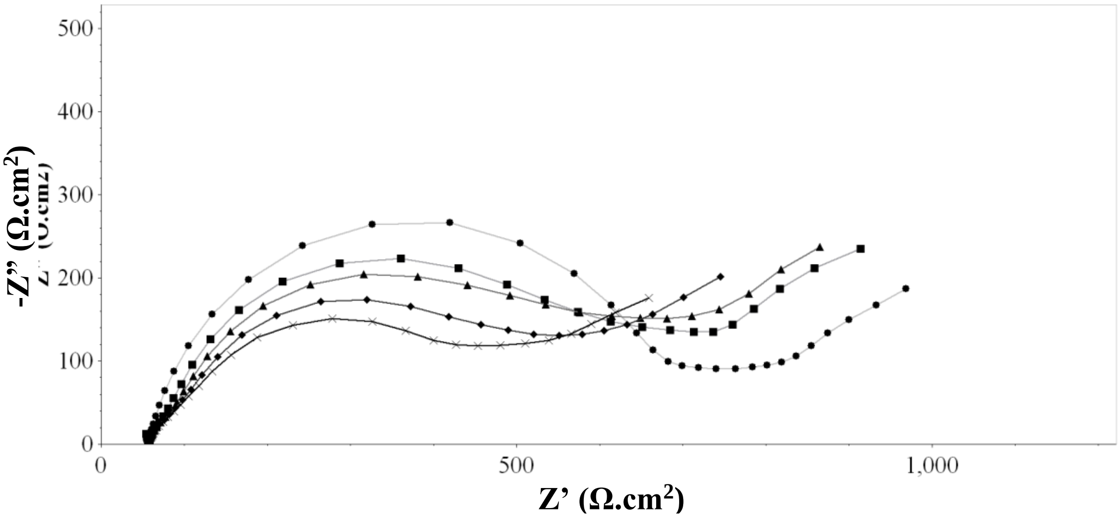

**Figure 4.9:** EIS Nyquist plots for HDG measured at ●) 1 hour, ■) 6 hours, ▲) 12 hours, ♦) 18 hours and X) 24 hours in 0.17 M NaCl solution.

The EIS data for HDG in **Figure 4.9** indicated two time constants; one depressed semi-circle and the appearance of a low frequency (LF) arc. The first semi-circle is attributed to charge transfer and characteristic of ionic double-layer capacitance that occurs at the interface between the corroding metal and solution [12]. The incomplete LF arc could be evidence of a more complex diffusion process associated with oxygen reduction on the surface [21]. The $R_p$ value consistently decreased over the period of 24 hours, suggesting a progressive decrease in the barrier properties of the corrosion product films with time as resistance to corrosive attack appears to decrease. This may be related to a localised alkalinisation of the coating surface as a result of oxygen reduction; zinc is an amphoteric metal, passivating with the formation of $Zn(OH)_2$ between pH 8.5 and pH 11 (**Figure 1.5**) at high pH, soluble $ZnO_2$ is formed. Previous work by Sziraki et al, using $Na_2SO_4$ as the electrolyte, states that localised oxide and hydroxide precipitation causes rapid and uneven distribution of white rust, increasing the activity of the surface perpetually [22].

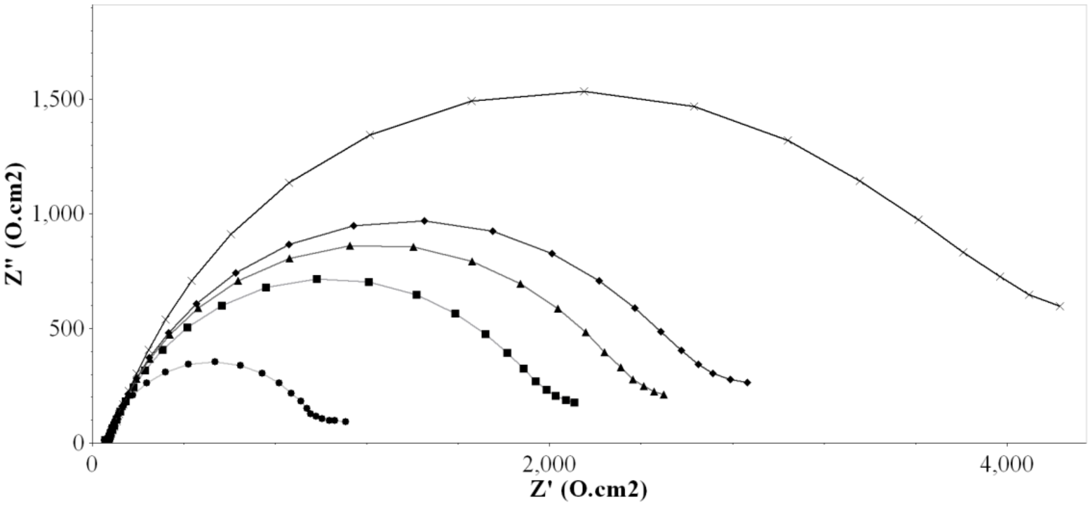

**Figure 4.10:** EIS Nyquist plots for ZMA measured at ●) 1 hour, ■) 6 hours, ▲) 12 hours, ♦) 18 hours and X) 24 hours in 0.17 M NaCl solution.

EIS analysis of the ZMA coating (**Figure 4.10**) showed the characteristic model for the ionic double layer of a corroding metal and solution interface. In contrast to the HDG coating, the $R_p$ values over the 24 hour period for ZMA increased significantly, indicating the formation of stable and protective corrosion products. Moreover, the polarisation resistance of ZMA after 6 hours immersion time was over double that for HDG, which is in agreement with previous observations of ZMA's improved corrosion resistance, compared to HDG, in chloride-containing media [3,23–31].

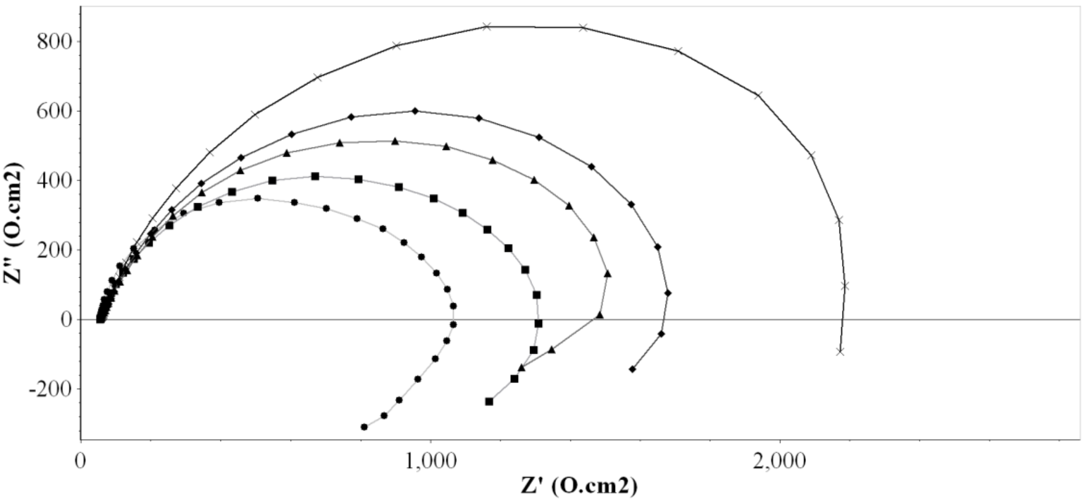

**Figure 4.11:** EIS Nyquist plots for PVD0 measured at i) 1 hour, ii) 6 hours, iii) 12 hours, iv) 18 hours and v) 20 hours in 0.17 M NaCl solution.

The EIS data presented for PVD0 in **Figure 4.11** showed greater polarisation resistance compared to HDG and a consistent increase in resistance over the 24 hour immersion. As with the ZMA coating, the increase in polarisation resistance suggests the formation of a stable corrosion product, which is unexpectedly opposite to the behaviour observed for HDG. One explanation could be the homogeneity of the PVD layer may play an important role in the nature of metal dissolution and subsequent oxide/hydroxide deposition. A commercial HDG coating is susceptible to morphological and compositional inconsistencies, such as alloyed aluminium and iron impurities, owing to the nature of the hot dip process [32], therefore it is possible that localised attack may have limited the overall polarisation resistance of the HDG coating. PVD0 also depicts an inductive loop or “low frequency hook” [33] which has not been previously observed for zinc or zinc coatings [34,35]. An inductive loop has, however, been observed consistently for high purity magnesium in chloride solution at OCP and anodic potentials in work conducted by King et al. [36]. In their work, the inductive loop was attributed to the accelerating anodic dissolution of magnesium, which cathodically activates the surface and subsequently results in a rise in anodic current. It is tentatively proposed that the observance of an inductive loop for the zinc PVD coating in this work, PVD0, the pores on the surface created by the rapid condensing of zinc vapour may act as sites for anodic initiation, driving the formation of many local anodes and thus increasing the overall anodic current.

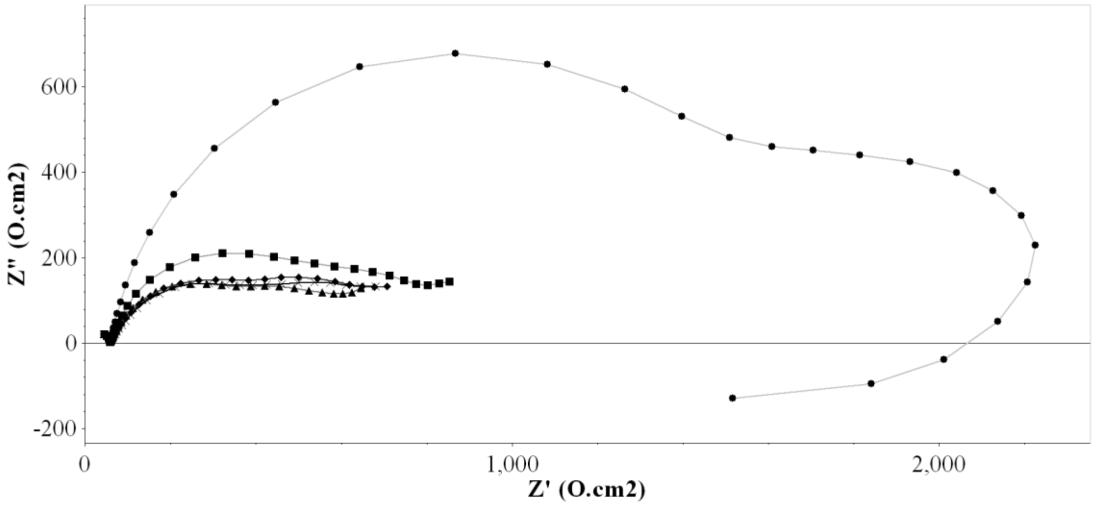

**Figure 4.12:** EIS Nyquist plots for PVD4 measured at ●) 1 hour, ■) 6 hours, ▲) 12 hours, ♦) 18 hours and X) 24 hours in 0.17 M NaCl solution.

In **Figure 4.12**, it is clear that after 1 hour the polarisation resistance of PVD4 increases, however there is a significant drop within the first 6 hours which is then comparable to that seen for HDG. This suggests an instability in the passive film which is a characteristic of pure zinc coatings. The relatively high polarisation resistance followed by a stabilisation of low resistance may be explained by the depletion of magnesium from the coating during the initial few hours of immersion; thus the stabilised behaviour reflects that of a pure zinc coating rather than an alloy.

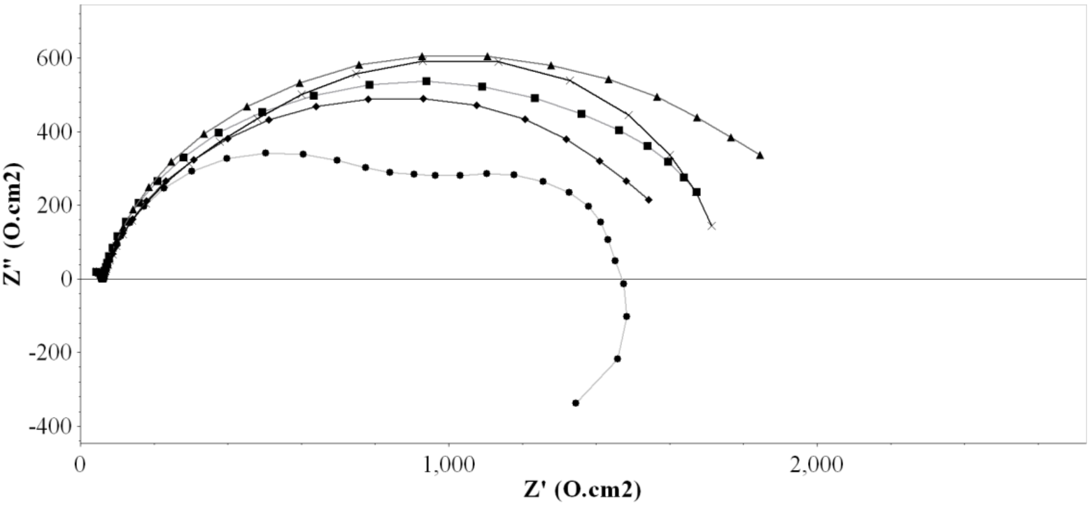

**Figure 4.13:** EIS Nyquist plots for PVD10 measured at ●) 1 hour, ■) 6 hours, ▲) 12 hours, ♦) 18 hours and X) 24 hours in 0.17 M NaCl solution.

At 1 hour, PVD10 (**Figure 4.13**) showed two time constants: the characteristic double-layer capacitance response in the high frequency domain, and a complex diffusion-based response in the low frequency domain. Beyond 6 hours, there was only one time constant visible, thus the corrosion process became dominated by the double-layer mechanism. Moreover, the polarisation resistance increased two-fold after 6 hours and was comparable with PVD0 and ZMA.

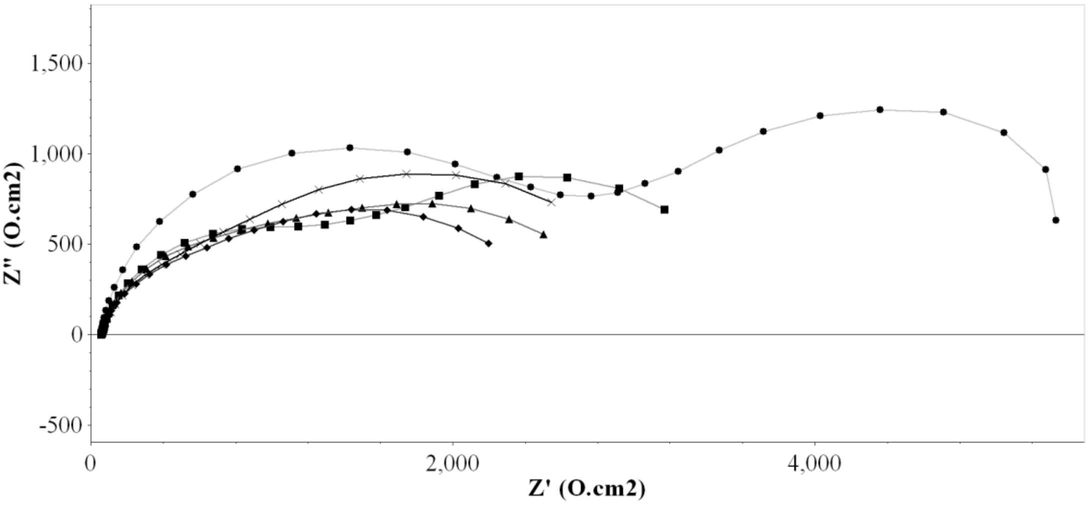

**Figure 4.14:** EIS Nyquist plots for PVD20 measured at ●) 1 hour, ■) 6 hours, ▲) 12 hours, ♦) 18 hours and X) 24 hours in 0.17 M NaCl solution.

The EIS response for PVD20, shown in **Figure 4.14:** EIS Nyquist plots for PVD20 measured at ●) 1 hour, ■) 6 hours, ▲) 12 hours, ♦) 18 hours and X) 24 hours in 0.17 M NaCl solution., suggested a significant drop polarisation resistance over the 24 hour test period, similar to PVD4. Furthermore, unlike PVD4 and PVD10 the system maintained a presence of two time constants over the 24 hour period, indicating a continuous influence of a finite layer diffusivity effect.

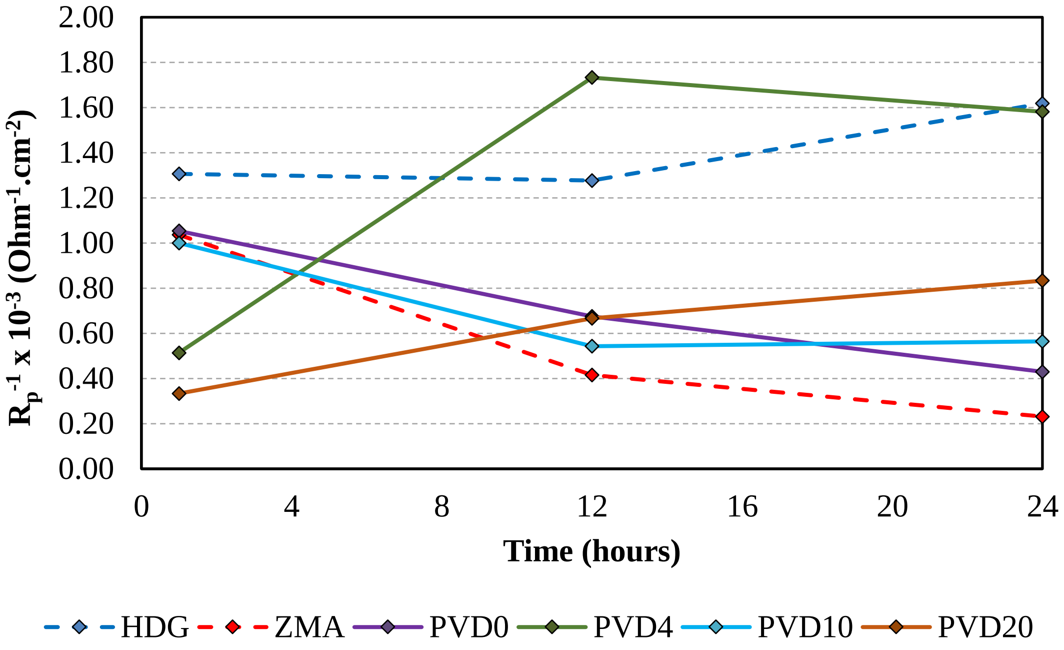

**Figure 4.15:** Inverse of $R_p$ values (relative corrosion rate) for all coatings immersed in 0.17 M NaCl plotted over time.

The $R_p$ values for all coatings were extracted and plotted as the reciprocal of $R_p$ (which is proportionate to the corrosion rate) in **Figure 4.15** to show the trend in corrosion rate over time. The behaviour of the PVD4 coating seems anomalous across multiple repeats of the EIS analysis; the data indicates a susceptibility of the zinc alloy coating to the extent that it performs worse than a "pure" zinc coating (HDG). Moreover, PVD0 appears to show a similar corrosion resistance to that of ZMA and PVD10.

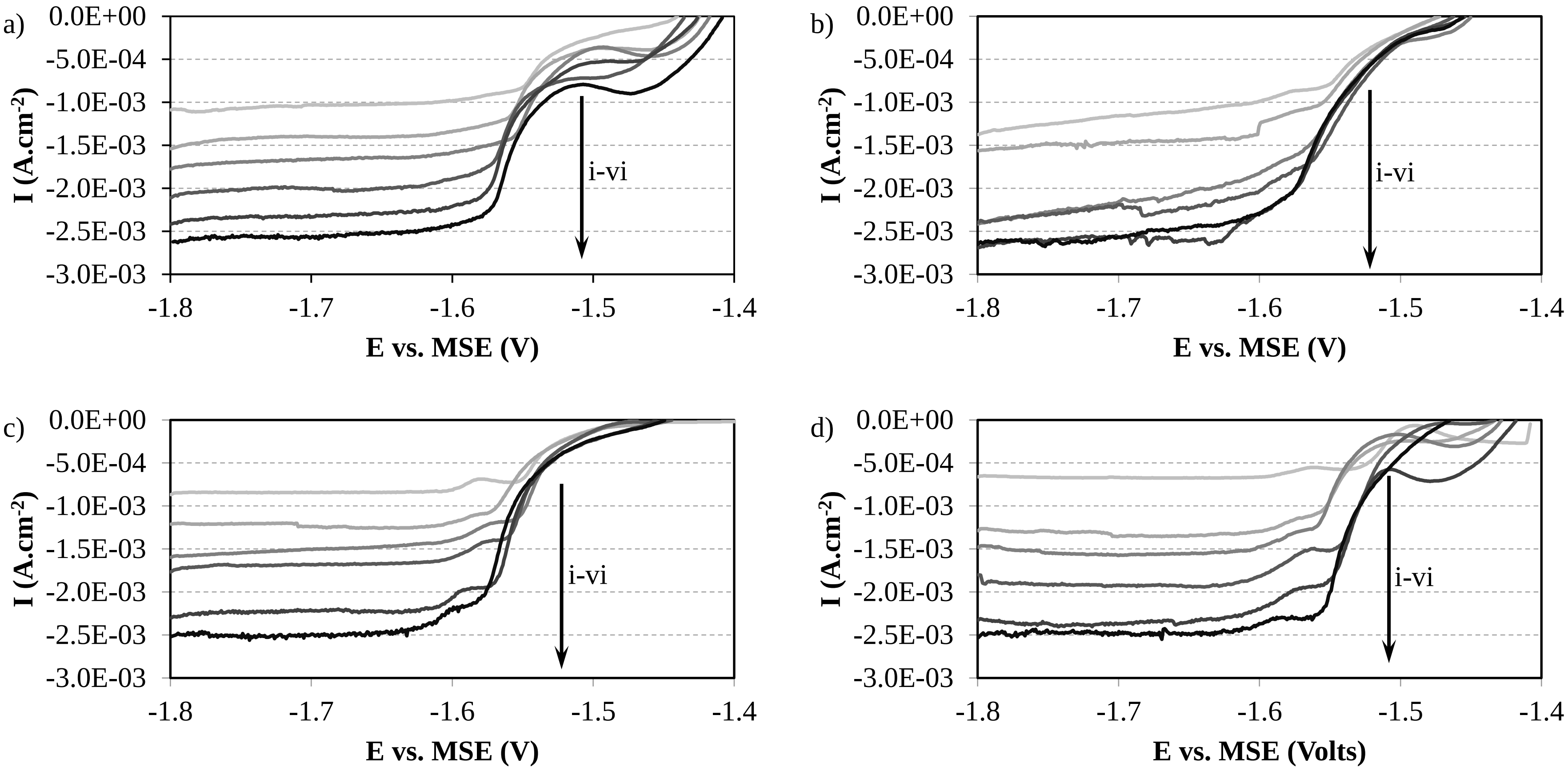

**Figure 4.16:** Anodic going polarisation curves obtained in aerated 0.5 M $Na_2SO_4$ buffered to pH 9.2, potential sweep rate $3.3 \times 10^{-4}$ $V.s^{-1}$ at angular velocities i) 55, ii) 108, iii) 163, iv.) 217, v.) 271 and vi) 314 $rad.s^{-1}$ for a) PVD0, b) PVD4, c) PVD10 and d) PVD20.

### *4.3.4 RDE*

**Figure 4.16** shows that for all coatings there was rotating speed dependence, which is indicative of a diffusion controlled process, which are therefore predictable using the Levich equation [37]:

$$i_L = -0.62nFcD^{2/3}v^{-1/6}\omega^{1/2} \tag{4.3}$$

where $i_L$ is the limiting current density ($A.cm^{-2}$), *n* is the number of electrons transferred per molecule of oxygen reduced, F is the Faraday constant (96485 $C.mol^{-1}$), c is the bulk concentration of dissolved oxygen ($mol.cm^{-3}$), D is the oxygen diffusion coefficient ($cm^2.s^{-1}$), *v* is the kinematic viscosity ($cm^2.s^{-1}$) and ω is the angular velocity ($rad.s^{-1}$). Values for c, D and *v* at 20°C were obtained from previous work [38] and are $2\times10^{-7}$ $mol.cm^{-3}$, $1.74 \times 10^{-5}$ $cm^2.s^{-1}$ and $10^{-2}$ $cm^2.s^{-1}$ respectively. The I vs $\omega^{1/2}$ plots shown in **Figure 4.17** are derived from the data in **Figure 4.16**, also displayed are the theoretical Levich plots for the $4e^-$ (equation 1.8) and $2e^-$ (equation 4.4) oxygen reduction reactions, with theoretical slopes of $69.3\text{x}10^{-6}$ $A.cm^{-2}.s^{-1/2}$ and $34.7\text{x}10^{-6}$ $A.cm^{-2}.s^{-1/2}$ respectively. Typically, the $4e^-$ ORR is observed on bare metal surfaces, whereas the $2e^-$ ORR is observed on oxide covered surfaces [17].

$$O_2 + H_2O + 2e^- \rightarrow HO_2^- + OH^- \tag{4.4}$$

The offset of the plotted sample data from theoretical values for the ORR is a result of the currents used not being wholly diffusion limited [39]. In previous work, the Levich slopes obtained for pure zinc, Zn-0.1Al and Zn-4.3Al correlated well with the theoretical slope for 4e$^-$ [17]. However, all plateaus observed in **Figure 4.16** are still consistent with diffusion controlled 4e$^-$ oxygen reduction to OH$^-$ via equation 1.8, which indicates that the presence of magnesium has relatively little influence on the cathodic oxygen reduction kinetic behaviour. This is inconsistent with previous work that ascribed the increased resistance of $MgZn_2$ to cathodic disbondment to the poor electrocatalytic properties of a magnesium-rich oxide layer [40,41].

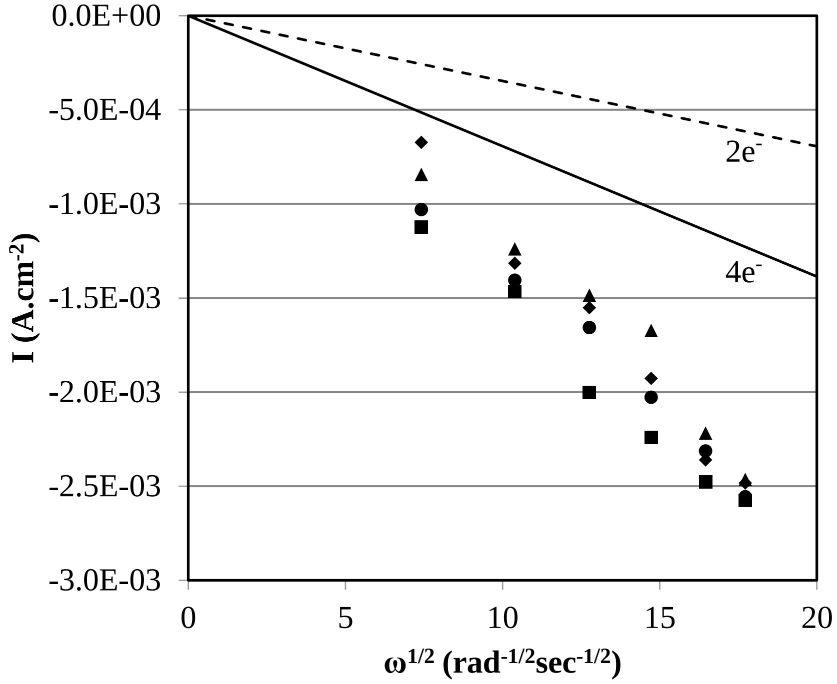

**Figure 4.17:** Levich slope obtained from anodic going potentiodynamic experiments for ● PVD0, ■ PVD4, ▲ PVD10 and ♦ PVD20 alongside theoretical values for 4e$^-$ oxygen reduction in aerated 0.5 M $Na_2SO_4$ buffered to pH 9.3.

## 4.4 Conclusions

The aim of this chapter was to provide the electrochemical characteristics of the novel PVD zinc magnesium coatings. The deposition and subsequent micro/nanostructures identified in Chapter 3 have undoubtedly influenced the unique behaviours highlighted in this work:

- The addition of magnesium to zinc coatings significantly depresses the initial immersion OCP, both for traditional galvanised layers and PVD deposited coatings. However, the stabilised OCP value for ZMA was equivalent to the pure zinc coatings, HDG and PVD0, whereas the magnesium containing PVD coatings exhibited correlative decreases in stabilised OCP.
- Potentiodynamic scans show a depression in $E_{corr}$ and $I_{corr}$ in relation to increasing Mg content, which indicates reduced corrosion rate overall in the systems.
- The EIS response for PVD0 in comparison to HDG suggests an improvement in corrosion resistance in relation to the improved surface uniformity. PVD0, as with ZMA, showed increased polarisation resistance over time, which is attributed to the precipitation of stable corrosion products.
- A key takeaway from the RDE study is the lack of ORR facilitation on PVD4, which would suggest improved cathodic delamination resistance in a complete coating system.

## 4.5 References

1. B. Schuhmacher, C. Schwerdt, U. Seyfert, O. Zimmer, Surf. Coatings Technol. 163–164 (2003) 703–709.
2. T. Koll, K. Ullrich, J. Faderl, J. Hagler, B. Schuhmacher, A. Spalek, (2004) 11–15.
3. N.C. Hosking, M.A. Ström, P.H. Shipway, C.D. Rudd, Corros. Sci. 49 (2007) 3669–3695.
4. S. Schürz, G.H. Luckeneder, M. Fleischanderl, P. Mack, H. Gsaller, A.C. Kneissl, G. Mori, Corros. Sci. 52 (2010) 3271–3279.
5. J. Han, K. Ogle, J. Electrochem. Soc. 164 (2017) C952–C961.
6. E. Diler, B. Rouvellou, S. Rioual, B. Lescop, G. Nguyen Vien, D. Thierry, Corros. Sci. 87 (2014) 111–117.
7. R. Baboian, National Association of Corrosion Engineers. Unit Committee T-3L on Electrochemical and Electrical Techniques for Corrosion Measurement and Control., Electrochemical techniques for corrosion engineering, National Association of Corrosion Engineers, (1986).
8. P.L. Cabot, M. Cortés, F.A. Centellas, J.A. Garrido, E. Pérez, J. Electroanal. Chem. 201 (1986) 85–100.
9. G. Williams, H.N. McMurray, Corrosion. 62 (2006) 231–242.
10. M.H. Lee, Y.W. Kim, K.M. Lim, S.H. Lee, K.M. Moon, Trans. Nonferrous Met. Soc. China (English Ed. 23 (2013) 876–880.
11. M. Curioni, Electrochim. Acta. 120 (2014) 284–292.
12. T.A. Vida, E.S. Freitas, N. Cheung, A. Garcia, W.R. Osório, Int. J. Electrochem. Sci. 12 (2017) 5264–5283.

13. D.G. Enos, L.L. Scribner, The Potentiodynamic Polarization Scan, (1997).

14. A. Lasia, Electrochemical Impedance Spectroscopy and its Applications, Kluwer Academic/Plenum Publishers, (1999).

15. M.E. Orazem, B. Tribollet, Electrochemical impedance spectroscopy, (2017).

16. H.S. Wroblowa, S.B. Qaderi, J. Electroanal. Chem. 295 (1990) 153–161.

17. H. Dafydd, D.A. Worsley, H.N. McMurray, Corros. Sci. 47 (2005) 3006–3018.

18. F. Thébault, B. Vuillemin, R. Oltra, C. Allely, K. Ogle, O. Heintz, Corros. Sci. 97 (2015) 100–106.

19. A. Leng, H. Streckel, M. Stratmann, Corros. Sci. 41 (1998) 579–597.

20. Y.J. Kwak, T.Y. Kim, D.Y. Lee, K.H. Nam, Y.H. Jung, W.S. Jung, M.J. Eom, S.J. Hong, Eur. Corros. Congr. EUROCORR 2016. 2 (2016) 1480–1486.

21. V. Barranco, S. Feliu, S. Feliu, Corros. Sci. 46 (2004) 2203–2220.

22. L. Sziraki, E. Szocs, Z. Pilbath, K. Papp, E. Kalman, Electrochim. Acta. 46 (2001) 3743–3754.

23. K. Nishimura, H. Shindo, H. Nomura, K. Katoh, Tetsu-to-Hagane. 89 (2003) 174–179.

24. S. Schuerz, M. Fleischanderl, G.H. Luckeneder, K. Preis, T. Haunschmied, G. Mori, A.C. Kneissl, Corros. Sci. 51 (2009) 2355–2363.

25. T. Prosek, N. Larché, M. Vlot, F. Goodwin, D. Thierry, Mater. Corros. 61 (2010) 412–420.

26. P. Volovitch, T.N.N. Vu, C. Allély, A. Abdel Aal, K. Ogle, Corros. Sci. 53 (2011) 2437–2445.

27. D. Persson, D. Thierry, N. LeBozec, T. Prosek, Corros. Sci. 72 (2013) 54–63.

28. R. Krieg, A. Vimalanandan, M. Rohwerder, J. Electrochem. Soc. 161 (2014) C156–C161.

29. T. Lostak, A. Maljusch, B. Klink, S. Krebs, M. Kimpel, J. Flock, S. Schulz, W. Schuhmann, Electrochim. Acta. 137 (2014) 65–74.

30. M. Salgueiro Azevedo, C. Allély, K. Ogle, P. Volovitch, Corros. Sci. 90 (2015) 472–481.

31. J. Sullivan, N. Cooze, C. Gallagher, T. Lewis, T. Prosek, D. Thierry, Faraday Discuss. 180 (2015) 361–379.

32. P. Saravanan, S. Srikanth, Int. J. Adv. Res. Chem. Sci. 5 (2018) 11–23.

33. D. Klotz, Electrochem. Commun. 98 (2019) 58–62.

34. A.M. Simões, J. Torres, R. Picciochi, J.C.S. Fernandes, Electrochim. Acta. 54 (2009) 3857–3865.

35. Y. Liu, H. Li, Z. Li, Int. J. Electrochem. Sci. 8 (2013) 7753–7767.

36. A.D. King, N. Birbilis, J.R. Scully, Electrochim. Acta. 121 (2014) 394–406.

37. V.G. Levich, Physicochemical Hydrodynamic, Prentice Hall Inc., (1962).

38. A. Bonnel, F. Dabosi, C. Deslouis, M. Duprat, M. Keddam, B. Tribollet, J. Electrochem. Soc. 130 (1983) 753.

39. N. Wint, S. Geary, H.N. McMurray, G. Williams, A.C.A. de Vooys, J. Electrochem. Soc. 162 (2015) C775–C784.

40. R. Hausbrand, M. Stratmann, M. Rohwerder, J. Electrochem. Soc. 155 (2008) C369.

41. R. Hausbrand, M. Stratmann, M. Rohwerder, Corros. Sci. 51 (2009) 2107–2114.

# Chapter 5. A study into the influence of Mg content on the localised corrosion behaviour of PVD Zn-Mg coatings using SVET-TLI

## 5.1 Introduction

Scale-up research produced by POSCO discovered that Zn-Mg coatings containing 9.2 wt% magnesium provided superior corrosion resistance compared to electrogalvanised or hot dig galvanised (HDG) reference samples when subjected to standard salt spray testing [1]. Aside from this instance, there has been no other research conducted into the bare metal corrosion of Zn-Mg PVD coatings. Therefore, the primary intention of this chapter is to characterise the localised bare metal corrosion of Zn-Mg PVD coatings by using the novel combination of a scanning vibrating electrode technique and in-situ time-lapse imaging (henceforth referred to as SVET-TLI). The scanning vibrating electrode technique (SVET) is an advanced method for spatially and temporally monitoring electrochemical behaviour and has been used extensively for the in-situ study of localised corrosion behaviour of metal surfaces under immersion conditions [2–10]. It detects potential gradients in solution above an actively corroding surface which are a result of ionic flow between anodic and cathodic sites. By converting the potential to current density values, via a calibration procedure [8], 2D and 3D maps can be generated to display the local electrochemical activity qualitatively. Furthermore, SVET-derived data can be utilised quantitatively to study the kinetics of anodic and cathodic propagation. An in-depth review of the SVET and its applications in electrochemistry has recently been published [11].

The resolution of the SVET is limited by the probe diameter and scan height, with a practical width at half maximum (whm) previously stated as 0.26 mm [5] for a scan height of 100 μm; simply put, if two or more electrochemical events are positioned within 0.26 mm of each other they will not be detected as individual instances but as a net effect. In terms of corrosion mechanisms, this limitation prevents the detection of general corrosion [12] or any corrosion cells with current pathways less than the whm. This poses an issue for alloys and alloy coatings that possess fine microstructural features which influence corrosion behaviour. This is particularly problematic in the study of ZMA coatings, when attempting to electrochemically determine the mechanisms responsible for the superior corrosion resistance, due to their heterogeneous microstructure. Hausbrand et al. overcame this issue by studying the $MgZn_2$ intermetallic, a common constituent in most ZMA coatings, in a pure cast form. Their initial work showed the superior delamination resistance of $MgZn_2$ compared to zinc as a result of a difference in defect and intact potentials stemming from the preferential formation of surface oxides [13]. The predominant formation of magnesium hydroxide $(MgOH)_2$ inhibited oxygen reduction and depressed the intact potential to a point where cathodic delamination was completely suppressed on the $MgZn_2$. However, with a potential gradient still present, $MgZn_2$ was instead found to be susceptible to anodic-type delamination. Moreover, $MgZn_2$ was found to corrode faster than zinc and at a lower potential, suggesting a possible sacrificial mechanism exhibited by $MgZn_2$ to protect zinc at the onset of corrosion. Therefore, it was stipulated that an optimum composition of zinc and $MgZn_2$, within a ZMA coating, could be achieved to eliminate the potential gradient and prevent both cathodic and anodic delamination behaviour [14,15]. Sullivan et al. were able to definitively prove the previously theorised preferential de-alloying of the $MgZn_2$ phase, within the binary and ternary eutectic structures in ZMA coatings, by devising an in-situ time-lapse microscopy method for monitoring microstructural attack [16].

It is therefore proposed that photographic images captured sequentially during an SVET-TLI study can be used as complementary data to confirm unresolved electrochemical events. In the Powell et al. SRET study, on the influence of corrosion inhibitors on galvanised sheet steel surface corrosion, photographic evidence is captured only at the end of the study and used to aid in the explanation of corrosion mechanisms [17]. Similarly, Glover and Williams, in a study of the inhibition of corrosion on hot dip galvanised coatings using phenylphosphonic acid, use photographs captured at the end of each SVET study to aid in the identification of corrosion products and mechanisms [18]. In both cases, there are assumptions made to correlate the photographic and electrochemical data and further relate the results to theoretical predictions. It can be said that these visual data do not provide strong evidence for or against the theoretical model; rather the known theory is applied as a “best fit” for the visual corrosion products and possible attack mechanisms. Furthermore, the majority of localised electrochemical studies on galvanised steel cut edge corrosion completely lack the inclusion of correlative visual data [19–22].

The technique presented in this work is a necessary evolution for the SVET. As such, this chapter first establishes the improved capability of SVET-TLI by investigating the corrosion behaviour of a hot dip galvanised coating, which has been extensively studied previously. This is then compared to a pure zinc PVD coating to determine the influence of the coating method and purity on localised corrosion mechanisms. A hot dip ZMA coating is analysed as a comparison for the Zn-Mg PVD coatings. The PVD coatings are systematically characterised to determine the influence of magnesium content on the microstructure and associated localised corrosion behaviour.

## 5.2 Experimental

### *5.2.1* Materials

This chapter studies the surface corrosion behaviour of HDG, ZMA, PVD0, PVD4, PVD10 and PVD20, all of which are fully described in **Table 2.1**.

### *5.2.2 Methods*

For SVET-TLI study, the coating surfaces were rinsed with ethanol and sectioned into 10 mm by 10 mm square coupons, upon which a 6 mm by 6 mm scan area was isolated using PTFE tape. Following SVET-TLI immersion studies, X-Ray powder diffraction (XRD) was undertaken via the procedure outlined in 2.2.3.

SVET calibration was carried out under standard procedure described in 2.4.2. Each sample was immersed in 0.17 M NaCl for the duration of each experiment; the surface of the electrolyte was approximately 2 cm above the surface of the sample and in contact with room air in a controlled 19 °C environment. The scan area was defined as 6 mm by 6 mm in the SVET software with 31 data point locations in both the x and y directions, giving a total of 961 data points separated by equal spaces of 0.2 mm. The SVET probe was positioned 100 µm above the sample surface and began scanning immediately after sample immersion. A scan took place every 10 minutes thereafter giving a total of 144 scans over 24 hours, with an average scan duration of 4 minutes and 20 seconds. The SVET-derived current density data were plotted as 2D false-colour surface plots using Golden Software's Surfer 8; the anodic current is presented as red, cathodic current blue and points where current density is zero are white.

The adaption of a scanning vibrating electrode technique, to include simultaneous visual data capture, was achieved by affixing a Supereyes Y002 waterproof microscope endoscope camera to the probe assembly. This camera is lightweight and waterproof, allowing prolonged immersion in salt solution without interfering with the functionality of the SVET probe assembly or motor control. The camera was attached using a custom, 3D-printed articulated arm and friction clamp which held the camera parallel to the vibrating tip of the SVET (**Figure 5.1**). A rest setting was added to the SVET scan setup, instructing the SVET probe assembly to move 40 mm in the x direction to align the camera at the end of each scan. The SVET would remain in the rest position until the start of the next scan.

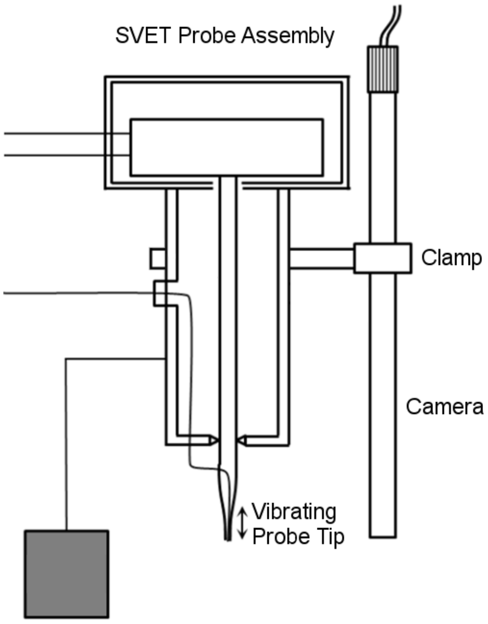

**Figure 5.1:** Schematic diagram of the SVET probe assembly with Supereyes Y002 waterproof microscope endoscope camera attached via 3D-printed articulated arm and friction clamp.

Automatic photograph capturing was managed by basic time-lapse freeware, Sky Studio, scheduled to capture images of the scan area every minute, ensuring a relationship of 30 seconds between the start or end of a scan and a corresponding photograph of the surface. To prevent distortion from the electrolyte-air interface, the camera was immersed for the entirety of the 24 hour study of each sample.

For each coating, three SVET-TLI experiments were conducted to confirm consistency in the observed behaviour. Only one experiment per sample was selected for the presentation of the photographic images and electrochemical false colour maps as reliable representatives.

## 5.3 Results and Discussion

### *5.3.1* HDG and PVD0

**Figure 5.2** displays false colour surface plots showing current density distributions, presented adjacent to the associated close up in-situ photographic images, for HDG, taken at different holding times while immersed in 0.17 M NaCl solution. The electrochemical surface plots show the formation and stabilisation of several focal anodes which are, in this instance, the dissolution of zinc as shown in equation 5.1.

$$Zn_{(s)} + 2e^{-} \rightarrow Zn^{2+}{}_{(aq)} \qquad (5.1)$$

Localised anodic features that remain constant on the surface of the HDG is a behaviour previously observed [18]; the corresponding photographic images in this work further reinforce this mechanism by displaying the associated surface roughening. White corrosion product was also shown to be deposited in the cathodic regions, separated from the anodes by areas of zero current density. The sample remained fully immersed in NaCl solution for the entire duration of the 24 hour experiment. Therefore, it can be assumed that the initial, stable corrosion product was zinc hydroxide ($Zn(OH)_2$), formed via equation 5.2, as opposed to zincite (ZnO) due to the abundance of $OH^-$ ions, generated by oxygen reduction (equation 5.3) at the cathodes. The Pourbaix diagram for zinc also demonstrates that the conditions of the experiment satisfy the stability domain for $Zn(OH)_2$ [23].

$$Zn^{2+}{}_{(aq)} + 2OH^-{}_{(aq)} \rightarrow Zn(OH)_{2\,(s)} \tag{5.2}$$

$$O_{2\,(g)} + 2H_2O_{(l)} + 4e^- \rightarrow 4OH^-{}_{(aq)} \tag{5.3}$$

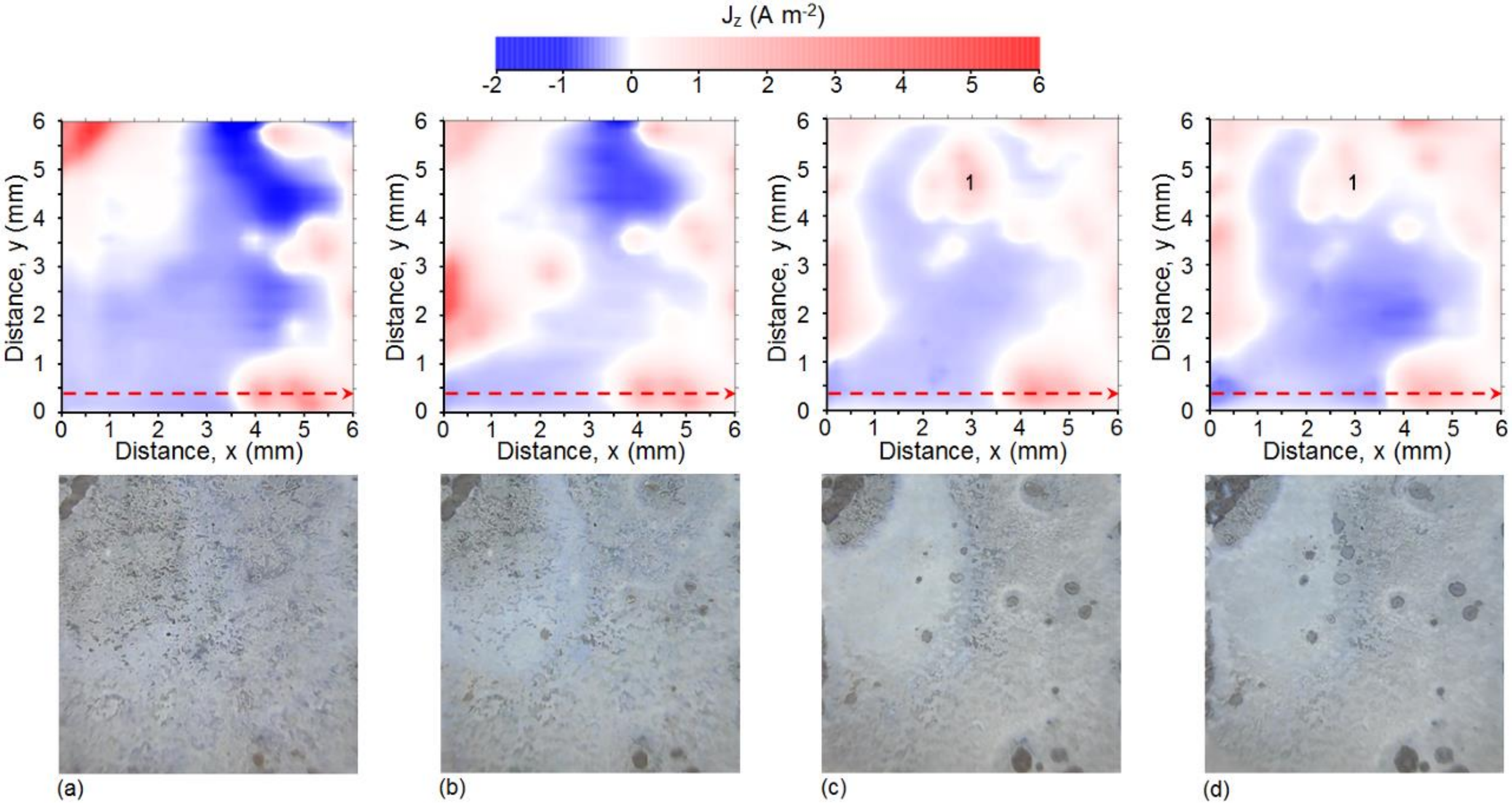

**Figure 5.2:** SVET-derived false colour surface plots showing the distribution of normal current density (top) with associated photographic images (bottom) above freely corroding HDG in aerated 0.17 M NaCl at (a) 4, (b) 8, (c) 16 and (d) 24 hours immersion time (a red dashed arrow has been added to indicate the location of the selected SVET profile extracted for **Figure 5.4a**).

After 16 hours immersion, the SVET plots show anodic activation of a previously cathodic region, resulting in a new net anodic area (labelled in **Figure 5.2c** and **Figure 5.2d** as feature 1). This event was supported by the growth of dark features in the corresponding photographic images. Zinc hydroxide is an amphoteric material; therefore, it will dissolve in solutions of elevated pH to form zincate ($ZnO_2^{2-}$) and bizincate ($HZnO_2^-$) via the reactions in equation 5.4 and equation 5.5 respectively.

$$Zn(OH)_{2\,(s)} + 2OH^-_{(aq)} \rightarrow ZnO_2^{2-}{}_{(aq)} + 2H_2O_{(l)} \qquad (5.4)$$

$$Zn(OH)_{2\,(s)} + OH^-_{(aq)} \rightarrow HZnO_2^-{}_{(aq)} + H_2O_{(l)} \qquad (5.5)$$

PVD0 can theoretically be compared to HDG in terms of corrosion resistance as both coatings are >99 wt% zinc. However, PVD0 coatings are disregarded in terms of potential to substitute commercial hot dip galvanising coatings as it is well understood that the corrosion protection offered by pure zinc coatings is proportional to the coating thickness [24,25]. Still, PVD0 offers insight into the influence of coating deposition method as it is considered a pure homogenous layer of zinc metal. HDG, on the other hand, is susceptible to inclusions that can negatively affect the coating properties, following the pickup of tramp elements during the hot dip process [26].

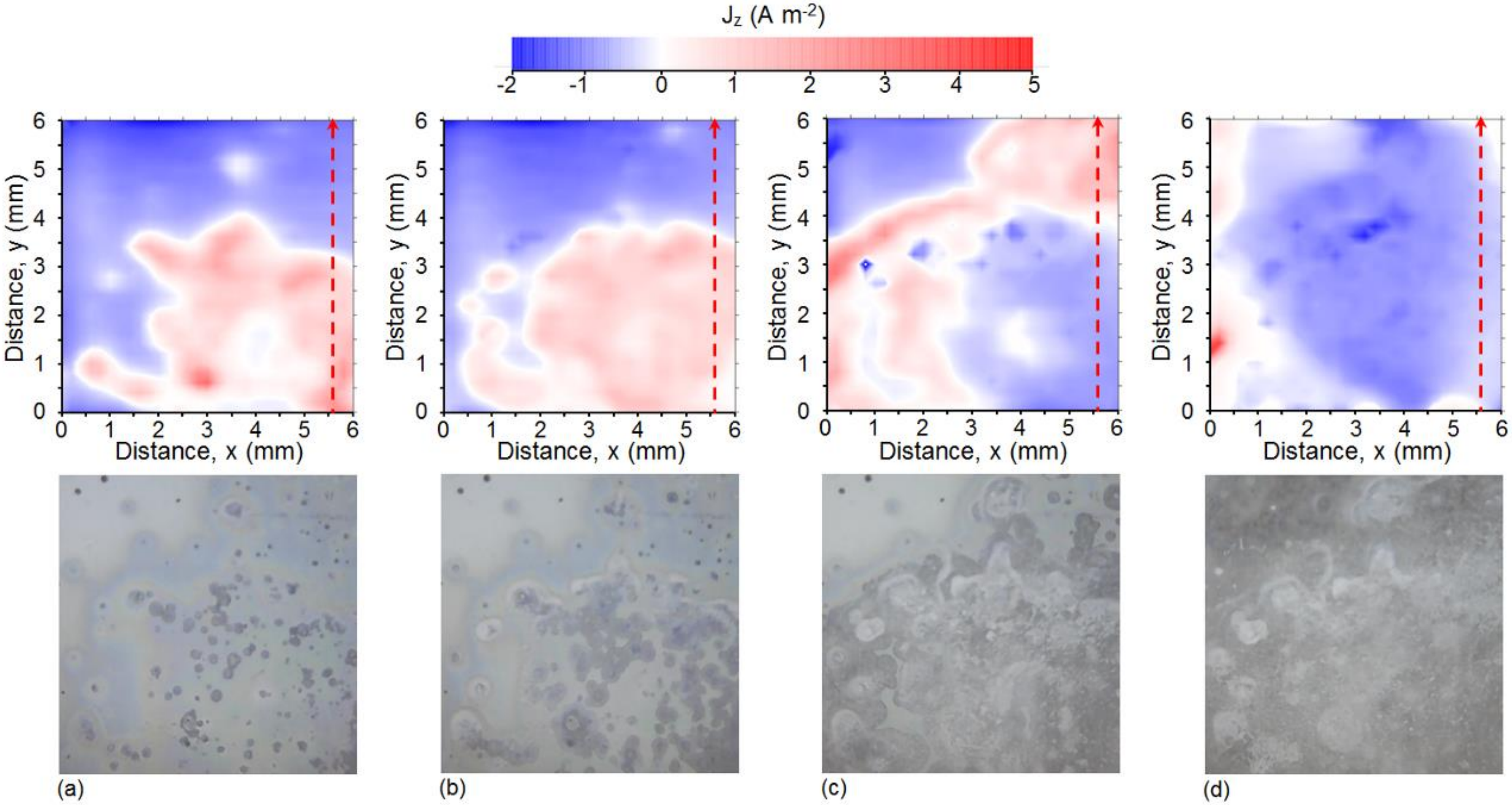

**Figure 5.3:** SVET-derived false colour surface plots showing the distribution of normal current density (top) with associated photographic images (bottom) above freely corroding PVD0 in aerated 0.17 M NaCl at (a) 4, (b) 8, (c) 16 and (d) 24 hours immersion time (a red dashed arrow has been added to indicate the location of the selected SVET profile extracted for **Figure 5.4b**).

**Figure 5.3** shows the SVET-TLI results taken at different holding times for PVD0 over the 24 hour immersion analysis. PVD0 appeared to exhibit the features of general corrosion with many anodic features too small to be resolved by the SVET and are only recognised with the complementary visual data. The SVET-derived maps display an anodic front which swept over the surface of the coating and the post-corroded areas became new cathodic sites for oxygen reduction. The photographic images show a mechanism of many anodic activation events that initiated en masse over the coating followed by corrosion product deposition on each site. There was no clear evidence of re-activation of the surface.

Wint et al. observed localised corrosion behaviour on the surface of pure zinc foil under similar testing conditions [27], which is highly comparable with the features seen on HDG, not PVD0. As there was no visual breakthrough to the steel substrate, nor the corresponding characteristic enhancement of cathodic activity in the post-corroded regions, it is proposed that the fine globular surface topography of these PVD coatings, previously reported [28,29], is the influencing factor as opposed to metal purity. The micro-crevices formed between joining globules are evenly spaced over the surface of the PVD coatings, serving as preferential initiation points for corrosion. Conversely, HDG coatings are well understood to exhibit relatively large (>1 mm) characteristic spangles [30]. Furthermore, the mean surface roughness value for PVD0, reported in **Table 3.1**, is 300 nm; for HDG the mean surface roughness value was 1.3µm as stated previously. Osório et al. [31] conducted a systematic study on the macrostructural morphology and grain size of HDG and zinc castings which revealed the positive correlation between grain size and corrosion resistance. The influence of grain morphology on corrosion resistance was attributed to the increased energy levels at grain boundaries caused by the accumulation of defects, impurities and plastic deformation. Therefore, it can be said that the grain boundaries are the preferential initiation sites for anodic attack.

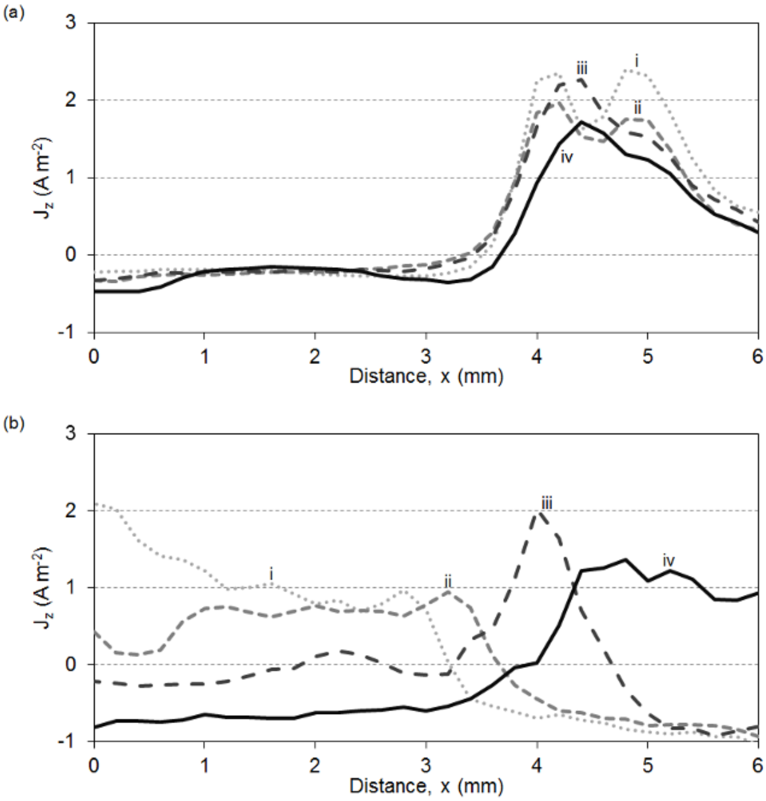

**Figure 5.4:** SVET-derived current density line profiles for (a) HDG taken from y = 0.4 mm in **Figure 5.2** at (i) 4, (ii) 8, (iii) 16 and (iv) 24 hours immersion time, and (b) PVD0 taken from x = 5.6 mm in **Figure 5.3** at (i) 4, (ii) 8, (iii) 12 and (iv) 16 hours immersion time in 0.17 M NaCl.

The contrasting nature of anodic activity for both coatings was best visualised by extracting line profile data from the SVET maps, at different immersion times, and plotting the current density against distance over the sample as shown in **Figure 5.4** (**Figure 5.2** and **Figure 5.3** indicate the selected line data location, for **Figure 5.4a** and **Figure 5.4b** respectively, with red dashed arrows). The anodic event on HDG (**Figure 5.4a**) is shown to have activated within the first 4 hours of immersion, displaying two anodic peaks which suggests the presence of two separate anodic sites that are only partially resolved by the SVET. Over the course of the experiment the spacing between the two peaks lessened, resulting in an overall current density peak of 3.06 A.m$^{-2}$ at 12 hours. However, it is clear that this anodic area remained in a fixed location and kept a constant overall width of 2.2 mm. In contrast, **Figure 5.4b** emphasises the progression of a characteristic anodic front on the surface of the PVD0 coating over the 24 hour study. The anodic activity of PVD0 was much broader, compared to HDG, during the first 8 hours (3.2 mm). As the ratio of uncorroded to corroded zinc became smaller, the anodic area became correspondingly narrower.

### *5.3.2* ZMA

The SVET-TLI maps and photographs for ZMA, immersed in 0.17 M NaCl for 24 hours, show the formation of localised anodic events in **Figure 5.5**. After 8 hours immersion, the focal anodes began to radially expand across the surface of the coating. The photographic images accurately corroborate this behaviour, showing the formation and growth of dark circles. As stated before, the $MgZn_2$ phase has previously been shown to corrode preferentially to zinc and the more electrochemically active element, magnesium, is de-alloyed via the reaction in equation 5.6 [13–16].

$$Mg_{(s)} + 2e^{-} \rightarrow Mg^{2+}{}_{(aq)} \tag{5.6}$$

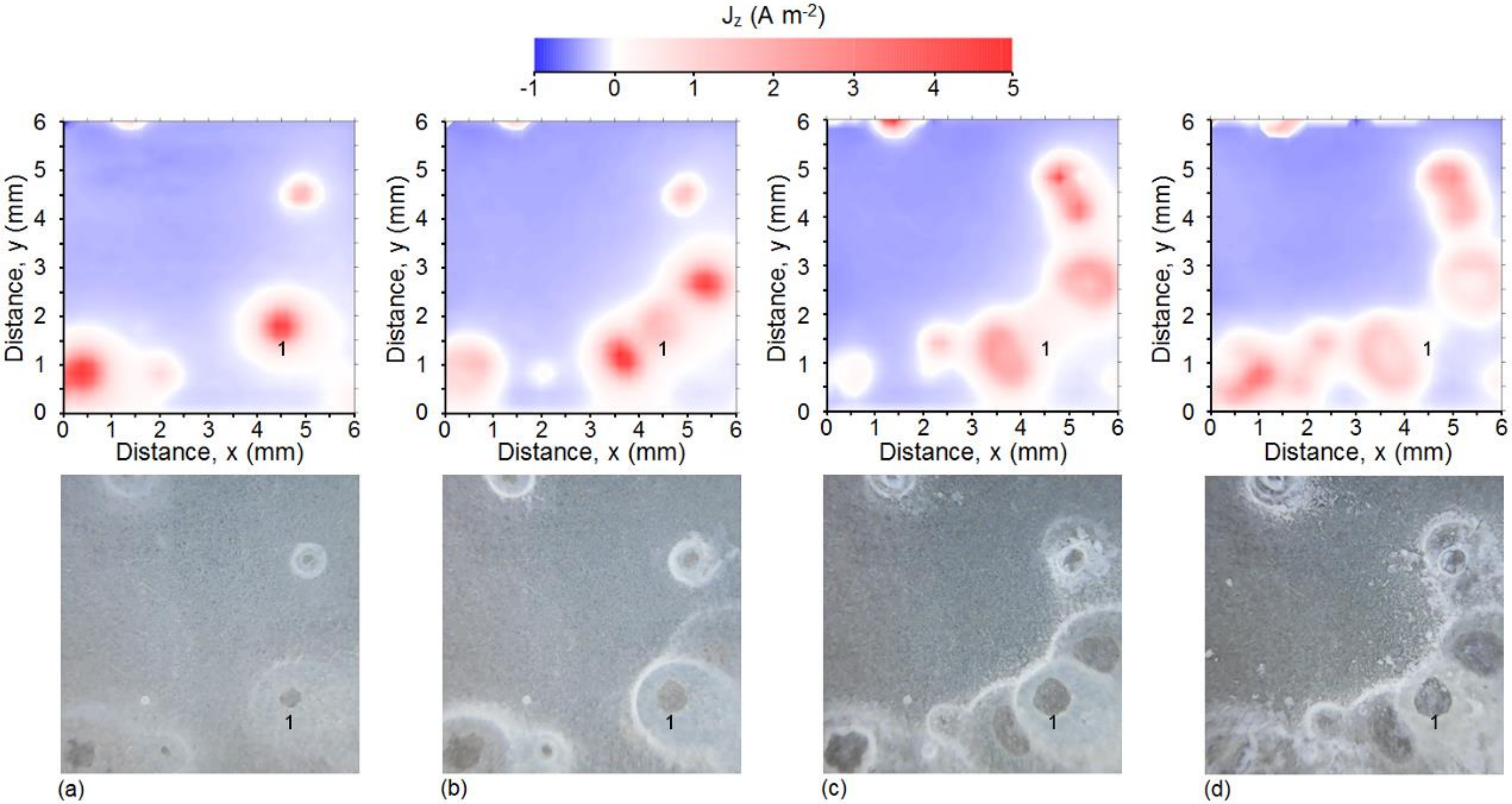

**Figure 5.5:** SVET-derived false colour surface plots showing the distribution of normal current density (top) with associated photographic images (bottom) above freely corroding ZMA in aerated 0.17 M NaCl at (a) 4, (b) 8, (c) 16 and (d) 24 hours immersion time.

In response to the dissolution of the coating, corrosion products were visually observed in the photographs to form a “halo” around the anodic sites, in the regions of zero current density displayed by the corresponding SVET maps. Literature suggests that, as in the case of $Zn(OH)_2$ for pure zinc corrosion, magnesium hydroxide ($Mg(OH)_2$) formation is more thermodynamically favourable than MgO in the presence of water, thus a method involving complete and continuous immersion would promote $Mg(OH)_2$ over MgO [32] via equation 5.7.

$$Mg^{2+}{}_{(aq)} + OH^{-}{}_{(aq)} \rightarrow Mg(OH)_{2\,(aq)} \tag{5.7}$$

$Mg(OH)_2$ is electrochemically inert at high pH [23], therefore the breakthrough behaviour seen in the HDG coating is not observed for ZMA.

Hosking et al. [33] state that $Mg(OH)_2$ formation takes place at the net cathodic regions due to the presence of $OH^-$ ions, which is possibly recognised in **Figure 5.5** by a visual dulling of the surface known to be occupied by cathodic activity. This proposed suppression of the oxygen reduction reaction (equation 5.3) and consequent moderation of pH plays a key role in the stabilisation of the compact corrosion product simonkolleite ($Zn_5Cl_2(OH)_8\cdot H_2O$). The formation of simonkolleite from ZnO occurs in the presence of $Cl^-$ via equation 5.8, according to Falk et al. [34]. $Mg(OH)_2$ deposits on cathode sites shift the equilibrium in favour of simonkolleite formation, which inhibits further corrosion by trapping $Cl^-$ ions and acting as a compact mass transport barrier. Further evidence of the improved corrosion resistance attributed to simonkolleite formation can be found elsewhere [35–38].

$$5ZnO_{(s)} + 2Cl^-_{(aq)} + 6H_2O_{(l)} \rightarrow Zn_5Cl_2(OH)_8{\cdot}H_2O_{(s)} + 2OH^-_{(aq)} \qquad (5.8)$$

The white “halos” of corrosion product correlate well with the formation of simonkolleite as they appeared to restrict the expansion of the anodic rings on the surface of the ZMA; the expansion of the supplementary anodes formed after 8 hours appear to have been retarded in the directions of the pre-existing corrosion product. Furthermore, the anode labelled as feature 1 is completely de-activated after 24 hours immersion time. Subsequent XRD analysis conducted on the ring of corrosion products adjacent to the anodic event confirmed the presence of the compact simonkolleite corrosion product (**Figure 5.6**).

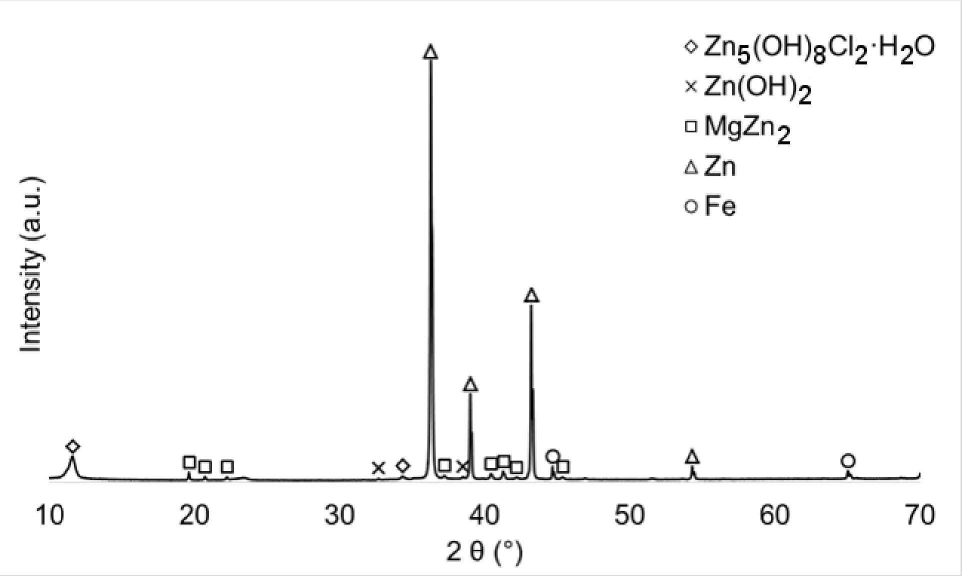

**Figure 5.6:** XRD spectra of the corrosion products visible on the ZMA coating after 24 hours immersion in 0.17 M NaCl.

### *5.3.3* Zn-Mg PVD

The $Mg_2Zn_{11}$ phase present in the PVD4 coating has previously been acknowledged to have superior corrosion resistance compared to the $MgZn_2$ phase found in ZMA [39].

**Figure 5.7** shows that the addition of magnesium to zinc PVD coatings had a dramatic effect on nature of corrosion in the NaCl solution compared to PVD0. Indeed, visually the coating appeared to exhibit behaviour characteristic of pure magnesium as the surface is “stained” black, as has been previously reported [8, 35,40]. However, unlike pure magnesium, the SVET-derived maps with correlating photographs suggest the staining of the surface occurred in the net cathodic regions, which appears to contradict the theory that the blackening is a result of magnesium dissolution [41]. The limited resolution of the SVET is a possible explanation for this phenomenon; anodic magnesium dissolution may have occurred evenly over the surface of the coating, but the fine distribution of zinc and $Mg_2Zn_{11}$ limited the ionic pathways of the galvanic effect to a scale not resolvable by the SVET. Światowska et al. have previously observed the dissolution of magnesium despite the application of a relatively large cathodic current (-80 $\mu A.cm^{-2}$ minimum value) in 0.01 M NaCl [42]. This was also shown in the recent work of Han and Ogle, where persistent and significant anodic dissolution of magnesium occurred while the working electrode was cathodically polarised [43].

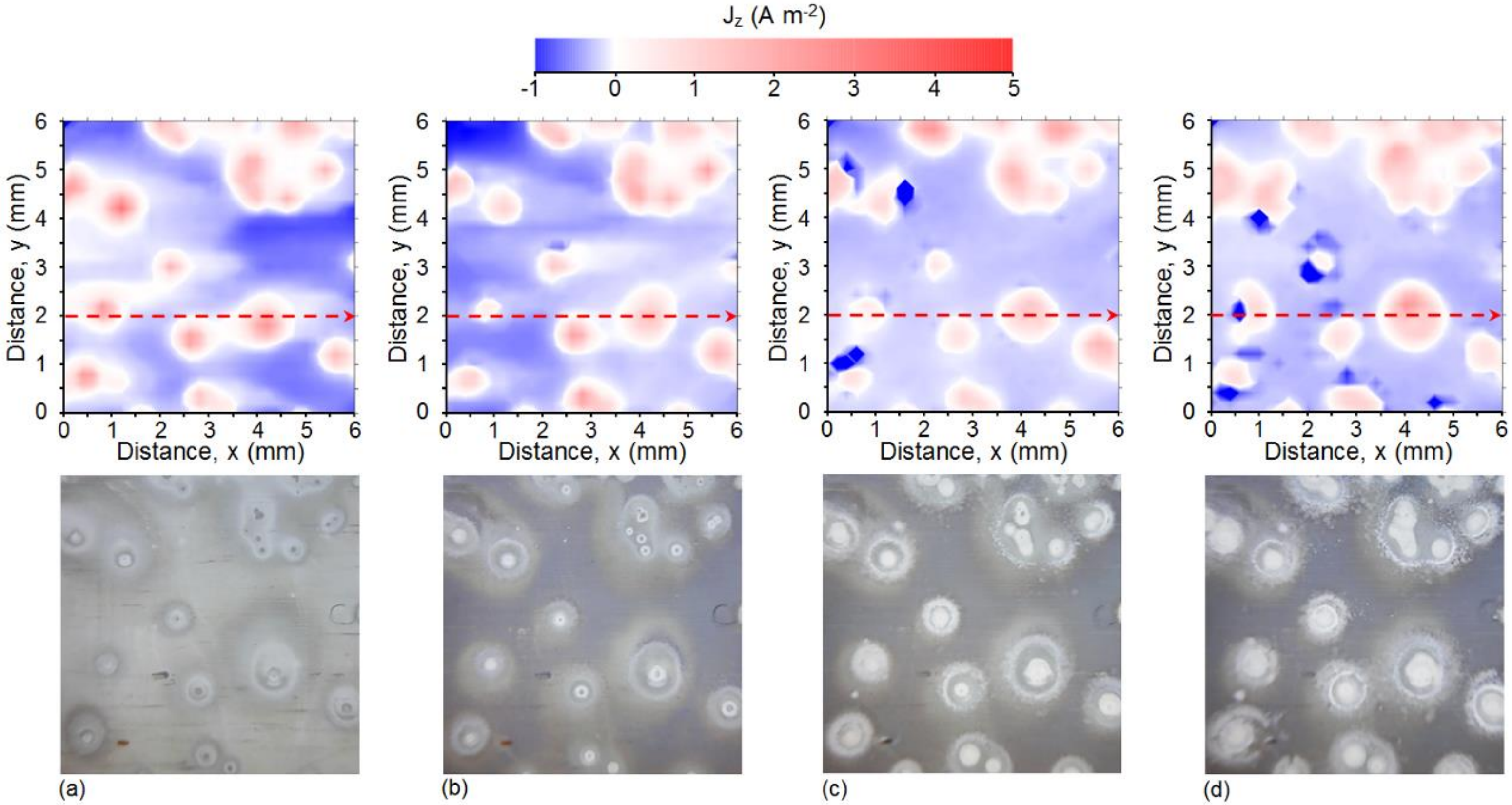

**Figure 5.7:** SVET-derived false colour surface plots showing the distribution of normal current density (top) with associated photographic images (bottom) above freely corroding PVD4 in aerated 0.17 M NaCl at (a) 4, (b) 8, (c) 16 and (d) 24 hours immersion time (a red dashed arrow has been added to indicate the location of the selected SVET profile extracted for **Figure 5.9a**). *Note: the intense cathodic features visible in (c) and (d) are artefacts cause by corrosion product impingement on the SVET tip and are to be disregarded.*

The fine structure present in PVD4 (chapter 3) also appears to have influenced the formation of the anodic sites identified in the SVET maps. When compared with ZMA, which showed a maximum of 10 individual anodic events, the PVD4 coating displays approximately 20 active sites. The scale of the microstructure found in PVD4 does not suggest a direct correlation between the distribution of phases and stable anodic events observed in **Figure 5.7**. In a previous study by Sullivan et al. [44], the in-situ microscope images of ZMA coatings freely corroding in 1 % NaCl suggest that, during the hours immediately following submersion, there are multiple sites of preferential attack on the magnesium-containing eutectic phase. These initial anodic events are approximately 50 µm in diameter at 4 hours in and are clustered together within a net anodic area of 200-300 µm. As stated before, the SVET used in this study is not capable of resolving features within 0.26 mm of each other. It is therefore proposed that the fine distribution of $Mg_2Zn_{11}$ phase in PVD4 influences the preferential locations for anodic initiation, with many small anodic events formed in the early hours of immersion. The stabilisation of the visible anodic events in **Figure 5.7** may be attributed to individual stabilisation of the microscopic anodes, unresolvable by the SVET, or by their merging. What is evident however, is that once localised corrosion becomes established (within the first 4 hours), no further anodic events initiate presumably because of elevated pH over the net cathodic regions which inhibits further magnesium dissolution from the $Mg_2Zn_{11}$ phase.

The expansion of the anodes on PVD4 was less apparent than that of the anodes on ZMA. The white corrosion product "halos" observed on ZMA were also present on PVD4, similarly constricting each anodic site. Contrary to ZMA, the white corrosion products on PVD4 were also formed directly on top of each anode; the persistence of each anodic site following initiation over the 24 hour immersion period suggests that these deposits do not serve to impede interfacial electron transfer or ionic current to or from these sites. It is important to also note the regions of cathodic activity directly adjacent to the “halos” that appear in the early stages of immersion; it is proposed that these are localised deposition sites for $Mg(OH)_2$ which formed rapidly in the experiment and prevented further de-alloying of magnesium by passivating the surface. PVD10 shows more of a resemblance to pure magnesium corrosion [8] with the characteristic staining and the development of a distinctive anodic ring in **Figure 5.8**. However, contrary to the behaviour of pure magnesium, the expanding ring was not driven by a strong cathodic interior. The corroded area left in the wake of the expanding anodic ring was deactivated by the development of corrosion products which can be seen in the images as white deposits. This contrasts with the PVD4 coating, which displayed many smaller anodic features that did not appear to have a passivated centre. It is therefore suggested that the nanostructure of PVD10 (**Figure 3.6b**) results in a finer distribution of magnesium in the coating, consequently exhibiting a more homogeneous response with relatively larger anodic events. As with PVD4, the cathodic region directly adjacent to the anodic ring shows no evidence of magnesium de-alloying, but a slight discolouration suggests that there was instead a rapid formation of corrosion product. It is interesting to note that the area of this protected zone appears to be related to the size of the corresponding anodic event.

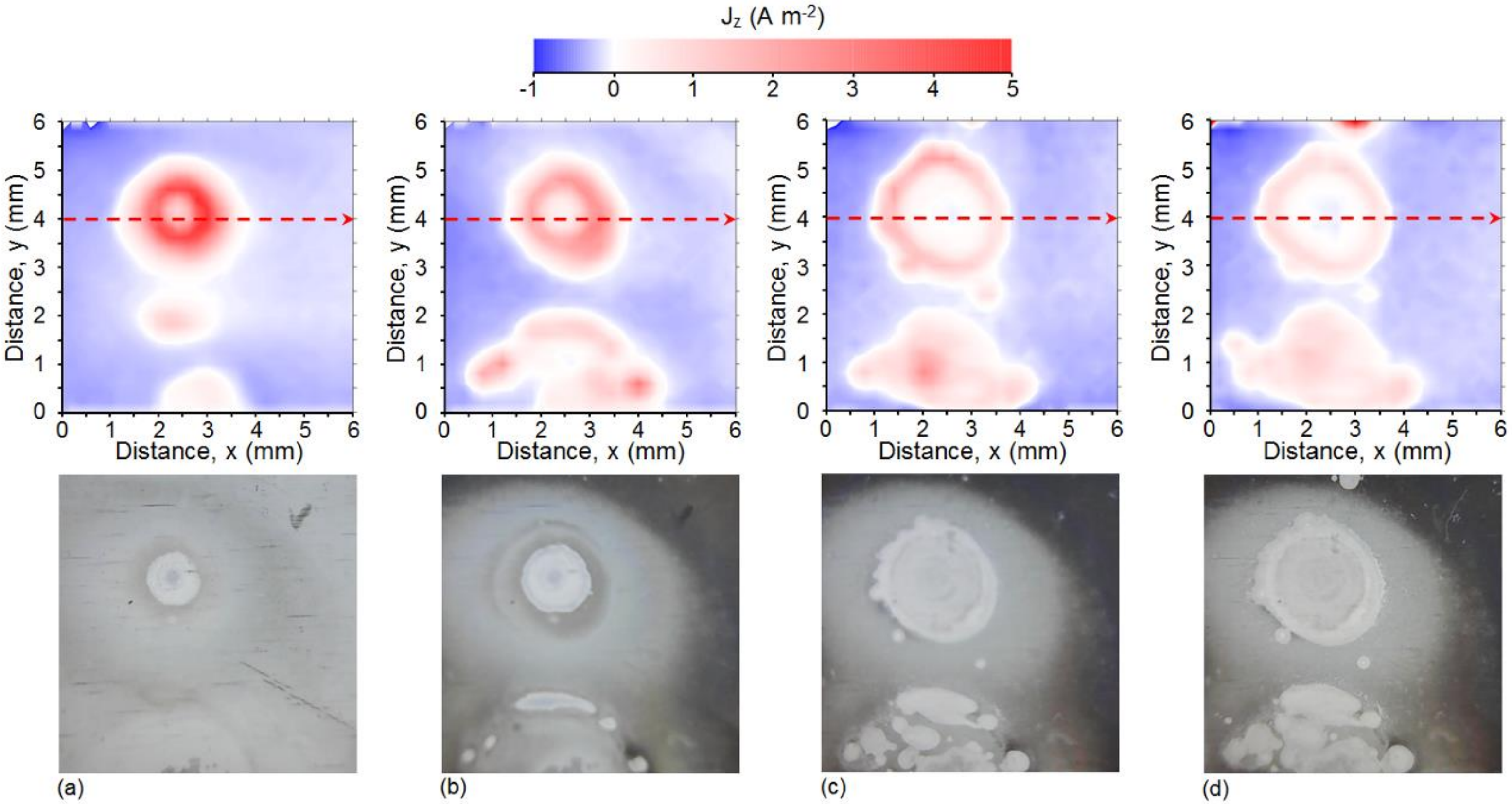

**Figure 5.8:** SVET-derived false colour surface plots showing the distribution of normal current density (top) with associated photographic images (bottom) above freely corroding PVD10 in aerated 0.17 M NaCl at (a) 4, (b) 8, (c) 16 and (d) 24 hours immersion time (a red dashed arrow has been added to indicate the location of the selected SVET profile extracted for **Figure 5.9b**).

**Figure 5.9a** provides further evidence of the limited size and growth of focal anodes on the surface of PVD4 by displaying the current density line profiles identified in **Figure 5.7** for different immersion times. A small drop in current density in the centre of feature 2 indicates possible de-activation. This significantly differs to the nature of the anodic ring on PVD10, shown in **Figure 5.9b** via current density line profiles, identified by **Figure 5.8**, at different immersion times. **Figure 5.9c** demonstrates the larger rate and size of the expanding anodic features on PVD10 compared to PVD4. Between 4 and 24 hours immersion time the diameter of the anodic ring on PVD10 grows by 1.2 mm which is significantly greater than the 0.4 mm growth shown by the anodic event on PVD4 during the same immersion period. This again relates to the fine nanostructure identified on PVD10 (**Figure 3.6b**), in contrast to the coarser discrete structure of PVD4 (**Figure 3.5a**), favours radial spreading of anodic events. This is consistent with recent work by Wint et al. [45] where lateral anodic spreading was shown to be disfavoured on discrete microstructures due to the hindrance of aggressive anodic electrolyte diffusion over the more noble zinc phase. On grain refined specimens, the more noble phases are finer and therefore the electrolyte could easily diffuse over and activate adjacent magnesium-rich phases.

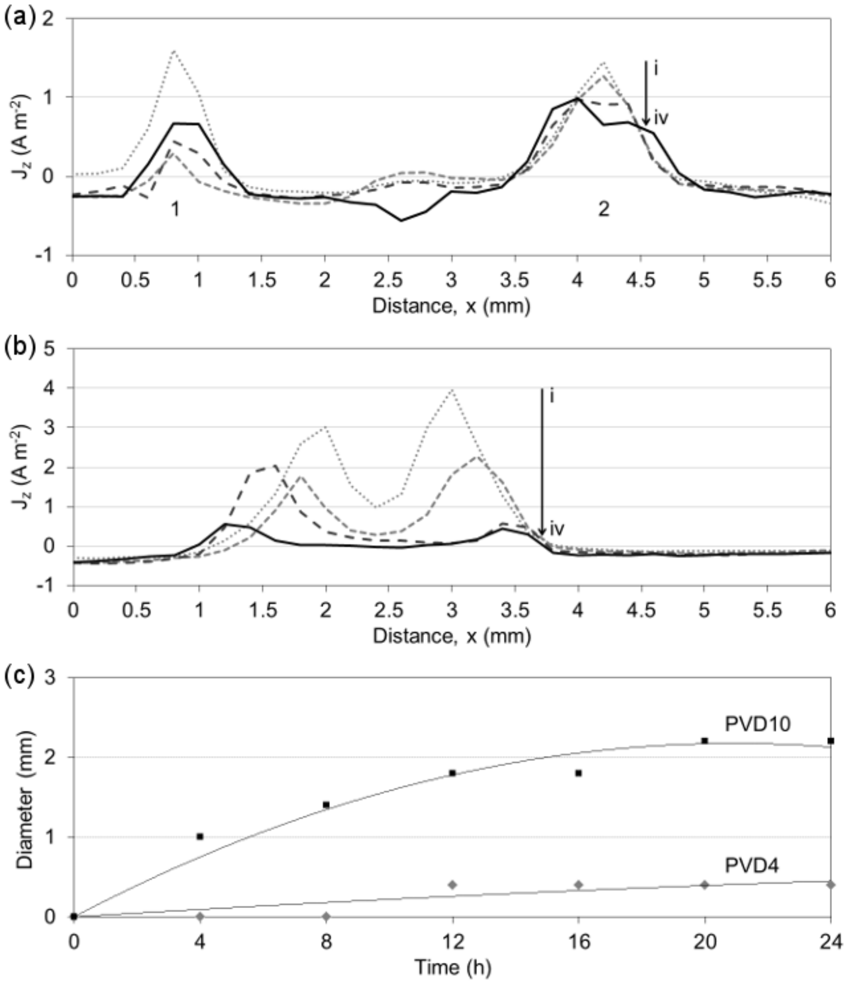

**Figure 5.9:** SVET-derived current density line profiles of (a) PVD4 taken from y = 2.0 mm in **Figure 5.7** and (b) PVD10 taken from y = 4.0 mm in **Figure 5.8** after (i) 4, (ii) 8, (iii) 16 and (iv) 24 hours freely corroding in 0.17 M NaCl. Using the peak anodic values, the diameters of the anodic rings observed on PVD4 and PVD10 are plotted over time in (c).

**Figure 5.9** also emphasises the difference in intensity between the anodic events observed on PVD4 and the anodic ring on PVD10. This suggests a correlation between the intensity and number density of anodic events, which is assumed to be a consequence of the magnesium content. The greater anodic current density of the anodic event on PVD10 measured at 4 hours into the experiment (approximately 5 $A.m^{-2}$) serves as possible evidence for the reduced number of anodic events: the free corrosion potential, $E_{corr}$, will correspondingly drop, in response to the emergence of a significant anodic current, to preserve electroneutrality. This in turn makes it less likely for further anodic events to initiate. This behaviour has previously been reported for the localised corrosion of commercial purity magnesium [8].

**Figure 5.10** shows a series of typical current density distribution maps, along with associated close up photographic images obtained for the highest magnesium composition used in this investigation (PVD20). As with the PVD4 and PVD10 samples, significant black staining is produced in the cathodic regions of the PVD20 surface. The photographic monitoring of the corroding surfaces reveals that the staining is correlated to the magnesium content, as the intensity of the staining was noticeably greater on PVD20 compared to PVD4 and PVD10. Additionally, PVD20 exhibits the characteristic anodic ring expansion shown by PVD10. However, in this case the expansion was significantly limited, and the anodic ring appeared to de-activate toward the final hours of immersion.

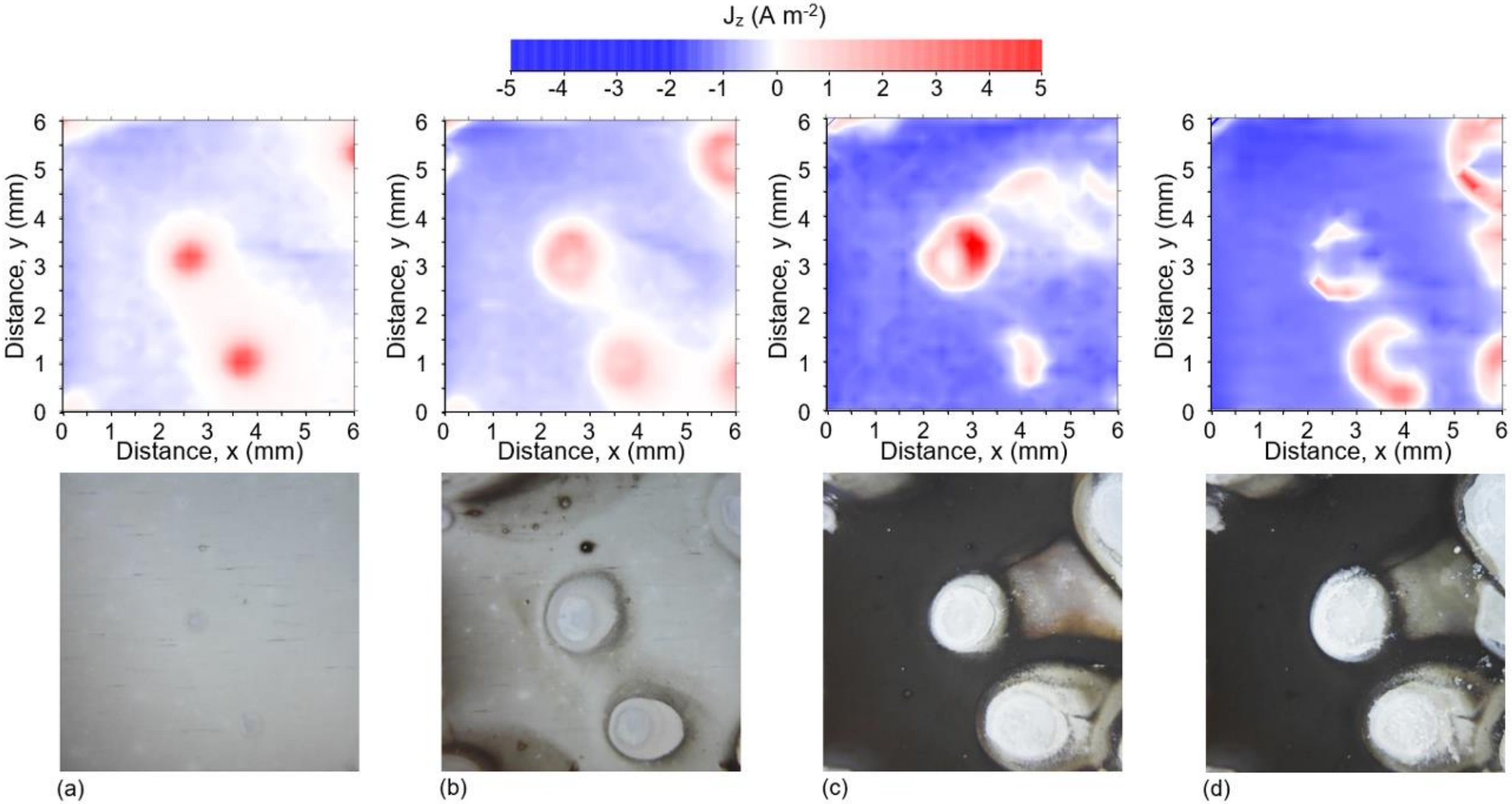

**Figure 5.10:** SVET-derived false colour surface plots showing the distribution of normal current density (top) with associated photographic images (bottom) above freely corroding PVD20 in aerated 0.17 M NaCl at (a) 4, (b) 8, (c) 16 and (d) 24 hours immersion time.

The XRD patterns identified for regions of white corrosion product on all four PVD samples are compared in **Figure 5.11**. The aforementioned phases present in PVD4 were confirmed as zinc and $Mg_2Zn_{11}$; PVD10 appeared to be comprised of these phases also. In contrast, PVD20 appeared to contain zinc and $MgZn_2$. Simonkolleite was identified on all four samples following the 24 hour immersion studies, suggesting a possible link between the formation of this particular corrosion product and the mobility of anodic events observed on ZMA and the PVD coatings.

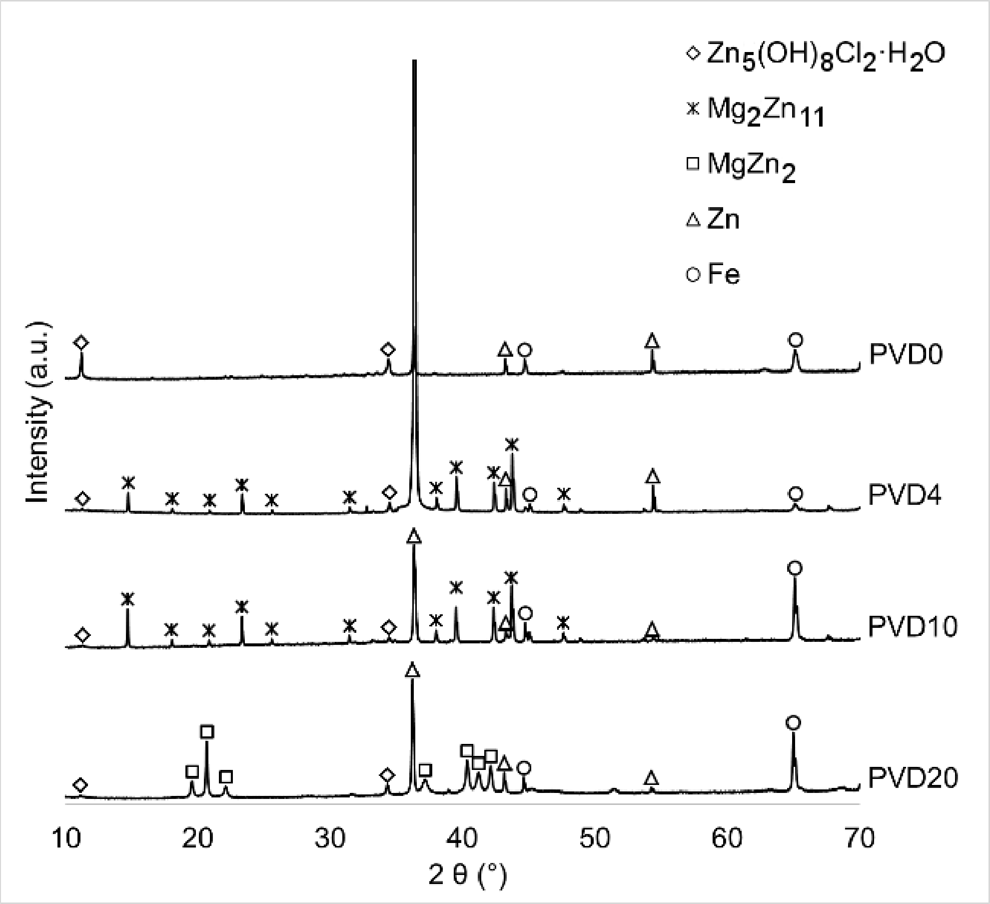

**Figure 5.11:** XRD spectra of the corrosion products visible on the PVD coatings after 24 hours immersion in 0.17 M NaCl.

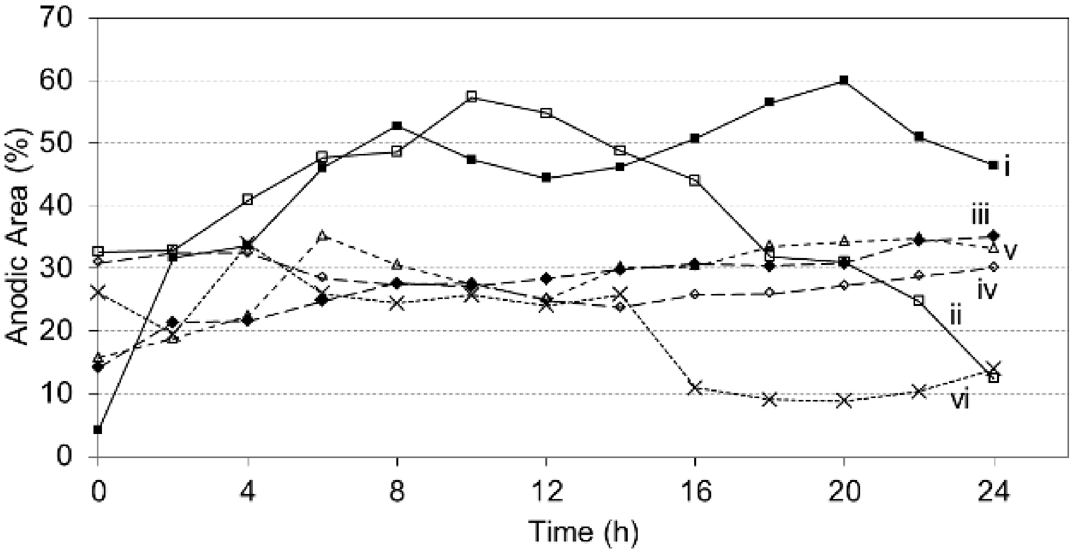

**Figure 5.12:** Percentage area coverage of anodic events, calculated from individual SVET current density maps for (i) HDG, (ii) PVD0, (iii) ZMA, (iv) PVD4, (v) PVD10 and (vi) PVD20 at 2 hour intervals during 24 hour immersion in 0.17 M NaCl solution.

**Figure 5.12** displays the percentage planar coverage of local anodes for all coatings over the period of immersion. The pure zinc coatings, HDG and PVD0, were susceptible to greater anodic coverage. However, as previously addressed, many anodic initiation events and subsequent de-activation caused lateral spreading of the anodic attack, increasing the overall anodic area to a point before reducing again as the uncorroded coating was depleted. The HDG anodic area increased to 50 % and appears to have maintained this area average for the remaining immersion time. The magnesium containing coatings showed more consistent and reduced anodic coverage during immersion. This suggests that the greatest local anode areas are observed in the absence of magnesium, therefore implying that the alloyed magnesium inhibits anodic area growth via the moderation of pH and subsequent stabilisation of simonkolleite over a greater distance across the surface. The PVD20 coating is of significance in this data as it demonstrated a clear drop in anodic coverage after 15 hours immersion, which in turn is directly related to the de-activation observed in **Figure 5.10**.

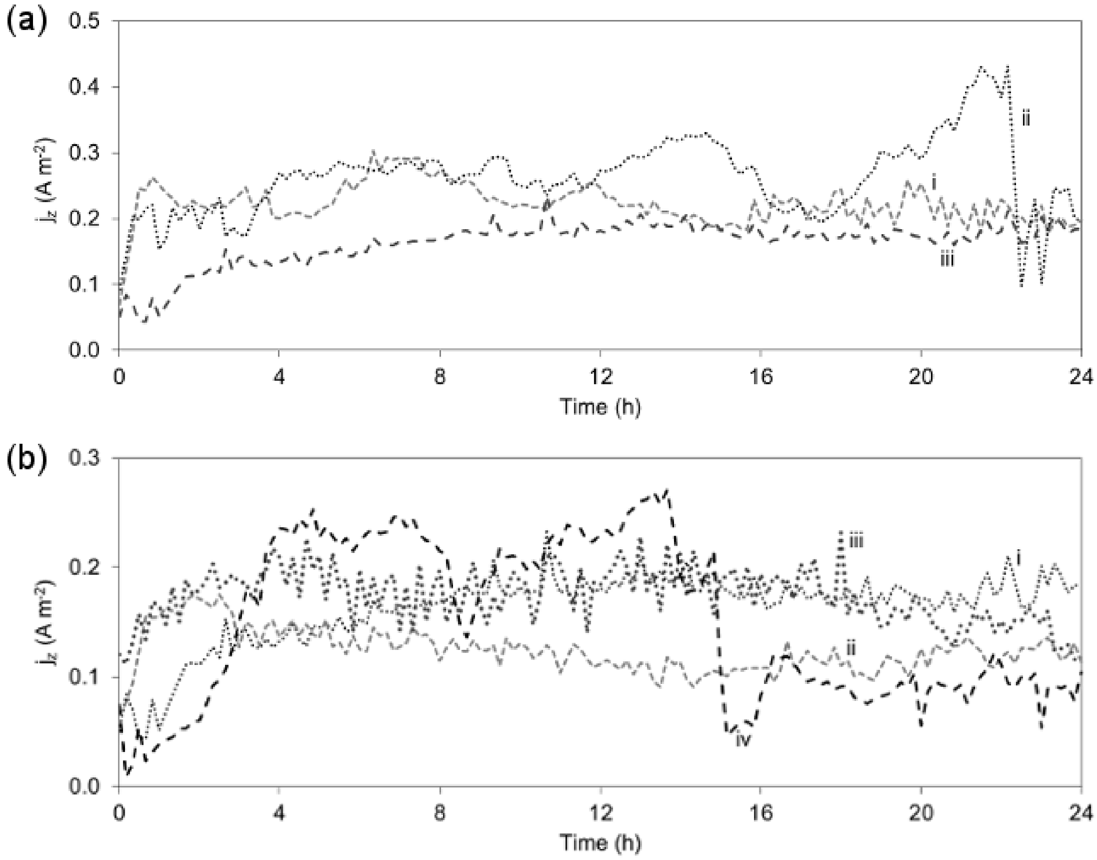

**Figure 5.13:** SVET-derived area-averaged anodic current density plotted against immersion time in 0.17 M NaCl for (a) (i) HDG, (ii) PVD0 and (iii) ZMA. In (b) ZMA is used as a reference, (i), for (ii) PVD4, (iii) PVD10 and (iv) PVD20.

The area-averaged total current density plotted as a function of immersion time is demonstrated in **Figure 5.13**. HDG, PVD0 and ZMA are compared in **Figure 5.13a** to demonstrate a notable influence of magnesium and aluminium in hot dip coatings, as ZMA demonstrated consistently lower integrated anodic current density throughout immersion compared to HDG and PVD0. ZMA was used as a reference in **Figure 5.13b** for the Zn-Mg PVD coatings. PVD4 and PVD10 exhibited similar time-dependent anodic current profiles to ZMA, but the current density values were slightly reduced for PVD4. This suggests that increasing the number of anodic sites may result in a more widespread coverage of corrosion product that then limits the overall anodic activity over the coating surface. The PVD20 current totals increased for the first 4 hours to a level above that of ZMA, before dropping abruptly at 16 hours immersion to values similar to PVD4, suggesting that the increased presence of magnesium in the PVD20 presented more aggressive anodic attack during the staining period where magnesium was de-alloyed from the coating. The drop in anodic current signifies the deactivation of the surface attack, as evident by the maps in **Figure 5.10 c** and **d**.

**Table 5.1:** Average anodic area coverage and total accumulated anodic current density after 24 hours immersion for all coatings.

| **Coating I.D.** | **Average Anodic Area Coverage (%)** | **Total Accumulated Anodic Current Density ($A.m^{-2}$)** |
|---|---|---|
| HDG | 43.9 ± 14 | 38.0 ± 6 |
| PVD0 | 39.0 ± 13 | 36.3 ± 8 |
| ZMA | 27.4 ± 6 | 21.1 ± 4 |
| PVD4 | 28.1 ± 3 | 20.1 ± 3 |
| PVD10 | 28.5 ± 6 | 25.2 ± 3 |
| PVD20 | 19.8 ± 8 | 27.9 ± 5 |

A summary of the key electrochemical characteristics discussed in this work is given in **Table 5.1**. Quantitative analysis of corrosion on all coatings during all 24 hour immersion tests and repeated tests suggests a correlation between magnesium content and anodic current density. A relatively small addition of magnesium to a zinc coating (<4 wt%) appears to restrict anodic attack, however, there exists a critical level of magnesium beyond which the magnesium content hinders corrosion resistance. This may be attributed to the refinement of the phase distribution or the increased reactivity exhibited by magnesium.

## 5.4 Conclusions

The work presented in this chapter has demonstrated the benefits of the combination method of SVET-TLI. Within one 24 hour immersion, the technique is able to simultaneously acquire spatially and temporally resolved electrochemical current density and rate data, with photographic evidence that can corroborate the electrochemical data with mechanistic information. For example, this work has concluded that the staining that occurs on the magnesium-containing zinc PVD coatings originates in net cathodic regions (**Figure 5.7**, **Figure 5.8** and **Figure 5.10**), whilst previous work attributed the staining to the anodic dissolution of magnesium [8, 35,41]. The resolution limitation of the SVET is partially remedied by collecting visual evidence for validation.

It has been shown that the deposition method and subsequent surface morphology of zinc coatings is more influential on the initiation of anodic events as the globular topography exhibited by PVD acts similarly to a fine grain structure. The finer the microstructure, the greater the number of initiation points.

The presence of magnesium and aluminium in ZMA significantly alters the corrosion behaviour that is observed electrochemically and visually. These alloying elements reduced the total anodic current density during 24 hour immersion and it is proposed in this work that this is a result of simonkolleite formation which retards the progression of anodic attack and also de-activates sites altogether. This is further echoed in the results for PVD10 and PVD20; the nanostructure observed for these coatings appears to have no influence over the relatively large anodic events that take place. However, it is proposed that the fine distribution of magnesium within these coatings is the cause for staining at the cathodes because there was a clear correlation between magnesium content and staining intensity.

The PVD coating containing 4 wt% magnesium is of particular interest as it appears that the combination of magnesium content and microstructure formation resulted in the lowest total anodic current density. Further study must be conducted into the exact cause for the improved behaviour.

## 5.5 References

1. T.-Y. Kim, M. Goodenough, Corros. Sci. Technol. 10 (2011) 194–198.
2. H.S. Isaacs, Corros. Sci. 28 (1988) 547–558.
3. H.S. Isaacs, A.J. Aldykiewicz, D. Thierry, T.C. Simpson, Corros. 52 (1996) 163–168.
4. D.A. Worsley, H.N. McMurray, A. Belghazi, Chem. Commun. 36 (1997) 2369–2370.
5. S. Böhm, H.N. McMurray, S.M. Powell, D.A. Worsley, Electrochim. Acta. 45 (2000) 2165–2174.
6. H.N. McMurray, S.M. Powell, D.A. Worsley, Br. Corros. J. 36 (2001) 42–48.
7. R.M. Souto, Y. González-García, A.C. Bastos, A.M. Simões, Corros. Sci. 49 (2007) 4568–4580.
8. G. Williams, H.N. McMurray, Electrochem. Soc. 155 (2008) C340–C349.
9. G. Williams, H.A.L. Dafydd, R. Grace, Electrochim. Acta. 109 (2013) 489–501.
10. B. Łosiewicz, M. Popczyk, M. Szklarska, A. Smołka, P. Osak, Solid State Phenom. 228 (2015) 353–368.
11. A.C. Bastos, M.C. Quevedo, O. V Karavai, M.G.S. Ferreira, J. Electrochem. Soc. 164 (2017) C973–C990.
12. H.S. Isaacs, "Paper 28", in: NACE Corros., New Orleans, (1989) pp. 17–21.
13. R. Hausbrand, M. Stratmann, M. Rohwerder, Steel Res. Int. 74 (2003) 453–458.
14. R. Hausbrand, M. Stratmann, M. Rohwerder, J. Electrochem. Soc. 155 (2008) C369.
15. R. Hausbrand, M. Stratmann, M. Rohwerder, Corros. Sci. 51 (2009) 2107–2114.
16. J. Sullivan, S. Mehraban, J. Elvins, Corros. Sci. 53 (2011) 2208–2215.

17. S.M. Powell, H.N. McMurray, D.A. Worsley, Corrosion. 55 (1999) 1040–1051.

18. C.F. Glover, G. Williams, J. Electrochem. Soc. 164 (2017) C407–C417.

19. K. Ogle, V. Baudu, L. Garrigues, X. Philippe, J. Electrochem. Soc. 147 (2000) 3654.

20. H. Dafydd, D.A. Worsley, H.N. McMurray, Corros. Sci. 47 (2005) 3006–3018.

21. J. Elvins, J.A. Spittle, J.H. Sullivan, D.A. Worsley, Corros. Sci. 50 (2008) 1650–1658.

22. J. Sullivan, C. Weirman, J. Kennedy, D. Penney, Corros. Sci. 52 (2010) 1853–1862.

23. M. Pourbaix, Atlas of electrochemical equilibria in aqueous solutions (English edition), Pergamon Press, Oxford, (1966).

24. M.S.N. Idora, M.M. Rahman, M. Ismail, W.S.W. Nik, Appl. Mech. Mater. 554 (2014) 213–217.

25. A. Sen, M.S.H. Tareq, Sci. Eng. Investig. 5 (2016) 134–137.

26. J. Gerdenitsch, R. Raucher, B. Schmitz, B. Schuhmacher, T. Koll, Influence of segregated tramp elements on the surface of cold-rolled steel sheet with regard to the metallic coating processes and application properties, Brussels, (2002).

27. N. Wint, K. Khan, J.H. Sullivan, H.N. McMurray, J. Electrochem. Soc. 166 (2019) C3028–C3038.

28. E. Zoestbergen, J. van de Langkruis, T.F.J. Maalman, E. Batyrev, Surf. Coatings Technol. 309 (2016) 904–910.

29. J.L. Davies, C.F. Glover, J. van de Langkruis, E. Zoestbergen, G. Williams, Corros. Sci. 100 (2015) 607–618.

30. A.R. Marder, Prog. Mater. Sci. 45 (2000) 191–271.

31. W.R. Osório, C.M. Freire, A. Garcia, Mater. Sci. Eng. A. 402 (2005) 22–32.

32. V. Fournier, P. Marcus, I. Olefjord, Surf. Interface Anal. 34 (2002) 494–497.
33. N.C. Hosking, M.A. Ström, P.H. Shipway, C.D. Rudd, Corros. Sci. 49 (2007) 3669–3695.
34. T. Falk, J. -E. Svensson, L. -G. Johansson, J. Electrochem. Soc. 145 (1998) 39–44.
35. P. Volovitch, T.N.N. Vu, C. Allély, A. Abdel Aal, K. Ogle, Corros. Sci. 53 (2011) 2437–2445.
36. P. Volovitch, C. Allely, K. Ogle, Corros. Sci. 51 (2009) 1251–1262.
37. T. Prosek, D. Persson, J. Stoulil, D. Thierry, Corros. Sci. 86 (2014) 231–238.
38. C. Yao, H. Lv, T. Zhu, W. Zheng, X. Yuan, W. Gao, J. Alloys Compd. 670 (2016) 239–248.
39. J.M. Byun, J.M. Yu, D.K. Kim, T.-Y. Kim, W.-S. Jung, Y. Do Kim, J. Korean Inst. Met. Mater. 51 (2013) 413–419.
40. M. Curioni, Electrochim. Acta. 120 (2014) 284–292.
41. M.E. Straumanis, B.K. Bhatia, J. Electrochem. Soc. 110 (1963) 357–360.
42. J. Światowska, P. Volovitch, K. Ogle, Corros. Sci. 52 (2010) 2372–2378.
43. J. Han, K. Ogle, J. Electrochem. Soc. 164 (2017) C952–C961.
44. J. Sullivan, N. Cooze, C. Gallagher, T. Lewis, T. Prosek, D. Thierry, Faraday Discuss. 180 (2015) 361–379.
45. N. Wint, N. Cooze, J.R. Searle, J.H. Sullivan, G. Williams, H.N. McMurray, G. Luckeneder, C. Riener, J. Electrochem. Soc. 166 (2019) C3147–C3158.

# Chapter 6. Organic coating delamination resistance of PVD Zn-Mg coatings as a function of Mg content and surface treatment

## 6.1 Introduction

PVD zinc magnesium coatings are of particular interest in the automotive industry as a low weight alternative to traditional galvanising [1–3]. Sacrificial zinc coatings in the automotive industry are a single component of a multi-layered paint system, therefore understanding organic coating failure from a defect in the organic layer down to the bare metal, and cut-edges, of galvanised steel is of much interest [4–8]. In particular, the influence of alloying elements in the improvement of disbondment resistance is a natural next step in the optimisation of these coating systems.

There is significant evidence in literature to support the alloying of zinc with magnesium for improved corrosion resistance for bare metal [9–18] as previously explored in chapter 5. Likewise, it has been previously established that the alloying of magnesium in zinc coatings provides a marked improvement to the delamination resistance of applied organic coatings [19–23]. Hausbrand et al. proposed that the intermetallic $MgZn_2$ found in Zn-Mg coatings promoted the formation of stable passive layers which inhibit oxygen reduction, subsequently preventing the progression of cathodic delamination [19]. Further study established the importance of magnitude and direction of a potential gradient setup between a defect and intact paint interface; the reversal in polarity of a potential gradient observed between an intact organic coating on the $MgZn_2$ intermetallic and a defect resulted in the complete hinderance of cathodic delamination and susceptibility to anodic undermining [20]. It was proposed that by adjusting the magnesium content and distribution of formed intermetallics within a zinc coating, it would be possible to create a system with no cathodic driving force and limited susceptibility to anodic attack. Previous work also introduced the benefits of magnesium for improved disbondment resistance of organic layers on PVD zinc coatings, suggesting that an optimum magnesium content exists at approximately 10 wt% [7].

Alkaline degreasing of zinc alloy coated steel is standard industry practice for surface treatment prior to painting [24]; it typically serves the purpose of removing traces of surface contamination to promote better adhesion to the primer coating. Further study into surface treatment of hot dip galvanised steel suggests that more aggressive alkaline treatment can etch the available aluminium surface oxides (for galvanised coatings with a significant aluminium presence), enriching the organic coating interface with zinc and thus improving the surface activity and uniformity prior to painting [25–27].

This work systematically investigates the influence of magnesium content on the mode and rate of delamination of a model organic coating, used in multiple previous works successfully to provide mechanistic information of corrosion driven cathodic disbondment on galvanised steel [4, 6,28–32] and also for anodic undermining on Zn-Mg-Al coatings [33], on the novel Zn-Mg PVD layers. The microstructure and present phases within the novel coatings were elucidated in chapter 3 and can provide potential cause for the delamination behaviour outlined in this work. Additionally, alkaline surface treatment will be explored as a method for tuning the interface between metallic and organic coatings.

## 6.2 Experimental details

### 6.2.1 Materials

In this chapter the PVD coated steel samples listed in **Table 2.1** were studied and compared to the commercially available HDG and ZMA coating strip steel, as received and ethanol rinsed.

### 6.2.2 Methods

All samples were prepared via the Stratmann method described in section 2.5.3 for cathodic delamination inducing SKP experiments, using a model organic coating (15.5% w/w PVB in ethanol) prepared as described in section 2.1.2. Cathodic disbondment was initiated using 0.86 M NaCl. For anodic undermining tests, a 10 mm long artificial defect was scribed into the PVB coated samples using a scalpel such that the steel substrate and zinc alloy coating was exposed to 2 µL of 1 M HCl electrolyte (**Figure 6.1**).

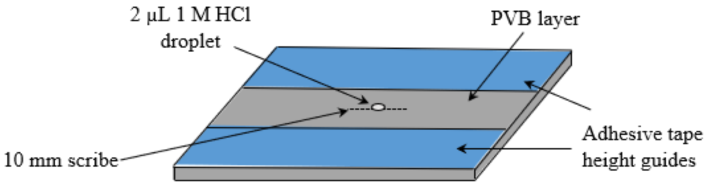

**Figure 6.1:** Diagram of sample design for anodic undermining SKP studies.

For the alkaline surface cleaning study, the samples were dipped in a 70°C pH 13 NaOH solution for a set amount of time, after which they were removed and rinsed with DI water followed by ethanol and dried with nitrogen gas. These samples were then prepared as Stratmann “double-cells” (**Figure 2.5**); data accumulation for time-lapse experiments was doubled by creating two artificial defects on the same coupon. The method for time-lapse capture is described in section 2.5.4.

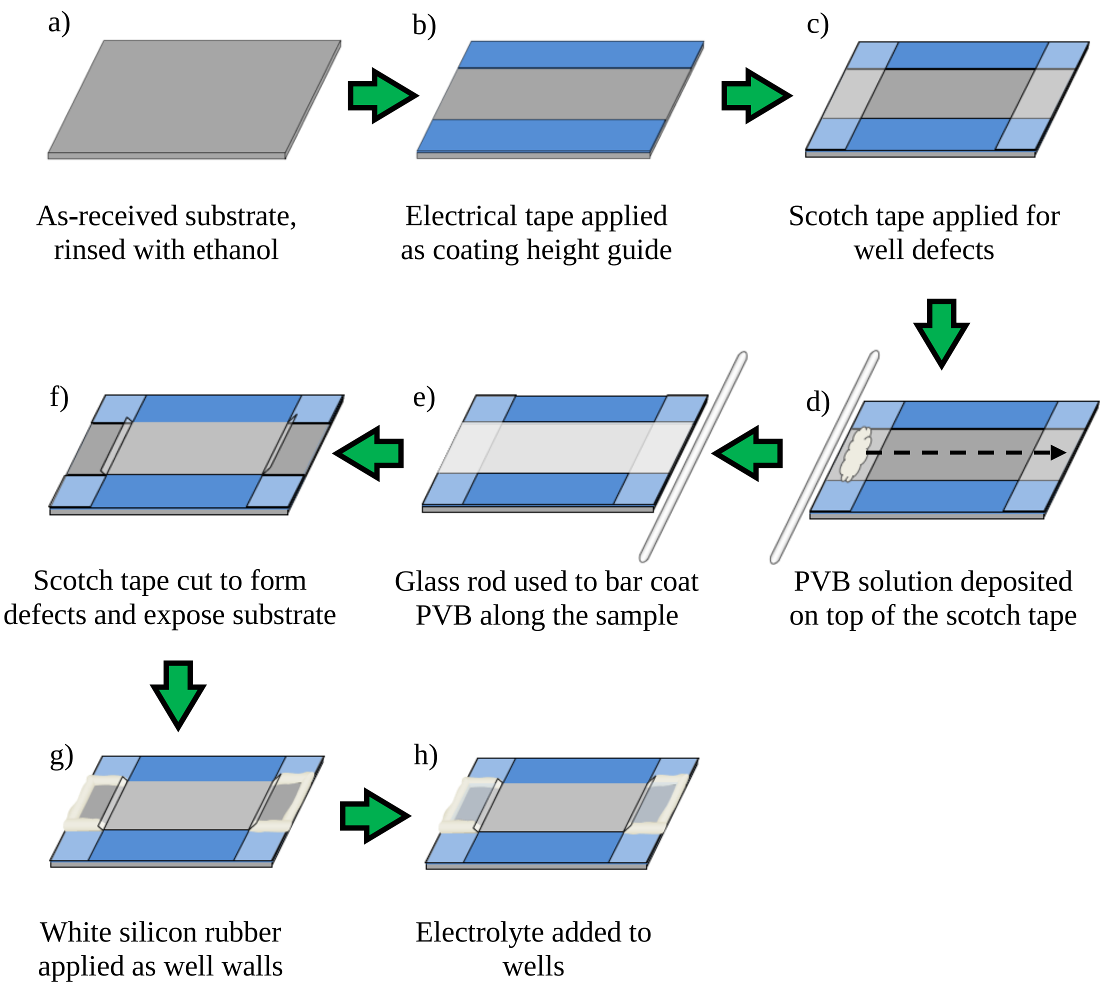

**Figure 6.2:** Method for preparing a Stratmann double-cell sample for time-lapse cathodic delamination studies.

## 6.3 Results and discussion

### *6.3.1 Cathodic delamination*

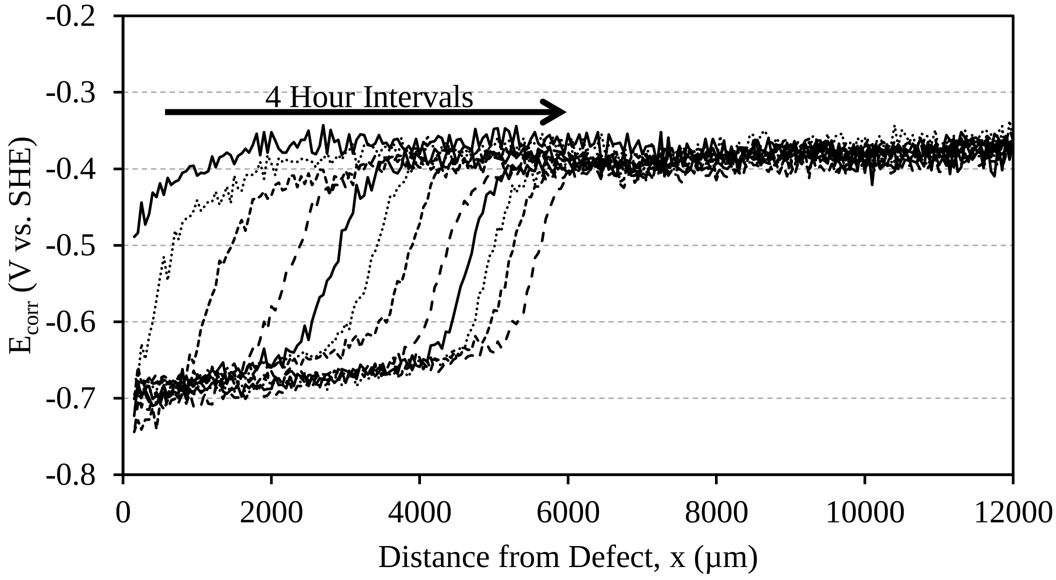

**Figure 6.3:** Typical $E_{corr}$ vs. distance (x) profiles for a HDG layer on strip steel overcoated with model PVB in 95 % R.H over 44 hours. Underfilm corrosion was initiated by 0.86 M NaCl (aq).

The HDG SKP profiles in **Figure 6.3** show that initiation occurred within the first two hours of the experiment. $E_{corr}$ values over the intact PVB coated surface ($E_{intact}$) remained constant at ca. -0.4 V vs. SHE and mostly uniform. It is noted that the values for $E_{intact}$ in this study were different to those found in previous papers with similar experimental parameters; $E_{intact}$ for pure Zn coatings, similar to HDG, has been documented as ca. -0.3 V vs. SHE [4, 6,7,34]. The difference between the values can be attributed to the surface preparation; in previous literature, Zn coatings are typically polished with alumina to remove surface dirt and oxides. In this work, the samples are rinsed with ethanol only prior to PVB application, therefore it is assumed the surface oxides remain and alter $E_{intact}$. This theory supported by the profiles in **Figure 6.4** for a sample of HDG has been prepared using alumina polishing. It is also clear that the rate of PVB disbondment is significantly increased, to ca. 2 mm every two hours, when the oxides are removed. A possible explanation for this is that the thicker layer of amphoteric oxide would require significantly more charge to be passed in the delamination cell in order for it to dissolve and product coating disbondment, thus if equal charge is passed in both experiments, the unpolished sample exhibits much slower delamination. The PVD samples cannot be alumina polished due to their limited coating thickness, thus all coatings have been studied as received with an ethanol rinse only.

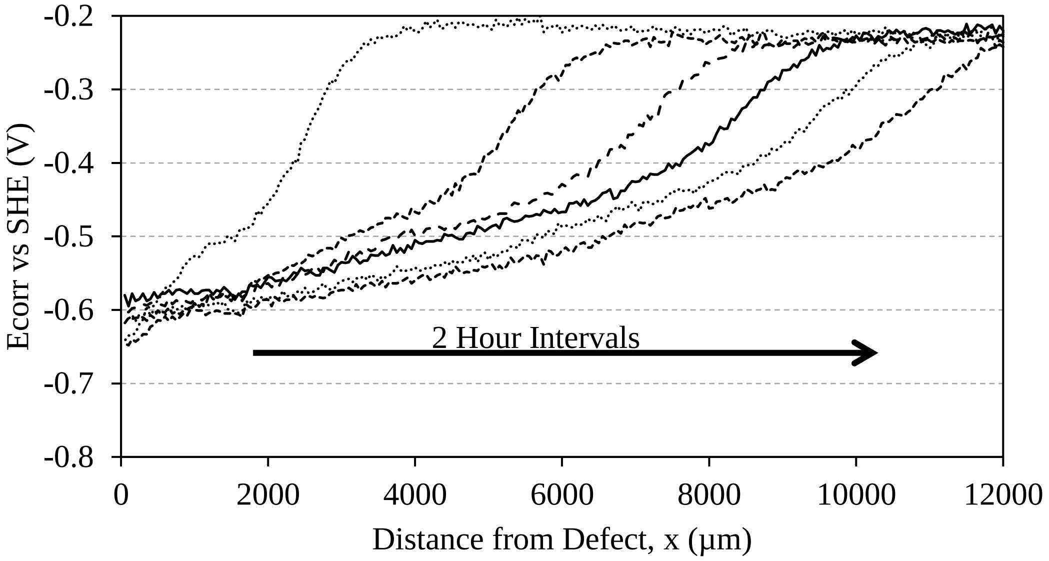

**Figure 6.4:** Typical Ecorr vs. distance (x) profiles for an alumina polished HDG layer on strip steel overcoated with model PVB in 95 % R.H over 12 hours. Underfilm corrosion was initiated by 0.86 M NaCl (aq).

The profiles in **Figure 6.3** show distinctive delamination fronts, separating the $E_{intact}$ region and the $E_{corr}$ bare metal zone (where $E_{corr}$ reflects the potential of HDG freely corroding in the presence of chloride-containing solution). During underfilm corrosion of the cell, the anodic and cathodic processes are linked via a thin layer of electrolyte which ingresses beneath the disbonded PVB and allows the ionic current. The rate of delamination is controlled by the migration of cations ($Na^+$) from the electrolyte well, where they are readily available, to the progressing delamination front. Therefore it has been previously deduced that the sharp potential drop in the SKP profiles is thought to be a result of ion ingression, disbondment of the PVB coating and the oxygen reduction reaction [6].

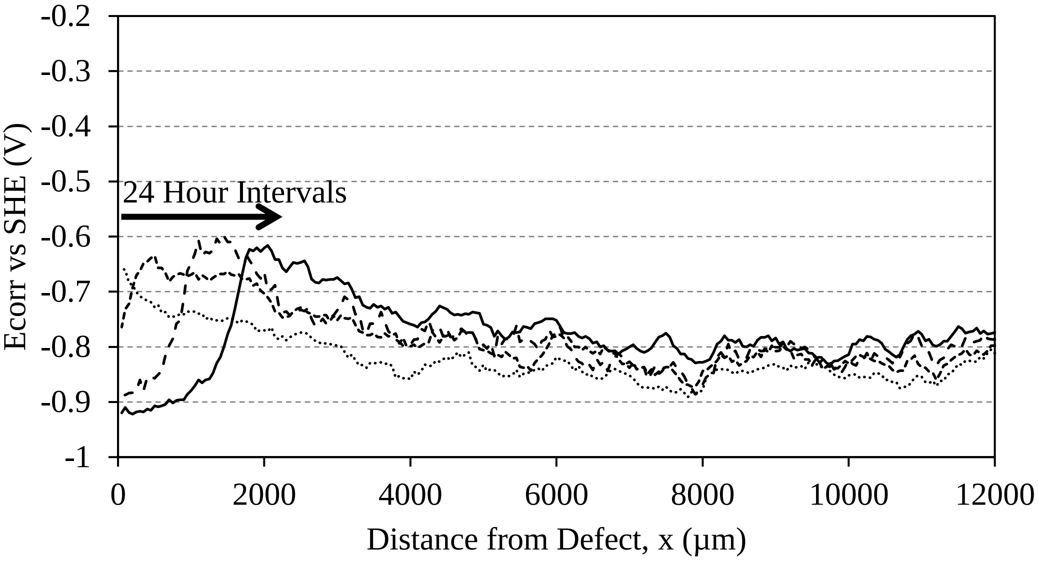

**Figure 6.5:** Typical $E_{corr}$ vs. distance (x) profiles for a ZMA layer on strip steel overcoated with model PVB in 95 % R.H over 96 hours. Underfilm corrosion was initiated by 0.86 M NaCl (aq).

The presence of magnesium and aluminium in the ZMA coating significantly increased the initiation time and rate of disbondment (0.6 mm every 24 hours), as shown in **Figure 6.5**. There is a well-defined front separating the $E_{intact}$ region, which has a mean value of -0.83 V vs. SHE (0.33 V lower than the $E_{intact}$ for HDG), and the bare metal zone which appears to have potentials approaching the open circuit potential (OCP) expected for ZMA coatings [18]. The similarity between $E_{intact}$ and $E_{corr}$, attributed to the alloying aluminium and magnesium, reduced the driving force for cathodic disbondment significantly, as previously seen by Hausbrand et al. when studying $MgZn_2$ [19]. Zn-Mg-Al coatings and Zn-MG intermetallics have previously been shown to resist cathodic delamination [19,20, 22,35] and recently been explored in their susceptibility for filiform corrosion (FFC) [33]. The SKP profiles shown in **Figure 6.5** do not correlate with those seen in work by Wint et al., therefore it is presumed that in this work, owing to the omission of surface polishing, the prevailing mechanism is cathodic disbondment, albeit at a much reduced rate compared to HDG.

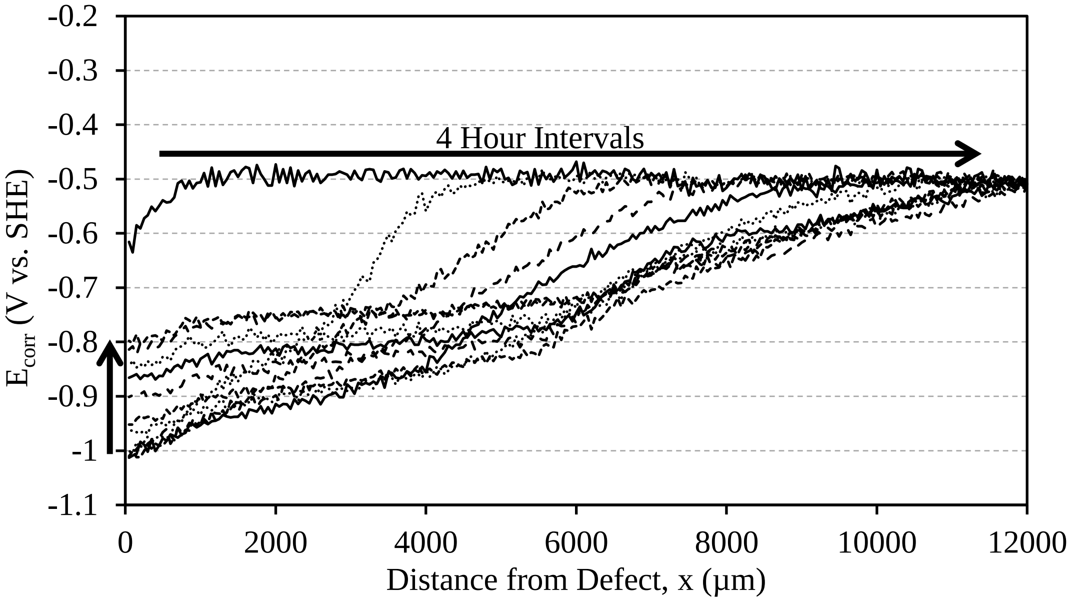

**Figure 6.6:** Typical $E_{corr}$ vs. distance (x) profiles for a PVD0 layer on strip steel overcoated with model PVB in 95 % R.H over 44 hours. Underfilm corrosion was initiated by 0.86 M NaCl (aq).

The $E_{corr}$ vs. distance profiles for PVD0 in **Figure 6.6** show an average $E_{intact}$ of -0.5 V vs. SHE and sloped potential drops to the disbonded zone. During cathodic delamination a local cathode is created by the ORR in the vicinity of the delamination front, which is the cause for coating disbondment. The anodic dissolution of zinc is restricted to the Stratmann well and exposed interface between the metallic coating and PVB layer (the artificial defect). The anodic and cathodic reactions are connected by ionic transport through the ingressed underfilm electrolyte, which causes a potential gradient between the defect and the delamination front. The profiles for PVD0 display a much shallower delamination front gradient compared to HDG, which indicates greater ingress of cations (here $Na^+$) prior to actual delamination for PVD0. This could be explained by the surface morphology of PVD, previously found to have a mean surface roughness ($S_a$) four times lower than HDG (chapter 3), providing a less turbulent ionic pathway. The rate of delamination is high at ca. 1 mm every four hours, with an initial rapid disbondment of 3 mm in the first four hours. The 44 hour profile was compared with a photographic image captured of the sample surface in **Figure 6.7** this establishes the correlation between visible delamination and the SKP-derived data. The visible delamination (identified as a darker/tarnished region on the metallic surface caused by the increased alkalinity of the underfilm electrolyte due to the ORR) appears to stop at approximately 5000 µm, however the SKP data profile shows evidence of further ion ingress beneath the “intact” region.

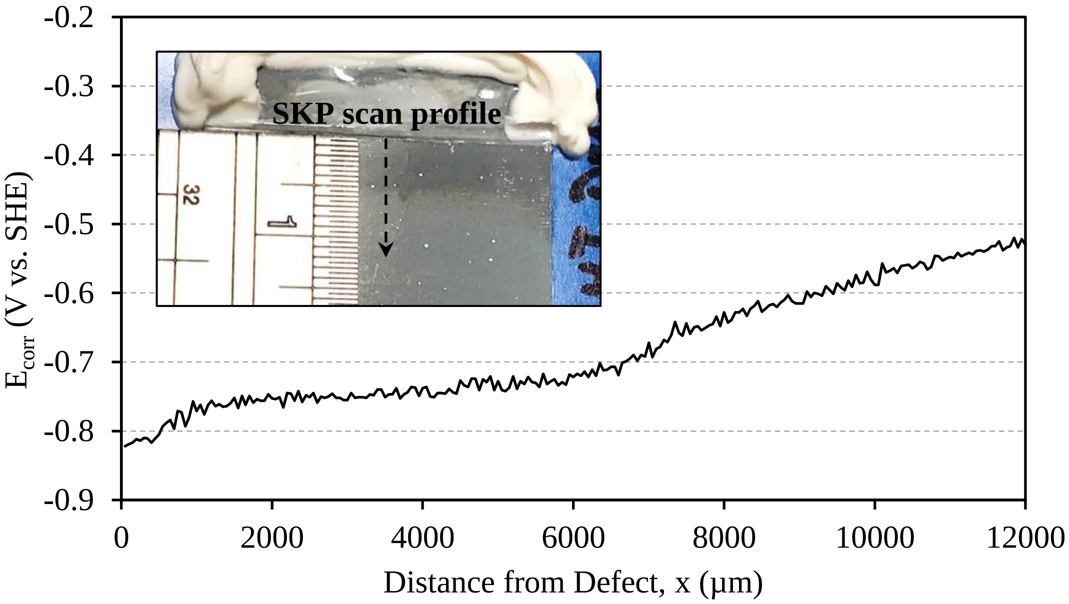

**Figure 6.7:** $E_{corr}$ vs. distance (x) profile at 44 hours for PVD0 comparison with a surface photograph taken immediately after the scan.

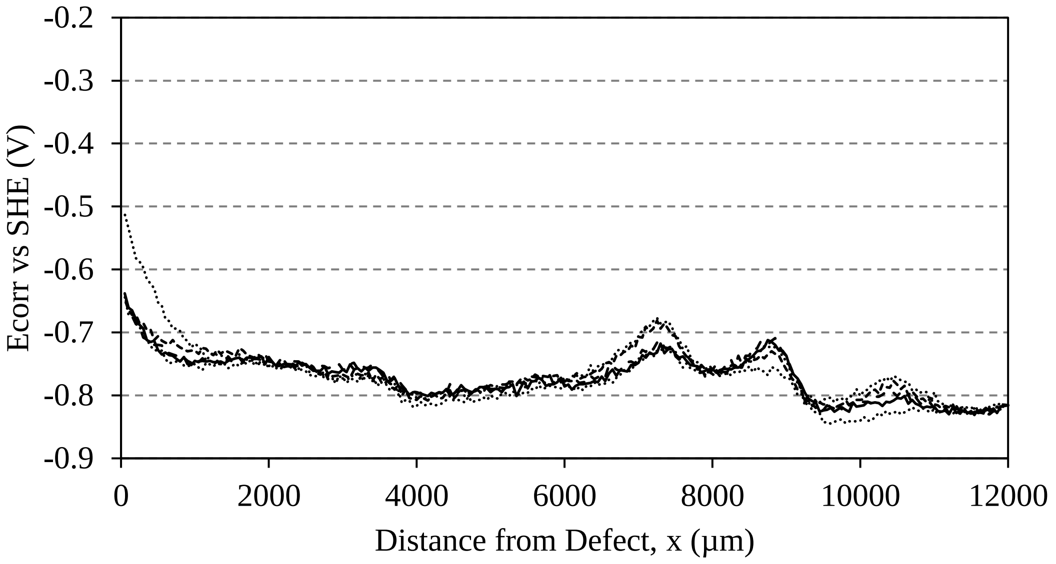

**Figure 6.8:** Typical $E_{corr}$ vs. distance (x) profiles for a PVD4 layer on strip steel overcoated with model PVB in 95 % R.H over 72 hours. Underfilm corrosion was initiated by 0.86 M NaCl (aq).

The addition of 4 wt% Mg to the PVD coating resulted in a depression of the average $E_{intact}$ value by 0.35 V to ca. -0.75 V vs. SHE, as shown in **Figure 6.8**. There is also no evidence of cathodic delamination susceptibility for PVD4, which was supported by a post-experiment physical examination which confirmed the PVB coating was still adhered to the PVD Zn-Mg layer. This is possibly due to the similarity between the intact potential and the OCP for Zn, which has been previously observed by Hausbrand et al. when studying the delamination behaviour on the $MgZn_2$ intermetallic [19]. It is also possible that the segregation of the Zn and $Mg_2Zn_{11}$ phases observed in chapter 3 (**Figure 3.5**) prevents the formation of a stable delamination front and the confinement of Mg to the $Mg_2Zn_{11}$ phase prevents the underfilm anodic activity. It is important to note that the results seen in this work disagree with Davies et al. study on a ~5 wt% Mg Zn PVD coatings [7]; although the PVD coating in that work was also produced using the EMELY line at Tata Steel IJmuiden, they were deposited using a wire-fed mechanism as opposed to the crucible melt method use for the samples studied in this thesis.

It can be assumed that the phase distribution in the wire-fed samples was significantly finer, therefore a continuous cathodic front was able to stabilise and propagate through the intact region. Conversely, it can be postulated that the discontinuous phase distribution in PVD4 observed in chapter 3 may have served to disrupt the formation of the delamination front, similar to the mechanism described in the work by Wint et al. [36].

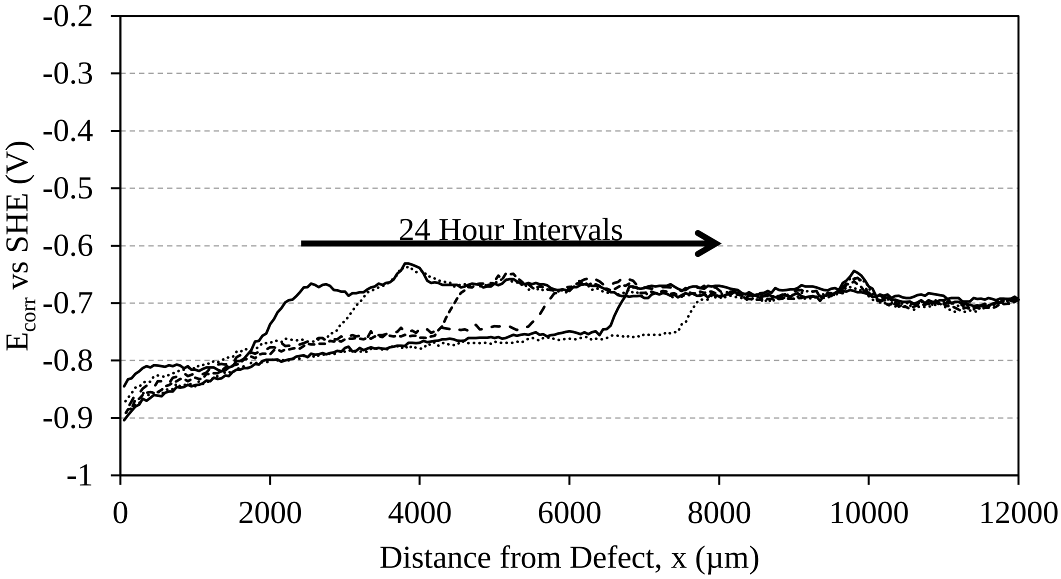

**Figure 6.9:** Typical $E_{corr}$ vs. distance (x) profiles for a PVD10 layer on strip steel overcoated with model PVB in 95 % R.H over 144 hours. Underfilm corrosion was initiated by 0.86 M NaCl (aq).

The potential vs. distance profiles for PVD10 (**Figure 6.9**) show an average intact potential value of -0.68 V vs SHE, which is 0.07 V different from the potential of the disbonded region. The increase in Mg content has therefore depressed the intact potential but not to the same extent as PVD4, despite the increased magnesium content.

The rate at which the delamination front progressed is substantially lower than the PVD0 coating (1.2 mm every 24 hours), which is understood to be a result of the reduced potential difference between the intact and disbonded regions.

Similarly to PVD4, the PVD20 profiles in **Figure 6.10** show no evidence of cathodic disbondment and a significantly depressed intact potential (ca. -0.9 V vs. SHE). This was expected and supported by the previous work by Davies et al. [7].

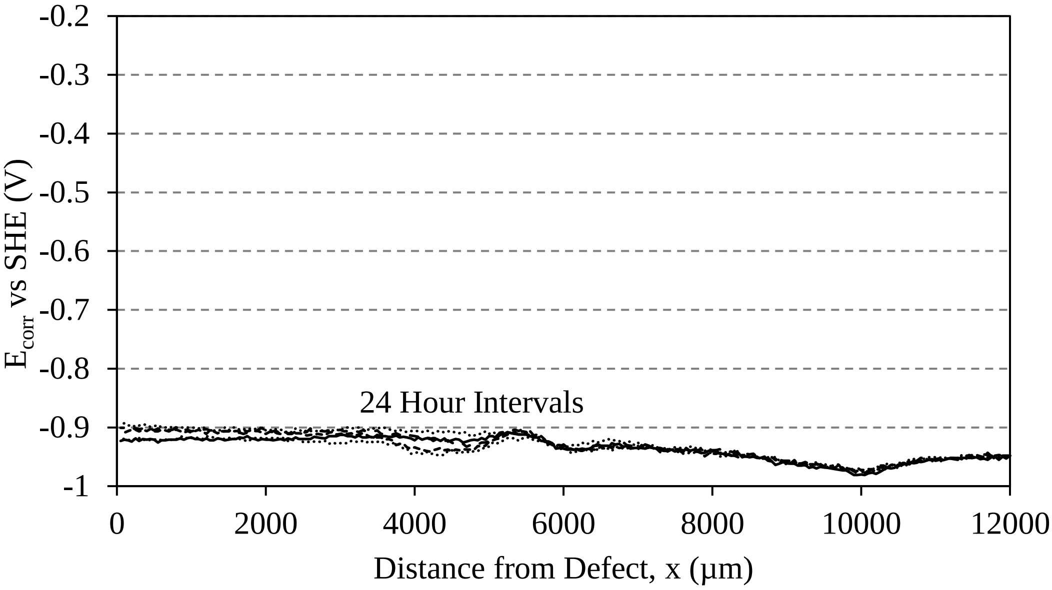

**Figure 6.10:** Typical $E_{corr}$ vs. distance (x) profiles for a PVD20 layer on strip steel overcoated with model PVB in 95 % R.H over 72 hours. Underfilm corrosion was initiated by 0.86 M NaCl (aq).

shows that the coatings which exhibited clear cathodic delamination (HDG, HDG polished, PVD0 and PVD10) progressed under parabolic kinetics, which suggests the rate controlling step is ion migration through the underfilm electrolyte as previously observed [37]. As the delamination front migrates further from the electrolyte well, the mass transport length for cations becomes longer and thus the rate of disbondment decreases [6]. Additionally, the figure shows a clear ranking for the coatings; the polished HDG coating delaminated at a significantly higher rate than the unpolished

HDG, PVD10 delaminated at a much lower rate than both PVD0 and HDG. Interestingly, in the first 20 hours PVD0 delaminated at a rate greater than HDG, however beyond 20 hours the rate dropped significantly, believed to be a result of simonkolleite deposition (chapter 5) which is less facilitative of the ORR. The susceptibility of HDG and PVD0 to cathodic delamination shown in this SKP work is supported by the steep cathodic branches shown in the potentiodynamic data in chapter 4 (**Figure 4.8**), indicating the facilitation of the ORR on the zinc surfaces. Likewise, the shallow cathodic branches in **Figure 4.8** for ZMA, PVD4 and PVD20 correlate with the resistance to cathodic disbondment as they indicate poor oxygen cathodes. PVD10 was also found to be a poor oxygen cathode, however the SKP data shows long term cathodic delamination.

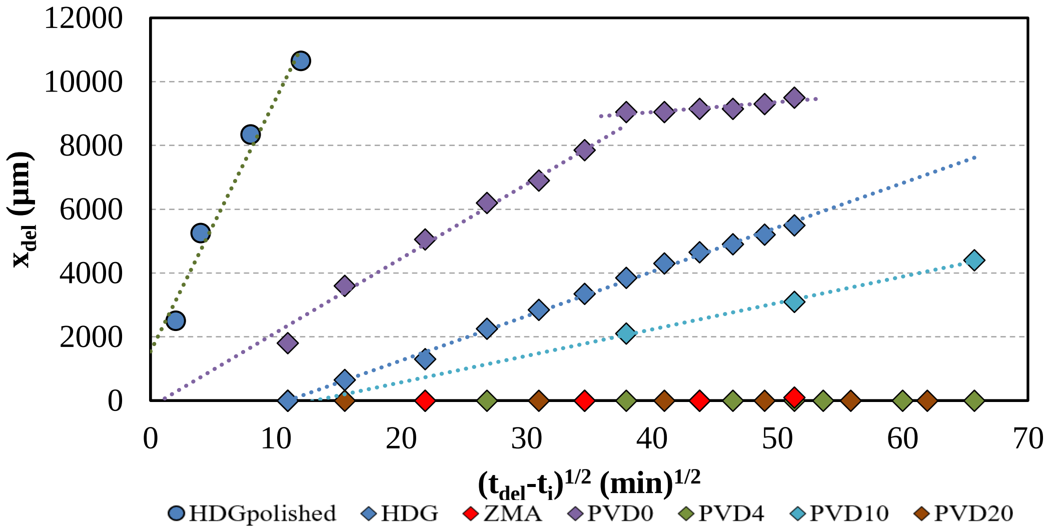

**Figure 6.11:** Plots of delamination distance ($x_{del}$) versus $(t_{del}-t_i)^{1/2}$ for all samples overcoated with model PVB in 95% R.H.. Underfilm corrosion was initiated by 0.86 M NaCl (aq).

### *6.3.2 Anodic delamination*

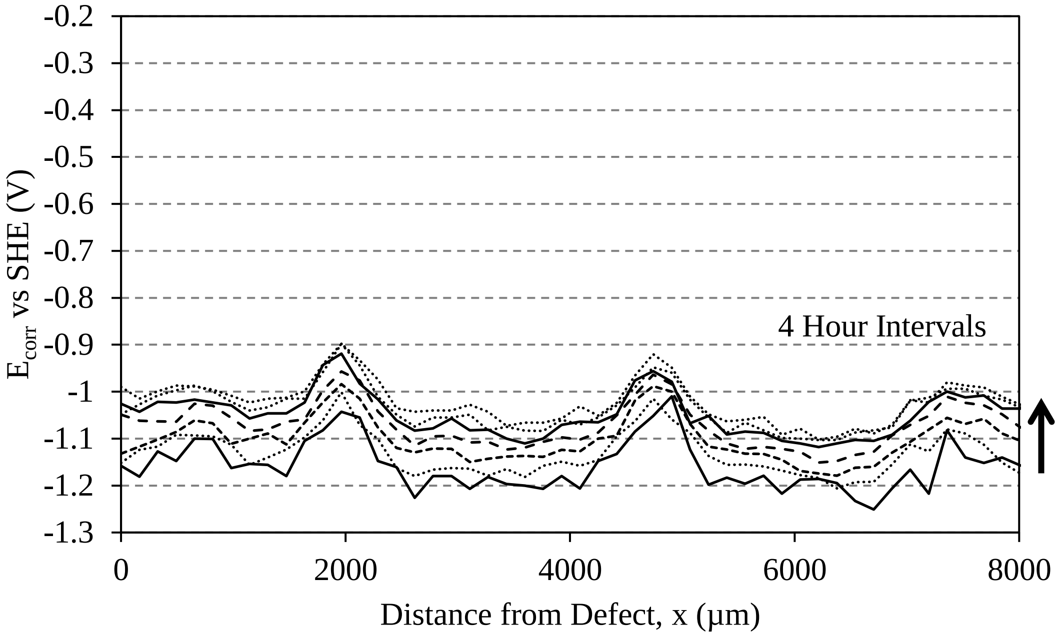

**Figure 6.12:** Typical $E_{corr}$ vs. distance (x) profiles for a PVD4 layer on strip steel overcoated with model PVB in 95 % R.H. over 24 hours. Underfilm corrosion was initiated by 1 M HCl (aq).

1 µL of 1 M HCl was used to initiate an anodic response beneath the organic coating, which has previously been used as a technique to study filiform corrosion on magnesium alloys [33,38,39] and anodic undermining for organic layers on PVD aluminium alloy metallic coatings [40]. PVD0 did not show any evidence of anodic undermining during a time-lapse anodic experiment and is therefore not included in this section. PVD4 also did not exhibit a predisposition toward anodic undermining (**Figure 6.12**), although a consistent rise in the intact potential (ca. -1.2 V to -1.0 V vs. SHE) along the scan profile over the 24 hours can be tentatively attributed to the formation of oxides over time at the PVD-PVB interface, as a result of oxygen permeation through the coating. This was not seen on the Stratmann cell variants, possibly due to oxygen more readily diffusing through the well to the defect.

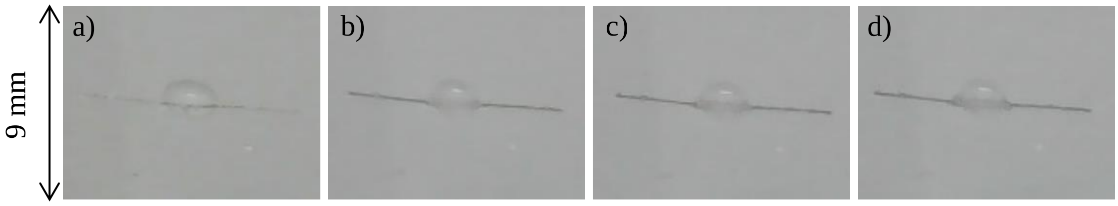

**Figure 6.13:** Photographic images of the scribe defect on PVD4 at a) 0, b) 24, c) 48 and d) 72 hours into an anodic undermining study, taken in-situ. 2 µL of 1 M HCl (aq) was applied to the centre of the defect. 95 % R.H. was maintained.

Alternatively, the initiating media in the anodic study was HCl which, although diluted, can be volatile and cause atmospheric corrosion of a normally intact PVB coated surface when gaseous HCl permeates through the organic layer. Photographic images captured over 72 hours (**Figure 6.13**), and a subsequent physical adhesion inspection, confirm resistance to the anodic undermining delamination mechanism on PVD4. PVD20 SKP scans given in **Figure 6.14** show the progression of an active anodic zone

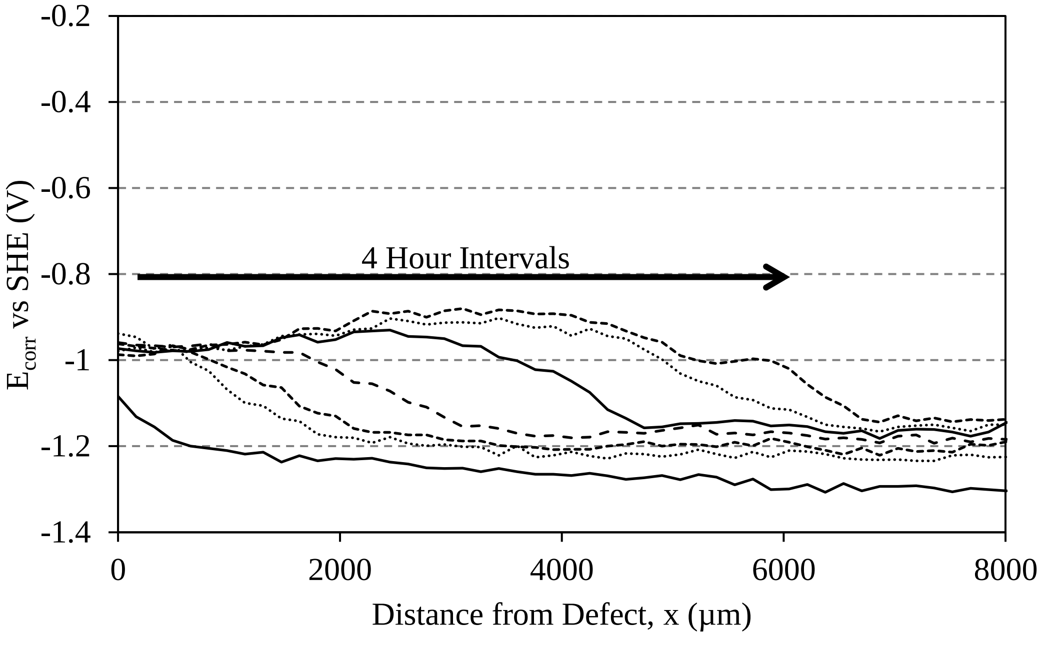

**Figure 6.14:** Typical $E_{corr}$ vs. distance (x) profiles for a PVD20 layer on strip steel overcoated with model PVB in 95 % R.H. over 24 hours. Underfilm corrosion was initiated by 1 M HCl (aq).

adjacent to the delamination front between -0.9 V and -1.0 V vs. SHE. The intact region remained more negative compared to the delaminated zone and, similar to PVD4, showed a gradual increase from ca. -1.3 V to -1.1 V vs. SHE. It is understood that a more negative intact region, compared to the delaminated zone, is caused by an enrichment of the PVB-PVD interface by Mg oxides [19,20,41]. The $E_{corr}$ value in the disbonded region is relatively similar to $E_{intact}$, therefore it is difficult to resolve the precise location of the delamination front. However, it can be said that the more positive value of $E_{corr}$ corresponds to freely corroding magnesium, thus can be attributed to the preferential de-alloying of magnesium from $MgZn_2$. This is further evident in **Figure** 6.15 as the characteristic black staining occurred visibly under the organic layer.

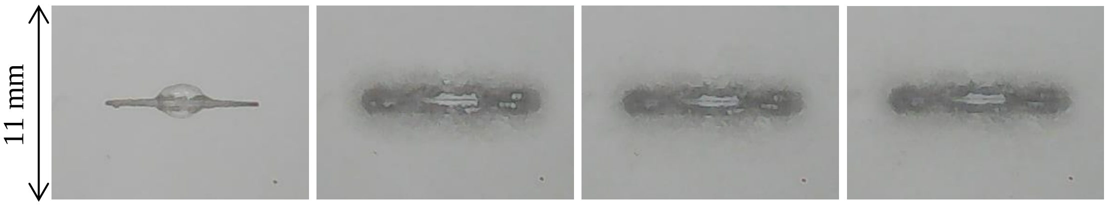

**Figure 6.15**: Photographic images of the scribe defect on PVD20 at a) 0, b) 24, c) 48 and d) 72 hours into an anodic undermining study, taken in-situ. 2 µL of 1 M HCl (aq) was applied to the centre of the defect. 95 % R.H. was maintained.

### *6.3.3 Alkaline cleaning*

Photographic monitoring of the HDG samples in **Figure 6.16** indicated a significant increase in delamination rate as a result of alkaline surface treatment. This suggests that, whilst the activation of the surface via alkaline degreasing is beneficial in terms of surface activity [27] for paint application, the metallic-organic interface becomes more facilitative of cathodic delamination.

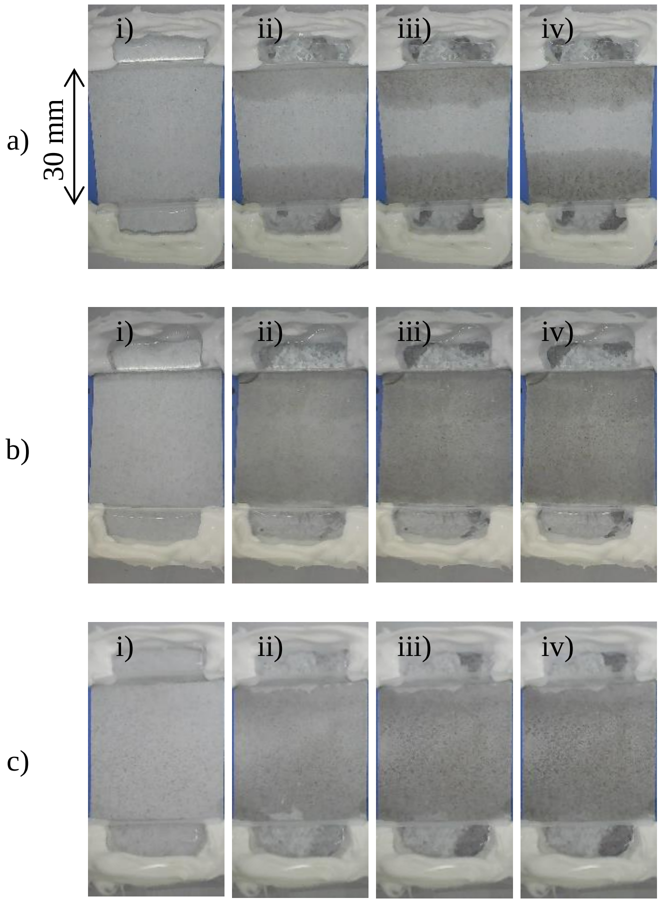

**Figure 6.16:** Photographic images of the HDG Stratmann double-cells in-situ: a) control, b) 1 min pH 13 dip clean and c) 2 min pH 13 dip clean taken at i) 0, ii) 24, iii) 48 and iv) 72 hours for each. Underfilm corrosion was initiated by 0.86 M NaCl (aq). 95 % R.H. was maintained.

Likewise, PVD0 appeared to become more susceptible to cathodic delamination as a result of the alkaline degreasing treatment (**Figure 6.17**) as a function of cleaning duration.

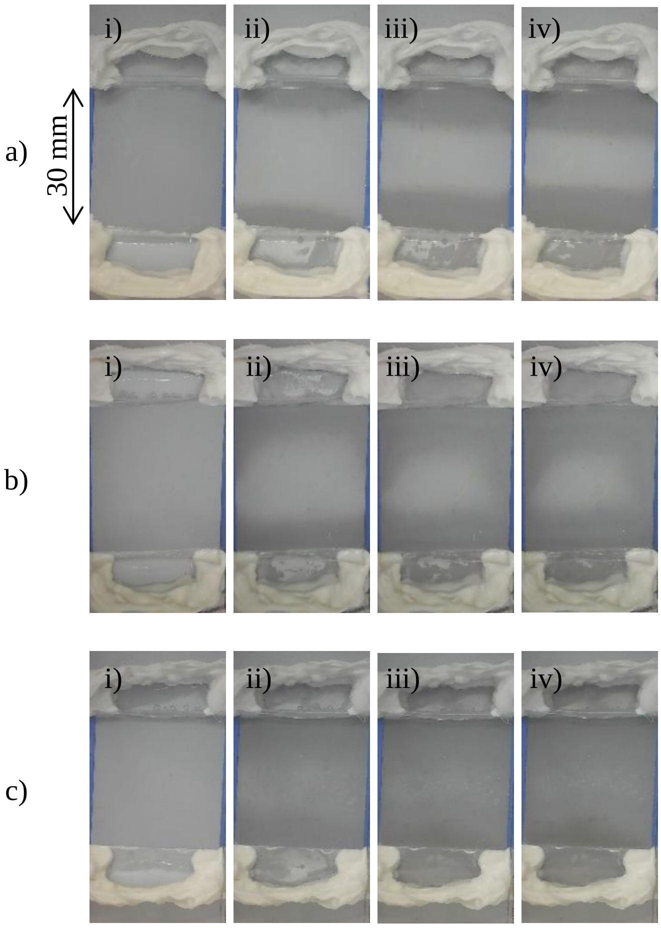

**Figure 6.17:** Photographic images of the PVD0 Stratmann double-cells in-situ: a) control, b) 1 min pH 13 dip clean and c) 2 min pH 13 dip clean taken at i) 0, ii) 24, iii) 48 and iv) 72 hours for each. Underfilm corrosion was initiated by 0.86 M NaCl (aq). 95 % R.H was maintained.

**Figure 6.18** shows evidence that a 2 minute alkaline degreasing treatment is beneficial for the PVD10 coating system. Moreover, the 1 minute treatment gives indication of a change in delamination mechanism as a speckled pattern was observed in the delaminated region. Black staining is associated with anodic attack of magnesium [42]; therefore, it can be tentatively assumed that the activation of the surface by alkaline treatment etched away the zinc present in the coating, leaving the surface enriched in magnesium. This enrichment shifted the mechanism of disbondment for PVD10 from cathodic to anodic, as indicated by the dark filiform-like threads originating from the defect region.

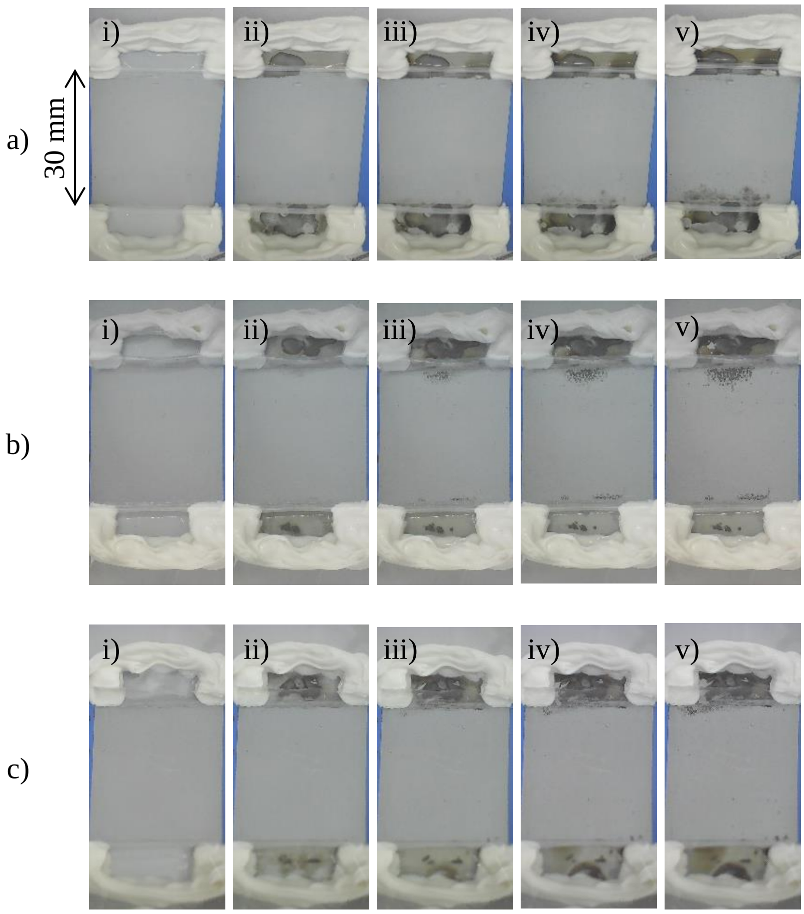

**Figure 6.18:** Photographic images of the PVD10 Stratmann double-cells in-situ: a) control, b) 1 min pH 13 dip clean and c) 2 min pH 13 dip clean taken at i) 0, ii) 24, iii) 48, iv) 72 and v) 96 hours for each. Underfilm corrosion was initiated by 0.86 M NaCl (aq). 95 % R.H.

## 6.4 Conclusions

The evaluation of commercial galvanised coating and the novel PVD coatings in this work has provided several key conclusions regarding the influence of magnesium content, microstructure and surface preparation:

- Surface abrasion (standard SKP practice) has a significant effect on delamination response: as-received, the PVB coated HDG sample underwent cathodic delamination at a rate of ca. 0.5 mm per 2 hours, conversely the alumina prepared HDG sample coated with PVB delaminated at a rate of 2 mm per 2 hours.

- Previous literature identified 10 wt% as an optimum magnesium content in PVD Zn-Mg novel coatings. The evidence in this work confirms that PVD10 is susceptible to cathodic delamination, although at a significantly reduced rate compared to PVD0 and HDG.
- PVD4 has been identified as resistant to cathodic delamination and anodic undermining failure mechanisms, as a combined result of magnesium content and microstructure.
- Alkaline degreasing in this work had a negative effect on the delamination resistance of HDG and PVD0, however it appeared to further reduce the cathodic delamination rate of PVD10.

## 6.5 References

1. B. Navinšek, P. Panjan, I. Milošev, Surf. Coatings Technol. 116–119 (1999) 476–487.
2. L. Guzman, G.K. Wolf, G.M. Davies, Surf. Coatings Technol. 174–175 (2003) 665–670.
3. E. Zoestbergen, J. van de Langkruis, T.F.J. Maalman, E. Batyrev, Surf. Coatings Technol. 309 (2016) 904–910.
4. G. Williams, H.N. McMurray, J. Electrochem. Soc. 148 (2001) B377–B385.
5. D.A. Worsley, H.N. McMurray, J.H. Sullivan, I.P. Williams, Corrosion. 60 (2004) 437–447.
6. G. Williams, H.N. McMurray, A. Bennett, Mater. Corros. 65 (2014) 401–409.
7. J.L.L. Davies, C.F.F. Glover, J. van de Langkruis, E. Zoestbergen, G. Williams, Corros. Sci. 100 (2015) 607–618.
8. T. Prosek, A. Nazarov, H.B. Xue, S. Lamaka, D. Thierry, Prog. Org. Coatings. 99 (2016) 356–364.
9. K. Nishimura, H. Shindo, H. Nomura, K. Katoh, Tetsu-to-Hagane. 89 (2003) 174–179.
10. N.C. Hosking, M.A. Ström, P.H. Shipway, C.D. Rudd, Corros. Sci. 49 (2007) 3669–3695.
11. S. Schuerz, M. Fleischanderl, G.H. Luckeneder, K. Preis, T. Haunschmied, G. Mori, A.C. Kneissl, Corros. Sci. 51 (2009) 2355–2363.
12. T. Prosek, N. Larché, M. Vlot, F. Goodwin, D. Thierry, Mater. Corros. 61 (2010) 412–420.

13. P. Volovitch, T.N.N. Vu, C. Allély, A. Abdel Aal, K. Ogle, Corros. Sci. 53 (2011) 2437–2445.

14. D. Persson, D. Thierry, N. LeBozec, T. Prosek, Corros. Sci. 72 (2013) 54–63.

15. R. Krieg, A. Vimalanandan, M. Rohwerder, J. Electrochem. Soc. 161 (2014) C156–C161.

16. T. Lostak, A. Maljusch, B. Klink, S. Krebs, M. Kimpel, J. Flock, S. Schulz, W. Schuhmann, Electrochim. Acta. 137 (2014) 65–74.

17. M. Salgueiro Azevedo, C. Allély, K. Ogle, P. Volovitch, Corros. Sci. 90 (2015) 472–481.

18. J. Sullivan, N. Cooze, C. Gallagher, T. Lewis, T. Prosek, D. Thierry, Faraday Discuss. 180 (2015) 361–379.

19. R. Hausbrand, M. Stratmann, M. Rohwerder, Steel Res. Int. 74 (2003) 453–458.

20. R. Hausbrand, M. Stratmann, M. Rohwerder, Corros. Sci. 51 (2009) 2107–2114.

21. R. Krieg, M. Rohwerder, S. Evers, B. Schuhmacher, J. Schauer-Pass, Corros. Sci. 65 (2012) 119–127.

22. A. Vimalanandan, A. Bashir, M. Rohwerder, Mater. Corros. 65 (2014) 392–400.

23. J.-W. Lee, B. Park, S.J. Kim, J. Korean Inst. Met. Mater. 57 (2019) 77–83.

24. ASTM International, ASTM Int. West Conshohocken, PA. 02 (2016) 1–12.

25. M. Wolpers, J. Angeli, Appl. Surf. Sci. 179 (2001) 281–291.

26. R. Berger, U. Bexell, N. Stavlid, T.M. Grehk, Surf. Interface Anal. 38 (2006) 1130–1138.

27. V. Saarimaa, C. Lange, T. Paunikallio, A. Kaleva, J.P. Nikkanen, E. Levänen, P. Väisänen, A. Markkula, J. Coatings Technol. Res. 17 (2020) 285–292.

28. G. Williams, H.N. McMurray, D.A. Worsley, J. Electrochem. Soc. 149 (2002) B154.

29. G. Williams, R.J. Holness, D.A. Worsley, H.N. McMurray, Electrochem. Commun. 6 (2004) 549–555.

30. G. Williams, H.N. McMurray, M.J. Loveridge, Electrochim. Acta. 55 (2010) 1740–1748.

31. G. Williams, S. Geary, H.N. McMurray, Corros. Sci. 57 (2012) 139–147.

32. N. Wint, C.M. Griffiths, C.J. Richards, G. Williams, H.N. McMurray, Corros. Sci. (2020) 108839.

33. N. Wint, D. Eaves, E. Michailidou, A. Bennett, J.R. Searle, G. Williams, H.N. McMurray, Corros. Sci. 158 (2019).

34. G. Williams, R.J. Holness, H.N. McMurray, D.A. Worsley, Electrochem. Commun. 6 (2004) 549–555.

35. R. Hausbrand, M. Stratmann, M. Rohwerder, J. Electrochem. Soc. 155 (2008) C369.

36. N. Wint, N. Cooze, J.R. Searle, J.H. Sullivan, G. Williams, H.N. McMurray, G. Luckeneder, C. Riener, J. Electrochem. Soc. 166 (2019) C3147–C3158.

37. W. Fürbeth, M. Stratmann, Prog. Org. Coatings. 39 (2000) 23–29.

38. G. Williams, H.N. McMurray, J. Electrochem. Soc. 150 (2003) B380.

39. G. Williams, C. Kousis, N. McMurray, P. Keil, Npj Mater. Degrad. 3 (2019) 1–8.

40. G.J. Reynolds, Z.S. Barrett, H.N. McMurray, G. Williams, Corros. Sci. 70 (2013) 82–92.

41. T. Prosek, A. Nazarov, U. Bexell, D. Thierry, J. Serak, Corros. Sci. 50 (2008) 2216–2231.

42. G. Williams, H.N. McMurray, Electrochem. Soc. 155 (2008) C340–C349.

# Chapter 7. Selection of corrosion resistant, chromate-free pigment technology compatible with PVD coatings

## 7.1 Introduction

Zinc-based metallic coatings provide sacrificial protection for strip steel, as described in the previous chapters. In the automotive and construction industry, these zinc alloy coatings are utilised in conjunction with several organic/inorganic layers, as previous addressed in section 1.6.2. The layer of interest in this work is the primer coating which is directly applied to the zinc alloy layer and contains corrosion inhibitor pigments, which are designed to complement the sacrificial function of the zinc alloy. Traditionally, chromate-based pigments have been selected to enhance the delamination resistance of the primer layer. However, recent European legislation [1] prohibits the use of chromate-base pigments due to their toxic and carcinogenic nature [2–4]. As such, research into safe, environmentally-friendly alternatives is of great interest [5–12].

Zinc phosphate has been established as a suitable alternative for strontium chromate due to its non-toxicity and low cost [13, 14]. It is understood that zinc phosphate pigment systems do not perform as well as chromates on galvanised steel in neutral and alkaline conditions [13, 15, 16], although Bethencourt et al. suggest that first and second generation zinc phosphates are more effective in acidic media than chromate [13]. There exists multiple theories regarding the mechanism by which zinc phosphate acts as a corrosion inhibitor, all of which are listed in Knudsen and Forgren’s *Corrosion Control through Organic Coatings* [17]. A significant number of previous work suggest a phosphatisation mechanism and the formation of complex compounds on the metallic surface [18–21].

It has previously been seen that the poor solubility of zinc phosphate limits its effectiveness as a corrosion inhibitor [15, 22, 23], as such there have been significant developments made to improve the solubility of zinc phosphate via chemical or physical modification [24–30]. Zinc aluminium polyphosphate (known as ZAPP) has shown promising results in literature [26, 29, 31] owing to the improvement of solubility therefore increase in release of the inhibiting species.

However, pigments based on zinc phosphates were classed as environmentally hazardous in 2004 following European Directive 2004/73/EC. Thus, further research has been on-going into “zinc-free” inhibitors, aluminium dihydrogen tripolyphosphate (ADTP) is among the more promising contender for corrosion-resistant coatings [32–36]. Improved performance was also seen with the synergistic modification of ADTP with MgO [36].

Magnesium hydrogen phosphate (newberyite) has not previously been studied as an anti-corrosion pigment, it is typically applied to steel in a phosphating step to form a continuous inorganic coating [37–40]. In the work of Fouladi and Amadeh, it was seen that the novel newberyite coatings exhibited improved corrosion resistance compared to a standard zinc phosphating treatment, although this may have been attributed to the increased thickness of the phosphate layer [39].

This work aims to test the efficiency of chromate-free pigments with PVD coatings at a fixed volume fraction, using HDG as a comparison. The efficiency of the pigments will be determined by measuring the rate of corrosion-driven cathodic disbondment using a combination of SKP and time-lapse photography. Furthermore, with environmental impact in mind, only one pigment is zinc phosphate based (PZ20), the additional three pigments explore more novel compositions: newberyite-based (PAT15), ADTP modified with ZnO (ePAZ) and ADTP modified with MgO (PAM).

## 7.2 Experimental details

### *7.2.1 Materials*

Coupons of HDG, PVD0, PVD10 and PVD20 were selected for this work as each coating showed a predisposition to organic coating failure within a reasonable timeframe. As previously established in chapter 6, PVD4 overcoated with the model PVB layer does not exhibit susceptibility to cathodic delamination or anodic undermining within a reasonable timeframe. Phosphate-based pigments were supplied by Société Nouvelle des Couleurs Zincique (SNCZ) and are listed in **Table 2.2**. Polyvinyl butyral-co-vinyl alcohol-co-vinyl acetate (PVB) powder and additional chemicals used in this work were supplied by Merck (Sigma-Aldrich).

### *7.2.2 Methods*

To analyse the cathodic delamination resistance, the coupons were as-received, ethanol rinsed and prepared as Stratmann cells as described in section 2.5.3. The organic coatings applied in this chapter were model 15.5 % w/w PVB in ethanol formulated with 0.10 volume fraction (V.F.), calculated and formulated using the methods in section 2.1.2, of corrosion inhibitor pigments listed in **Table 2.2**. SKP calibration, setup and analysis are fully described in chapter 2. Cathodic disbondment was initiated with 0.86 M and measured over 44 hours. Time-lapse photography was used to monitor cathodic delamination on PVD10 and anodic undermining on PVD20.

## 7.3 Results and discussion

### 7.3.1 Pigment characterisation

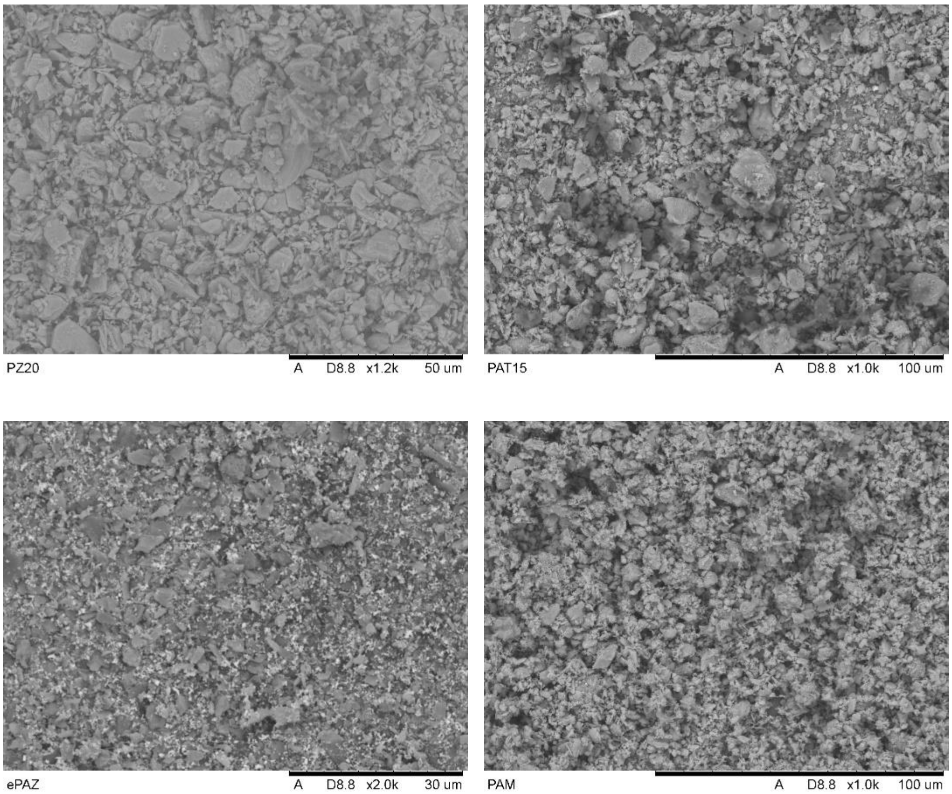

**Figure 7.1:** SEM images of PZ20, PAT15, ePAZ and PAM pigment powders.

**Table 7.1:** Particle size of each pigment type, measured using SEM.

| **Pigment I.D.** | **Average Particle Size (µm)** |
|---|---|
| Zinc Phosphate PZ20 | 9.62(3) |
| NOVINOX PAT15 | 9.61(3) |
| NOVINOX ePAZ | 4.46(1) |
| NOVINOX PAM | 7.93(2) |

SEM imaging (**Figure 7.1**), combined with calibrated measuring software, provided the average particle sizes for the four inhibitor pigments used in this work, shown in **Table 7.1**. The full compositions of the pigments are given in **Table 2.2**, with the exception of PAM. SNCZ do not provide information on 30 % of the pigment composition in the MSDS due to the non-toxic nature of the omitted compound. Subsequent EDX analysis, shown in **Figure 7.2**, suggests this unknown compound is MgO.

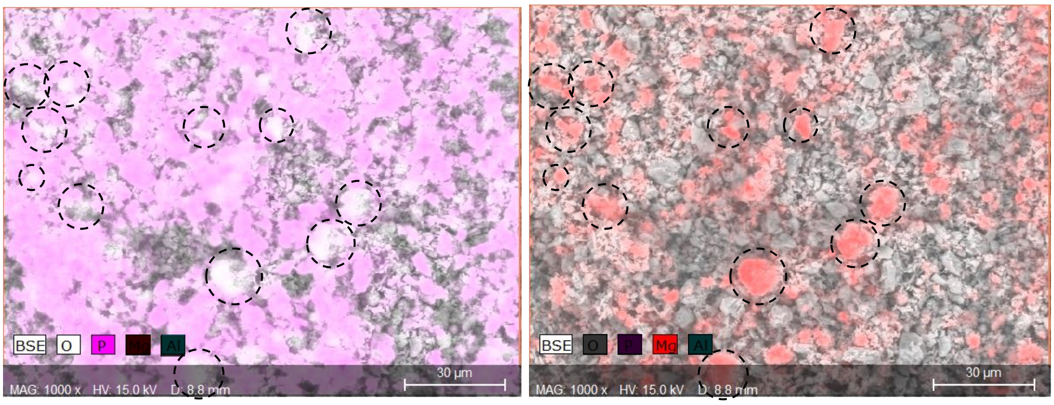

**Figure 7.2:** EDX analyses of PAM pigment: a phosphorous and oxygen map (left) and a magnesium map (right).

### *7.3.2 PZ20*

The time-dependent SKP profiles shown in **Figure 7.3** correspond to a coupon of HDG, overcoated with PVB containing 0.10 V.F. PZ20, where cathodic disbondment has been initiated with 0.86 M NaCl. The intact region potential, $E_{intact}$, was measured at ca. -0.60 V vs. SHE with a drop of 0.30 V to the defect potential, $E_{defect}$. $E_{intact}$ appears to have been depressed with the presence of PZ20 when compared with the unpigmented experiment results (**Figure 6.3**). For the first 28 hours of the experiment delamination rate was maintained at ca. 0.40 mm per 2 hours before slowing to 0.10 mm per 2 hours to a total delamination distance of 5.4 mm. Within this timeframe, it is suggested that 0.10 V.F. of PZ20 dispersed in the PVB layer had a small influence on the rate and overall delamination distance on HDG. The inhibitive influence of PZ20 in this work is less than previously observed for the same volume fraction [11], however this inconsistency can be attributed to the difference in surface preparation, addressed in chapter 6.

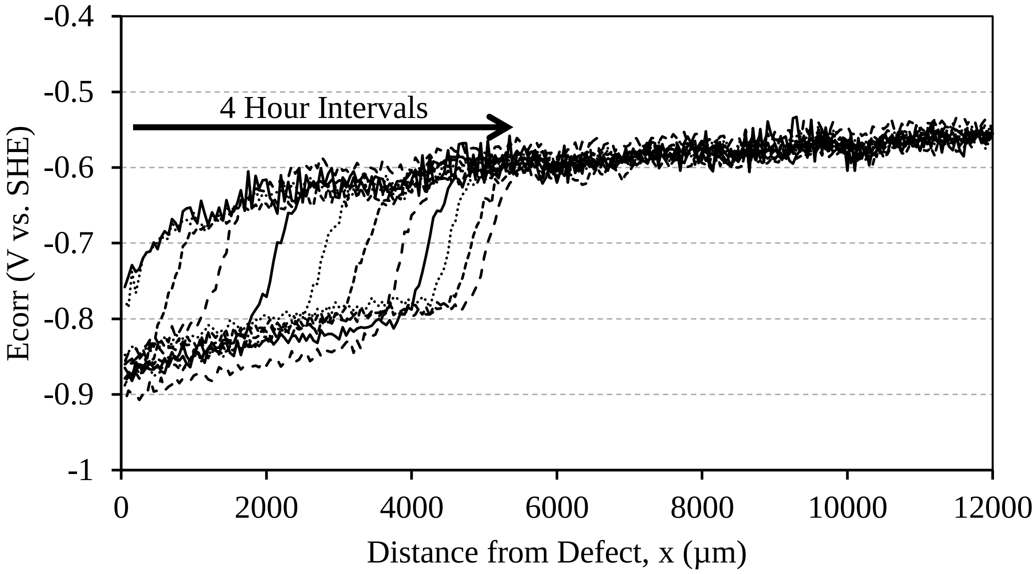

**Figure 7.3:** Typical $E_{corr}$ vs. distance (x) profiles for a HDG overcoated with 0.10 V.F. PZ20 inhibitor pigment containing PVB in 95 % R.H. over 44 hours. Underfilm corrosion was initiated by 0.86 M NaCl.

**Figure 7.4** shows the time-dependent SKP profiles for PVD0 coated with PVB containing 0.1 V.F. PZ20 inhibitor pigment. $E_{intact}$ values remained constant at ca. -0.50 V vs. SHE. The $E_{intact}$ values were ca. -0.90 V vs. SHE, similar to those measured on the HDG defect in **Figure 7.3**, which is lower than the open circuit potential of zinc (-0.70 V vs. SHE) [41–43]. However, the $E_{corr}$ measured adjacent to the delamination front remains at ca. -0.69 V vs. SHE which suggests the active corrosion of zinc progresses with the ingress of electrolyte. There is a notable reduction in the final length of delamination after 44 hours (9 mm) compared to the final length of delamination observed in the uninhibited system shown in **Figure 6.6** (11 mm). An important distinction between the uninhibited and PZ20 inhibited system disbondment rates measured was within the initial 4 hours of the experiment; the uninhibited system delaminated by ca. 3 mm in that time, whereas the inhibited system delaminated by ca. 2 mm. Moreover, the slope of the $E_{corr}$ vs. distance plot is much greater for the PZ20 experiment compared to the control study in chapter 6, which indicates an increase in resistivity in the underfilm electrolyte caused by the release of inhibitor species. However, it is important to note that although the rate of delamination is reduced, the kinetics of delamination remained parabolic for both HDG and PVD0, which Wint et al. have also previously observed [11]. Parabolic disbondment has been previously attributed to the mobility of cations ($Na^+$) through the ingressed underfilm electrolyte for the rate determining step [44, 45]. As the mechanism for disbondment did not change, the marginal reduction in delamination rate can be attributed to either an increase in underfilm electrolyte resistance or a change in the interfacial chemistry. It has been previously noted [6, 9, 11, 16, 20, 22] that a significant shortcoming of zinc phosphate as a corrosion inhibitor is its limited solubility in water ($K_{sp}$ $9x10^{-33}$ $mol^5dm^{-15}$ [46]).

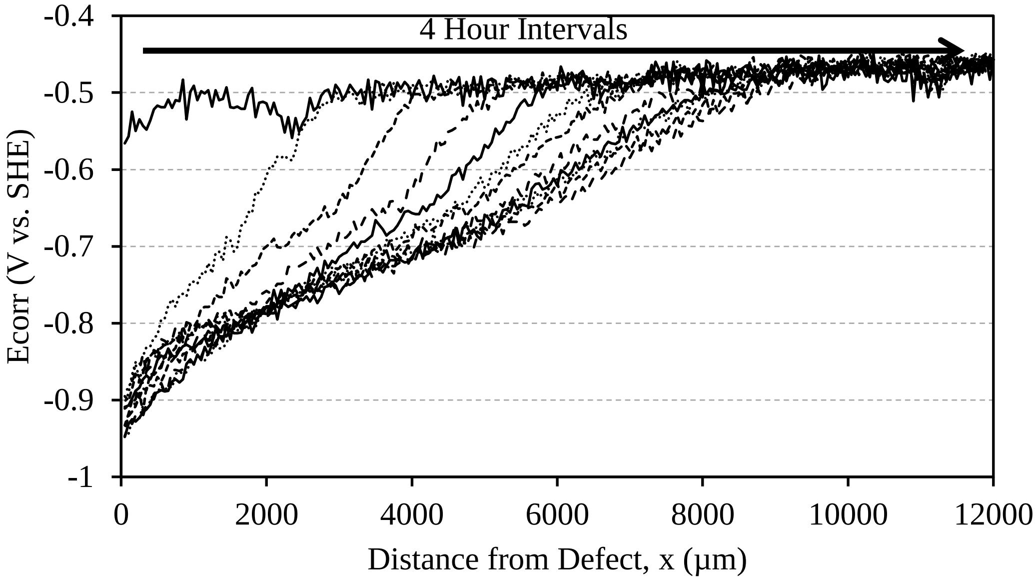

**Figure 7.4:** Typical $E_{corr}$ vs. distance (x) profiles for a PVD0 overcoated with 0.10 V.F. PZ20 inhibitor pigment containing PVB in 95 % R.H. over 44 hours. Underfilm corrosion was initiated by 0.86 M NaCl.

In chapter 6 it was found that PVD10 exhibited cathodic delamination at a significantly slower rate that all other samples following the same mechanism. The incorporation of

PZ20 inhibitor pigment reduced the rate of disbondment to the extent where it was no longer reasonably measurable in the lab environment, and any comparison was beyond the scale of other cathodic disbondment tests. **Figure 7.5** shows photographic images taken over a week of visual study; characteristic black staining was observed in the defect area as a bare metal response, however no disbondment was visible nor evident during post-experimental physical inspection.

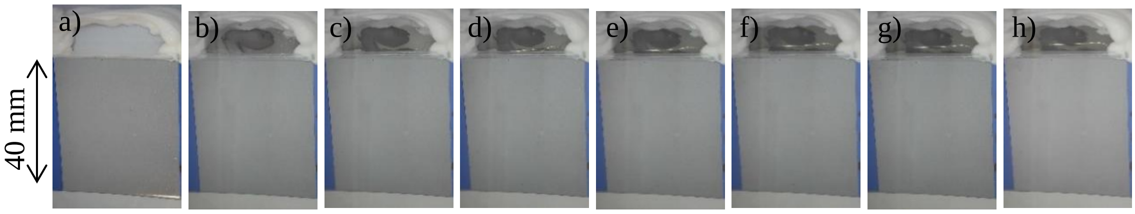

**Figure 7.5:** Photographic images of the PVD10 Stratmann cell coated with 0.10 V.F. PZ20 PVB taken in-situ at a) 0, b) 24, c) 48, d) 72, e) 96, f) 120, g) 144 and h) 168 hours. Underfilm corrosion was initiated by 0.86 M NaCl (aq). 95 % R.H maintained.

The influence of PZ20 on the anodic undermining on PVD20 is evident in **Figure 7.6** when compared to **Figure 6.14**; there was an overall reduction in disbondment area.

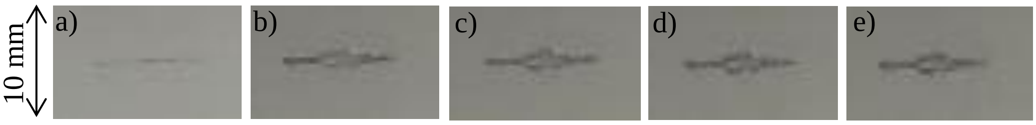

**Figure 7.6**: Photographic images of the scribe defect on PVD20 coated with 0.10 V.F. PZ20 PVB taken in-situ at a) 0, b) 24, c) 48, d) 72 and e) 96 hours. Underfilm corrosion was initiated by 1 M HCl (aq). 95 % R.H maintained.

### *7.3.3 PAT15*

**Figure 7.7** shows a marked improvement in delamination resistance on HDG with the incorporation of the PAT15 inhibitor pigment. $E_{intact}$ remained relatively constant at ca. -0.55 V vs. SHE during the experiment and $E_{defect}$ was equal to the potential measured at the delamination front (ca. -0.80 V vs. SHE). There was also a shift in delamination kinetics from parabolic to linear (when comparing unpigmented and PAT15 pigmented coating delamination), indicating a change in the rate-controlling step from ion diffusion through the underfilm electrolyte to interfacial electron transfer. This effect has been previously observed for organic coatings containing inhibitor pigments such as graphene nano-platelets [47] and benzotriazole modified zinc phosphate inhibitor pigments [11].

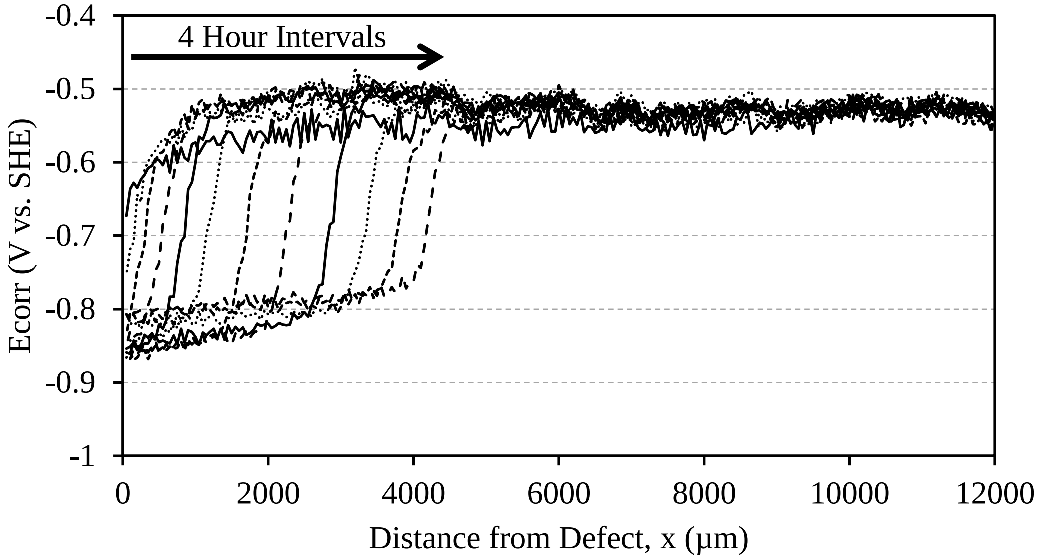

**Figure 7.7:** Typical $E_{corr}$ vs. distance (x) profiles for a HDG overcoated with 0.10 V.F. PAT15 inhibitor pigment containing PVB in 95 % R.H. over 44 hours. Underfilm corrosion was initiated by 0.86 M NaCl.

The SKP profiles displayed in **Figure 7.8** indicate rapid underfilm disbondment of 2.5 mm within the initial 4 hours of the experiment (similar to the unpigmented PVD0 response), followed by a significant rate drop and subsequent complete stop in delamination progress after 12 hours at 4.3 mm. The $E_{intact}$ value remained at -0.40 V vs. SHE and the $E_{defect}$ was ca. -0.80 V vs. SHE. It can be seen that the cease in delamination coincides with a stark increase in the delamination front gradient, suggesting the formation of insoluble corrosion products which provided a physical barrier to ion migration within the electrolyte. PAT15 is a majority newberyite

($MgHPO_4.3H_2O$) commercial pigment, as such the improved resistance observed on HDG and PZ20 compared to PZ20 (a majority $Zn_3(PO_4)_2$ commercial pigment) may be attributed to the improved solubility of $MgHPO_4.3H_2O$ in water ($K_{sp}$ 1.67x$10^{-6}$ mol$^2$dm$^{-2}$ [48]). Solubility of the pigment plays an important role in its inhibitive power; the higher the solubility in the electrolyte, the more kinetically available the inhibitor species [20].

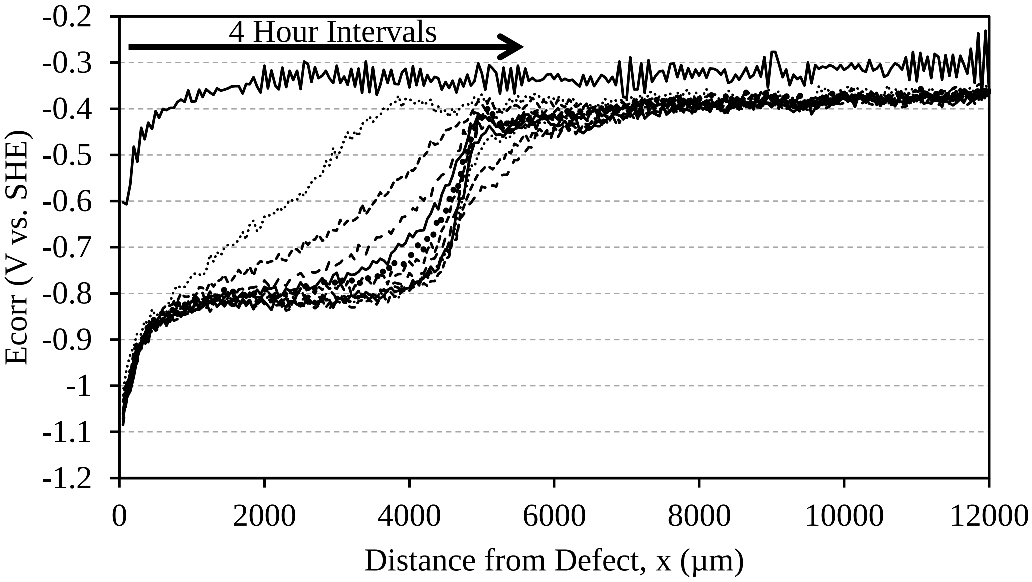

**Figure 7.8:** Typical $E_{corr}$ vs. distance (x) profiles for a PVD0 overcoated with 0.10 V.F. PAT15 inhibitor pigment containing PVB in 95 % R.H. over 44 hours. Underfilm corrosion was initiated by 0.86 M NaCl.

The time-lapse results for PVD20 in **Figure 7.9** suggest a similar response with PAT15 present as seen for PZ20; there is little underfilm attack visible. It is difficult to resolve differences in inhibitive effect due to the significantly reduced rate of underfilm attack.

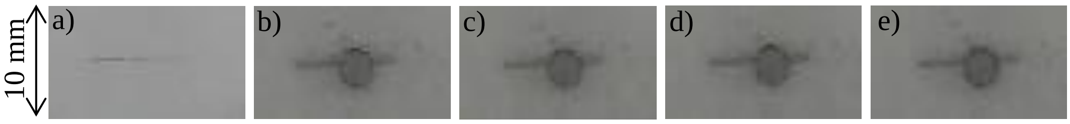

**Figure 7.9:** Photographic images of the scribe defect on PVD20 coated with 0.10 V.F. PAT15 PVB taken in-situ at a) 0, b) 24, c) 48, d) 72 and e) 96 hours. Underfilm corrosion was initiated by 1 M HCl (aq). 95 % R.H maintained. *Note: the dark circle visible in b-e was caused by direct attack through the organic coating, as such does not represent underfilm progression from the defect.*

### *7.3.4 ePAZ*

**Figure 7.10** shows an $E_{intact}$ value maintained at ca. -0.50 V vs. SHE for HDG overcoated with PVB containing 0.10 V.F. ePAZ. However, the $E_{defect}$ shows an increase from -0.80 V vs. SHE to -0.75 V vs. SHE at 36 hours and a further increase to -0.70 V vs. SHE at 40 hours. The first increase in $E_{defect}$ coincides with a significant decrease in rate from the initial 1.2 mm per 4 hours to 0.50 mm per 4 hours. As with PAT15, the inclusion of the inhibitor pigment has altered the delamination kinetics from parabolic (unpigmented) to linear, which, in this case, has resulted in a poor inhibitive power. The coatings delaminated by 9.5 mm over the 44 hours experiment, a notable decrease in disbondment resistance compared to the uninhibited coating.

Conversely, 0.10 V.F. of ePAZ in the model PVB coating applied to PVD0 showed a significant inhibitive effect (**Figure 7.11**). Indeed, the maximum delamination distance reached during the 44 hour experiment was 3.2 mm. Moreover, it is evident that the delamination kinetics remained parabolic, as with the unpigmented study. $E_{intact}$ remained constant at ca. -0.37 V vs. SHE and $E_{defect}$ at -0.80 V vs. SHE.

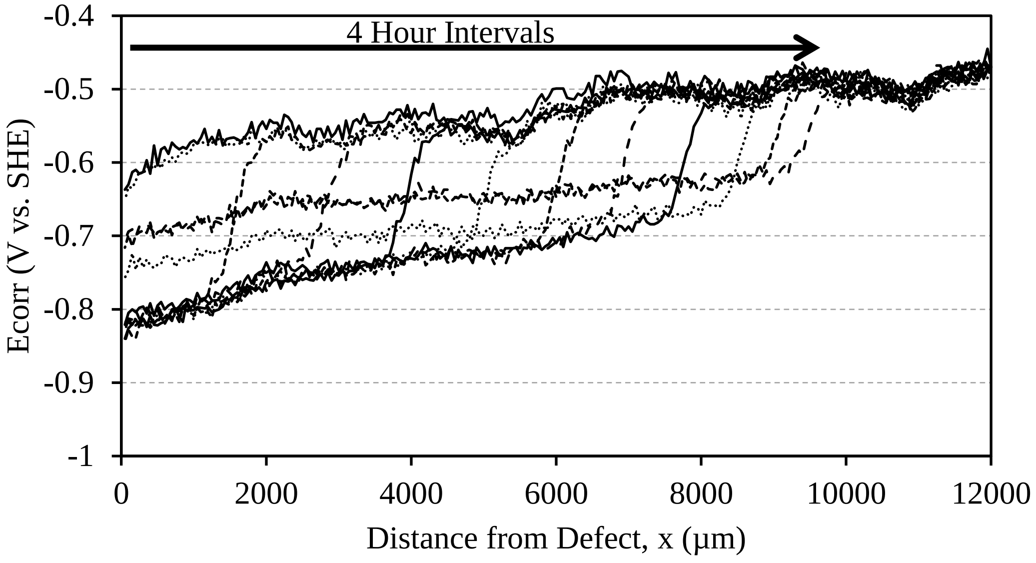

**Figure 7.10:** Typical $E_{corr}$ vs. distance (x) profiles for a HDG overcoated with 0.10 V.F. ePAZ inhibitor pigment containing PVB in 95 % R.H. over 44 hours. Underfilm corrosion was initiated by 0.86 M NaCl.

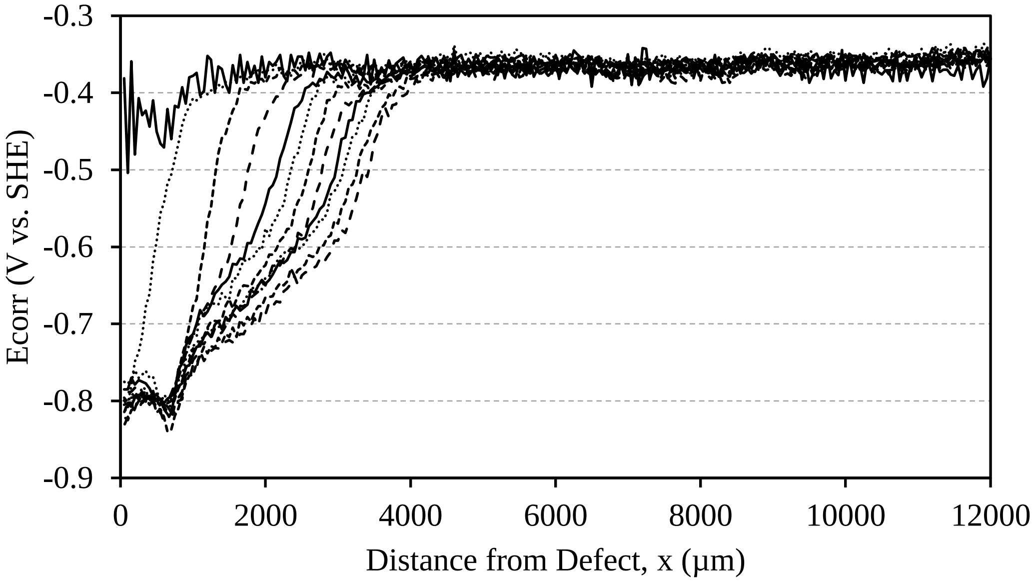

**Figure 7.11:** Typical $E_{corr}$ vs. distance (x) profiles for a PVD0 overcoated with 0.10 V.F. ePAZ inhibitor pigment containing PVB in 95 % R.H. over 44 hours. Underfilm corrosion was initiated by 0.86 M NaCl.

**Figure 7.12** shows little difference in the influence of ePAZ on PVD20 anodic undermining compared to the previous two pigments, however there was a noticeable reduction in visible delamination compared to the unpigmented study.

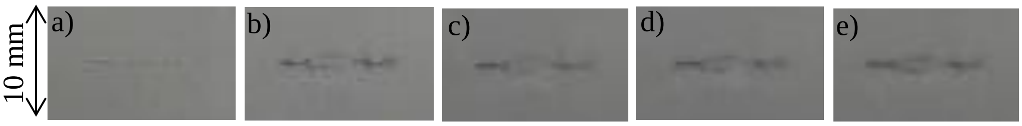

**Figure 7.12:** Photographic images of the scribe defect on PVD20 coated with 0.10 V.F. ePAZ PVB taken in-situ at i) 0, ii) 24, iii) 48, iv) 72 and v) 96 hours. Underfilm corrosion was initiated by 1 M HCl (aq). 95 % R.H maintained.

### *7.3.5 PAM*

PVB containing 0.10 V.F. PAM pigment demonstrated the greatest reduction in cathodic delamination for HDG; the maximum delamination distance was 4.35 mm during the 44 hour experiment. The disbondment kinetics were linear, maintaining a rate of ca. 0.65 mm per 4 hours. $E_{intact}$ was much lower for this coating system compared to previous samples, measured at ca. -0.65 V vs. SHE, with $E_{defect}$ increasing from -0.81 V vs. SHE to -0.75 V vs. SHE over the 44 hour experiment. It is likely that the lower $E_{intact}$ value contributed toward the decrease in delamination rate as the difference in $E_{intact}$ and $E_{defect}$ represents the driving force for disbondment.

Similarly to HDG, the 0.10 V.F. PAM PVB coating on PVD0 (**Figure 7.14**) provided the greatest reduction in maximum delamination distance (2.5 mm), which implies it was the most effective inhibitor. The delamination kinetics remained parabolic, as with unpigmented. $E_{intact}$ was maintained at -0.55 V vs. SHE and $E_{defect}$ was -0.96 V vs. SHE.

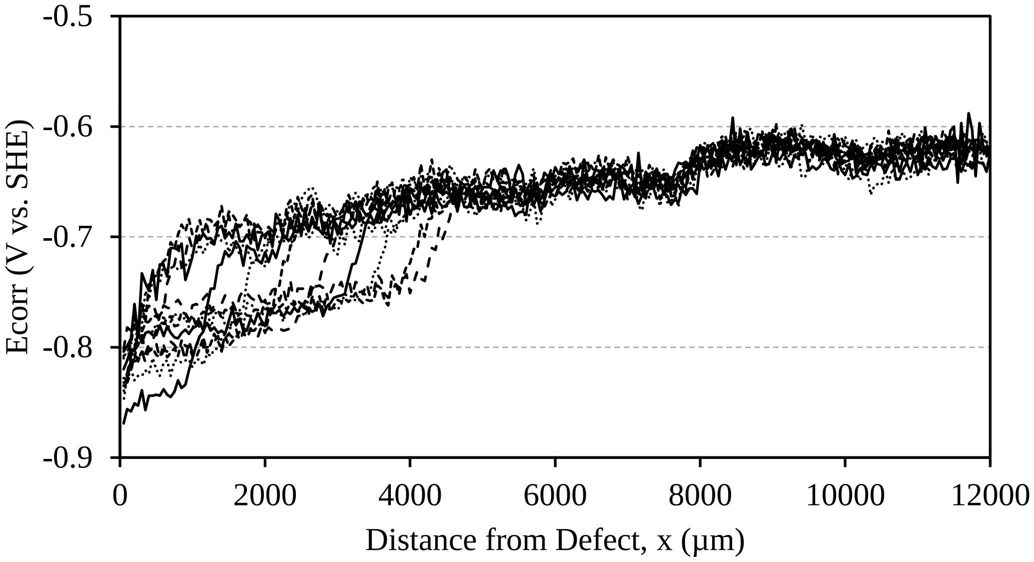

**Figure 7.13:** Typical $E_{corr}$ vs. distance (x) profiles for a HDG overcoated with 0.10 V.F. PAM inhibitor pigment containing PVB in 95 % R.H. over 44 hours. Underfilm corrosion was initiated by 0.86 M NaCl.

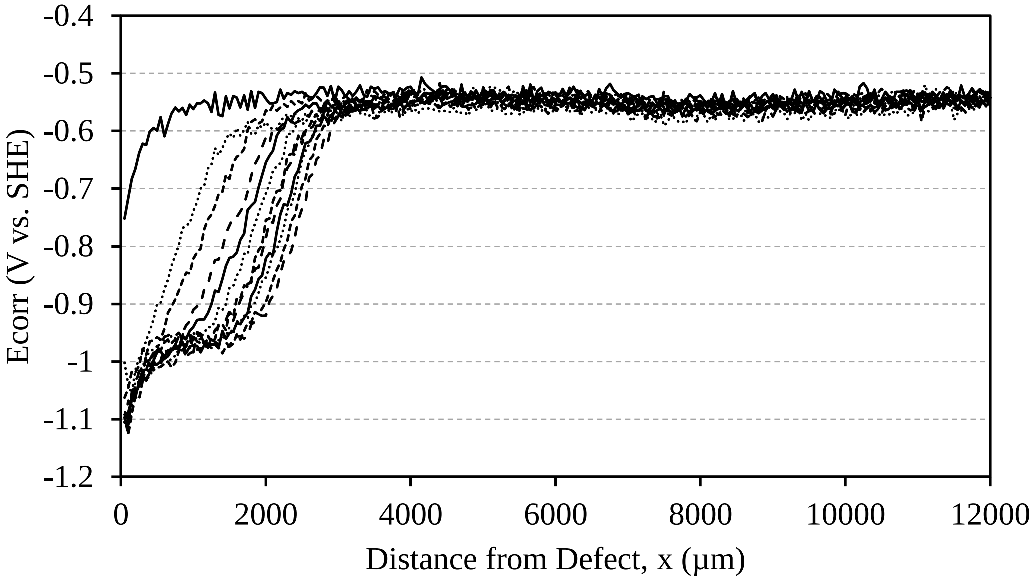

**Figure 7.14:** Typical $E_{corr}$ vs. distance (x) profiles for a PVD0 overcoated with 0.10 V.F. PAM inhibitor pigment containing PVB in 95 % R.H. over 44 hours. Underfilm corrosion was initiated by 0.86 M NaCl.

There appeared to be greater anodic undermining on the PVD20 sample overcoated with 0.10 V.F. PAM PVB (**Figure 7.15**) compared to the previous pigments investigated.

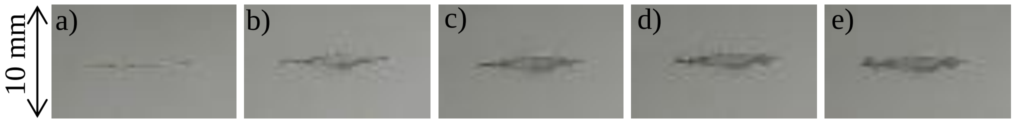

**Figure 7.15:** Photographic images of the scribe defect on PVD20 coated with 0.10 V.F. PAM PVB taken in-situ at i) 0, ii) 24, iii) 48, iv) 72 and v) 96 hours. Underfilm corrosion was initiated by 1 M HCl (aq). 95 % R.H maintained.

The performances of all pigments are summarised and compared to data for the unpigmented studies in **Figure 7.16**. The collection of plots confirm linear kinetics for all pigments on HDG, a shift from the parabolic behaviour shown for the unpigmented experiment in chapter 6. Similarly, most pigments on PVD0 (PZ20, ePAZ and PAM) also show linear kinetics in corrosion-driven cathodic disbondment. Interestingly, there was a clear three part process that occurred for the PAT15-containing PVD0 system; exhibiting linear kinetics in the first 12 hours as the pigment was released into the underfilm electrolyte, followed by a 20 hour pause in underfilm progression. In the final 14 hours it appears there was a shift back to parabolic kinetics as the pigment was exhausted. For both HDG and PVD0, PAM showed the greatest overall reduction in disbondment rate, which is most likely due to the presence of MgO in the pigment composition, providing $Mg^{2+}$ cations as the MgO was hydrated. The incorporation of $Mg^{2+}$ to the system via the pigment may have afforded the zinc coatings resistance to corrosion-driven cathodic disbondment in the similar way to magnesium-containing alloy coatings; by promoting the formation of stable passive layers which inhibit oxygen reduction. [49]

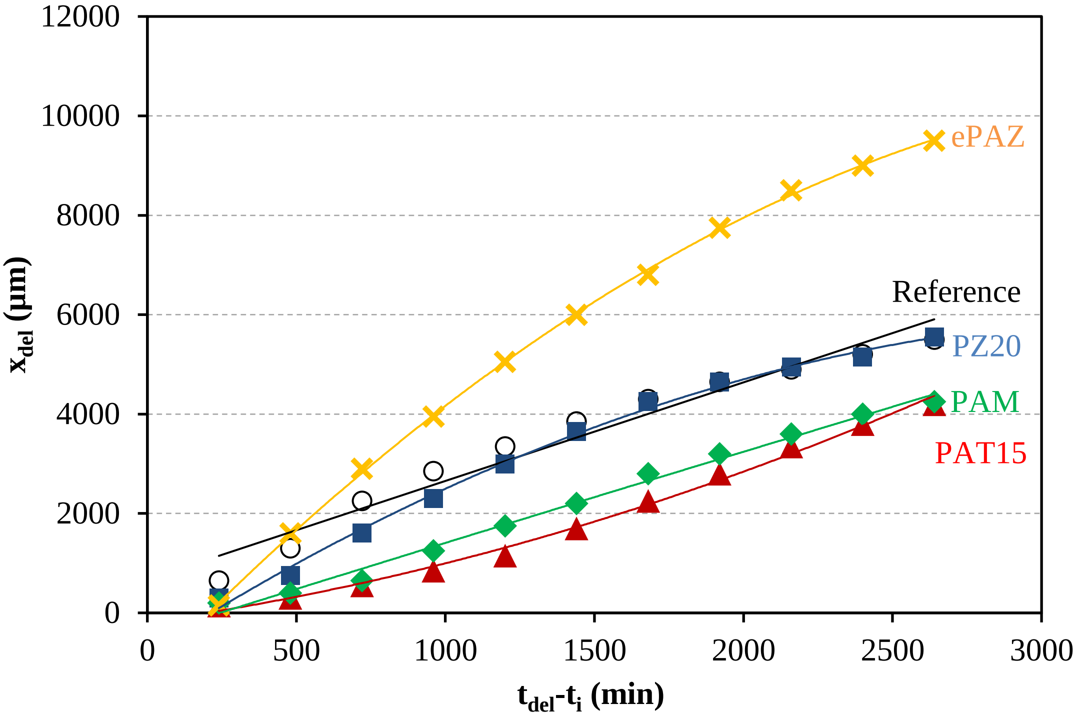

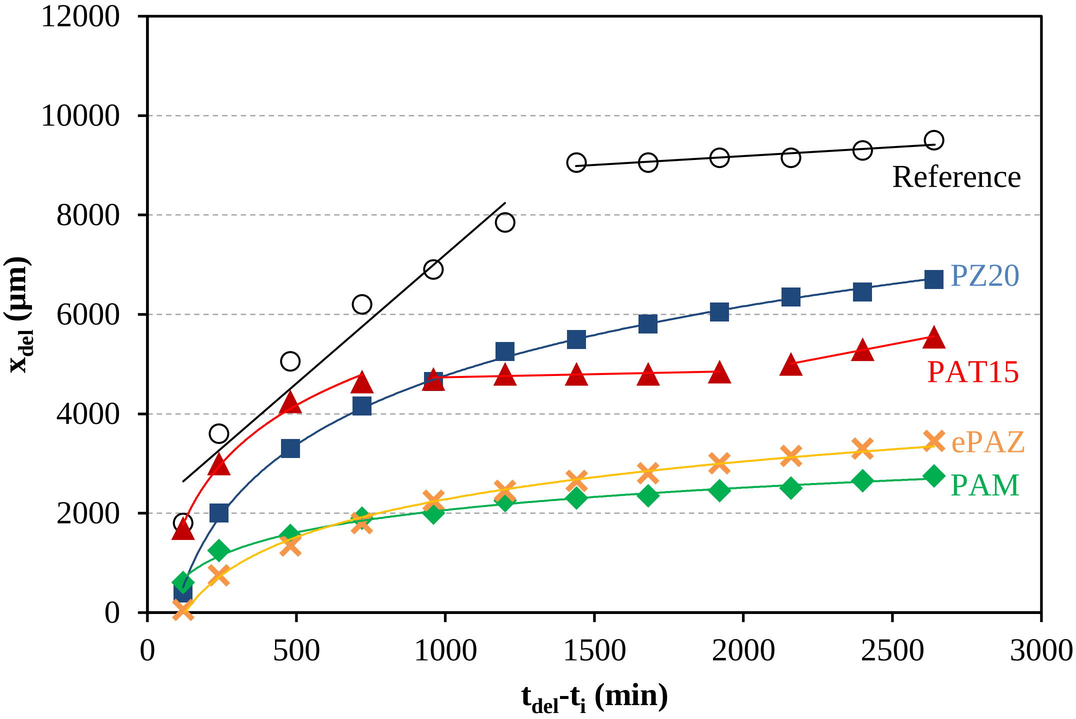

**Figure 7.16:** Plots of mean distance of underfilm corrosion advance vs. post-initiation holding time for HDG (top) and PVD0 (bottom). Underfilm corrosion was initiated with 0.86 M NaCl.

## 7.4 Conclusions

A systematic examination of chromate-free pigment performance in PVB overcoated on PVD Zn, PVD Zn-Mg and HDG metallic coatings has been reported. PVD4 was omitted from this work as laboratory delamination studies extended beyond a reasonable timeframe, and thus should be considered for long-term salt spray analysis in future. PVD10 exhibited exceptional performance with the presence of the zinc phosphate pigment, PZ20, showing no evidence of delamination (including post-experimental examination) during the 168 hour study. PVD20 showed noticeable reduction in anodic undermining for all pigments compared to the unpigmented experiment.

The SKP analysis for pigment compatibility on HDG and PVD0 provided the following key conclusions:

- All pigments used in combination with HDG resulted in a kinetics shift from parabolic (unpigmented) to linear.
- PZ20 had little effect on the delamination rate and overall delamination advancement on HDG, whereas PAM and PAT15 appear to have reduced the overall advancement marginally.
- For PVD0, there is a clear order of inhibitive power for the studied pigments: PAM > ePAZ > PAT15 > PZ20. Suggesting that the novel ADTP complex pigment, modified with ZnO or MgO, is highly compatible with PVD0 and should be considered for further longer term studies on PVD coatings.

## 7.5 References

1. COMMISSION REGULATION (EU) No 301/2014, Brussels, (2014).
2. A. Sheffet, I. Thind, A.M. Miller, D.B. Louria, Arch. Environ. Health. 37 (1982) 44–52.
3. S. Langard, T. Vigander, Br. J. Ind. Med. 40 (1983) 71–74.
4. S.A. Katz, H. Salem, J. Appl. Toxicol. 13 (1993) 217–224.
5. K. Aramaki, Corros. Sci. 43 (2001) 591–604.
6. S. Dalbin, G. Maurin, R.P. Nogueira, J. Persello, N. Pommier, Surf. Coatings Technol. 194 (2005) 363–371.
7. G. Grundmeier, B. Rossenbeck, K.J. Roschmann, P. Ebbinghaus, M. Stratmann, Corros. Sci. 48 (2006) 3716–3730.
8. R. Berger, U. Bexell, T. Mikael Grehk, S.E. Hörnström, Surf. Coatings Technol. 202 (2007) 391–397.
9. B. Ramezanzadeh, E. Ghasemi, F. Askari, M. Mahdavian, Dye. Pigment. 122 (2015) 331–345.
10. F. Askari, E. Ghasemi, B. Ramezanzadeh, M. Mahdavian, Corrosion. 72 (2016) 1526–1538.
11. N. Wint, C.M. Griffiths, C.J. Richards, G. Williams, H.N. McMurray, Corros. Sci. (2020) 108839.
12. O. Gharbi, S. Thomas, C. Smith, N. Birbilis, Npj Mater. Degrad. 2 (2018) 12.
13. M. Bethencourt, F.J. Botana, M. Marcos, R.M. Osuna, J.M. Sánchez-Amaya, Prog. Org. Coatings. 46 (2003) 280–287.
14. M. Zubielewicz, W. Gnot, Prog. Org. Coatings. 49 (2004) 358–371.

15. A.C. Bastos, M.G.S. Ferreira, A.M. Simões, "Comparative electrochemical studies of zinc chromate and zinc phosphate as corrosion inhibitors for zinc", in: Prog. Org. Coatings, Elsevier, (2005) pp. 339–350.

16. A. Amirudin, C. Barreau, R. Hellouin, D. Thierry, Prog. Org. Coatings. 25 (1995) 339–355.

17. O.O.Ø. Knudsen, A. Forsgren, Corrosion control through organic coatings, second edition, Second, CRC Press, Taylor & Francis Group, 6000 Broken Sound Parkway NW, Suite 300, Boca Raton, FL 33487-2742, (2017).

18. L.L. Chromy, E. Kaminska, E. Kamińska, Prog. Org. Coatings. 18 (1990) 319–324.

19. W. Kozlowski, J. Flis, Corros. Sci. 32 (1991) 861–875.

20. J. Sinko, Prog. Org. Coatings. 42 (2001) 267–282.

21. G. Blustein, M.C. Deyá, R. Romagnoli, B. Del Amo, Appl. Surf. Sci. 252 (2005) 1386–1397.

22. J.A. Burkill, J.E.O. Mayne, J. Oil Colour Chem. Assoc. 71 (1988) 273–275.

23. M. Mahdavian, M.M. Attar, Prog. Org. Coatings. 53 (2005) 191–194.

24. M.A. Hernández, F. Galliano, D. Landolt, Corros. Sci. 46 (2004) 2281–2300.

25. P. de Lima-Neto, A.P. de Araújo, W.S. Araújo, A.N. Correia, Prog. Org. Coatings. 62 (2008) 344–350.

26. S.M. Mousavifard, P.M.M. Nouri, M.M. Attar, B. Ramezanzadeh, J. Ind. Eng. Chem. 19 (2013) 1031–1039.

27. R. Naderi, M.M. Attar, Prog. Org. Coatings. 77 (2014) 830–835.

28. F. Askari, E. Ghasemi, B. Ramezanzadeh, M. Mahdavian, Dye. Pigment. 124 (2016) 18–26.

29. R. Naderi, M.M. Attar, Dye. Pigment. 80 (2009) 349–354.

30. R. Naderi, M.M. Attar, Prog. Org. Coatings. 69 (2010) 392–395.

31. A. Darvish, R. Naderi, M.R.M. Attar, Pigment Resin Technol. 45 (2016) 419–425.

32. M. Deyá, V.F. Vetere, R. Romagnoli, B. Del Amo, Pigment Resin Technol. 30 (2001) 13–24.

33. S.N. Roselli, B. del Amo, R.O. Carbonari, A.R. Di Sarli, R. Romagnoli, Corros. Sci. 74 (2013) 194–205.

34. D. Song, J. Gao, L. Shen, H. Wan, X. Li, J. Chem. 2015 (2015).

35. N.I. Matskevich, A.J. Wright, T. Wolf, I. V. Vyazovkin, O.I. Anyfrieva, M.Y. Matskevich, J. Chem. Thermodyn. 111 (2017) 27–30.

36. W. Song, L. Yang, X. Ma, G. Liang, Ind. Eng. Chem. Res. 57 (2018) 13578–13585.

37. M.F. Morks, Mater. Lett. 58 (2004) 3316–3319.

38. M. Fouladi, A. Amadeh, Electrochim. Acta. 106 (2013) 1–12.

39. M. Fouladi, A. Amadeh, Mater. Lett. 98 (2013) 1–4.

40. P. Pokorný, Koroze a Ochr. Mater. 62 (2018) 129–133.

41. W. Fürbeth, M. Stratmann, Corros. Sci. 43 (2001) 207–227.

42. W. Fürbeth, M. Stratmann, Corros. Sci. 43 (2001) 229–241.

43. W. Fürbeth, M. Stratmann, Corros. Sci. 43 (2001) 243–254.

44. A. Leng, H. Streckel, M. Stratmann, Corros. Sci. 41 (1998) 579–597.

45. W. Wang, H. Leidheiser, "MODEL FOR THE QUANTITATIVE INTERPRETATION OF CATHODIC DELAMINATION.", in: Electrochem. Soc. Ext. Abstr., (1984) p. 343.

46. D.R. Lide, CRC Handbook of Chemistry and Physics, 84th ed., CRC Press LLC, (2003).

47. C.F. Glover, C.A.J. Richards, G. Williams, H.N. McMurray, Corros. Sci. 136 (2018) 304–310.

48. R.M.H. Verbeeck, P.A.M.D. De Bruyne, F.C.M. Driessens, F. Verbeek, Inorg. Chem. 23 (1984) 1922–1926.

49. R. Hausbrand, M. Stratmann, M. Rohwerder, Steel Res. Int. 74 (2003) 453–458.

# Chapter 8. Conclusions and Future Work

## 8.1 Conclusions

This body of work established numerous key findings essential for further progress in the field of physical vapour deposited zinc and Zn-Mg coatings, summarised below:

- A pure zinc PVD coating (PVD0) was confirmed to be significantly thinner than the commercial HDG zinc layer and comprised of hexagonal microplates. The Zn- 4 wt% Mg (PVD4) coating was comprised of discrete structure of zinc and $Mg_2Zn_{11}$ phases, considerably finer than commercial Zn-Mg-Al (ZMA). PVD Zn- 10 wt% Mg and PVD Zn- 20 wt% Mg possessed nanostructures of zinc with $Mg_2Zn_{11}$ and $MgZn_2$ respectively. All PVD coatings were found to be approximately five times smoother than the commercial galvanised coatings.
- Electrochemical analysis established a trend in decreasing initial OCP and stabilised OCP values as a function of magnesium content for the PVD coatings. Potentiodynamic studies also showed a decrease in $E_{corr}$ and $I_{corr}$ related to the increase in magnesium content, suggesting a correlation of increased corrosion resistance with increased magnesium content. The improved homogeneity of PVD0 correlated with an improvement in polarisation resistance compared to HDG during electrochemical impedance spectroscopy analysis. PVD4 was also identified as a poor cathodic surface during rotating disk electrode campaigns, suggesting an innate resistance to cathodic disbondment.
- The novel augmentation of the scanning vibrating electrode technique (SVET) explored in chapter 5 established a strong benefit to simultaneous photographic image capture during the electrochemical SVET study. SVET-TLI (scanning

vibrating electrode technique time-lapse imaging) was utilised to correlate the characteristic staining of Zn-Mg PVD coatings to the net cathodic regions, which contrasts the staining of anodic regions on ZMA and pure magnesium. Moreover, the microstructures of the PVD coatings was attributed to the localised anodic events observed electrochemically and visually. There was a distinct correlation between the increase in magnesium content of the PVD coatings and a reduction in average anodic area coverage and accumulated anodic current density, with an optimum magnesium content identified as PVD4.

- Scanning kelvin probe (SKP) studies identified HDG, PVD0, ZMA and PVD10 as susceptible to cathodic disbondment, though the disbondment observed on ZMA and PVD10 having a significantly slower rate to the magnesium-free zinc coatings HDG and PVD0. PVD20 showed a resistance to cathodic delamination but a susceptibility to anodic undermining. PVD4 showed no susceptibility to delamination of any kind within reasonable laboratory timeframes. Alkaline cleaning proved detrimental for the zinc coatings HDG and PVD0 but provided further resistance to cathodic delamination for PVD10 via surface activation of the magnesium.
- The inclusion of commercial pigments to the organic overcoat of HDG and PVD0 shifted delamination kinetics from parabolic to linear, suggesting a resistive effect imposed by the pigments as they leach into the underfilm electrolyte. The novel aluminium dihydrogen tripolyphosphate (ADTP) pigment in combination with MgO had the most beneficial impact on

delamination resistance for both HDG and PVD0, owing to the release of magnesium cations into the underfilm electrolyte.

This work highlights the positive influence of alloying zinc coatings with magnesium, in terms of overall reduction in corrosion rate on the bare alloy surface and also an increase in delamination resistance. Indeed, the galvanic coupling of magnesium and zinc works to depress the intact potential of an organic overcoat to eliminate the driving force for film disbondment. Moreover, the discrete microstructures formed specifically by the physical vapour deposition process also contribute significantly in the breakdown of ionic pathways. The systematic variance of magnesium content worked to identify an optimum amount to produce a metallic coating highly resistant to both anodic and cathodic disbondment, indicating a real opportunity for much thinner sacrificial zinc coatings, which would result in greater fuel efficiency and less demand on our finite zinc resources.

## 8.2 Future Work

This thesis has provided a significant contribution to the area of PVD Zn-Mg coatings, however there is still much more research to be done to deepen the understanding of the PVD process and unlock the potential for PVD coatings to emerge into industry.

Primarily there needs to be a systematic study into the influence of PVD process parameters and the resulting microstructure of the PVD coatings. The PVD pilot line in IJmuiden has already undergone the change from wire-feeding to batch crucible evaporation which is assumed to have a major effect on the structure of the deposited coatings. Furthermore, there is room for optimisation of the melt and strip temperatures to further control the output coating characteristics. In this work, the microstructure of

PVD4 emerged as a successful combination of processing parameters, however the precise correlation between the parameters used and resulting structure is not fully understood.

As a starting point, the PVD4 coating in this work has shown highly promising evidence as an optimum Zn-Mg alloy coating. As such, further production of this coating should be undertaken, and additional corrosion testing should be conducted. This work focused solely on accelerated testing for corrosion study, and it is well debated whether these methods are comparable to real life application. Therefore, long term exposure testing should be done and compared to the current commercial Zn-Mg alloy coatings (salt spray, long term exposure outdoors, environmental chamber studies).

Furthermore, in this work a model polyvinyl butyral coating was used in delamination studies for the sole purpose of accelerated results. Moving forward, commercial organic coatings should be applied to the optimum PVD Zn-Mg metallic coating formulation for further delamination study. Additionally, this work has offered a range of corrosion inhibitor pigments which should be considered for primer layer addition.

## Appendix 1: List of publications

Below is a list of journal publications and conferences papers in relation to this work:

1. **Studying the Influence of Mg Content on the Microstructure and Associated Localized Corrosion Behavior of Zn-Mg PVD Coatings Using SVET-TLI**
   *Rebecca Bolton, Thomas Dunlop, James Sullivan, Justin Searle, Helge Heinrich, Ruud Westerwaal, Christiaan Boelsma and Geraint Williams*
   Journal of the Electrochemical Society
   2019
   DOI: 10.1149/2.0391911jes
2. **A novel in-situ integration of Time-Lapse Imaging with a Scanning Vibrating Electrode Technique (SVET-TLI) for the study of sacrificial zinc coatings in salt solution**
   *Rebecca Bolton, Justin Searle, Geraint Williams*
   European Corrosion Congress (EUROCORR) and 20th International Corrosion Congress and Process Safety Congress, Prague, Czech Republic, 2017.
3. **SVET-TLI: A novel combination of scanning vibrating electrode technique and time-lapse imaging for studying the localised corrosion of sacrificial zinc coatings**
   *Rebecca Bolton, Justin Searle, Geraint Williams*
   11th International Conference on Zinc and Zinc Alloy Coated Steel Sheet (Galvatech), Tokyo, Japan, 2017.